MICROBEAM ANALYSIS SOCIETY

TUTORIAL AND PROCEEDINGS

NINTH ANNUAL CONFERENCE

CARLETON UNIVERSITY
OTTAWA, CANADA
JULY 22-26, 1974

NINTH ANNUAL CONFERENCE

Presented by

MICROBEAM ANALYSIS SOCIETY

July 22-26, 1974

Carleton University

Ottawa, Canada

PREFACE

This is the Ninth Annual Conference of the Society, time enough for a fixed pattern to have set in, but instead we see continuing change both in emphasis and content, each indicative of a growing and vital organisation. It is particularly pleasing that the members at large are contributing in good measure to these changes. This promises well for the future of the Society.

While recognising that virtue is its own reward there is still great pleasure in thanking all those who gave, in one way or another, to make this meeting a success.

Rod Packwood,
Chairman   MAS 74

MICROBEAM ANALYSIS SOCIETY

1974 NATIONAL OFFICERS

President

Paul Lublin
GTE Labs

Past President

Don Beaman
Dow Chemical Co.

President-Elect

John Colby
Bell Telephone Lab

Treasurer

Dennis Brown
Naval Research Laboratory

Secretary

Mary Ann Giles
810 Prospect Ave.
Bethlehem, Pa.

Members at Large

Dave Kyser
IBM Research Lab

John Woodhouse
University of Illinois

Eugene White
Penn State University

ORGANIZING COMMITTEE

General Chairman	Rod Packwood
Vice Chairman	George Plant
Treasurer	Gerry Lachance
Technical Programme	Don Harris
Registration	Ken Pickwick
Tutorial Session	Jim Brown
Social Programme	John Taylor
Exhibits	Bernie Piwczyk
Ladies Programme	Prue Packwood Diane Harris

Others who have assisted include: Pierre Blais, Vic Chartrand, Terry Gould, Geoff Haggis, Camille Hanlan, Jim Hanlan, Vera Moore, Peter Sewell, Gunter Springer, and Vernon Sulway.

MICROBEAM ANALYSIS SOCIETY

COMMITTEES 1974

Awards Committee (all awards - student, Macres, photo exhibit)

L.S. Birks - Chairman		
O. Wells	G. Judd	J. Tabock
J. Colby	K. Heinrich	
J. Coleman	J. Bomback	
J. Woodhouse	D. Beaman	

Membership
M.A. Giles - Chairman
G. Fisher (Public Relations & Membership Drives)

Sustaining Membership
D. Beaman - Chairman
J. Tabock

Legal
P. Lublin - Chairman
M.A. Giles

Standards
A. Chodos - Chairman
D. Beaman
J. Bomback

Employment Services
J. Woodhouse - Chairman

Future Meeting Sites
P. Lublin - Chairman
J. Colby
A. Chodos
D. O'Boyle

Conference Committee
P. Lublin - Past
G. Plant - Present
A. Chodos - Future

Section Liaison (speakers tour, section support)

J. Colby - Chairman
D. Wittry
Chairmen of local sections

International Users Liaison
E. Lifshin - Chairman

Educational
G. White - Chairman
D. Beaman
D. Brown
J. Goldstein
J. Woodhouse

Publications
J. Goldstein - Chairman

Certificates & Scrolls
D. Kyser - Chairman

INVITED SPEAKERS

R. Jenkins
Philips Electronics Instruments
Mount Vernon, New York

E. Chatfield
Ontario Research Foundation
Mississauga, Ontario

J. Bomback
Ford Motor Company
Dearborn, Michigan

F. Claisse
Laval University
Quebec, P.Q.

W.C. Nixon
Cambridge University
Cambridge, England

P. Statham
Cambridge University
Cambridge, England

J. Morabito
Bell Telephone Labs.
Allentown, Pennsylvania

G. Springer
Falconbridge Nickel Mines Limited
Thornhill, Ontario

E. Lifshin
GE Research and Development Centre
Schenectady, New York

A.V. Crewe
University of Chicago
Chicago, Illinois

O.C. Wells
IBM Thomas J. Watson Research Centre
Yorktown Heights, New York

A.J. Tousimis
Tousimis Research Corporation
Rockville, Maryland

J. Goldak
Carleton University
Ottawa

W.T. Kane
Corning Glass Works
Corning, New York

N.C. MacDonald
Physical Electronics Industries, Inc.
Edina, Minnesota

G.K. Wehner
University of Minnesota
Minneapolis, Minnesota

SUSTAINING MEMBERS

1974

AMR CORPORATION
Burlington, Massachusetts

APPLIED RESEARCH LABORATORIES
Glendale, California

CAMECA INSTRUMENTS INC.
Elmsford, New York

CANBERRA INDUSTRIES INC.
Meriden, Connecticut

COATES AND WELTER INSTRUMENT CORPORATION
SUBSIDIARY OF AMERICAN OPTICAL CORPORATION
Sunnyvale, California

CPS, INC.
Sunnyvale, California

EDAX INTERNATIONAL, INC.
Prairie View, Illinois

ETEC CORPORATION
Hayward, California

HI-REL LABORATORIES
San Marino, California

IMAGE ANALYSING COMPUTERS, INC.
Monsey, New York

SUSTAINING MEMBERS
1974

INTERNATIONAL SCIENTIFIC INSTRUMENTS, INC.
Palo Alto, California

JEOL USA INCORPORATED
Medford, Massachusetts

KENT CAMBRIDGE SCIENTIFIC INC.
Morton Grove, Illinois

KEVEX CORPORATION
Burlingame, California

McCRONE ASSOCIATES
Chicago, Illinois

MICROPROBE SPECIALTIES COMPANY
Stanford, California

ORTEC INC.
Oak Ridge, Tennessee

PERKIN-ELMER ULTEK, INC.
Palo Alto, California

PHYSICAL ELECTRONICS INDUSTRIES, INC.
Edina, Minnesota

PRINCETON GAMMA-TECH, INC.
Princeton, New Jersey

The Corning Award

The Corning Glass Research Laboratory is sponsoring an annual award, worth $300, for "the year's most outstanding publication in the field of Microbeam Analysis."

The winner will be announced in Micronews in 1975.

Victor Macres Memorial Award

The Victor Macres Memorial Award was established in 1973 for the outstanding contribution in instrumentation presented at the annual meeting. The recipient will receive a citation and a $250 award. Selection will be announced during the annual meeting.

Previous Award Winner

1973:   Noel C. MacDonald
        Physical Electronics Industries, Inc.
        "The Third Dimension in Scanning Electron
        Microscopy: Scanning Auger Microscopy."

STUDENT AWARD RECIPIENTS

1974 winners to be announced.

Previous Award Winners:

1973: E.J. Barrett, A.J. Gancarz, and W.N. Lin

1972: K.Y. Chiu, T.E. Keller, H.C. Marciniak, B.J. Panessa, and R.R. Warner

1971: M.R. Jackson, W.K. Jones, J. Lebiedzik, J.C. Potosky, and R. Warner

MEETING ANNOUNCEMENT

TENTH NATIONAL CONFERENCE OF THE MICROBEAM ANALYSIS SOCIETY AND

SECOND JOINT CONFERENCE WITH THE ELECTRON MICROSCOPE SOCIETY OF AMERICA

Location: MGM Grand Hotel
            Las Vegas, Nevada

Date: August 11 - 15, 1975

For information concerning this meeting, please contact:

            Arrangements Chairman: Mr. A.A. Chodos
                                     Caltech 170-25
                                     Pasadena, CA 91109

            Program Chairman: Dr. Eric Lifshin
                                     General Electric Company
                                     Corporate R & D Center
                                     P.O. Box 8
                                     Schenectady, N.Y. 12301

The meeting will include a tutorial session on Monday, August 11th,
and technical sessions on Tuesday through Friday, August 12 - 15.
There will be a commercial exhibit in connection with the meeting.
The technical sessions will include all aspects of electron probe
analysis, energy dispersive spectrometry, scanning electron microscopy,
secondary ion mass analysis, Auger electron spectroscopy, ion scattering
spectrometry, electron spectroscopy chemical analysis, soft x-ray
emission, computer control and data reduction, instrumentation, and
applications.

Contributed papers are welcome and instructions to authors will be
provided through meeting announcements and the MicroNews.

TUTORIAL SESSION

Alumni Theatre B
Jim Brown, Chairman

Registration

Introductory Remarks by P. Lublin, President, MAS

INVITED SPEAKERS

Panel Discussion Session

PROCEEDINGS

SESSION I - SCANNING ELECTRON MICROSCOPY

Tory Theatre
William C. Nixon, Chairman

Registration

Introduction of MAS Officers

Paper
Number

1   INVITED PAPER: *"The Scanning Transmission Electron Microscope-Present Status and Future Prospects"*; A.V. Crewe, The University of Chicago.

2   INVITED PAPER: *"Backscattered and Low-Loss Electron Images in the SEM"*; O.C. Wells, IBM.

3   *"Dual Gun Electron Microscope for High Resolution TEM and SEM"*; P.S. Ong, University of Texas System Cancer Centre, and C.L. Gold, Technical Equipment Corp., Denver.

Intermission

4   *"SEM Backscattered Electron Imaging -- An Aid to Dust and Particulate Characterization"*; P.B. DeNee and J.L. Abraham, Appalachian Laboratory for Occupational Respiratory Diseases, Morgantown, W. Virginia.

⑤   *"Use of Time Derivative Transformations for Electron Micrograph Signal Processing"*; C.E. Fiori, D.E. Newbury, H. Yakowitz and K.F.J. Heinrich, National Bureau of Standards.

6   *"Monte Carlo Calculations of Type II Magnetic Contrast in the SEM"*; D.E. Newbury, H. Yakowitz and R.L. Myklebust, National Bureau of Standards.

Lunch

SESSION II A - BIOLOGICAL APPLICATIONS

Tory Theatre
Geoff Haggis, Chairman

Paper
Number

7   INVITED PAPER: *"Scanning Electron Microscopy and Microanalysis of Biological Materials"*; A.J. Tousimis, Tousimis Research Corp.

8   *"A Method for Electron Probe Microanalysis of Organic Components in Picoliter Samples"*; J.V. Bonventre and C. Lechene, Harvard Medical School.

9   *"Electron Probe Microanalysis of Isolated Cells: Red Blood Cells"*; C. Lechene, Harvard Medical School, C. Bronner and R.G. Kirk, Duke University.

10   *"SEM Identification of Biogenic Silica in Jute: Silica in Human Lung Following Exposure to Burning Jute"*; P.B. DeNee, J.L. Abraham, A.H. Gelderman, Appalachian Laboratory for Occupational Respiratory Diseases, Morgantown, W. Virginia, and G.B. Shaw, Jackson, Miss.

Intermission

11   *"Backscattered Electron Signal for Background Monitoring with Biological Tissue Samples"*; F.D. Ingram and M.J. Ingram, University of Iowa.

12   *"The Use of Frozen Sections in the Analysis of Bone"*; J.R. Coleman, P. Batt, P. Moran, University of Rochester, and R.R. Warner, Yale University School of Medicine.

13   *"Applications of Electron Microprobe Analysis to the Study of Silicon in Plants"*; S.L. Soni, Department of Agriculture, Ottawa.

End Session

SESSION II B - APPLICATIONS AND OTHERS

Alumni Theatre B
Mabel Corlett, Chairman

Paper
Number

14   INVITED PAPER: *"Applications for High Power Electron Beams"*; J. Goldak and M. Bibby, Carleton University.

15   *"Thin Films and Bulk Specimen X-ray Microanalysis in the Electron Microscope"*; A. Armigliato, CNR-Lamel, Bologna, P. Bergamini, CISE, Milano, and L. Morettini, Universita di Bologna.

16   *"An Investigation of Natural Deterioration of Aboriginal Rock Paintings by Scanning Electron Microscopy and X-ray Microanalysis"*; R.M. Myers and J.M. Taylor, National Museums of Canada.

17   *"Electron Energy Deposition Profiles in Thin Polymer Films"*; D.F. Kyser and K. Murata, IBM Research Laboratory.

Intermission

18   *"Real-Time Cathodoluminescent Spectroscopy"*; C. Michel and A. Sicignano, Philips Laboratories.

19   *"Experimental X-ray Mass Attenuation Coefficients between the M_I and M_V Absorption Edge of Gold"*; W.J. Steele, University of California.

20   *"Simultaneous Microprobe Analysis of Silicates for Nine Elements using Wavelength Dispersive System"*; E. Jarosewich, C. Obermeyer and J. Nelen, Smithsonian Institute.

End Session

Reception and Buffet

SESSION III - ENERGY DISPERSIVE ANALYSIS

Tory Theatre
George Plant, Chairman

Paper
Number

21   INVITED PAPER: *"A Comparison of Some Quantitative Techniques for Treating Energy Dispersive X-ray Spectra"*; P. Statham, University of Cambridge.

22   *"Quantitative Microanalysis with Minimum Pure Element Standards"*; J.C. Russ, EDAX Laboratories.

23   *"Quantitative Analysis of Sulphides and Sulphosalts Using an Energy Dispersive Spectrometer"*; M.I. Corlett and M. McDonald, Queen's University.

24   *"Comprehensive Qualitative and Quantitative Analysis of Energy Dispersive X-ray Spectra"*; T.D. Kirkendall, COMSAT Laboratories.

Intermission

25   *"Collimator for Energy Dispersive X-ray Analysis of Radioactive Materials in a Scanning Electron Microscope"*; U.E. Wolff, General Electric, and R.C. Wolf, Microspec Inc.

26   *"Advances in Quantitative Energy Dispersive Spectrometry"*; D. Beaman and L.F. Solosky, The Dow Chemical Company.

Discussion of Session Papers

Lunch

SESSION IV A - SCANNING ELECTRON MICROSCOPY

Tory Theatre
Oliver Wells, Chairman

27   INVITED PAPER: *"Television Scanning Electron Microscopy of Dynamic Events"*; W.C. Nixon, Cambridge University.

28   *"A New System for Dynamic Stereo Observation in the SEM"*; E.J. Chatfield and V. Nielsen, Ontario Research Foundation.

29   *"A Rapid Assessment of Mercury Ion Implantation Damage in Boron-Doped Silicon Using the Scanning Electron Microscope"*; E.M. Schulson and D.A. Marsden, Atomic Energy of Canada Ltd.

30 *"Field Emission Microscopy Using High Probe Current Densities"*;
L.M. Welter, Coates and Welter Instrument Corp.

31 *"Plasma Etching for SEM and EMP Examination of Microelectronic
Devices"*; A.M. Sheble, T.P. Teel, J.R. Devaney, Hi-Rel Labs.

End Session.

SESSION IV B - AUTOMATION AND COMPUTER APPLICATIONS

Alumni Theatre B
Gunter Springer, Chairman

32 INVITED PAPER: *"A CAMAC Automated Electron Microprobe"*;
W.T. Kane, Corning Glass Works.

33 *"Applications with a Computer Controlled Electron Probe
Microanalyzer System"*; S. Okudera, H. Ohyi and Y. Harada,
JEOL Ltd.

(34) *"Automation of an Electron Probe for Biological Analyses"*;
T. Moher, C.M. Aden, R. Beeuwkes, A. Sanderson and C. Lechene,
Harvard University.

(35) *"Electron Microprobe Computer Imaging"*; W.B. Estill, H.D. Jones
and D. Benthusen, Sandia Laboratories.

Intermission

36 *"Data Reduction System for Electron Probe Microanalysis"*;   With drawn
E.D. Glover, University of Wisconsin.

37 *"A Real Time Approach to Laboratory Automation"*; W.T. Hatfield,
M.F. Ciccarelli, R.B. Bolon and E. Lifshin, General Electric
Company.

End Session.

MAS Business Meeting (Tory Theatre)

Cash Bar

Banquet

SESSION V - QUANTITATIVE APPLICATIONS

Alumni Theatre B
John Rucklidge, Chairman

Paper
Number

38   INVITED PAPER: *"Quantitative Electron-Probe Analysis: Review of Iterative Procedures and Evaluation of Electron Backscattering"*; G. Springer, Falconbridge Nickel Mines Ltd.

39   *"The Measurement of Depth Distribution Curves at Electron Energies from a few to 15 KeV"*; J.D. Brown and L. Parobek, The University of Western Ontario.

40   *"Testing and Development of a Monte Carlo Program for Modelling Electron - Specimen Interactions"*; R.L. Myklebust, D.E. Newbury, H. Yakowitz and K.F.J. Heinrich, National Bureau of Standards.

41   *"Microprobe Technique using APL for Nondestructively Determining the Concentration Profile of Si in AL/4 Cu Thin Films"*; G. DiGiacomo, IBM.

Open Discussion.

Lunch

SESSION VI A - AUGER, SECONDARY ION MASS SPECTROMETRY AND ION MICROPROBE

Tory Theatre
J.M. Morabito, Chairman

42   INVITED PAPER: *"Scanning Auger Microanalysis"*; N.C. MacDonald, Physical Electronics Industries, Inc.

43   INVITED PAPER: *"Sputtering Aspects in Surface Analysis Methods"*; G.K. Wehner, University of Minnesota.

44   *"Quantitative Auger Spectroscopy of a Copper-Gold Binary Alloy Series"*; D.K. Conley and D.F. Lesher, Western Electric Co.

Intermission

45   *"Auger Electron Images in a Scanning Electron Microscope"*; E.K. Brandis, IBM.

46   *"Changes in the TiO_2 Auger and Appearance Potential Spectra Induced by Incident Electron Beam Interaction"*; J.S. Solomon, University of Dayton, M.B. Chamberlain and W.L. Baun, Wright Patterson Air Force Base.

47   *"A Comparison of Surface Chemistries Obtained by Using Ion Scattering Spectrometry and Auger Electron Spectroscopy"*; W.D. Bingle, National Steel Corp.

48   *"Ion Scattering Spectrometry Depth Profile Analysis Using Beam Rastering and Signal Gating"*; J.A. Leys, J.T. McKinney and T.W. Rusch, 3M Company.

Lunch

SESSION VI B - AUGER, SECONDARY ION MASS SPECTROMETRY AND ION MICROPROBE

Tory Theatre
Noel MacDonald, Chairman

49   INVITED PAPER: *"Materials Characterization by Secondary Ion Mass Spectrometry 'SIMS'"*; J.M. Morabito, Bell Telephone Laboratories.

50   *"A High Mass Resolution Capability for the CAMECA Ion Analyser"*; R.K. Lewis and J. Vastel, Cameca Instruments Inc.

51   *"Metallurgical Applications of Secondary Ion Mass Spectrometry"*; J.M. Walsh, Pratt and Whitney Aircraft.

52   *"Ion Scattering Spectrometry and Secondary Ion Mass Spectroscopy: Two Complementary Techniques"*; J.A. Leys and J.T. McKinney, 3M Company.

Intermission

Panel Discussion on Surface Analysis

Don Beaman, Chairman

G. Mateescu, Case Western Reserve University
G.K. Wehner, University of Minnesota
R.F. Goff, 3M Company
R. Weber, Physical Electronic Industries
P. Sewell, National Research Council
E. Brandis, IBM
J. Morabito, Bell Telephone Laboratories

Canadian Probe Users' Group Business Meeting

SESSION VII - ENERGY DISPERSIVE ANALYSIS

Alumni Theatre B
Don Beaman, Chairman

Paper
Number

53   INVITED PAPER: *"The Use of Solid State X-ray Detectors for Obtaining Fundamental X-ray Data"*; E. Lifshin, General Electric Company.

54   *"TEM X-ray Analysis of Submicron Particles"*; L. Berenbaum and A. Cammarano, IBM.

55   *"The Application of the Harwell Active Pulse Processor to Energy Dispersive X-ray Analysis in the Electron Microprobe"*; P. Statham, University of Cambridge.

56   *"A Monochromatic X-ray Probe for the Analysis of Trace Elements"*; P.S. Ong and H.L. Cox, The University of Texas System Cancer Center.

Intermission

Session devoted to Late-breaking Developments and Highlights of the Russian Meeting.

SUMMARY
OF
PAPERS

Design and Application of Detection Systems in Electron Probe Microanalysis

R. Jenkins
Philips Electronic Instruments
750 South Fulton Ave.
Mount Vernon, New York 10550

General

All X-ray detectors work by making use of the fact that X-rays ionise matter. Ionisation produces electrons and positive ions and the difference between the various classes of detector is the subsequent fate of these electrons.

There are many classes of X-ray detectors including photographic film, Geiger detectors, gas proportional detectors, scintillation detectors and semi-conductor detectors. In electron probe microanalysis, the gas proportional detector is by far the most common detector although the Si(Li) semi-conductor detector has gained in popularity during the past few years. The Si(Li) semi-conductor detector is of great importance since it also provides the basis of the energy dispersive spectrometer which is particularly attractive in E.M. and S.E.M. work.

Both the gas proportional detector and the Si(Li) semi-conductor detector are "proportional" detectors. A proportional detector is one in which the size of the voltage pulse produced by the detector is proportional to the energy of the measured X-ray photon. This feature allows discrimination against unwanted energies by rejecting certain pulse sizes.

A "counter system" generally involves a detector, a pre-amplifier, a main amplifier, a pulse shaper, a pulse height detector and a pulse counter.

FIGURE |

THE GAS FLOW PROPORTIONAL COUNTER

Consists of:

1) Cylindrical chamber (typically 2 cm diameter)

2) Anode wire (typically 50 μm diameter)

3) Window (typically thin plastic or a supported organic film)

4) Collimator

5) Flow gas connectors allowing the continuous replacement of gas which may leak through the thin entrance window

6) Pre-amplifier.

The counter is filled with an ionizable gas and a "quench" gas. The ionizable gas is the source of ionized electrons and the quench gas reduces the influence of positive ions. Typical gas mixtures are

P10   90% Ar + 10% CH_4 (or CO_2)

P50   50% Ar + 50% CH_4 (or CO_2)

Pure methane

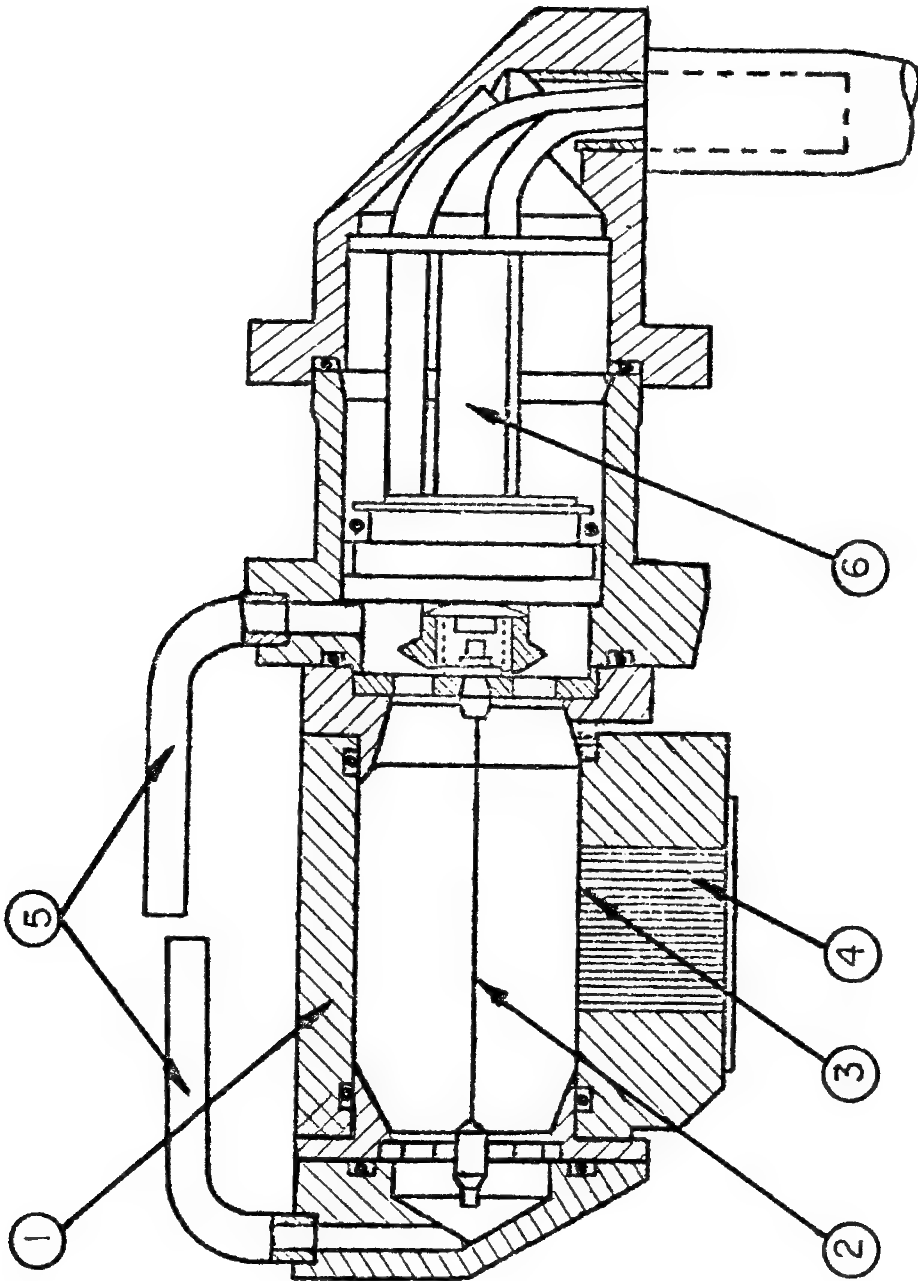Ne + 3% isobutane

He + 10% CH_4

Fig. 1

FIGURE 2

THE BASIC CIRCUITRY OF THE GAS PROPORTIONAL COUNTER

A high voltage of about 1.5 kV is applied via the leak resistor R_2. The main function of the leak resistor is to inhibit charge leakage from C_2 during the decay period. The capacity of the detector itself is indicated schematically by Cd and is typically 100 pF. The size of the voltage pulse produced at C_2 can be calculated thus.

eg., A CuKα photon has an energy of 8.05 kV. This will yield $8040/26 \simeq 300$ ion pairs. Assuming a gas gain of 10^4 then 3×10^6 electrons per photon will be produced. The charge carried by a single electron is 1.6×10^{-19}C, the total charge will equal 4.8×10^{-13}C. For a capacitance of Cd = 10^{-10}F, the voltage would be

$$\frac{4.8 \times 10^{-13}}{10^{-10}} \simeq 5 \text{ mV}$$
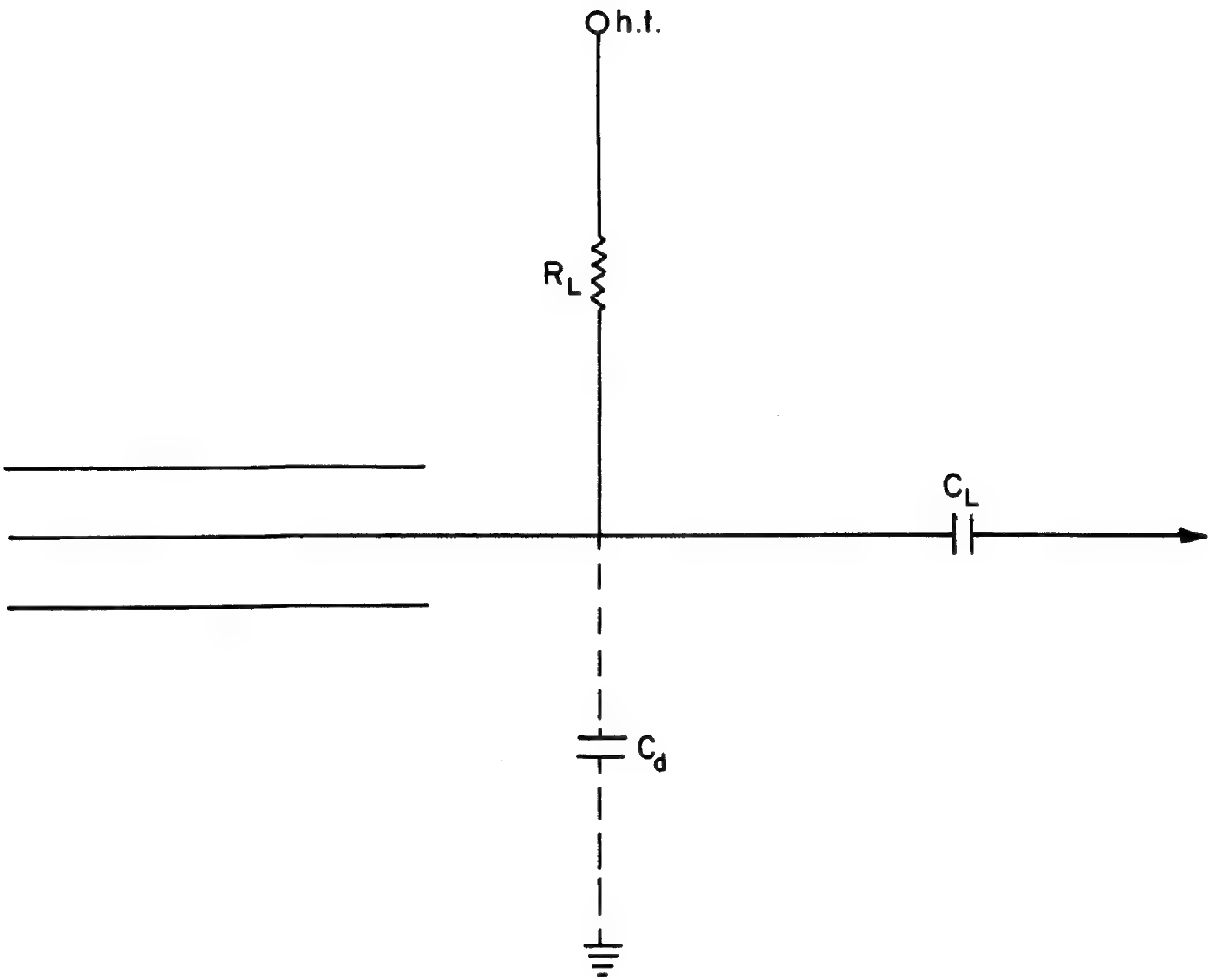
Fig. 2

FIGURE 3

RESOLUTION OF THE GAS PROPORTIONAL COUNTER

The usual statistical processes can be used to calculate the resolution of a detector from the number (n) of primary electrons. The standard deviation should equal $\sqrt{n}$, however in practice this is reduced by an amount described by the Fano factor (F), typically between 1/2 and 1/3 for the Ar/CH₄ detector. The theoretical resolution R for an argon detector (argon requires about 26.4 eV to produce an ion pair) for a photon of energy E is equal to

$$R = F \cdot n^{1/2} \qquad \text{or} \qquad \frac{F \times 100}{\sqrt{n}} \quad \%$$

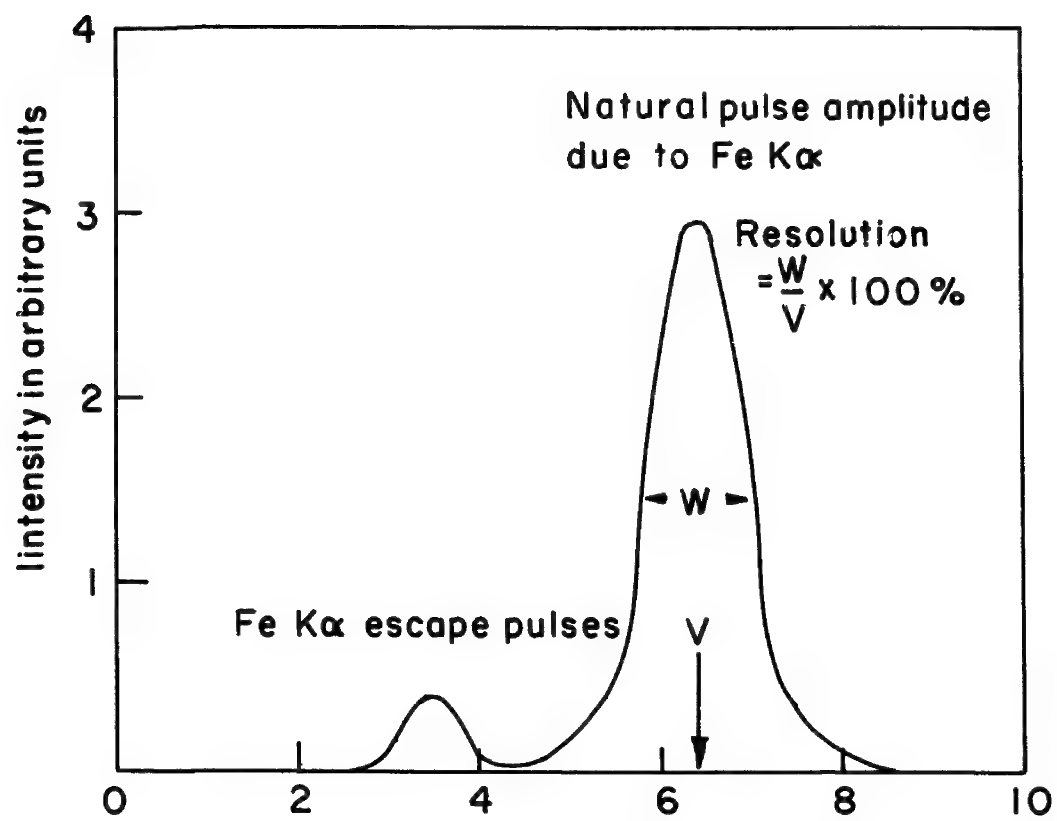$$= 2.36 \times 100 \times \sqrt{\frac{(0.0264)}{E}} \qquad \approx \frac{38}{\sqrt{E}} \quad \%$$

Fig. 3

FIGURE 4

SHIFT IN PULSE HEIGHT WITH COUNTING RATE

This occurs when too many pulses arrive within a given time period to allow individual pulses to be resolved. An artificial baseline may be set up $E_A - E_B$ at a higher level than the time baseline E_A. This causes the measured pulse height to shift to lower values at higher counting rates.
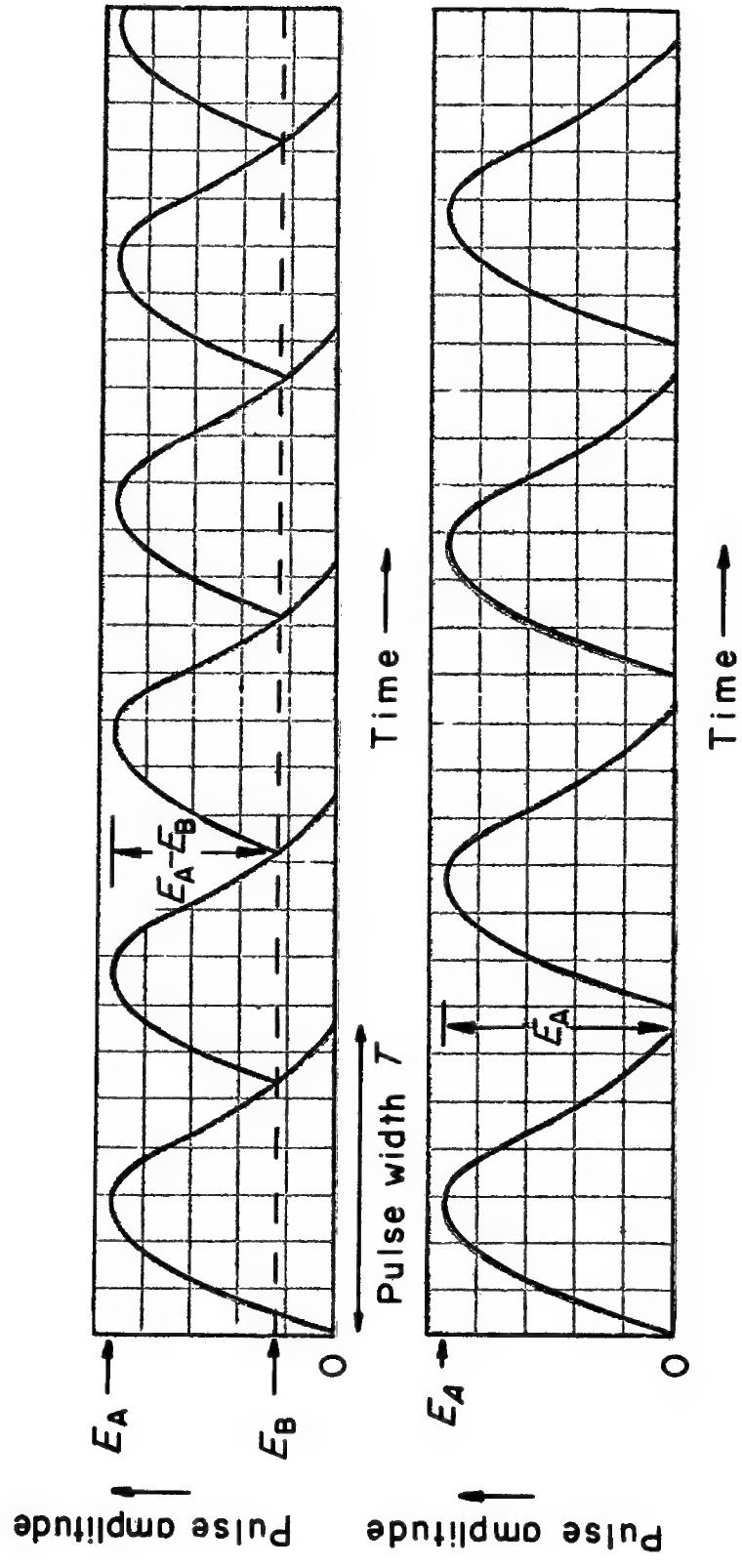
Fig. 4

FIGURE 5

VARIATION OF FIELD AS FUNCTION OF DISTANCE FROM THE ANODE WIRE

Roughly 2×10^4 volts per cm are required to initiate gas amplification. The figure shows the variation of the field as a function of distance from the anode, for different anode diameters. The radius (Ir) of the volume of amplification is given by

$$Ir = \frac{Va}{Er} \cdot \frac{1}{\ln (r_2/r_1)}$$

where Va is the applied voltage, r_2 the radius of the counter body and r_1 the radius of the anode wire.
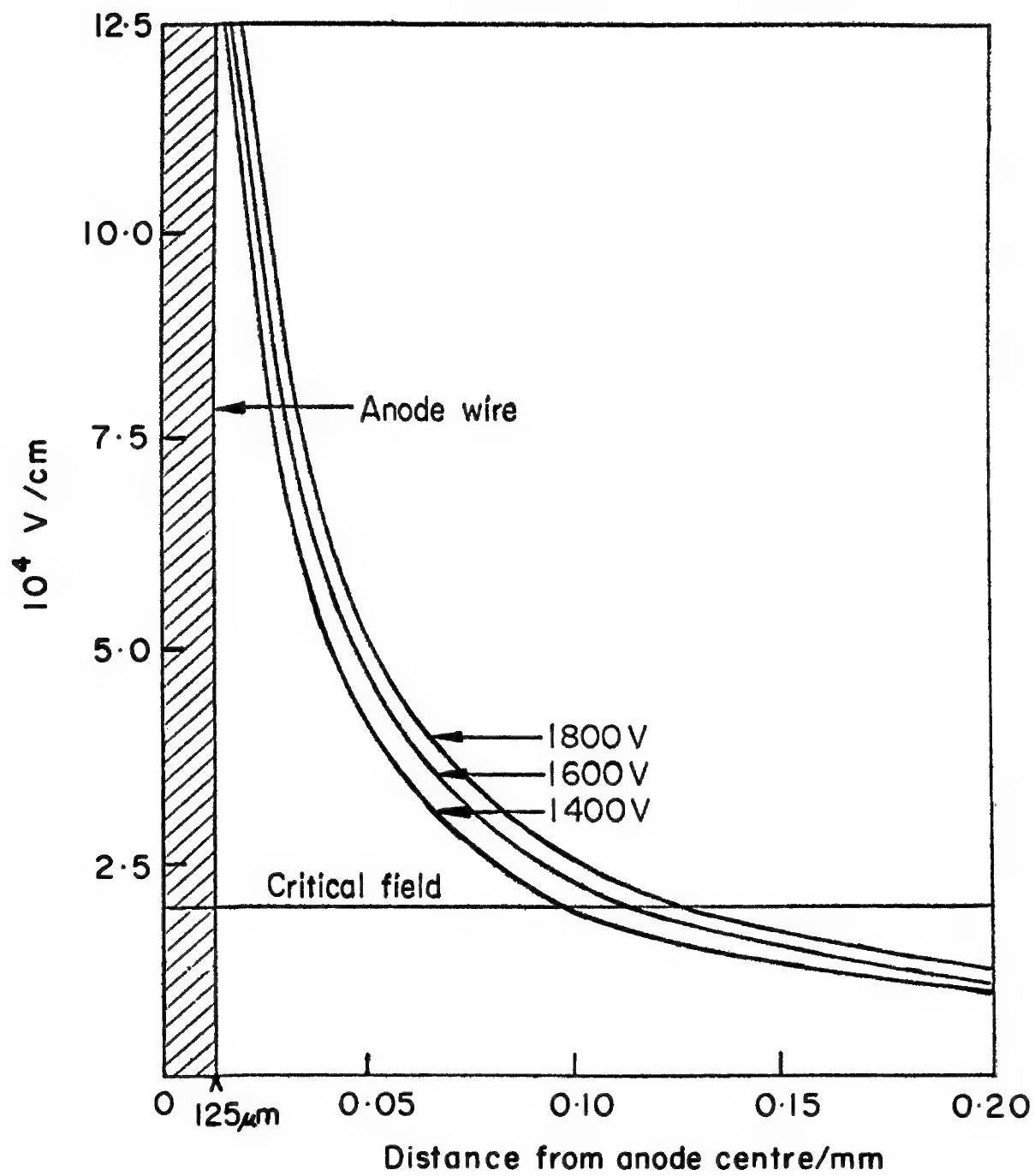
Fig. 5

FIGURE 6

THE Si(Li) DETECTOR DIODE

Semi-conductor detectors operate by the creation of electron/hole pairs in the depletion layer of a reversed p-i-n junction. The detector is a piece of high purity silicon, "drifted" with lithium to increase the intrinsic or "sensitive" layer. An X-ray photon produces a "cloud" of electron hole pairs which are swept from the detector by a potential applied across the detector.

The resolution of the Si(Li) detector is given by

$$R = \sqrt{(\sigma \text{ noise})^2 + (2.35 \ (e.F.E.)^{1/2})^2}$$

where σ noise is about 100 eV and e is equal to about 3.8 eV. F is about 0.125 for Si(Li).

4-16 mm diameter

n-Type Si

Gold

Schottky barrier contact

0.1 μm Si dead layer

Si(Li)

3-5 mm

-1000 V

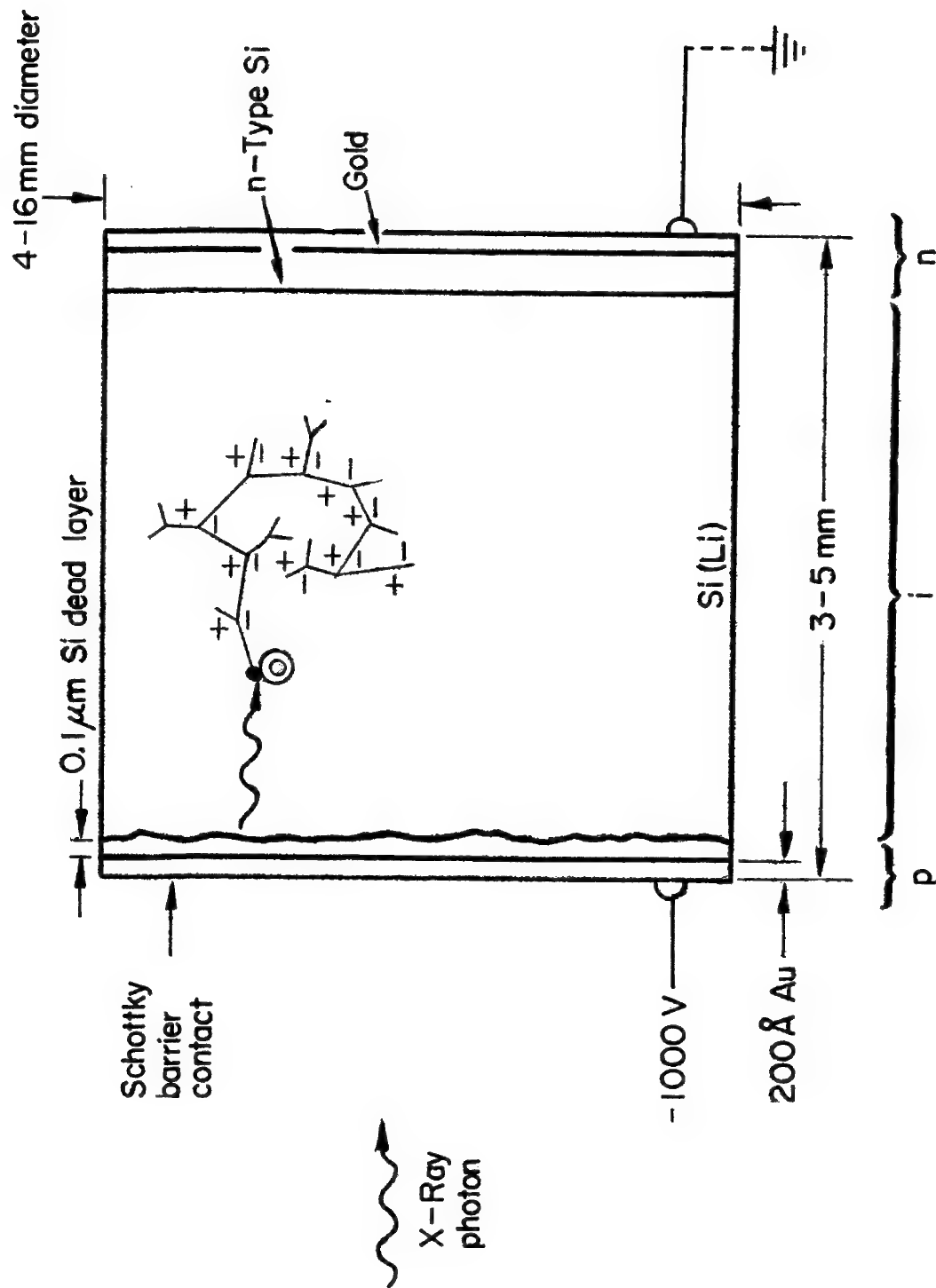200 Å Au

X-Ray photon

n

i

p

Fig. 6

FIGURE 7

THE PULSE HEIGHT SELECTOR

Since voltage pulses are proportional to photon energy, rejection of certain voltage pulses effectively removes certain photon energies. An acceptance window is selectable and only pulse levels around V_B fall within this window. Use of the pulse height selector can reduce background and remove harmonic overlaps. These overlaps occur since a crystal of given 2d set at a given θ angle will diffract the 1st order of λ, the second order of $\lambda/2$, the third order of $\lambda/3$, and so on, since all of these conditions satisfy the Bragg Law. Since, however, λ has energy E, $\lambda/2$ energy of 2E, $\lambda/3$ energy of 3E, etc., pulse height selection can be employed to remove 2E and 3E, hence $\lambda/2$ and $\lambda/3$.
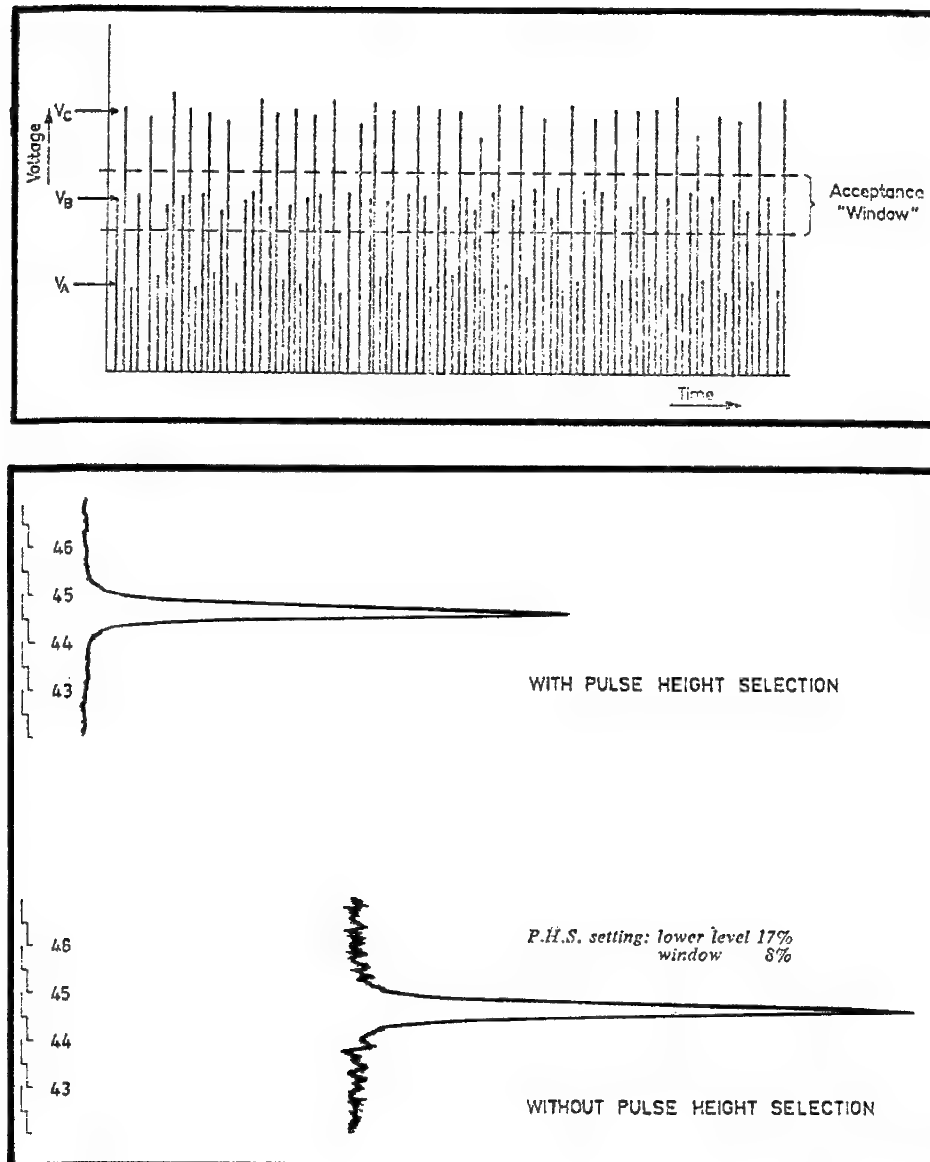
Fig. 7

SOME PRACTICAL ASPECTS OF MICROPROBE ANALYSIS

by

E. J. Chatfield
Department of Applied Physics
Ontario Research Foundation
Sheridan Park, Mississauga
Ontario, Canada

ABSTRACT

This discussion introduces the novice microprobe user to some of the practical problems encountered, especially in the handling of unusual specimens. Various methods of information display are considered, including qualitative, semi-quantitative and accurate quantitative techniques.

Image improvement techniques, such as signal differentiation and pulse rate discrimination are described, and simple methods to prepare colour composition X-ray distribution micrographs are discussed. Associated computer programmes have been prepared which permit automatic multi-element searches to be made, and other simple programmes are described which facilitate the conversion of quantitative elemental data into compound concentrations and molecular ratios where these are required.

Several examples are given in which the microprobe's application to air pollution and legal investigations is illustrated.

INTRODUCTION

The microprobe analyser, or the SEM with X-ray measurement facilities, offers a very versatile method of solving many industrial problems. The new user, particularly in a service capacity, will often be asked to deal with a very wide range of specimens, many of which will require the development of special techniques. This paper is directed towards users who have yet to encounter many of the vicissitudes of the microprobe analyst's life. Examples are given illustrating a number of techniques, most of which have found regular application in the author's laboratory.

LOCATION OF ANALYSIS AREA IN THE MICROPROBE

A frequent request is for analysis of a specific feature or inclusion on a relatively featureless polished section of material which has been located under the optical microscope. Relocation of this area in the microprobe is often not easy, since the feature may only be a few microns in size, in a specimen measuring several centimetres. The design of a microprobe analyser also precludes the incorporation of a good light optical system; in general, by the time the electron optics, X-ray optics and electron collectors have been accommodated, there is little available space for optical components. However, all microprobes have light optics systems which are adequate for specimen location, but often it is

difficult to align the light optical axis exactly with the electron optical axis. In this case, although the feature of interest could be relocated using the light optics, the electron optical image on the CRT would be of a different area. The light optics generally produce an image of a few hundred times magnification, and if the feature is to be located on the CRT image, a search must be conducted at a similar electron optical magnification. Unless the two optical axes are badly misaligned, the feature will eventually be found. The process is aided by use of a microscope marking objective. This device replaces one of the objectives of the optical microscope, and permits a diamond to scribe a small circular scratch on the specimen surface; the desired feature is then contained within the circle.

Some specimens, for example a polished cement section, do not lend themselves to this technique since their surfaces are brittle. An attempt to use a marking objective will pull out areas of the surface close to that being studied. Furthermore, the detail in such a sample is very complex and requires the use of high magnifications: thus relocation of a specific crystallite only a few microns in size is a major problem. To add to the problems, cement consists of elements which have similar atomic numbers; thus all of the crystallites have about the same grey levels in a backscattered or specimen current image. Light optical contrast is normally obtained by etching, but for the microprobe examination the specimen must be lightly repolished to eliminate preferential etching effects on the analysis results. Thus we have a sample in which a specific crystal has been selected for relocation in the microprobe; it is then repolished, after which both optical and electron optical contrasts are poor, even assuming that the crystallite has survived the repolishing operation.

One method by which relocation in some samples can be achieved is by use of "alphabet" copper support meshes sometimes used in conventional transmission electron microscopy. A typical grid of this type is shown in Figure 1. Such a grid can be cut along its diameter using a scalpel, and under the microscope it is cemented to the specimen surface using conducting silver paint. A map reference can then be used to locate a crystallite to within a few microns. In practice, optical micrographs at low and high magnifications assist in relocation in the instrument.

A more serious problem is encountered if the specimen has to be repolished after the optical examination. In this case a device is used which is designed to fit a 1 inch metallurgical mount, and consists of a number of alphabet grids cemented into holes in the end face of a cylindrical cup. The device is rotated so that the desired feature is under one of the grids. The screw is tightened, leaving an indentation in the side of the mount. A map reference is then taken from the grid, and micrographs are taken at low and high magnifications to assist in relocation. Using the same device, or an identical one, the selected area can be relocated to within a few microns, when the selected crystallite can be found by comparison of the electron optical image with the optical micrographs.

This technique has been used so that a client in a California laboratory could specify particular 10μm features for analysis in a microprobe situated elsewhere, after the specimens had been lightly repolished. A point worth mentioning is that some microscopes produce laterally inverted micrographs, leading to considerable confusion when relocating a feature if this characteristic is not known. A typical optical image of such a cement is shown in Figure 2. After repolishing,

the contrast was extremely poor, but the same area can still be located, as shown in Figure 3. The corresponding low contrast specimen current image using high video gain is shown in Figure 4. It can be seen that the required features are recognisable, despite the loss of some crystallites during the polishing operation.

NON-CONDUCTING SPECIMENS

A specimen which contains non-conducting inclusions, or which is totally non-conducting, may charge up under the electron beam. Eventually, these local charges deflect the beam and result in an unsatisfactory image. Application of a thin vacuum deposited film of a conducting material to the surface eliminates this problem. The usual materials for this purpose are carbon or aluminum, though alternative materials are sometimes used. It is obviously important that the coating material should not be any one of the elements being analysed. Where accurate quantitative results are to be obtained from such a coated specimen, it is also important that the standards be coated in a similar manner. If the specimen and standards are coated simultaneously, using similar source-surface geometries, the coating thicknesses on both will in general be similar. If two coating operations are used, one for the specimen and one for the standards, it is difficult to ensure similarity of the coatings.

The vacuum coating operation should be performed shortly before the measurements are made. In common with gold coatings often used in scanning microscopy, the surface sometimes distorts on exposure to the atmosphere, leading to electrically isolated areas and charging problems.

CHOICE OF INFORMATION DISPLAY

When working with a sample in the instrument, many different methods are available to the operator for presentation of the output data.

Initially, it is determined whether quantitative, semi-quantitative or qualitative output is required.

QUALITATIVE DISPLAYS

There are two principal methods of qualitative display, the X-ray distribution image and the line scan. The choice between these is made after consideration of the individual problem. To produce an X-ray distribution image, a well focussed electron image is initially formed. The spectrometer is adjusted to an X-ray line of the desired element, and a scan of the same area is made, displaying X-ray pulses as intensity modulation on the CRT in place of the specimen current. A typical specimen current image is shown in Figure 5, and the corresponding X-ray distribution image for chromium is shown in Figure 6. These figures show segregation of chromium carbides in a steel sample. In general, if a well resolved X-ray image is to be produced, more than 10^5 X-ray counts are required during the exposure. This procedure can be repeated for all the elements of interest in the sample. If count-rates are low, then exposures up to 10 minutes or more can be used to accumulate a satisfactory image. If desired, X-ray distribution images from three elements can be prepared as one colour micrograph, using colour separation filters.[1] There are a number of techniques which can be used to achieve this. Three distributions can be combined on colour film using colour filters during the exposure, but this involves investment of perhaps 30 minutes exposure time on the instrument before the image can be seen. During this time the image may have drifted on even the best instrument, leading to a loss of registration between the three images. A further reason for rejection of this approach is that the phosphor on many display CRT's is very deficient in red. Indeed, exposures for the red

image may not even be possible because of film reciprocity failure. Experience has shown that the most satisfactory technique is to record the three images separately on black and white film. The images are then combined photographically using colour filters and a colour film. Polacolor is an excellent medium for this process.

A further refinement on the colour display technique was reported by Yakowitz and Heinrich,[2] in which the poor resolution of the X-ray distribution was recognised and improvement on this is achieved by combination with both the specimen current image and the differentiated image. This process may be regarded as colouring of a partially differentiated specimen current image according to its composition. The presence of three spectrometer channels on an instrument permits the use of simultaneous tri-colour display of three elements, using a colour display CRT. However, the simplicity of photographic composition techniques is reflected in their cost, and it is doubtful if the expense of more sophisticated display methods can be justified.

In the cases of high background count-rates, pulse rate analysis[3] is sometimes applied to the signal forming the X-ray image. In the ordinary way, all X-ray pulses, perhaps already selected by pulse height discrimination, are displayed on the CRT to form the image. Using pulse rate analysis, these pulses are passed to the CRT only if they occur within a specified time interval following the preceding one. An increase in the contrast of the X-ray image is thus obtained.

Where the X-ray count-rate is low, accumulation of a satisfactory X-ray distribution image will often be time consuming, and if the background is significant, the image may not have adequate contrast. In these cases, the line scan is usually used as the display method. In this

case a double exposure is made, in which a graph of X-ray count-rate is
superimposed on the electron image, corresponding to a particular straight
line across the specimen. A typical line scan is shown in Figure 7,
illustrating the lead content in a transverse section of pottery glaze,
where an attempt had been made to cover the surface with glaze of a lead
free formulation. Although the result is not quantitative, conclusions
can be drawn about relative concentrations, and for this reason the line
scan and uncorrected point X-ray counts are referred to as semi-quantitative
data.

QUANTITATIVE OUTPUT

Where accurate quantitative results are required, it is necessary to
correct the observed X-ray count-rates for dead time, background, atomic
backscatter, mass absorption, and fluorescence effects. For this purpose
there are probably rather more computer programmes available than there are
microprobe operators. Copies of these programmes are generally available
from the particular author, and the newcomer to the field would be well
advised to use one of these, at least initially. The most well known of
these are the various versions of MAGIC,[4] which are simple to use in that
all of the required atomic data are either held in an internal computer file
or are calculated at execution time. A minimum of input data is required to
use the programme, and the majority of elemental systems are handled
satisfactorily. However, there are many others, and the final one chosen is
a matter of personal preference. Inevitably, some requirement will arise
which is not covered by existing multi-element programmes, and the programme
SEQUA developed by the author is one example of this. It is basically a
single element version of Colby's MAGIC, for use where one element is
measured, and only the ratios of the remaining elemental concentrations are

known. Such programmes are useful where the other elements are not amenable to quantitative microprobe measurements, e.g., H-Ne, or where some of the elemental concentrations are already known accurately. In general, the correction procedures allow results to be obtained to an accuracy of about 1% of the amount found.

The precautions required in order to obtain this accuracy are well known. As little as 1° error in the take-off angle can be a serious effect which gives noticeable errors.[5] The specimen height is critical, especially at low take-off angles. It is particularly important that the specimen and the standards are in turn accurately positioned on the Rowland circle during the X-ray counting periods. This is usually arranged by optically focussing the surface under examination, using the microprobe light optics. The effects of topography are also serious, becoming more so when low energy X-ray lines are being measured.

ASSOCIATED COMPUTER TECHNIQUES

On-line applications of both the mini-computer and larger machines to the microprobe have been reported by a number of authors at this conference in previous years. Some degree of automation has been achieved, and in many cases the results are corrected before output. If an automated or programmed spectrometer is incorporated on the instrument, a convenient alternative to the on-line mini-computer is available. The spectrometer can be pre-programmed to count at specific principal X-ray lines for a number of elements, outputting the counting results on paper tape. This can then be processed by time-shared computer, which performs significance tests and compares the counts with a file of standard counts obtained previously. The programme can then report the elements present and their uncorrected concentrations. Such a semi-automated approach permits release of the operator for other duties whilst a

routine elemental search is made. A typical output from such a programme is shown in Figure 8. However, it should be appreciated that interfering X-ray lines will sometimes cause errors of identification. Using this technique, absence of a significant X-ray count at a principal line position indicates absence of the element concerned, but a detected peak should be confirmed manually to eliminate the possibility of interference by another element.

The elemental concentrations found in an accurate quantitative analysis are often not the final results desired. Results expressed as oxides, carbides, sulphides, etc, are frequently required, and it has been found that a programme to convert to these is useful. A file of named compounds is stored and conversion of elemental concentrations to compound concentrations and molecular ratios is performed automatically.

EFFECTS OF TOPOGRAPHY

A rough specimen surface will result in a shielding effect in some areas, where X-rays generated at the bottom of a depression are absorbed by the surrounding higher areas en route to the detector. Nevertheless, the microprobe user will often be required to examine surfaces which are not ideal; it is important, therefore, that the user interpret these effects correctly. For example, an X-ray distribution image is virtually meaningless if the specimen surface is rough. However, some semi-quantitative conclusions can be drawn if the electron image is compared with point counting results or line scans. In particular, detection of soft X-rays from a point may be taken as evidence for a direct line of sight to the detector. In this analysis, the direction of the X-ray spectrometer on the electron image must be known. This can be determined easily by examination of a specimen having known topography.

The examination of small particles is required frequently in air

pollution work, and topography is of particular importance. An understanding of the spectrometer direction, combined with specimen rotation, allows approximate compositions of most areas of such particles to be obtained. In a similar way, tilting of the specimen permits the interior surfaces of corrosion pits to be examined.

UNUSUAL PROBLEMS AND TECHNIQUES

The microprobe analyst is frequently confronted by problems which demand the use of unusual techniques. A combination of microprobe analysis with some chemical interpretation is a very powerful tool in the solution of many industrial problems. The following are a few of the more interesting examples.

THIN SURFACE FILMS

A razor blade produced by a well known British manufacturer was investigated on behalf of an equally well known North American manufacturer. The presence or absence of a pure chromium film, 200Å thick, on the blade surface was to be determined. The blade material was stainless steel, which itself contains chromium. In Figure 9, the chromium intensity ratio is plotted as a function of accelerating voltage, down to 1kV. This approaches unity at low kV, thus indicating the presence of such a film. The presence of chromium in the substrate converted an otherwise simple problem into one demanding a more specialized approach.

FLUORINE ANALYSIS IN POLYMERS

Conventional determination of halogens in halogenated polymers, particularly in mixed polymers such as Kel-F, gives rise to some difficulty. The microprobe offers an alternative means of quantitative analysis for such materials. A focussed beam at 10kV, however, damages the specimen, and a static probe is capable of producing a deep cavity. These specimens can be

successfully analysed using a defocussed beam, with lithium fluoride as the fluorine standard. The polymers were coated with aluminum, as was the standard. The results are processed by a computer programme SEQUA, based on Colby's MAGIC, assuming that the ratios only of other elements present are known. Typical results are shown in Table 1 for two fluorinated polymers of known composition. The results indicate that accurate quantitative analysis of light elements is sometimes possible if the matrix elements are also of low atomic numbers.

AIR POLLUTION AND LEGAL INVESTIGATIONS

Many environmental investigations are aided by the microprobe, and a proportion of these terminate in a court appearance, in which microprobe data is interpreted as part of expert testimony. In these cases it is important to prepare reports which are informative to the legal profession. Several such cases have already been completed in which the microprobe data was critical. In one such case, the first conviction under new Ontario legislation for "property damage by emission of a damaging substance" was recently obtained. In this case, proof was obtained by the microprobe that staining of the painted surfaces of automobiles was due to iron dust fallout from a nearby foundry, and not as a consequence of corrosion of the steel substrate. Fractured sections of paint chips demonstrated that the stains consisted of iron oxides, and that these did not extend below the surface.

In another case, the entire complement of vehicles on a parking lot were found to have their aluminum trim components badly corroded after only a few hours exposure. The corrosion pits contained sulphur compounds and localised iron particles. The presence of a metal plating operation using sulphuric acid only 400 yards upwind on the day in question was quite

sufficient to implicate the company concerned.

A company advertising the adherence properties of its paint to rusted metal surfaces was taken to court by a user, who had found that this paint flaked away a short period after application. Microprobe analysis of paint sections showed that a graphite primer had been used, a procedure specifically excluded in the printed instructions. The manufacturer was then able to argue successfully in court that he could hardly be held responsible for the adherence of another manufacturer's graphite primer. Adherence problems in paint have often been investigated, and even where the colours of the various coats are identical, it is usually possible by line scans to detect any faults in the technique of application. Frequently the user has applied one or other coat too thickly, which results in flaking.

MICROINCINERATION AND OTHER SPECIAL PREPARATION TECHNIQUES

In many cases the specimen may be entirely unsuitable for direct microprobe work. Biological samples, and a bottle of Athabasca tar sand are two examples. It is often possible to prepare suitable samples from such materials in order to answer specific questions. Plasma oxidation methods permit low temperature ashing of biological sections,[6] leaving the unashable materials in situ. The specimen can then be analysed easily in the microprobe, and compared both with the optical and transmission electron microscope images obtained prior to the ashing step. In the case of the tar sand extract, the presence or absence of clays in the $3\mu m$ to $0.1\mu m$ size range was to be determined. The oil was solvent extracted, filtered and the filter examined for particles containing both aluminum and silicon. Further investigation by selected area electron diffraction confirmed the presence of clays having hexagonal symmetry, and the SEM

permitted a size distribution to be obtained. This was an example where all three major instruments were required for a complete investigation.

Preparation of particulate materials for the microprobe often involves selection and remounting of individual particles 5μm or larger in diameter. This can be routinely achieved under a binocular microscope after some practice, and the technique permits the application of microprobe techniques to such problems as bearing seizures, a range of air pollution investigations, and most cases where for reasons of size or composition the substrate is unsuitable.

MICROPROBE ANALYSIS OF FLUORINATED POLYMERS

Polymer	Composition	Formula Fluorine Concentration, %	Microprobe Results (5 Measurements
Teflon	$CF_2.CF_2$	76	74.0, 74.4, 74.5 74.6, 76.2
Tedlar	$CHF.CH_2$	41	40.0, 41.3, 41.5 41.7, 42.0

Table 1

REFERENCES

1. H. Pullan and E. J. Chatfield, Canadian Research and Development, January 1971.

2. H. Yakowitz and K. R. J. Heinrich, J. Res. NBS, 73A, 113-120 (1969).

3. J. P. Smith and L. R. Reid, Fourth National Conference on Electron Microprobe Analysis, 62, (1969).

4. J. W. Colby, Seventh National Conference on Electron Microprobe Analysis, Tutorial B, (1972).

5. P. J. Killingworth, Sixth National Conference on Electron Microprobe Analysis, 63, (1971).

6. R. S. Thomas and M. I. Corlett, M.I., Proceedings, Electron Microscopy Society of America, (1973), 334-335.

31
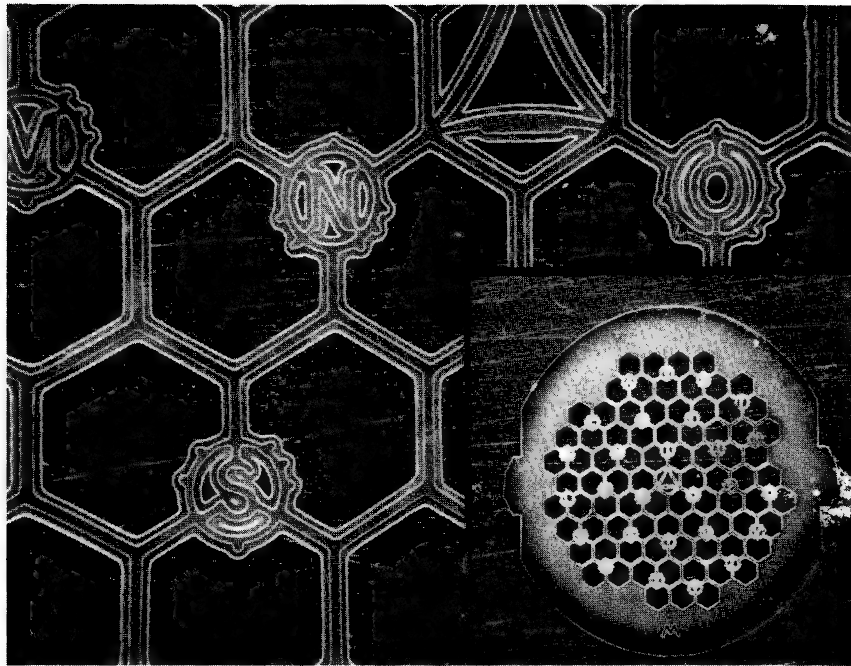
Figure 1. Hexagonal "Alphabet" Grid
Used for Specimen Relocation.

Figure 2. Sectioned Cement Sample,
X800, Etched for Optical Contrast.

Figure 3. Sectioned Cement Sample,
X600, After Repolishing. Note the
Poor Contrast.

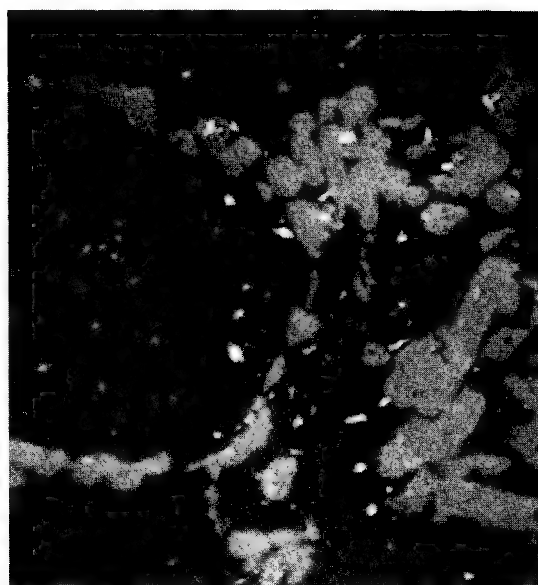Figure 4. Sectioned Cement Sample,
X500, Specimen Current Image.

Figure 5. Steel Sample, X300,
Specimen Current Image.

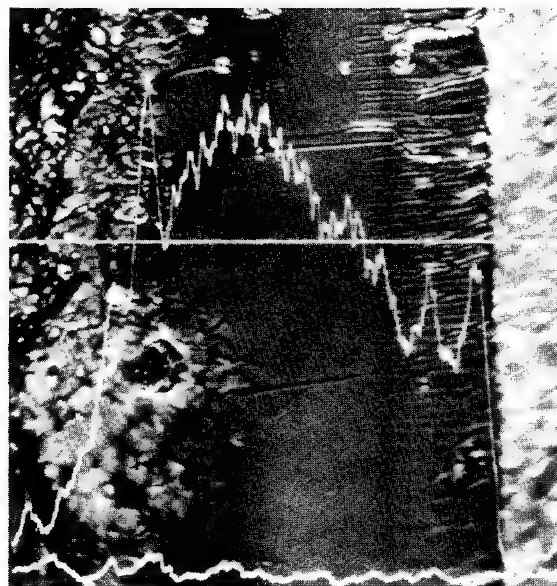Figure 6. Steel Sample of Figure 5,
X300, CrKα X-ray Distribution.

Figure 7. Sectioned Glazed Pottery,
X200, PbMα Line Scan.

QUALITATIVE ELECTRON MICROPROBE EXAMINATION

DESCRIPTION: RESIDUE ON FILTER

    THE APPROXIMATE COMPOSITION SHOWN BELOW IS THE RESULT OF AN
AUTOMATED ELEMENTAL SEARCH.   THE PERCENTAGES QUOTED ARE NOT
ACCURATE QUANTITATIVE DATA - THEY REPRESENT ONLY ORDER OF
MAGNITUDE ESTIMATES OF THE CONCENTRATIONS OF THE MAJOR ELEMENTS
PRESENT.

    MAJOR ELEMENTS DETECTED AND APPROXIMATE CONCENTRATIONS

ELEMENT		APPROX. WEIGHT PERCENT.
OXYGEN		9
CARBON	LESS THAN	1
NICKEL		5
IRON		9
MANGANESE		7
TITANIUM		5
SILICON		15
ALUMINUM	LESS THAN	1
MAGNESIUM	LESS THAN	1
SODIUM		3
CHLORINE		8
SULPHUR		11
CALCIUM		6
TOTAL		81

THIS SAMPLE WAS CHECKED FOR THE PRESENCE OF THE FOLLOWING
ELEMENTS:

O	N	F	C	B	SE	AS	AU	PT	ZN	CU	NI
CO	FE	MN	CR	V	TI	NB	ZR	P	SR	W	SI
AL	MG	GE	GA	NA	CL	BI	PB	S	MO	BA	TA
K	BR	TE	CA	SB	SN	IN	U	CD	AG		

Figure 8. Results of Automated Spectrometer Elemental Search.
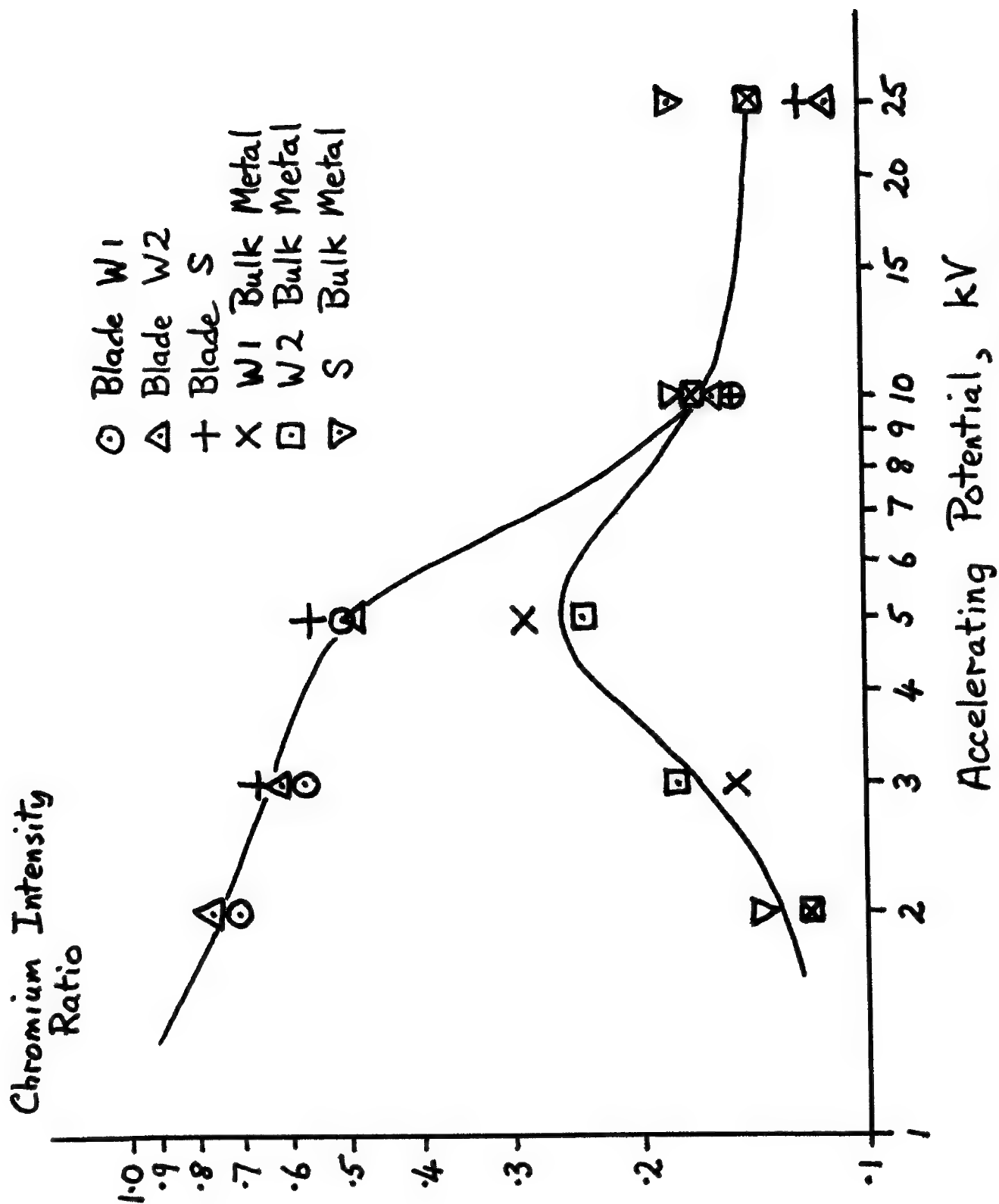
Figure 9   Chromium Intensity Ratio vs kV for Various Razor Blade Edges

QUANTITATIVE ELECTRON PROBE ANALYSIS

John L. Bomback

Scientific Research Staff
Ford Motor Company
Dearborn, Michigan 48121

I. Introduction

The electron probe analyzer is a sophisticated micro analytical tool capable of determining the elemental content of an extremely small volume of solid material. By monitoring the characteristic X-ray spectrum produced in that volume by a finely focused electron beam, both qualitative and quantitative elemental concentrations can be determined. The measured X-ray spectrum results from a complex set of interactions between electrons, X-rays, and matter. One approach to quantitative analysis with this instrument involves accounting for these phenomena in a semirigorous manner. It is the purpose of this tutorial to qualitatively examine the physical basis of the interactions and describe a procedure which accounts or corrects for them. The procedure uses models which approximate the complex physical reality and yet lead to relatively simple mathematical formulae. Particular emphasis is placed on describing concepts which are difficult to visualize such as the mass stopping power of a material for electrons and its effect on characteristic X-ray generation.

The essential elements of electron probe analysis are shown schematically in Figure 1. A finely focused beam of high energy (~ 2 to 50 kev) electrons strikes and penetrates into a solid target. A fraction of the electrons are scattered back through the surface while the others remain in the target and eventually come to equilibrium with it. As the electrons are scattered and

decelerated, some may occasionally ionize an inner electronic shell of a target atom, Figure 2. As the excited atom decays back to its ground state it may emit either an X-ray photon or an Auger electron, each having an energy characteristic of the atom. Of the fraction of ionization events which result in X-ray production, the resulting photons will be distributed in a series of X-ray lines, Figure 3. Only one of these lines is measured for a particular element during an analysis, therefore, the fraction of ionizations which produce useable information is further reduced. The remaining useable photons are further diminished in number by absorption within the target before they reach the surface. Of those that are emitted through the surface, only a small fraction are directed toward the X-ray spectrometer(s). The spectrometer has a finite detection efficiency which results in still another reduction of intensity. The final X-ray signals detected by the spectrometer(s) constitute the basic information of electron probe analysis.

From this description it might seem unlikely that very many X-ray photons will ever be detected by a spectrometer. However, under normal operating conditions, the incident electron beam current is between 10^{-6} and 10^{-9} amperes which represents roughly 10^{10} to 10^{13} electrons striking the target per second. Under these conditions, X-ray photons can be counted at rates exceeding 10^4 per second.

Quantitative analysis of a material of unknown composition may often be preceeded by a qualitative analysis to determine which elements are present. Next, the characteristic X-ray intensities, I, emitted from the material are measured for all (or most) of the elements present. These intensities are compared with the corresponding intensities emitted from standard materials of known

concentration (often pure elements). The ratio, k, of unknown to standard intensity for each element is determined and the set of k values uniquely specifies the unknown concentration. The traditional procedure has been to apply certain "corrections" to the k values in order to arrive at this concentration. Castaing showed in his thesis [1] that the weight fraction, C_A, of element A in a multielement target A,B... was equal, in a first approximation, to the ratio of characteristic intensity from A generated by the electron beam in the target to the corresponding intensity in pure element A (under identical excitation conditions).

$$C_A \cong \left. \frac{I_A^{A,B\ldots}}{I_A^0} \right) \text{ generated} \tag{1}$$

where the superscripts A,B... and O refer to a multielement target and pure A, respectively. If this were a true equality and if it were possible to measure the X-ray intensity generated by the electron beam, quantitative electron probe analysis would be a simple matter. However, several complications exist. Castaing further pointed out that the approximation deviates significantly from an equality when the average atomic numbers of unknown and standard differ substantially because energetic electrons behave differently in high and low atomic number materials. Electron backscatter reduces the number of X-ray photons which otherwise would be generated in the absence of this phenomenon and the reduction is greater in high atomic number targets which backscatter a greater fraction of the incident electrons.

The atomic number dependence of the electron mass stopping power works in the opposite direction to the dependence of electron backscattering, i.e., causing fewer X-ray photons to be produced by a given weight fraction of an element A

contained in a low atomic number matrix than are produced in a heavy matrix containing the same weight fraction of A. This is because the incident electrons are slowed down through interactions with the atomic electrons in the matrix which are more numerous in a given mass of a light matrix than in the same mass of a heavy matrix. For example, one gram of carbon contains 3.0×10^{23} electrons whereas one gram of uranium only contains 2.3×10^{23} electrons. Thus, the incident electrons "see" less mass as they are slowed by the electrons of the light matrix. For a given weight fraction of element A, it follows that in the light matrix the incident electrons will pass fewer A atoms as their energies drop to the critical value for A X-ray generation and, therefore, will produce fewer A characteristic photons. These two (backscatter and stopping power) deviations from Castaing's first approximation are known collectively as the "atomic number effect" and can be treated by separate backscatter and stopping power terms together referred to as the ATOMIC NUMBER CORRECTION.

While this complication is due to the interaction of electrons with target atoms, two further complications exist due mainly to the interaction of X-rays with the target. X-ray absorption by the photoelectric effect results in the total disappearance of X-ray photons and the ionization of the target atoms, Figure 4. The ionized atoms may then emit characteristic X-ray photons. This process, called the "fluorescence effect," can make a significant contribution to the total generated characteristic intensity of the fluoresced element under certain circumstances. The contribution is accounted for by the FLUORESCENCE CORRECTION.

X-ray photons are generated inside the target and a fraction of them are absorbed before they reach the surface. The magnitude of this "absorption

effect" depends on the X-ray mass absorption coefficient $\left(\frac{\mu}{\rho}\right)$ which is different for unknown and standard, the angle ψ at which the spectrometer views the target surface, the angle θ at which the electron beam strikes the surface, Figure 1, and the distribution of X-ray generation with depth beneath the surface. The latter parameter depends in turn on the energy of the electron beam, the critical energy for producing the measured X-ray line, and the manner in which the target slows and scatters the electrons. The ratio of the fraction of photons which escape absorption and are emitted from the unknown to the corresponding fraction which are emitted from the standard constitutes the ABSORPTION CORRECTION.

These considerations are summarized as follows:

1. Characteristic X-ray intensity generated by the electron beam is not proportional to concentration due to atomic number effects.

2. Total generated characteristic intensity may be greater than electron beam generated characteristic intensity due to fluorescence effects.

3. Relative characteristic intensity emitted from the surface is not proportional to relative generated characteristic intensity due to absorption effects.

In addition, several other items must be considered:

4. Total intensity emitted from the surface is not equal to emitted characteristic intensity due to the presence of background radiation from the continuous spectrum, Figure 5.

5. Detected intensity is not proportional to total emitted intensity due to dead time and other electronic, spectral and geometrical effects, see Table I.

6. The precision with which X-rays can be measured is limited by the random nature of X-ray generation. [2]

7. The calculated corrections use physical constants such as mass absorption coefficients whose values are not always accurately known.

The problem of quantitative electron probe analysis is complex but not impossible as evidenced by the continued refinement and ever increasing application of the technique. A detailed account of the present status of quantitative probe analysis and extensive references can be found in recent review articles by Beaman and Isasi [3] and Martin and Poole [4] and in an NBS book [5] edited by Heinrich.

II. Experimental Requirements

Accurate quantitative analyses depend on experimental as well as theoretical and computational considerations. Accurate intensity measurements and careful attention to the preparation and use of samples and standards are prerequisite. Table I lists some sources of experimental error and references where they are discussed in detail.

TABLE I

Sources of Experimental Error
in Measuring the Intensity Ratio, k

1. Electronic Effects

    A. Beam current instability leads to a proportional instability in measured X-ray intensity. [6]

    B. Accelerating energy, Eo, instability causes a proportionally greater instability of measured characteristic X-ray intensity since the latter is roughly proportional to $(E_o - E_c)^{1.7}$ where E_c is the critical excitation energy.

C. Uncertainty in the absolute value of E_o introduces an error in the correction factors. Some high voltage power supply meters read the voltage on the Wehnelt cylinder which differs from E_o by the bias voltage. E_o can be determined with an X-ray energy spectrometer by measuring the maximum energy in the X-ray continuum. [3] Alternatively, the fine structure in the electron channeling patterns of high perfection crystals is a sensitive measure of E_o. [7]

D. Detector dead time causes the detected count rate to become progressively less than the true count rate as the latter increases. The effect can be calculated if the dead times are known. [8]

E. The output pulse amplitude distribution from a flow proportional counter may decrease as the input count rate increases [9] causing some pulses to be rejected by the base line of the pulse height analyzer.

2. Spectral Effects

A. Background intensity from the continuous spectrum, Figure 5, must be subtracted from the measured intensity in order to arrive at the characteristic X-ray intensity. [10] The effect becomes progressively more important as the concentration of the measured species decreases. The effect decreases as the spectral resolution of the spectrometer increases.

B. When measuring the intensity from an element, overlapping spectra from other elements contained in the target contribute a background intensity. This may be the result of multiple order reflections in crystal spectrometers. The possibility of occurrence of this effect decreases as the spectral resolution of the spectrometer increases.

C. Spectral peak wavelength shift with chemical bonding [11] introduces an error into the measured intensity ratio if the crystal spectrometer is not "peaked up" on each individual target. This effect increases as the spectral resolution of the spectrometer increases.

3. Geometric and Topographic Effects

A. Carbonaceous contamination decreases emitted X-ray intensity [12] of all elements except carbon and must be eliminated if quantitative carbon analysis is required. [13]

B. Oxide, sulfide, etc. films on metal targets reduces X-ray intensity in a similar fashion from the underlying metal. Samples and standards should be freshly polished and/or stored under non-corrosive conditions.

C. Surface irregularities give rise to unpredictable absorption and fluorescence effects, Figure 6. [14] Samples and standards should be polished flat using standard metallographic and petrographic procedures. [1]

D. Small changes in the X-ray take-off angle, ψ, due to inadvertant tilting of the sample can have a large effect on emitted X-ray intensity in those instruments which have a low nominal take-off angle.

E. Electron and X-ray penetration within the target [16] can give rise to X-ray contributions from phases remote from the point of electron beam impact giving misleading results, Figure 6b.

F. Drift in the alignment of the spectrometer or sample changes the Bragg angle and moves the spectrometer off-peak. Changes in ambient temperature may cause a change in d-spacing of the diffracting crystal and a corresponding drift of an X-ray line off-peak. These effects increase as the spectral resolution of the spectrometer increases and are totally absent in X-ray energy spectrometers.

III. A Correction Procedure

Many methods have been devised to deduce elemental concentrations from X-ray intensity ratios. They can roughly be grouped into four categories: empirical, Monte Carlo, transport equation, and the classical ZAF approach. Empirical methods [17,18] rely on the establishment of a calibration between intensity and concentration based on results from standards of known concentration. The disadvantage of this approach is the difficulty in preparing large numbers of standards with accurately known concentrations which are homogeneous on a micron scale. The Monte Carlo method [19] simulates the paths of individual electrons as they are slowed down and scattered within the target. These simulations require large high speed computers and have not yet been economically applied to routine analyses. The transport equation [20] approach uses a numerical solution of a differential equation to determine the probability that an electron will reach a given depth in the target with a given energy and direction. With this information it is possible to predict X-ray generation and absorption and thus to quantitatively relate the measured k ratio to concentration.

The ZAF approach is the most widely used and one version of it will be described here. It involves treating each of the three effects (atomic number, $\underline{Z}$; absorption, $\underline{A}$; and fluorescence, $\underline{F}$) as separate multiplicative terms. The final form of the equation can be written:

$$\left. \frac{I_A^{A,B\cdots}}{I_A^0} \right)_{emitted} = C_A \cdot Z \cdot A \cdot F \qquad (2)$$

It is worth noting that by taking the ratio of intensities measured under identical conditions, several terms which affect the unknown and the standard

in exactly the same manner cancel out. These include: W, the fluorescence yield factor which is the fraction of initial ionizations which lead to photon emission; the fraction of photons from the ionization of an electronic shell which are in the particular X-ray line being measured; the efficiency of the spectrometer system in detecting that line; the solid angle subtended by the X-ray spectrometer from the point source of X-rays; and i_b, the electron current striking the target. We are concerned with relative, not absolute intensities.

Only normal electron beam incidence will be treated here, $\theta = 90°$, Figure 1. Analysis with inclined sample surfaces (non-normal incidence) is becoming more important due to the geometry of some scanning electron microscope/X-ray energy spectrometer systems which preclude normal electron beam incidence. Correction procedures for non-normal incidence have been considered [21] but nearly all theoretical and experimental work to date has been with normal incidence, $\theta = 90°$.

A. The Atomic Number Correction

Several schemes have been proposed to account for the effect that the target atomic number has on characteristic X-ray production. The method of Duncumb and Reed [22] will be described here since it is ameanable to both hand and computer calculation and gives good results in most cases. The correction is comprised of two terms which consider the ability of the target to decelerate and to backscatter incident electrons, respectively. A brief digression will be given of the former effect since it has been the source of some confusion in the past.

The simplified model shown in Figure 7 illustrates how characteristic X-ray production in a target depends on its ability to slow down the incident electrons. In Figure 7a, two hypothetical alloys are constructed: uranium - 9.0909... wt. % titanium and carbon - 9.0909... wt. % titanium. (The weight fraction of Ti is exactly 1/10 that of the major constituent in each alloy.) The alloys are made to have the same density and, therefore, have the same number of Ti atoms per unit volume. The atomic weights of the three elements are rounded off for convenience. Each unit volume contains one Ti atom and contains 40 C atoms or 2 U atoms respectively in the two alloys. Each unit volume contains 262 atomic electrons in the C alloy and 206 in the U alloy.

Since incident electrons are slowed down through interactions with the atomic electrons, it can be expected that for a given initial energy, incident electrons will travel further through the U alloy than through the C alloy before they no longer can produce Ti characteristic X-rays. The most widely used model for electron deceleration is the Bethe Law [23] which can be written:

$$\frac{dE}{dx} = K\left(\frac{Z}{A} N^\circ \rho\right) \frac{1}{E} \ell n \frac{1.166E}{J} \tag{3}$$

where E is electron energy, x is length along the electron path, K is a constant, A is atomic weight, N° is Avagadro's number, ρ is density, and J is a mean ionization energy which increases with atomic number. The term in parentheses equals the number of atomic electrons per unit volume. Neglecting for the moment the logarithmic term which is not predominant, Equation 3 shows that the distance, x, that an incident electron travels through the target before its energy falls below the critical value for Ti

X-ray production is inversely proportional to the number of electrons per unit volume. An incident electron will, therefore, travel 27% further through the U alloy (which has less atomic electrons) based on this simple model. The logarithmic term will reduce this value slightly. If the probability for producing a Ti characteristic photon as the electron passes through a unit volume containing a Ti atom is roughly constant, the number of Ti photons produced should be 27% greater in the U alloy than in the C alloy.

In Figure 7b, the U alloy is compressed to a higher density. This would be expected in practice since although a uranium atom is 20 times heavier than a carbon atom, it occupies only slightly more volume in a solid. Equation 3 states that the rate of energy loss is proportional to the target density, ρ. As the solid is compressed to a higher density, the incident electron traverses the same "mass thickness" ρx and, therefore, passes through the same number of unit volumes. This assumes that the atomic electrons are not acting in a collective manner but that each acts independently to slow down the incident electrons. (Some energy loss mechanisms such as plasmon excitation result from a collective interaction of the atomic electrons and are therefore "density dependent" but this will also be neglected in this simple treatment.)

Finally, in Figure 7c, the electrons are allowed to scatter. In the heavy U matrix, scattering at large angles is much more frequent. The incident electrons again however travel through the same number of unit volumes as in Figures 9a and 9b and produce the same number of Ti characteristic photons. It is worth noting here that x in Equation 3 refers to distance along the electron's path and z in Figure 7 refers to the depth from the surface.

Figure 7c can now be used to resolve the "penetration paradox" which states
on the one hand that electrons penetrate deeper into low atomic number
materials and on the other that low atomic number materials have higher
stopping powers which limits electron penetration and X-ray production.
Incident electrons penetrate light elements more on a z scale due to their
lower densities and lesser scattering abilities. Incident electrons penetrate
heavy elements more on a ρx scale because of their lower mass stopping power
due to fewer atomic electrons per unit mass. Alternatively, we can think of
the heavy elements being diluted with neutrons which do not contribute to the
electron slowing-down process.

Figure 7c can also be used to describe the "atomic number dependence" of the
absorption correction, page 24. The Ti photons will be produced, on the
average, closer to the surface in the U alloy due to the increased scattering.
The fact that the X-rays will be produced closer to the surface also because
of the increased density is not important since X-ray absorption is handled
in terms of mass depth, ρz.

The number of photons, n_A, of a particular characteristic line $\left(K_{\alpha_1}, \ L_{\alpha_1}, \text{ etc.}\right)$
of element A generated by an electron, is the product of several terms. These
include: the number of A atoms per unit volume; the probability, Q_A, for
ionizing an A atom while an electron traverses unit path length of material
with a concentration of one A atom per unit volume; the total length, X,
traversed by the electron from the time it enters the surface until its energy
drops below the critical excitation energy for the X-ray ionization level of
interest; the fraction, W, of these ionization which lead to photon emission;
and the fraction, G_A, of these photons which comprise the X-ray line of interest.
If we assume that Q does not vary with electron energy,

$$n_A = \left(\frac{C_A N_0 \rho^{A,B\ldots}}{A_A} \right) Q_A \; X_{A,B\ldots} \; W_A \; G_A \tag{4}$$

(number of A atoms per unit volume)

where N_0 is Avagadro's number, A_A is the atomic weight of A, and $\rho^{A,\;B\ldots}$ is the target density. The ratio of generated X-ray intensity in the target containing A, B... to that generated in pure A is then given by

$$\left. \frac{I_A}{I_A^0} \right)_{generated} = C_A \frac{\left(\rho X_A \right)^{A,B\ldots}}{\left(\rho X_A \right)^0} \tag{5}$$

As noted above, many of the physical constants cancel when relative intensities are computed. It is assumed that Q_A, which is a function of energy, can be cancelled by imagining a mean value for Q in the energy interval between E_0 and E_c.

The path length is given by

$$X = \int_{E_0}^{E_c} \frac{dE}{dE/dx} \tag{6}$$

Duncumb and Reed use the Bethe law, Equation 3, to compute the rate of energy loss and define the mass stopping power, S, as

$$S = - \frac{dE}{dx} \times \frac{1}{\rho} \tag{7}$$

Values for J in Equation 3 were determined empirically by Duncumb and Reed. The Bethe law, Equation 3, models electron energy loss as a continuous process whereas in fact, an electron loses energy in small discrete amounts due to individual inelastic scattering events. This continuous energy loss model

greatly simplifies the calculations without adversely affecting accuracy.

The integral in Equation 6 is eliminated by using a mean mass stopping power, $\overline{S}$, evaluated for an energy midway between the incident energy E_o and the critical excitation energy, E_c

$$\overline{S} = \frac{Z}{A} \, \ell n \left(\frac{1.166\overline{E}}{J} \right) \tag{8}$$

where

$$\overline{E} = (E_o + E_c)/2 \tag{9}$$

The constant K and term 1/E, Equation 3, are dropped since they cancel when the intensity ratio is computed, Equation 5.

The path length which an electron traverses before it can no longer produce characteristic A X-rays is

$$X = \frac{E_o - E_c}{\rho \overline{S}} \tag{10}$$

The generated intensity ratio, Equation 5 becomes

$$\left. \frac{I_A^{A,B\ldots}}{I_A^0} \right)_{generated} = C_A \frac{\overline{S}_A^0}{\overline{S}_A^{A,B\ldots}} \tag{11}$$

$\overline{S}^{A,\,B\ldots}$ is assumed to be a weight fraction average of the mass stopping powers of the individual elements;

$$\overline{S}_A^{A,B\ldots} = \Sigma_i \, C^i \, \overline{S}_A^i \tag{12}$$

analogous to the mass absorption coefficient of an alloy for X-rays which is also a weight fraction average of the mass absorption coefficients of

the individual species. It is important to remember that each element j

analyzed has a unique value for $\bar{S}_j^{A,B\cdots}$ since each has a unique critical

excitation energy, E_c.

Equation 11 gives the relative electron generated X-ray intensity in the

absence of electron backscatter. X-ray generation depends on atomic number

mainly through the dependence of $\bar{S}$ on Z/A, Equation 8. For the electrons

which do not backscatter, proportionally more photons of element A will be

generated for a given concentration of A in a high atomic number matrix

which has a lower Z/A than in a low atomic number matrix.

Electron backscatter from a target of atomic number Z results from the

deflection of the incident electrons as they come in close proximity with

atomic nuclei which have a charge of + Z. The probability of a large angle

Rutherford type scattering event is proportional to Z^2. An electron entering

a target composed of heavy atoms has a higher probability of being scattered

in such a manner that it will reemerge through the surface and leave the

target. The fraction, η, of electrons incident normal to the surface which

are backscattered is plotted as a function of atomic number in Figure 8. [24]

The energy distribution of electrons backscattered from Al and Pt is shown in

Figure 9, also for normal electron beam incidence. [25] Not only are more

electrons backscattered from heavy targets but their average energy is also

higher.

A certain fraction of these backscattered electrons have energies in excess

of the critical excitation energy for X-ray generation (shown as the shaded

area in Figure 9 for the case where $E_o/E_c = 2$). As the incident electron

energy, E_o, is increased, a greater fraction of those which are backscattered

fall into this category while the total fraction, η, which are backscattered

remains roughly constant.

These high energy backscattered electrons result in a loss of X-ray intensity which would have been generated had all the electrons remained in the target. The fractional loss is designated by (1-R) where R is the fraction which actually are generated. The total atomic number correction then becomes:

$$\left.\frac{I_A^{A,B...}}{I_A^O}\right)_{generated} = C_A^{A,B...} \quad \frac{\overline{S}_A^O}{S^{A,B...}} \quad x \quad \frac{R_A^{A,B...}}{R_A^O} \tag{13}$$

Each X-ray emitter in a multielement target has its own unique value of R since each has a unique critical excitation energy, E_c.

Duncumb and Reed evaluated R as a function of E_O/E_c $\left(= \frac{1}{U}\right)$ and Z from values of the backscatter coefficient, η (Z), and the energy distribution of back-scattered electrons and tabulated values of R for certain values of $\frac{1}{U}$ and Z. R for specific values of $\frac{1}{U}$ and Z can be obtained through linear interpolation of the tabulated values. R approaches unity as the incident electron energy approaches E_c (the shaded area moves to the right in Figure 7) and as Z approaches zero (fewer electrons are involved).

For a target with n elements, it is assumed that each element contributes to R in proportion to its weight fraction:

$$R_j^{A,B...} = C_A \; R_j^A + C_B \; R_j^B + \cdots \tag{14}$$

R must, therefore, be evaluated for each element of the n elements in the matrix for each radiation used, i.e., n^2 times if all elements are detected, $n(n-1)$ times if one element is determined by difference, etc.

The magnitude of the atomic number correction is illustrated by considering the Al_3Pt system which has a large correction and Co - 50 wt. % Mn which has a negligible correction. The corrections in these binary systems involve cross terms which account for the effect each element in the target has on the X-ray emission from itself and from the other element. The data and calculations for Al_3Pt are shown below. Al K_α and Pt M_α lines are monitored at E_o = 8 kev. The subscript j refers to the emitting element.

	j →	Al	Pt
Z_j		13	78
$C_j^{Al_3Pt}$ (wt. %)		.293	.707
$E_{c,j}$ (kev)		1.560	2.133
E_c/E_o		0.195	0.267

The relevant portion of Duncumb and Reed's table of R values is reproduced below. Values in boxes were obtained by linear interpolation.

			(Al K_α)		(Pt M_α)	
E_c/E_o →		0.1	0.195	0.2	0.267	0.3
	Z					
	10	.944		.953		.961
(Al)	13	.923	.932	.933	.940	.944
	20	.873		.888		.903
	70	.663		.687		.713
(Pt)	78	.644	.668	.669	.686	.695
	80	.639		.665		.691

$j \rightarrow$	Al	Pt	
R_j^{Al}	.932	.940	
R_j^{Pt}	.668	.686	
$R_j^{Al_3Pt}$	.745	.761	(Eq. 14)
$(R_j^{Al_3Pt}/R_j^0)$	.799	1.11	

The results show that 20% fewer Al K_α photons are produced in Al_3Pt
(29.3 wt. % Al) than would be produced in a matrix containing 29.3 wt. % Al
and having an average atomic number equal to that of Al (e.g., a Mg-Al-Si
alloy) due to increased backscatter from Pt atoms. The Pt M_α intensity is
enhanced by 11%.

The stopping power effect works in the opposite direction:

$j \rightarrow$	Al	Pt	
J (kev)	.142	1.057	Ref. J
$E_{c,j}$ (kev)	1.560	2.133	(Ref. L)
$\overline{E}_j$ (kev)	4.78	5.066	(Eq. 9)

$\overline{S}$ for Al K_α generated in Pt at 8 kev is calculated as follows:

$$\overline{S}_{Al}^{Pt} = \left(\frac{Z}{A}\right) \quad \ell n \ \left(\frac{1.166 \ E_{c, \ Al}}{J^{Pt}}\right)$$

$$= .3998 \cdot \ \ell n \ \left(\frac{1.166 \cdot 4.78}{1.057}\right)$$

$$= .6644$$

The other $\bar{S}$'s are calculated in a like manner:

$j \rightarrow$	Al	Pt	
$\bar{S}_j^{Al}$	1.768	1.796	
$\bar{S}_j^{Pt}$	.6644	.6875	
$\bar{S}_j^{Al_3Pt}$	.9851	1.012	(Eq. 12)
$\bar{S}_j^0/\bar{S}_j^{Al_3Pt}$	1.791	.6795	

The total atomic number correction becomes:

$j \rightarrow$	Al	Pt
$\left(R_j^{Al_3Pt}/R_j^0\right) \cdot \left(\bar{S}_j^0/\bar{S}_j^{Al_3Pt}\right)$	1.43	0.754

It can be seen that in this example, that the stopping power term predominates. This is true in general. The generated X-ray intensity ratio, Equation 13, for a light element in a heavy matrix is always greater than its weight fraction while the reverse is true for a heavy element in a light matrix.

The final results for the Co - 50 Wt. % Mn system are listed below:

$j \rightarrow$	Mn	Co
R_j^{Co-Mn}/R_j^0	.994	1.006
$\bar{S}_j^0/\bar{S}_j^{Co-Mn}$	1.009	0.991
$\left(R_j^{Co-Mn}/R_j^0\right) \cdot \left(\bar{S}_j^0/\bar{S}_j^{Co-Mn}\right)$	1.003	0.997

Again the stopping power term dominates but the overall effect is negligible.

B. The Absorption Correction

Castaing established the basis for the absorption correction by defining the functions $\varphi(\rho z)$ and $f(\chi)$. $\varphi\left(\rho z\right)_A^{A,B\cdots}$ is the X-ray intensity generated by the electron beam in a thin slab of pure element A located at mass depth ρz below the surface of a target A,B... divided by the intensity generated under the same conditions in an identical slab suspended freely in space. $f(\chi)_A^{A,B\cdots}$ is the fraction of characteristic X-ray intensity from element A generated in a target A, B... which escapes absorption and emerges from the surface at a given angle, ψ. $f(\chi)$ is related to $\varphi(\rho z)$ through the expression

$$f(\chi)_A^{A,B\cdots} = \frac{F(\chi)_A^{A,B\cdots}}{F(0)_A^{A,B\cdots}} = \frac{\int_0^\infty \varphi(\rho z)^{A,B\cdots} \, e^{-\varphi^{A,B\cdots} \rho z} \, d(\rho z)}{\int_0^\infty \varphi(\rho z)_A^{A,B\cdots} \, d(\rho z)} \qquad (15)$$

where

$$\chi_A^{A,B\cdots} = \left(\frac{\mu}{\rho}\right)_A^{A,B\cdots} \csc \psi = \csc \psi \left[Ca\left(\frac{\mu}{\rho}\right)_A^A + C_B\left(\frac{\mu}{\rho}\right)_A^B + \cdots \right] \qquad (16)$$

and $\left(\frac{\mu}{\rho}\right)_A^j$ is the X-ray mass absorption coefficient of element j for characteristic radiation from element A. Similar functions are defined for the generation and absorption of A radiation in a target of pure element A, i.e., $\varphi(\rho z)_A^O$ and $f(\chi)_A^O$.

$\varphi(\rho z)$ is shown in Figure 10 for Al and Au [26]. The values at the surface $(\rho z = 0)$ exceed unity due to an intensity contribution from electrons which are backscattered up through the surface from beneath with energies greater than E_c. The increment above one increases with target atomic number due to the atomic number dependencies shown in Figures 7 and 8. The function, $\varphi(\rho z)$, initially increases beneath the surface due to lateral scattering of

the electrons which causes them to travel greater distances through the slabs at these depths. Finally, $\varphi(\rho z)$ decreases at large ρz as electron retardation begins to predominate.

The absorption correction is made by multiplying the generated X-ray intensity ratio, Equation 13) by the ratio of the fraction of intensity escaping absorption in the unknown to the corresponding fraction from the pure element standard:

$$\left. \frac{I_A^{A,B...}}{I_A^0} \right)_{measured} = \left. \frac{I_A^{A,B...}}{I_A^0} \right)_{generated} \cdot \frac{f(\chi)_A^{A,B...}}{f(\chi)_A^0} \tag{17}$$

$$= C_A \; \frac{\bar{S}_A^0}{\bar{S}_A^{A,B...}} \cdot \frac{R_A^{A,B...}}{R_A^0} \cdot \left[\frac{f(\chi)_A^{A,B...}}{f(\chi)_A^0} \right] \tag{18}$$

where the bracketed item is the absorption correction. This measured intensity ratio considers only X-rays produced by electrons and neglects fluorescence effects.

The numerator in Equation 15, $F(\chi)$, is proportional to the characteristic A X-ray intensity _emitted_ _from_ the surface at a given takeoff angle, ψ, and subtending a given solid angle whereas the denominator, $F(0)$, is proportional to the corresponding intensity _generated_ _within_ the target which is directed toward the surface within the same solid angle. It is erroneous to assume that the atomic number correction is implicit in the absorption correction through the term $F(0)$ which deals with X-ray generation. Both $F(\chi)$ and $F(0)$ contain the distribution of generated X-rays, $\varphi(\rho z)$. When their ratio is taken, the magnitude of this generation function cancels out leaving the fraction of X-ray intensity escaping absorption, $f(\chi)$.

Several experimental [26,27] and theoretical [21] methods have been devised

to determine $f(\chi)$ for different materials and radiations. Philibert [28]

has proposed an analytical expression for $f(\chi)$ which was subsequently modified

by Duncumb and Shields [29] and by Heinrich. [30] Like the atomic number

correction of Duncumb and Reed, Philibert's absorption correction is easy to

use and gives reliable results when absorption conditions are not severe.

The expression takes the form:

$$f(\chi) = \frac{1 + h}{\left(1 + \frac{\chi}{\sigma}\right)\left[1 + h\left(1 + \frac{\chi}{\sigma}\right)\right]}$$ (19)

where

$$h = \frac{1.2\,\overline{A}}{\overline{Z}^2}$$ (20)

σ is an electron mass absorption coefficient. $\overline{A}$ and $\overline{Z}$ are the average atomic

number and average atomic weight of the target respectively. Philibert rec-

ommended using averages based on atomic concentrations although little error is

introduced into the final result by using weight fraction averages.

Duncumb and Shields [29] noted that the depth distribution of X-ray production,

$\varphi(\rho z)$ in a given target depends not only on the accelerating energy of the

incident electrons, but also on the critical excitation energy, E_c, of the

X-ray line measured. They proposed accounting for this dependence through,

σ, the electron absorption coefficient:

$$\sigma = \frac{K}{E_o^n - E_c^n}$$ (21)

Heinrich [30] proposed the values 4.25×10^5 and 1.65 for the constants K and

n respectively when E_o and E_c are expressed in kev. As E_o increases or E_c

decreases, the electrons can reach deeper into the sample and still produce characteristic X-rays. $f(\chi)$ decreases in this case because a higher fraction of generated X-ray photons are absorbed as they travel to the surface.

The parameter h, Equations 19 and 20, accounts for electron scattering in the target. As Z increases, h decreases, and $f(\chi)$ increases, i.e., there is a smaller absorption effect in heavy targets. This is qualitatively reasonable since high atomic number targets scatter electrons more strongly and, therefore, restrict X-ray generation to a shallower mass depth, ρz. This leads to less absorption as the X-rays travel a distance, $\rho z \csc \psi$, to the surface.

$f(\chi)$ is plotted for Al K_{α_1} (E_c = 1.56 kev) generated in pure Al pure Pt, and Al_3 Pt in Figure 11a at 8 and 20 kev. Figure 11b is an analogous plot for Pt M_{α_1} (E_c = 2.13 kev). It can be seen that the following promote a high fractional absorption: large mass absorption coefficient (χ), large E_o, small E_c, small atomic number matrix.

The absorption correction for measuring Co K_{α_1} in Co - 50 wt. % Mn is given below for E_o = 20 kev and ψ = 52.5°:

$$\left(\frac{\mu}{\rho}\right)^{Co}_{Co\ K_{\alpha}} = \left(\frac{\mu}{\rho}\right)^{Mn}_{Co\ K_{\alpha}} = 422.5 \qquad\qquad [Ref. 31]$$

$$E_{c,Co\ K_{\alpha}} = 7.7095\ kev \qquad\qquad [Ref. 32]$$

$$\csc 52.5° = 1.2605$$

$$\chi^o_{Co\ K_{\alpha}} = 1.2605 \times 64.9 = 81.81$$

$$\chi^{Co-Mn}_{Co\ K_{\alpha}} = 1.2605\ (0.5 \times 64.9 + 0.5 \times 422.5) = 243.7$$

$$h^{Co} = \frac{1.2 \times 58.933}{(27)^2} = 0.097 \qquad \text{(Eq. 20)}$$

$$\sigma_{Co\ K_\alpha} = \frac{4.25 \times 10^5}{20^{1.65} - 7.71^{1.65}} = 3.82 \times 10^3 \qquad \text{(Eq. 21)}$$

$$f(\chi)^o_{Co\ K_\alpha} = \frac{1 - 0.097}{\left(1 + \frac{81.81}{3820}\right)\left[1 + 0.097\left(1 + \frac{81.81}{3820}\right)\right]} = .9772 \qquad \text{(Eq. 19)}$$

$$h^{Co-Mn} = 1.2 \frac{(0.5 \times 58.933 + 0.5 \times 54.938)}{(0.5 \times 27 + 0.5 \times 25)^2} = 0.10106$$

$$f(\chi)^{Co-Mn}_{Co\ K_\alpha} = \frac{1 + 0.10106}{\left(1 + \frac{243.7}{3820}\right)\left[1 + 0.10107\left(1 + \frac{243.7}{3820}\right)\right]} = 0.9346$$

The absorption correction for Co K_α in Co - 50 wt. % mn at 20 kev and $\psi = 52.5°$ becomes

$$\boxed{\frac{f(\chi)^{Co-Mn}_{Co\ K_\alpha}}{f(\chi)^o_{Co\ K_\alpha}} = \frac{0.9346}{0.9772} = 0.9564}$$

For measuring Mn K_α in Co-Mn, the absorption correction is negligible since the mass absorption coefficients for Mn K_α in Co and Mn do not differ significantly:

$$\left(\frac{\mu}{\rho}\right)^{Co}_{Mn\ K_\alpha} = 100.8 \qquad\qquad \left(\frac{\mu}{\rho}\right)^{Mn}_{Mn\ K_\alpha} = 79.5$$

$$E_c,\ Mn\ K_\alpha = 6.538$$

The final result is:

$$\frac{f(\chi)^{Co-Mn}_{Mn\ K_\alpha}}{f(\chi)^{0}_{Mn\ K_\alpha}} = \frac{0.9666}{0.9704} = 0.9962$$

These results for Co K_α can be combined with those from the atomic number correction calculation (pg. 20) into Equation 18 to obtain the entire correction since there is no fluorescence correction for Co K_α:

$$\left. \frac{I^{Co-Mn}_{Co\ K_\alpha}}{I^{0}_{Co\ K_\alpha}} \right)_{measured} = 0.5 \times 0.997 \times 0.9564 = .476$$

At 20 kev and $\psi = 52.5$, the measured intensity ratio of Co K_α is 5% less than the true concentration of Co.

The results for Al_3 Pt at 8 kev and $\psi = 52.5°$ are:

$j \rightarrow$	Al K_α	Pt M_α
$\left(\frac{\mu}{\rho}\right)^{Al}_{j}$	385.7	2212
$\left(\frac{\mu}{\rho}\right)^{Pt}_{j}$	2432.6	1192
$E_{c,j}$	1.560	2.133

$$\left. \frac{f(\chi)^{Al_3\ Pt}_{j}}{f(\chi)^{0}_{j}} \right)_{E_o = 8\ kev} \qquad \frac{0.852}{0.962} = 0.886 \qquad \frac{0.883}{0.905} = 0.976$$

Neglecting the slight fluorescence of Al K_α by Pt M_α the measured intensity ratios become via Equation 18.

$j \rightarrow$		Al K_α	Pt M_α
$\dfrac{I_j^{Al_3\ Pt}}{I_j^0}\Bigg)\ E_o = 8$ kev		.371	.520
C_j		0.293	0.707

The atomic number correction is the dominant correction is this system.

C. The Fluorescence Correction

Characteristic X-rays from element A, in addition to being generated by the incident beam, will also be generated by characteristic X-rays from elements B, C, ... present in the target provided the energies of these X-rays are greater than the critical excitation energy of element A. This process is referred to as secondary fluorescence and its magnitude is greatest when the concentration of element B (or C, ...) is large, when the overvoltage $E_o/E_{c,b}$ for that element is also large, and when the mass absorption coefficient of element A for element B radiation is large. In practice, this implies that the effect is greatest when the energy of B (or C, ...) radiation is just slightly greater than the critical excitation energy for element A, $E_{c,A}$.

Characteristic X-rays from element A are also generated by the continuous spectrum [33] but this contribution can frequently be neglected because it tends to cancel out of the intensity ratio. A fluorescence effect by the

continuum may be important when the there is a large difference in average atomic number between unknown and standard.

As with the atomic number and absorption corrections, Castaing [1] established the theoretical basis for the characteristic fluorescence correction in his thesis. The fluorescence correction takes the form of an additive term, γ, which is the fractional increase in the _emitted_ intensity ratio due to the fluorescence effect:

$$\left.\frac{I_A^{A,B\ldots}}{I_A^0}\right)_{measured} = k_A = C_A \left[\overset{Z}{\frac{R_A^{A,B\ldots}}{R_A^0}} \cdot \frac{\bar{S}_A^0}{\bar{S}_A^{A,B\ldots}}\right]\left[\overset{A}{\frac{f(\chi)_A^{A,B\ldots}}{f(\chi)_A^0}}\right]\left[\overset{F}{1 + \sum_i \gamma_A^i}\right] \tag{22}$$

where the summation is over all i elements which are capable of fluorescing element A. γ_A^i is defined as the ratio of emitted A intensity excited by X-rays from element i to the emitted A intensity generated by the incident electron beam:

$$\gamma_A^i = \left.\frac{I_A^{A,B\ldots} \text{ (due to i X-rays)}}{I_A^{A,B\ldots} \text{ (due to incident electrons)}}\right)_{emitted} \tag{23}$$

Reed [34] modified Castaing's original treatment of γ and arrived at the following expression for element B fluorescing element A:

$$\gamma_B^B = 0.5 \; P_{ij} \; C_B \; \frac{r_A - 1}{r_A} \; W(B) \; \frac{A}{B} \; \left(\frac{U_B - 1}{U_A - 1}\right)^{1.67} \; \frac{\mu_B^A}{\mu_B} \; \left[\frac{\ln(1+x)}{x} + \frac{\ln(1+y)}{y}\right] \tag{24}$$

The physical significance of the terms in Equation 24 are discussed below. The term 0.5 accounts for the fact that roughly one-half of the primary

electron excited B radiation is directed upward out of the sample and does not produce fluorescence radiation. P_{ij} accounts for relative intensity differences when K lines excite L or M lines, L lines excite K or M lines, etc. P_{ij} equals 1 for K lines exciting K lines, etc. The contribution X-rays of element B make on the intensity of element A is proportional to the weight fraction, C_B, of element B. $(r_A - 1)/r_A$ is the fraction of B photons absorbed in element A which excite the A shell of interest. r_A is the ratio of the total mass absorption coefficient of A for B radiation divided by the contribution to this mass absorption coefficient from ionization of all shells except the one of interest, Figure 12. The latter contribution can be evaluated from the expression

$$\left(\frac{\mu}{\rho}\right) = C\lambda^n \tag{25}$$

The ratio $(r_A - 1)/r_A$ for exciting K radiation of element A becomes

$$\frac{r_A - 1}{r_A} = 1 - \frac{C_{KL}}{C_K}\lambda^{\left(n_K - n_{KL}\right)} \tag{26}$$

where the constants C and n are defined and tabulated in Reference 31. W(B) is the fluorescence yield factor for element B and A/B is the ratio of atomic weights of A and B, respectively:

$$U_j = E_o/E_{c,j} \tag{27}$$

$\dfrac{\mu_B^A}{\mu_B}$ is the ratio of the mass absorption coefficient for element B radiation in pure A and in the sample, respectively. The logarithmic terms in x and y are geometrical factors where

$$x = \frac{\mu_A}{\mu_B}\ csc\ \psi \tag{28}$$

and

$$y = \frac{\sigma}{\mu_B} \qquad (29)$$

and σ is evaluated by Equation 21 using E_c for element B.

Characteristic fluorescence is for example important in the Co - Mn system since Co K_α radiation has an energy just in excess of the critical energy for Mn K ionization ($E_{Co\ K_\alpha} = 6.9$ kev, $E_{c,Mn\ K} = 6.5$ kev). γ_{Mn}^{Co} is evaluated from Equation 24 and the following data for Co - 50 wt. % Mn at 20 kev and $\psi = 52.5°$:

$$C_{Co} = 0.5$$

$$\frac{r_{Mn} - 1}{r_{Mn}} = 1 - \frac{10.45}{86.7} \times 1.789^{(2.72 - 2.73)} \qquad (Eq.\ 26)$$

$$= 0.874$$

$$W(Co) = 0.358 \qquad [Ref.\ 35]$$

$$\frac{A_{Mn}}{A_{Co}} = \frac{54.938}{58.933} = 0.9332$$

$$\left(\frac{U_{Co} - 1}{U_{Mn} - 1}\right)^{1.67} = \left(\frac{20/7.710 - 1}{20/6.538 - 1}\right)^{1.67} = 0.6226$$

$$\frac{\mu_{Co}^{Mn}}{\mu_{Co}^{Co - Mn}} = \frac{422.5}{0.5 \times 422.5 + 0.5 \times 64.9} = 1.7337$$

$$x = \frac{\mu_{Mn}^{Co - Mn}}{\mu_{Co}^{Co - Mn}} \times csc\ \psi = \frac{90.2}{243.7} \times 1.2605 = 0.4665$$

$$\ln \frac{(1 + x)}{x} = 0.821$$

$$y = \frac{\sigma}{\mu_B} = \frac{3820}{243.7} = 15.68 \qquad \text{(Pg. 25)}$$

$$\ln \frac{(1 + y)}{y} = 0.179$$

$$\gamma_{Mn}^{Co} = 0.079$$

The complete correction for measuring Mn in Co - 50 wt. % Mn becomes:

$$\left. \frac{I_{Mn}^{Co - Mn}}{I_{Mn}^{0}} \right)_{\text{measured}} = 0.5 \times \overset{Z}{1.003} \times \overset{A}{0.9962} \times \overset{F}{(1 + 0.079)}$$

$$\boxed{= 0.5 \times 1.078 = 0.539}$$

The measured intensity ratio for Mn is nearly 8% higher than the concentration and this deviation is due almost entirely to the fluorescence effect.

D. Using the Correction Equations

The final form of the correction, Equation 22, is arranged with the correction terms on the right side along with the concentration. The worked examples (Al_3 Pt and Co - 50 wt. % Mn) evaluated the corrections for known concentrations to see what effect they had on the intensity ratio, k. In practice, the problem is just the reverse, i.e., to solve for the unknown concentration using

correction terms which are themselves concentration dependent. Iteration techniques must therefore be used whereby trial concentrations are assumed, new concentrations are calculated and used as trial concentrations in the next iteration, etc. The process is repeated until the latest set of concentrations agrees with the penultimate concentrations to within a predetermined increment or, if convergence fails, for a maximum number of iterations.

In the absence of any apriori knowledge of the unknown concentration, the set of k values normalized to unity can be used as the first set of trial concentrations. All subsequent trial concentrations should sum to unity since any other case would not be physically realizable. If all k values for elements in an unknown are measured, the sum of the calculated concentrations acts as a check on the data. It is therefore important to report unnormalized results. If their sum differs significantly from unity, an error exists although the converse is not necessarily true. If one element is determined by difference, there is no such check on the data although the same iteration procedure must be used. In some systems, an element can be determined by stoichiometry, e.g., oxygen in oxides, provided valences are known for all cations. In this case, the sum of the individual oxides acts as a check on the data. It may be possible to determine one element by stoichiometry and another by difference. In recent years, computer programs [36] have been developed and refined to make these iterative calculations.

It is sometimes necessary and/or advantageous to use multielement standards. In this case, the terms R_A^0, $\bar{S}_A^0$, and $f(\chi)_A^0$ in Equation 22 which refer to pure element standards are replaced by their respective values for the multielement target. It may also be necessary to include a fluorescence term $(1 + \sum_i \gamma_A^i)$

in the denominator to account for fluorescence effects in the multielement standard. If homogeneous, well characterized standards are available in the concentration range of the unknown, their use will decrease errors in the calculations due to an inadequate model or poorly known values for physical constants since these will tend to cancel out of Equation 22.

Acknowledgment

The author wishes to thank Dr. M. A. Short and Mr. J. Tabock of the
Ford Motor Company Scientific Research Staff for their critical comments
and helpful discussions during the preparation of this paper.

REFERENCES

1. R. Castaing, "Applications of Electron Probes to Local Chemical and Crystallographic Analysis," Doctoral Thesis, University of Paris, 1951.

2. R. E. Evans, The Atomic Nucleus, McGraw-Hill, New York, 1955

3. D. R. Beaman and J. A. Isasi, "Electron Beam Microanalysis," ASTM STP 506, 1972.

4. D. M. Poole and P. M. Martin, "Electron Probe Microanalysis: Instrumental and Experimental Aspects," Met. Revs., 14, 61, 1969.

5. Quantitative Electron Probe Microanalysis, ed. K. F. J. Heinrich, NBS Spec. Pub., 298, 1968.

6. S. J. B. Reed, "Probe Current Stability in Electron Probe Microanalysis," J. Sci. Inst., Ser. 2, 1, 136-9, 1968.

7. E. D. Wolf and T. E. Everhart, "Electron Beam Channeling in Single-Crystal Silicon by Scanning Electron Microscopy," Appl. Phys. Lit., 14, 299, 1969.

8. K. F. J. Heinrich, et.al., "Correction for Non-Linearity of Proportional Counter Systems in Electron Probe X-Ray Analysis," Adv. in X-Ray Anal., 9, 208, 1966.

9. N. Speilberg, "Characteristics of Flow Proportional Counters for X-Rays," Adv. in X-Ray Anal., 10, 534, 1966.

10. N. G. Ware and S. J. B. Reed, "Background Corrections for Quantitative Electron Microprobe Analysis Using a Lithium Drifted Silicon Detector," J. Phys. E., 6, 286, 1973.

11. W. L. Baun, "Instrumentation, Spectral Characteristics, and Applications of Soft X-Ray Spectroscopy," Appl. Spect. Rev., 1, 379, 1968.

12. R. Castaing, "Electron Probe Microanalysis," Adv. Elect. and Electron Physics, Academic Press, 317, 1960.

13. E. Eichen, et.al., "An Electron Microprobe Technique for Detecting Low Carbon Concentrations in Iron," Metallog. 5, 151, 1972.

14. J. L. Bomback, "Practical Limitations of X-Ray Analysis in the Scanning Electron Microscope," U.S. Steel Corp. P. R. 654, 1970.

15. H. Yakowitz, "Evaluation of Specimen Preparation and the Use of Standards in Electron Probe Microanalysis," ASTM STP 430, 383, 1968.

16. S. J. B. Reed and J. V. P. Long, "Electron Probe Measurements Near Phase Boundries," X-Ray Optics and X-Ray Micro, H. H. Pattee, et.al. eds., Academic Press, 317, 1963.

REFERENCES (Continued)

17. T. O. Ziebold and R. E. Ogilvie, "An Empirical Method for Electron Microanalysis," Anal. Chem., 36, 322, 1964.

18. A. E. Bence and A. L. Albee, "Practical Correction Factors for the Electron Microanalysis of Silicates and Oxides," J. Geology, 76, 382, 1968.

19. M. Green, "A Monte Carlo Calculation of the Spatial Distribution of Characteristic X-Ray Production in a Solid Target," Proc. Phys. Soc., 82, 204, 1963.

20. D. B. Brown, et.al., "Prediction of X-Ray Production and Electron Scattering in Electron Probe Analysis Using a Transport Equation," J. Appl. Phys., 40, 1627, 1969.

21. H. E. Bishop, "The Absorption and Atomic Number Corrections in Electron Probe X-Ray Microanalysis," Brit. J. Appl. Phys., 1, 673, 1968.

22. P. Duncumb and S. J. B. Reed, "The Calculation of Stopping Power and Backscatter Effects in Electron Probe Microanalysis," Quant. Elect. Probe Anal., ed. K. F. J. Heinrich, NBS Spec. Pub. 298, 133, 1968.

23. H. A. Bethe, et.al., Proc. Am. Phys. Soc., 78, 573, 1938.

24. E. Weinryb and J. Philibert, "Measurement of the Backscatter Coefficient for 5 to 30 kev Electrons," Comptes Rendus, 258, 4535, 1964.

25. H. Kulenkampff and W. Spyra, Zeit. fur Phys., 137, 416, 1954.

26. R. Castaing and J. Deschamps, J. Phys. Radium, 16, 304, 1955.

27. M. Green, "The Target Absorption Correction in X-Ray Microanalysis," X-Ray Optics and X-Ray Microanalysis, H. H. Pattee, et.al., eds., Academic Press, 361, 1963.

28. J. Philibert, "A Method for Calculating the Absorption Correction in Electron Probe Microanalysis," X-Ray Optics and X-Ray Microanalysis, H. H. Pattee, et.al., eds., Academic Press, 379, 1963.

29. P. Duncumb and P. K. Shields, "Effect of Critical Excitation Potential on the Absorption Correction," The Electron Microprobe, T. D. McKinley, et.al., eds., John Wiley and Sons, 284, 1966.

30. K. F. J. Heinrich, "Common Sources of Error in Electron Probe Microanalysis," Adv. in X-Ray Anal., 11, 40, 1968.

31. K. F. J. Heinrich, "X-Ray Absorption Uncertainty," The Electron Microprobe, T. D. McKinley, et.al., eds., John Wiley and Sons, 296, 1966.

32. J. A. Bearden, "X-Ray Wavelengths," Dist. by Clearinghouse - NBS, Wash. D.C., 1964.

REFERENCES (Continued)

33. J. Henoc, "Fluorescence Generated by the Continuum," Quant. Elect. Probe Microanal., Ed. K. F. J. Heinrich, NBS Spec. Pub., 298, 197, 1968.

34. S. J. B. Reed, "Characteristic Fluorescence Corrections in Electron Probe Microanalysis," Brit. J. Appl. Phys., 16, 913, 1965.

35. J. L. Colby, "Quantitative Microprobe Analysis of Thin Insulating Films," Adv. in X-Ray Anal., 11, 287, 1968.

36. D. R. Beaman and J. A. Isasi, "A Critical Examination of Computer Programs Used in Quantitative Electron Microprobe Analysis," Anal. Chem., 42, 1540, 1970.

Electron Trajectory

X-Ray Trajectory

Target Surface

1   2

θ

ψ

X-Ray Spectrometer

A

A

R
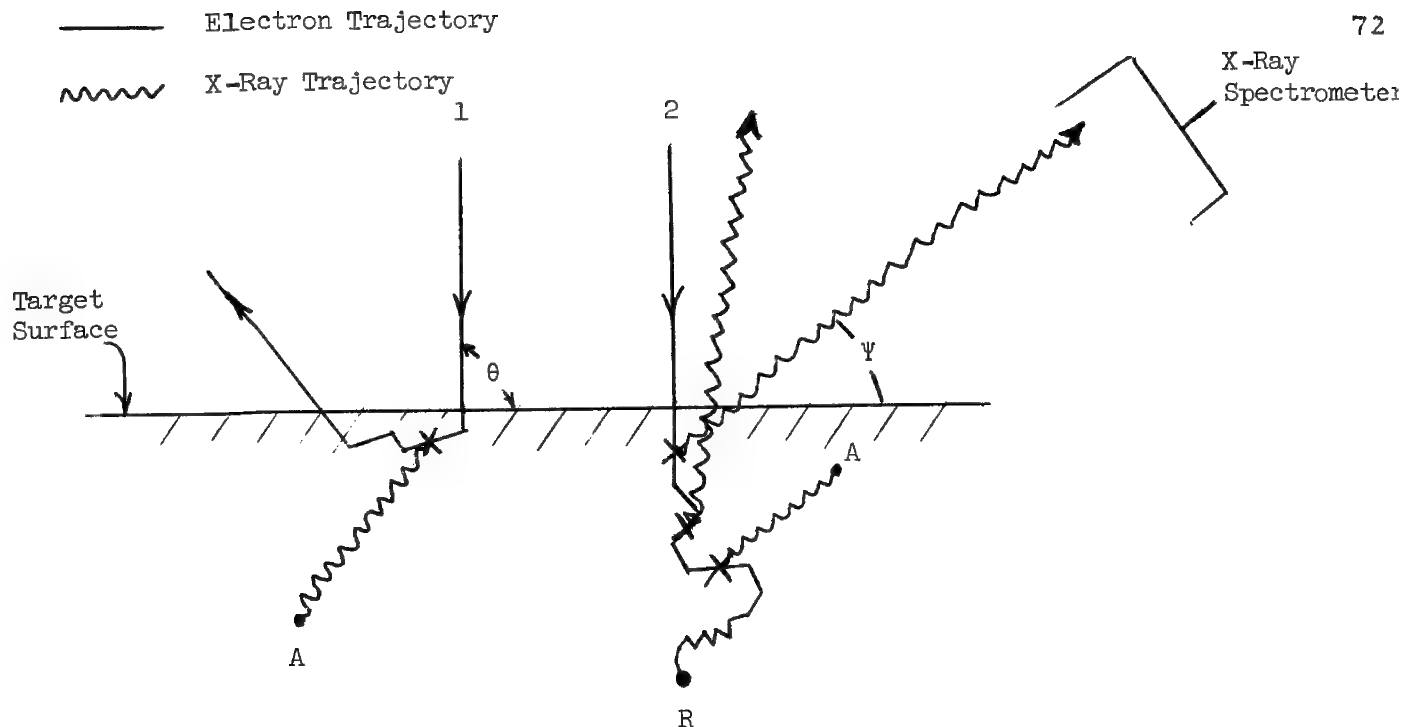
Figure 1. Schematic of Electron Probe Analysis. Two electrons (1 and 2) are shown striking a target producing characteristic photons at points marked X. Some photons are absorbed at points marked A. Electron No. 1 creates fewer photons since it is scattered back through the target surface. Electron No. 2 comes to equilibrium with the target at R.

electron vacancy

X-ray photon

K L M

K L M

ejected electron

incident electron

a.

b.
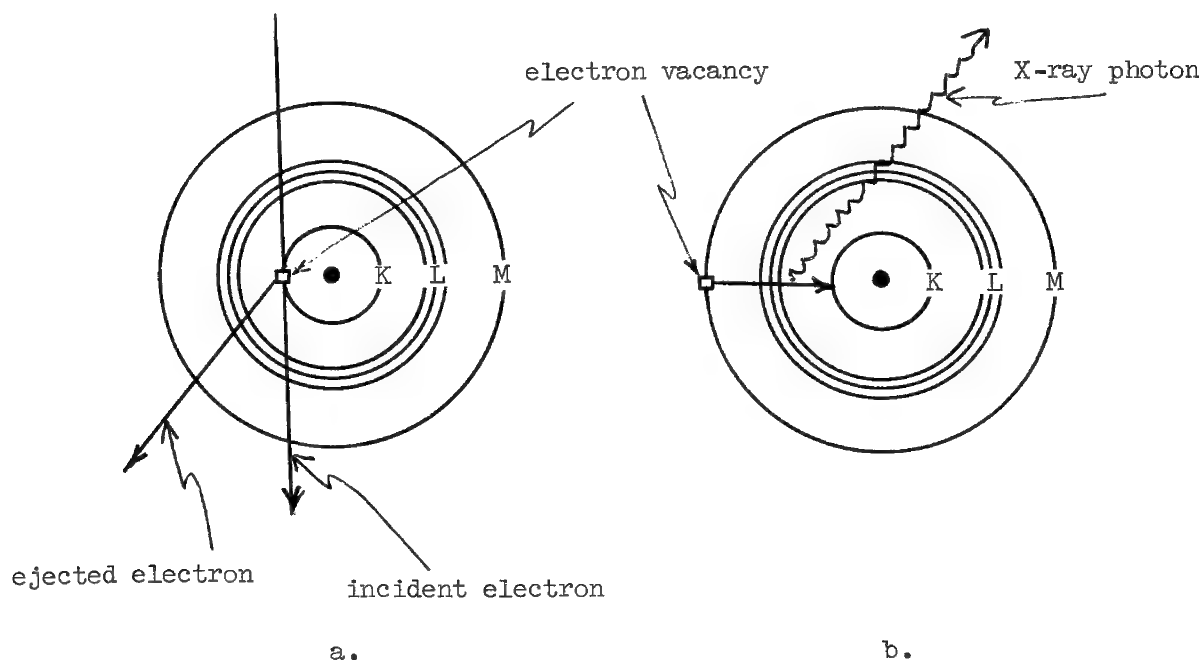
Figure 2. An incident electron ejects an atomic electron creating a vacancy in the K shell. An outer M electron falls into the K shell leaving a vacancy behind in the M shell. An X-ray photon is created by this transition.
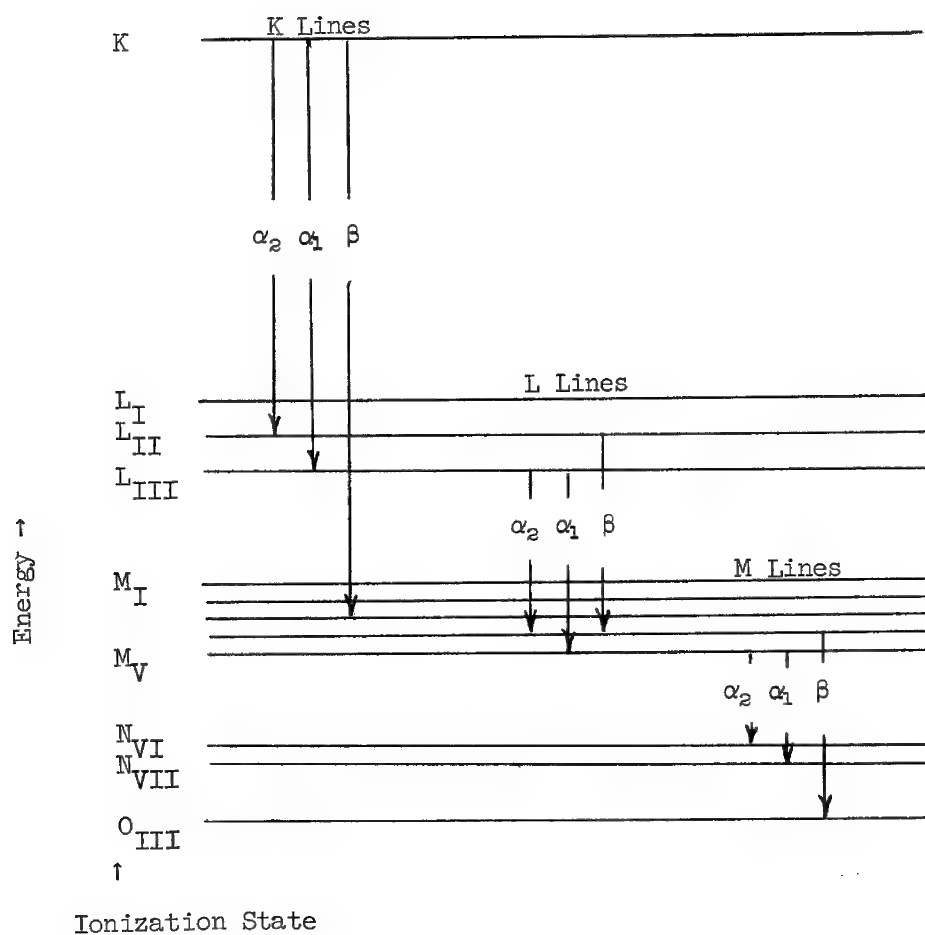
Figure 3. Schematic X-Ray Energy Level Diagram. Thè arrows represent transitions of an ionized atom which lead to characteristic X-ray emission. There is one K state, 3 L states, 5 M states, etc.
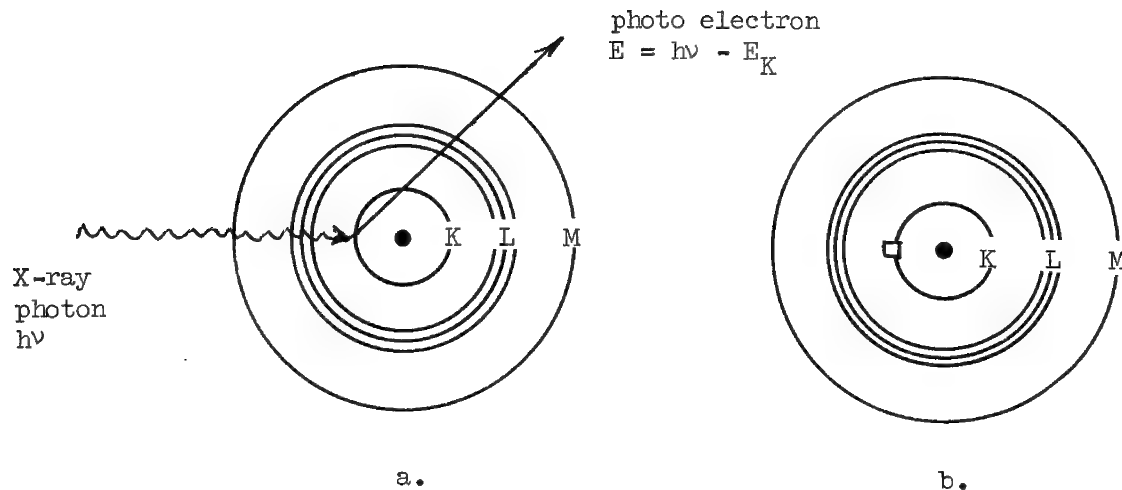
Figure 4. The Photo Electric Effect. In a, an incident X-ray photon
of energy $h\nu(kev) = 12.3/\lambda(A°)$ ejects an inner shell electron.
This "photo electron" has a kenetic energy equal to the energy
of the incident photo minus the critical excitation energy for
the shell in the atom. In b, the atom is left in an ionized
or excited state exactly as in Figure 2a and the initial X-ray
photon no longer exists. The excited atom now decays to its
ground state through X-ray or Auger electron emission.
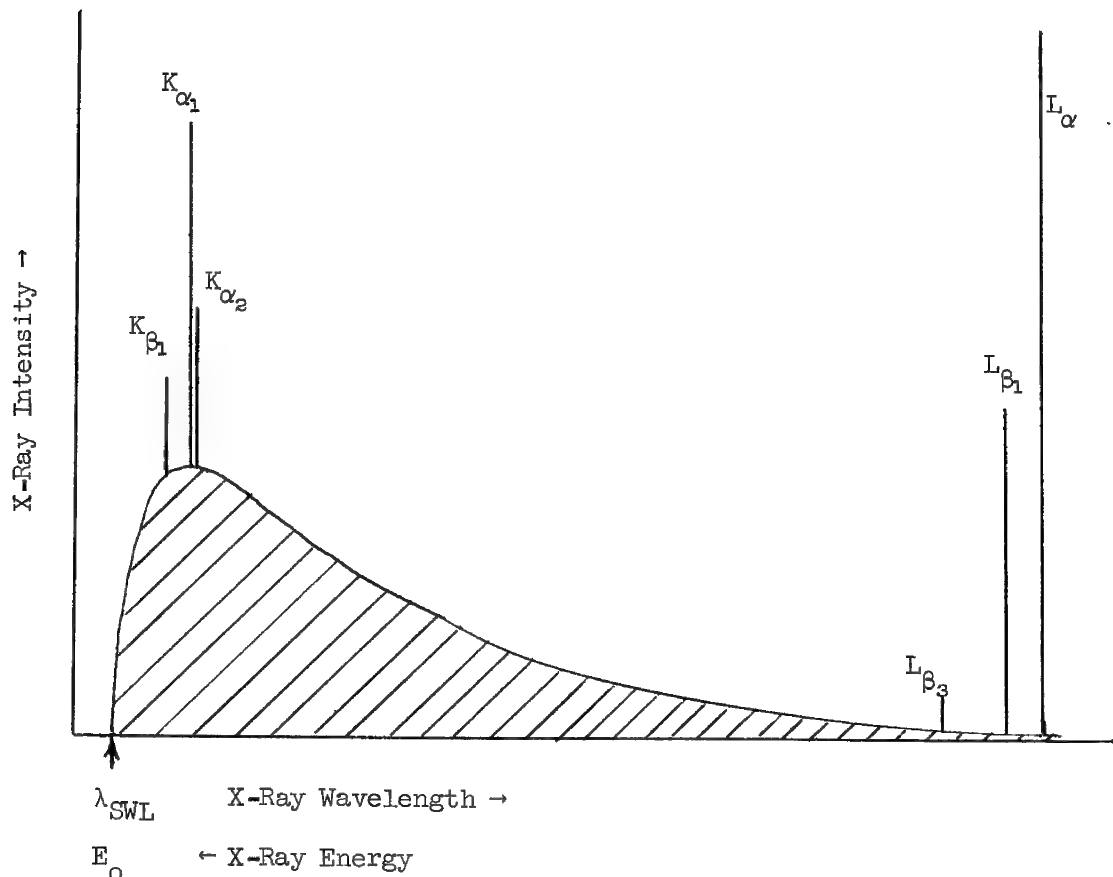
Figure 5. The X-Ray Spectrum Generated in a Solid Target by an Electron
Beam. The sharp vertical peaks are the characteristic lines
produced by discrete electronic transitions within the atoms.
The shaded region is the continuous spectrum (white radiation
or Bremstrallung) produced by the deceleration of incident
electrons near atomic nuclei.
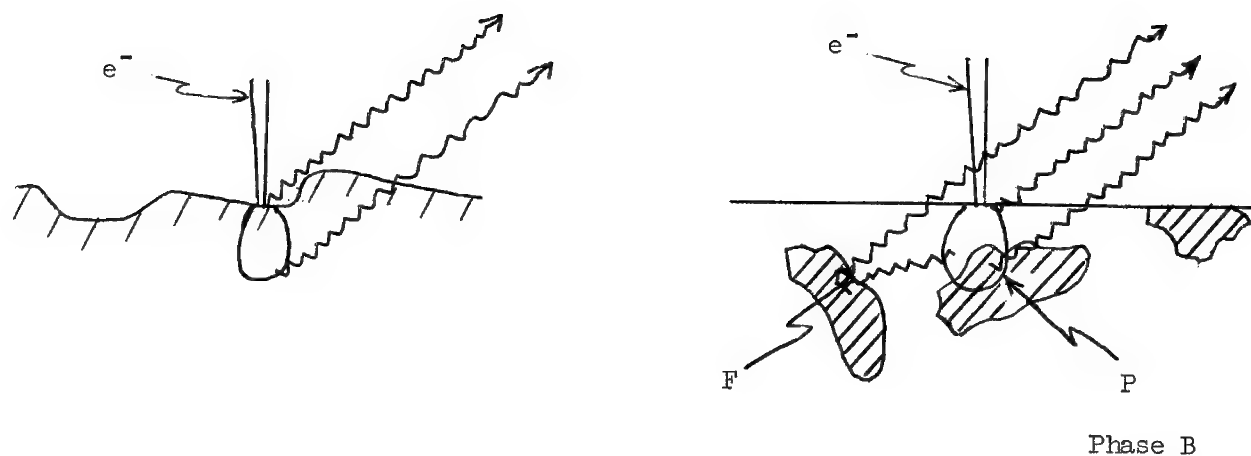
Phase B

a. Surface roughness gives rise to
    unpredictable absorption effects.

b. X-rays are produced in phase B
    (at P) although the incident
    beam is entirely "on" the matrix
    phase. Phase B can also be excited
    by primary X-rays by the fluorescent
    effects as at F.

Figure 6. Topographic Effects.
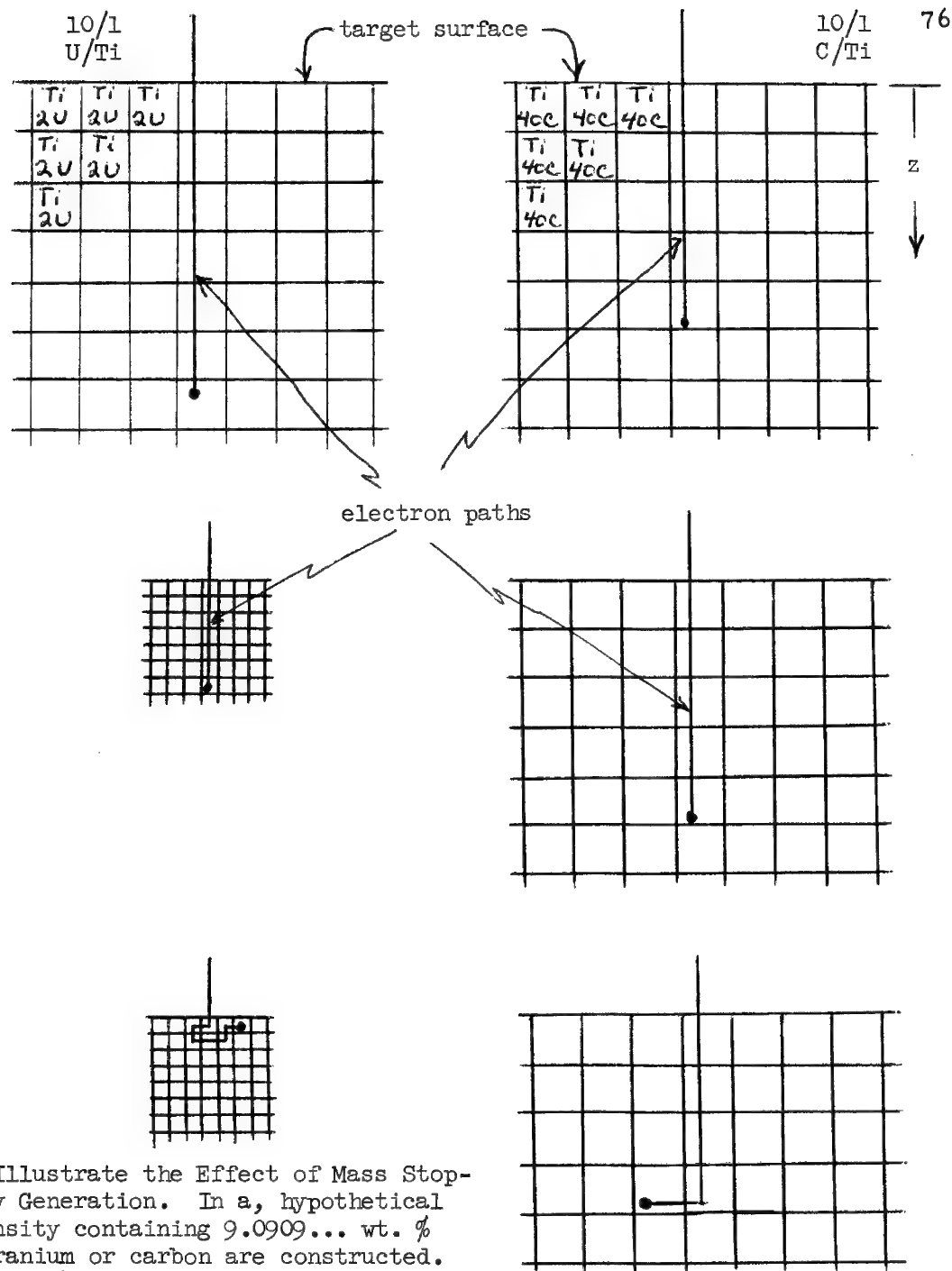
Figure 7.

A Simple Model to Illustrate the Effect of Mass Stop-
ping Power on X-Ray Generation. In a, hypothetical
alloys of equal density containing 9.0909... wt. %
titanium balance uranium or carbon are constructed.
Atomic weights of 48, 240, and 12 are assumed for the
three respective elements. Each unit volume in the
uranium alloy contains one Ti atom, 2 U atoms with 206 electrons while in the carbon alloy
there are one Ti atom, 40 C atoms with 262 electrons per unit volume. An incident electron
penetrates further into the U alloy since it encounters fewer atomic electrons. In b, the
U alloy is compressed to a higher density. The penetration of the incident electron on ρz
basis remains the same. In c, the incident electrons are allowed to scatter. In the U allo
where scattering is more frequent, the electron penetration on a z basis is reduced propor-
tionally more by scattering but the total distance x measured along the electron path remains
the same as in b. The incident electron passes more Ti atoms in the U-Ti alloy than in the
C-Ti alloy and, therefore, produces more Ti K_α X-rays.
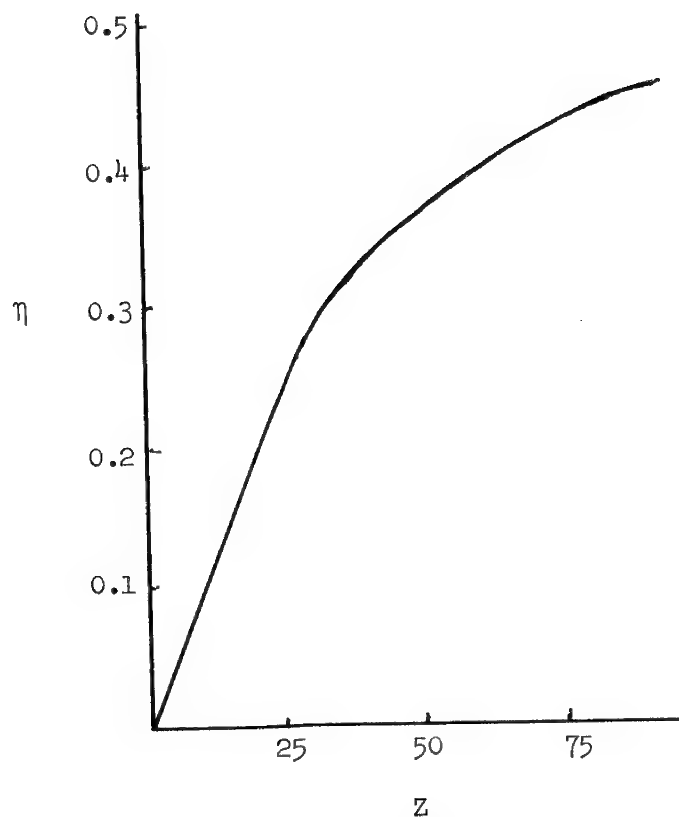
Figure 8. The Atomic Number Dependence of the Backscattered Electron Coefficient. [24]
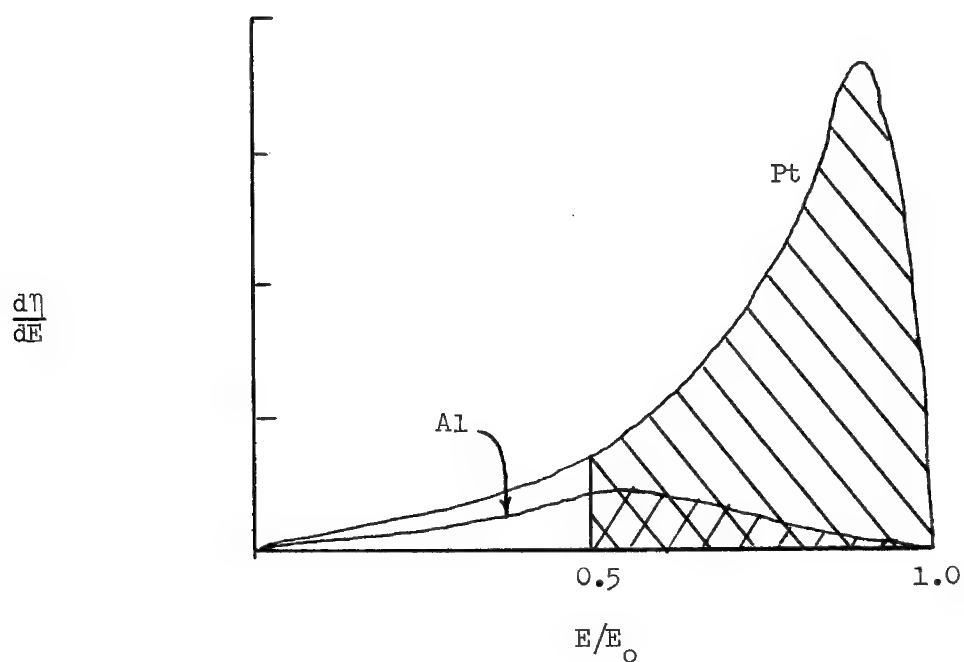
Figure 9. The Energy Distribution of Backscattered Electrons from Al and Pt. [25] The shaded regions represent the proportions of backscattered electrons which could have produced characteristic X-rays had they remained within the target for an overvoltage $(U = E_o/E_c)$ of 2.
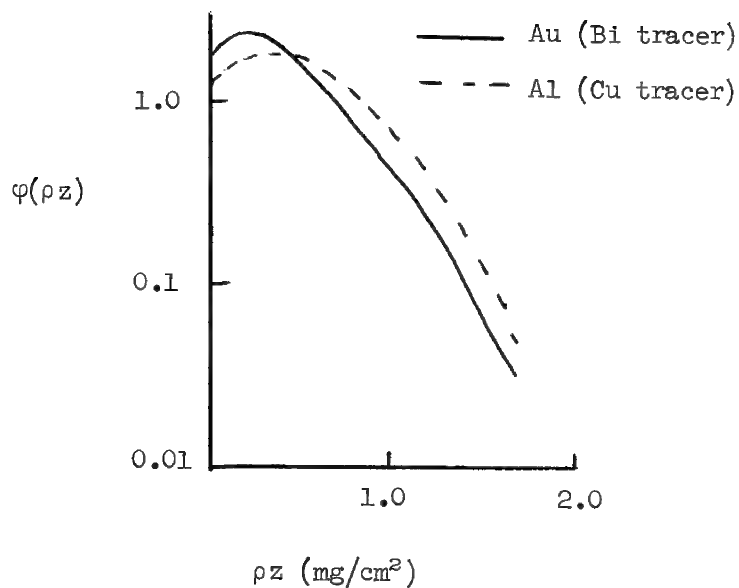
Figure 10.   The Distribution with Mass Depth of Characteristic
X-Ray Production.

a.

b.
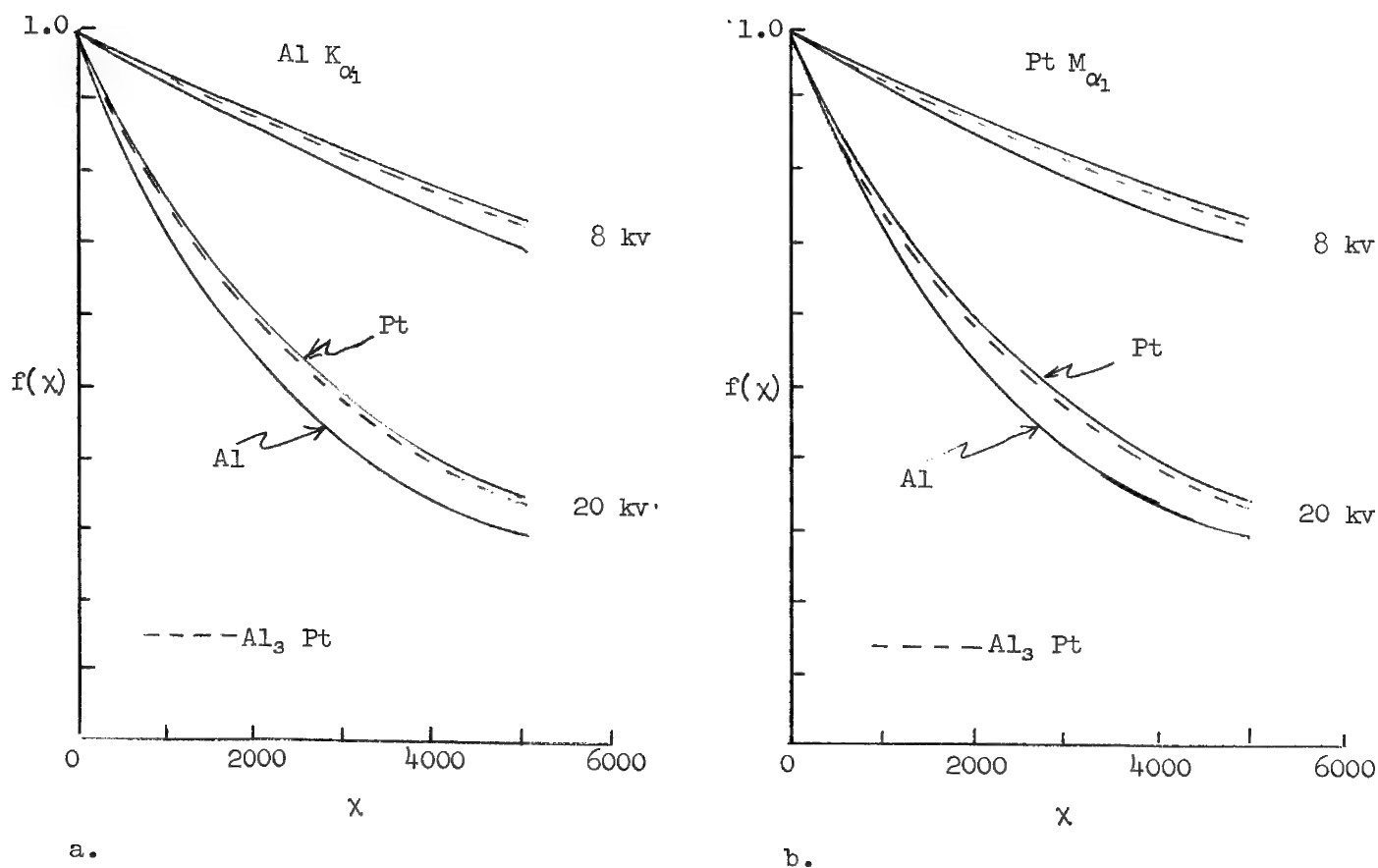
Figure 11.   The Absorption Correction, $f(\chi)$.   High absorption [small $f(\chi)$] is
promoted by high accelerating energy, low atomic number matrices
and high values of $\chi = \left(\dfrac{\mu}{\rho}\right) \csc \theta$.
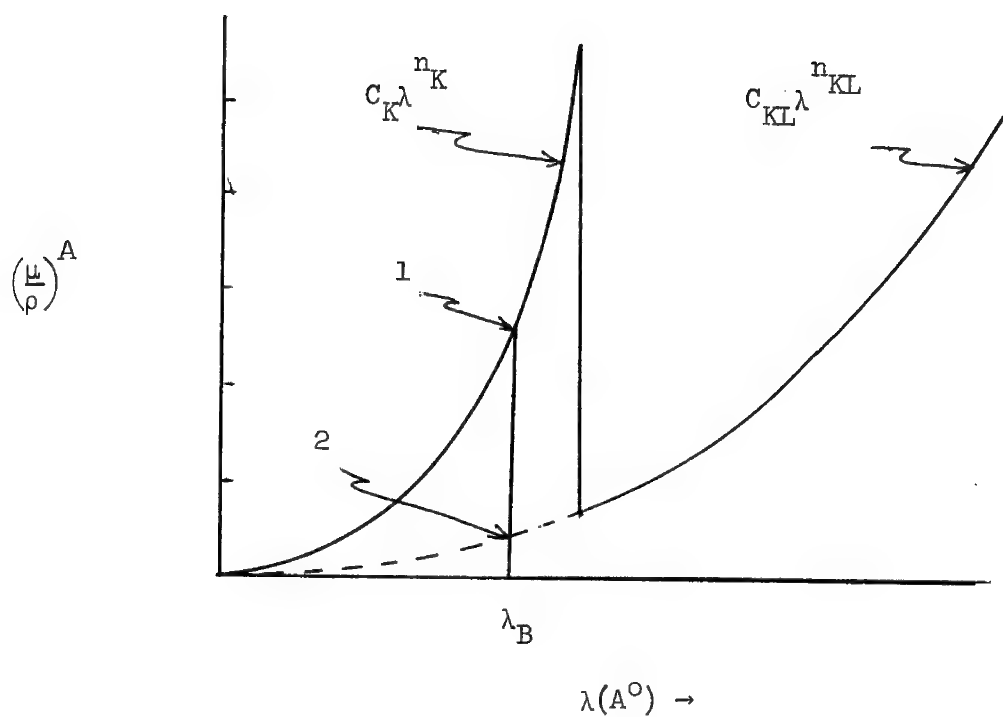
Figure 12. Evaluation of r_A, Equation 26. r_A equals $\left(\frac{\mu}{\rho}\right)_B^A$ (point #1) divided by the extrapolated value at point #2.

"INFLUENCE COEFFICIENTS IN QUANTITATIVE ANALYSIS"

BY

FERNAND CLAISSE

DEPT. OF METALLURGY, UNIVERSITE LAVAL

INTRODUCTION

Microprobe analysis has now attained a level of development such that quantitative analysis has become next to a routine procedure. Gone are the days when a highly competent operator only would be allowed to operate the probe. Now, with a minimum of knowledge about the operation of the probe a person can easily collect data necessary to calculate the composition of a sample under examination.

Collecting data is not enough for a correct determination of the composition of a sample and, also, a minimum amount of knowledge is necessary concerning the various conditions under which the measurements are taken; for example:

- background position in presence of an absorption edge
- measurements taken near a two-phase boundary
- measurements on small particles or on thin films
- influence of alignment and geometrical factors on intensities etc., etc

These topics have been discussed by previous authors and will be assumed to be sufficiently understood.

The relation between X-ray intensities and element concentration has been discussed also and it has been shown that the phenomena

by which the energy of fast elections is converted into X-ray emission is rather well known.

It is indeed a satisfaction to observe that the sample on which the probe operator works is always a simple system as compared for example to samples used in X-ray fluorescence work. In the latter case samples are frequently agglomerates of particles, and sometimes with particles of different compositions. As soon as such inhomogeneities must be taken into account the exact mathematical description of the specimen state becomes so complex that an exact analysis is impossible.

On the other hand, the sample under examination in a microprobe is so small that it is always a single particle with a uniform composition. It is a solid solution, that is, a nearly perfect mixture of elements on an atomic scale and the full description of the sample requires only the concentration of each of its elements. In such circumstances, it becomes possible to obtain mathematical expressions for the X-ray intensity of each emission line. The quantitative determination of the concentrations becomes a mathematical operation only; the solution is the concentrations which yield calculated x-ray intensities that match best the measured x-ray intensities. With the availability of modern powerful computers these operations are no longer a problem.

Direct Calculation Method

However, there are still some annoying aspects in the actual procedures for the calculation of concentrations. Here are some:

1. The calculations include corrections for back scatter and election absorption. These phenomena are represented by several mathematical expressions which are rather correct but which contain some approximations, each expression being more valid for a certain type of elements or for some conditions. Each author proposes his own combination of functions with the result that several expressions

between composition and x-ray intensities are available. Although the differences are not large, one always looks for the best relation for each particular case. This means that ideally the computer should contain several different programs in its memory and that the operator should be competent enough to make the best choice in each case.

2.   When an electron loses its kinetic energy on the samples the x-ray emission is a wide spectrum of radiations made up of a continuum with a few monochromatic lines and each radiation may excite monochromatic radiation of the elements of the sample by x-ray fluorescence. In practical applications, the contribution of the continuum is never taken into account because is is small and almost negligeable and because the amount of computer work is very high and does not appears justifiable in view of the only small increase of accuracy that would result.

3.   The calculation of N components in the sample is done by an iteration procedure. From x-ray intensities, the computer calculates approximate values of the concentrations by going through the whole complex mathematical relation, once for each element, then repeats the procedure again and again until the final concentrations are obtained. Although a computer works fast, computer time is expensive.

4.   Unless lots of information are stored in the computer, the operator must give to the computer some information pertinent to his problem each time, for example, absorption coefficients of the elements of the sample for the emission lines measured, and for the lines which cause x-ray fluorescence.

5.   Finally, the calculation of compositions from theoretical expressions is absolutely unpractical without a computer, even when the number of samples is small and when the composition is simple.

INFLUENCE COEFFICIENTS METHOD

One way to go over most of those inconveniences is to use the method of the "Influence Coefficients". In this method, empirical relations between x-ray intensities and concentrations are written in very simple forms and contain empirical coefficients. Several such expressions have been proposed but several of them have been shown to be equivalent or nearly so. To my opinion, the most prac'ical relation among the simplest ones has been proposed by Lachance & Traill; it is written:

$$C_A = I_A \left(1 + \alpha_{AB} C_B + \alpha_{AC} C_C + - - - \right) \tag{1}$$

$$I_A = \frac{\text{intensity of A in sample}}{\text{intensity of A in pure element A}} \tag{2}$$

where C_i = concentration of element i

I_i = normalized x-ray intensity of element i

α_{ij} = influence coefficient of element j in the analysis of element i.

This relation states that:

1. The concentration of an element in a sample is roughly equal to its normalized intensity; as a matter of fact if the α's are made small, then:

$$C_A \approx I_A \tag{3}$$

2. The corrections to apply for the presence of another element are contained in the α coefficients and are proportional to the concentration of the element present and proportional to the concentration of the other elements, or:

$$\Delta C_A = \text{cte} \cdot C_A C_B \tag{4}$$

and from eq. 3:

$$\Delta C_A = \text{cte } I_A \, C_B \tag{5}$$

which is the second term in eq. 1.

A more versatile but similar equation has been proposed by Claisse and Quintin in which second order corrections are considered:

$$C_A = I_A \left(1 + \alpha_{AB}C_B + - - - \alpha_{ABB} \, C_B^2 + \alpha_{ABC} \, C_B C_C + --- \right) \tag{6}$$

The application of eq. 1 is best shown by an example, for instance the analysis of a Fe-Ni alloy. The measured intensity of Fe in the sample is 4270 cps and that of pure Fe is 8650 cps which gives 0.494 for the normalized intensity of Fe. Similarly the value of I_{Ni} is found to be 0.525. These values mean that the approximate concentrations of Fe and Ni are 49% and 52% respectively. Now, using this approximate composition and knowing the values of the influence coefficients $\alpha_{FeNi} = -.159$ and $\alpha_{NiFe} = 0.146$,

eq. (1) gives:

$$C_{Fe} = 0.494 \, (1 - 0.159 \times 525) = 0.452$$

$$C_{Ni} = 0.525 \, (1 + 0.146 \times 494) = 0.562$$

These concentrations are better than the approximate values and can be used instead in eq. 1 to give still better values of concentrations:

$$C_{Fe} = 0.494 \, (1 - 0.159 \times 0.562) = 0.444$$

$$C_{Ni} = 0.525 \, (1 + 0.146 \times 0.452) = 0.559$$

The same procedure would be used for more complex samples; the calculation would be longer but would not necessarily require a computer.

The Claisse & Quintin relation is used in the same way; it contains more terms but yields more accurate results. The potential of relations like that of Lachance & Traill has been recognized: the calculations are easy, simple and fast and the results are good. The main objection to its use is the difficulty to determine the α coefficients with accuracy, for all possible combinations of elements and for all experimental conditions. Of course, this also applies to the Claisse & Quintin relation.

Determination of Influence coefficients

Up to now two methods were available to determine the influence coefficients; they are rather tedious or difficult to use but recently a new and simpler method has been developed by Rousseau & Claisse I will now describe the three methods since they are all valuable methods.

1. The Experimental Coefficients

In this method eqs 1 and 6 are applied to several specimens of known composition and the α's are calculated. For example, consider a binary system; Eq. 1 writes:

$$C_A = I_A (1 + \alpha_{AB} C_B) \tag{7}$$

and

$$\frac{C_A}{I_A} - 1 = \alpha_{AB} C_B \tag{8}$$

Then, a graph of $\frac{C_A}{I_A} - 1$ as a function of C_B would give a straight line with slope equal to α_{AB}.

Since experimental values of I_A have some uncertainty
several samples should be used to determine the α value. This is
shown in Fig. 1. It is observed that indeed a constant α value exists
nearly, throughout the entire composition range. However, in some
cases, small deviations from linearity occur, which means that the L
& T relation may need second order correction. This is what the C
& Q relation does.

In that cases for a binary system eq. 6 yields:

$$\frac{1}{C_B} \left(\frac{C_A}{I_A} - 1\right) = \alpha_{AB} + \alpha_{ABB} C_B \qquad (9)$$

and a plot of the left side of eq. 9 as a function of C_B should yield
a straight line where α_{AB} is the intercept at the origin and α_{ABB} is
the slope. An example is shown in fig. 2.

Ternary standards are required for the determination
of the α_{ABC} coefficients in the C & Q relation. Since the α_{AB} and
α_{AC} values are based on x-ray measurements where   a small error exists,
the α_{ABC} value is rather inaccurate. This is one reason why the C. & Q.
relation has not become popular.

Even the L. & T. relation has not become popular because
the determination of the α coefficients requires many standards which
are extremely difficult to prepare for the microprobe.

2.   The graphical-theoretical coefficients of Lachance.

Lachance has proposed a theoretical approach to determine
the α coefficients. These are determined graphically as shown in figs
1 and 2 but theoretical values of I's are used instead of experimental
values. The theoretical values are calculated for various compositions

using the usual theoretical relations between x-ray intensities and composition. Then, α coefficients become theoretical coefficients and the only error is in the graphical estimation of the best fitting line. The results are good but the determination of the influence coefficients for complex systems represents a large amount of work. One definite advantage is that this technique requires no standards at all.

3. The theoretical coefficients of Rousseau & Claisse.

This method for the determination of influence coefficients has been developed initially for x-ray fluorescence but it is so general that it applies as well to microprobe analysis, using either the L. & T. equation, the C. & Q. equation or any similar relation.

Fig. 3 represents the normalized x-ray intensities of one element A in a ternary system of elements A, B and C. These intensities can be either measured or theoretical because we now know rather well the exact relations between intensities and composition. We also know that the C. & Q. relation is a simple expression which must be adjusted to closely fit the x-ray intensities. Since the I_A surface must follow the relation:

$$C_A = I_A (1 + \alpha_{AB} C_B + \alpha_{AC} C_C + \alpha_{ABB} C_B^2 + \alpha_{ACC} C_C^2 + \alpha_{ABC} C_B C_C) \quad (10)$$

which contains 5 coefficients, it is only necessary to force eq. 10 to pass through 5 selected points on the surface to make it fit the whole surface. Then the intensity I_A at the 5 selected points is calculated from theoretical expressions and eq. 10 is solved for the 5 coefficients. The 5 most convenient points are shown in fig. 3. Four points are on the sides of the triangle and correspond to the binary systems A-B and A-C; they yield values of α_{AB}, α_{ABB}, α_{AC} and α_{CC}.

The fifth point is near the center of the triangle and takes into account the additional curvature of the surface between the two sides; it yields the value of the α_{ABC} coefficient. The five equations can be put in matrix form:

$$
\begin{pmatrix} \alpha_{AB} \\ \alpha_{ABB} \\ \alpha_{AC} \\ \alpha_{ACC} \\ \alpha_{ABC} \end{pmatrix} = \begin{pmatrix} -\dfrac{5}{12} + \dfrac{20}{3} & 0 & 0 & 0 & -\dfrac{25}{4} \\ \dfrac{5}{24} - \dfrac{5}{6} & 0 & 0 & 0 & \dfrac{5}{8} \\ 0 & 0 & -\dfrac{5}{12} & \dfrac{20}{3} & 0 & -\dfrac{25}{4} \\ 0 & 0 & \dfrac{5}{24} & -\dfrac{5}{6} & 0 & \dfrac{5}{8} \\ -\dfrac{5}{56} & -\dfrac{15}{14} & -\dfrac{5}{56} & -\dfrac{15}{14} & \dfrac{4}{49} & \dfrac{439}{196} \end{pmatrix}
\tag{11}
$$

$$
X \begin{pmatrix} T_A\ (0.2,\ 0.8,\ 0) \\ T_A\ (0.8,\ 0.2,\ 0) \\ T_A\ (0.2,\ 0,\ 0.8) \\ T_A\ (0.8,\ 0,\ 0.2) \\ T_A\ )0.3,\ 0.35,\ 0.35) \\ 1 \end{pmatrix}
\tag{12}
$$

with

$$
T(A,B,C) = \frac{C_A}{I_A(C_A, C_B, C_C)}
$$

Thus, if the theoretical intensities of each element are calculated at 5 points in a ternary diagram, all α coefficients related to this ternary diagram and to its 3 binary diagrams are obtained. If such α values are calculated for all ternary diagrams, the results can be used for the analysis of any system as complex as it may be.

Validity of the Rousseau - Claisse theoretical coefficients

Example: analysis in the Fe-Cr-Ni system. ARL microprobe, 20 KV.

The theoretical coefficients for this system
are given in Table I. The analysis of any sample in this ternary dia-
gram can be determined from its x-ray emission intensities. For exam-
ple, the x-ray intensities of a 25% Fe, 25% Cr, 50% Ni sample were
calculated from theoretical expressions: they are given in Table II.
Using these intensities and the C. & Q. relation with the data in
Table I, the composition of the sample is calculated and found to be
the same as the starting composition (Table II).

The operations done in this example can be represented
by a loop. In the first part of the loop, starting with composition,
the x-ray intensities are calculated by means of the complex but correct
mathematical expression which takes into account election scattering
and absorption, x-ray absorption and fluorescence, and geometrical
factors. In the second part of the loop, the reverse operation is
done, starting with x-ray intensities and calculating the composition
by means, this time of an empirical and simple expression. Since the
calculated composition is the same as the initial assumed composition
the C. - Q. relation with its theoretical α coefficients is shown to
be the equivalent to the inversion of the complex and irreversible
expressions of x-ray intensities as a function of composition.

In the above samples it is noted that x-ray intensities
are nearly equal to concentrations, meaning that interelement effects
are small. An example where interelement effects are very large is
given in Tables III and IV. Note the large value of some influence
coefficients; nevertheless, the agreement between initial composition
and calculated composition is good.

Now, when one deals with measured x-ray intensities
instead of theoretical intensities the results are not expected to
be as good because of experimental errors and of some uncertainty
in the theoretical relation. Some results are given in Table V.

Conclusion

At some later date tables of α coefficients will certainly be available for selected experimental conditions and for particular theoretical relations.

In the meantime, any user can build his own tables adapted to his specific conditions and needs. This can be done even if no computer is available.

I have not discussed the various possibilities of application of influence coefficients. I will only mention some.

Instead of using pure elements as comparison standards, other standards more similar to the samples can be used. It is easy to calculate α coefficients that apply to such cases. If the standard is sufficiently close to the samples it is observed that the L.-T. equation applies well and no second-order coefficients are needed.

In the case of mineral analysis, α coefficients can be determined so that concentrations are obtained directly as percentages of oxides. The coefficients can also be determined for cases of fused and diluted samples, for example, borax beads as used in x-ray fluorescence which can also be used in the microprobe.

Acknowledgement

TABLE I

Influence coefficients in the Fe-Cr-Ni system (ARL probe, 20 KV)

Analyzed element A \ Influencing element B or C	Fe		Cr		Ni		
	α_{Fe}	α_{FeFe}	α_{Cr}	α_{CrCr}	α_{Ni}	α_{NiNi}	α_{BC}
Fe			0.1427	0.0032	-0.0782	-0.1419	0.0389
Cr	-0.0805	-0.1279		-	-0.0235	-0.0639	-0.0981
Ni	0.0900	0.0004	0.0729	0.0013		-	0.0019

TABLE II

Analysis of a Fe-Cr-Ni alloy

	Fe	Cr	Ni
Theoretical concentrations	0.250	0.250	0.500
Theoretical intensities	0.2578	0.2677	0.4803
Calculated concentration	0.249	0.249	0.500

TABLE III

Influence coefficients in the Mg-Al-Fe system (ARL probe, 20 KV)

Analyzed element A \ Influencing element B or C	Mg		Al		Fe		
	α_{Mg}	α_{MgMg}	α_{Al}	α_{AlAl}	α_{Fe}	α_{FeFe}	α_{BC}
Mg			0.0187	-0.0336	2.0136	-0.1582	-0.0861
Al	1.6133	0.4151	–	–	1.2087	-0.1237	-0.1104
Fe	0.2265	-0.0162	0.1899	-0.0106		–	-0.0263

TABLE IV

Analysis of a Mg-Al-Fe alloy

	Mg	Al	Fe
Theoretical concentrations	.500	.250	.250
Theoretical intensities	.3355	.1147	.2169
Calculated concentrations	.500	.251	.250

TABLE V

Analysis of real samples using influence coefficients

	Measured intensities	Calculated concentration	True concentration
Cr	0.117	0.103	0.099
Co	0.797	0.805	0.806
Mo	0.077	0.099	0.094
		1.007	0.999
Fe	0.494	0.448	0.436
Ni	0.525	0.559	0.566
		1.007	1.002
Ti	0.326	0.346	0.350
Nb	0.620	0.652	0.650
		0.998	1.000
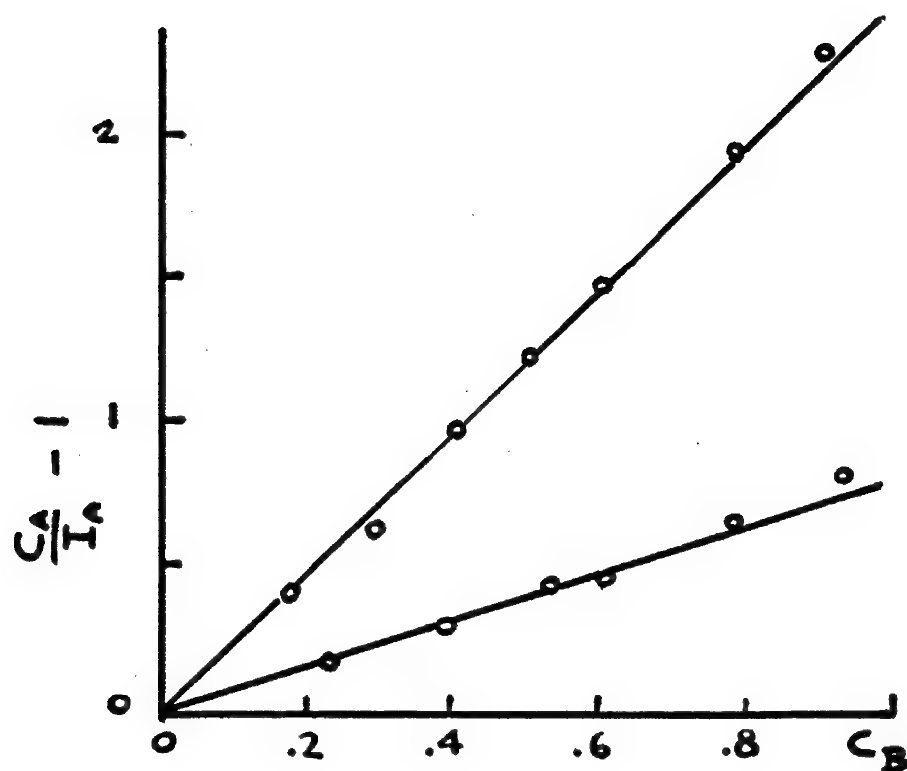
Fig. 1 - Graphical determination of the α_{AB} coefficients in the Lachance-Traill relation.
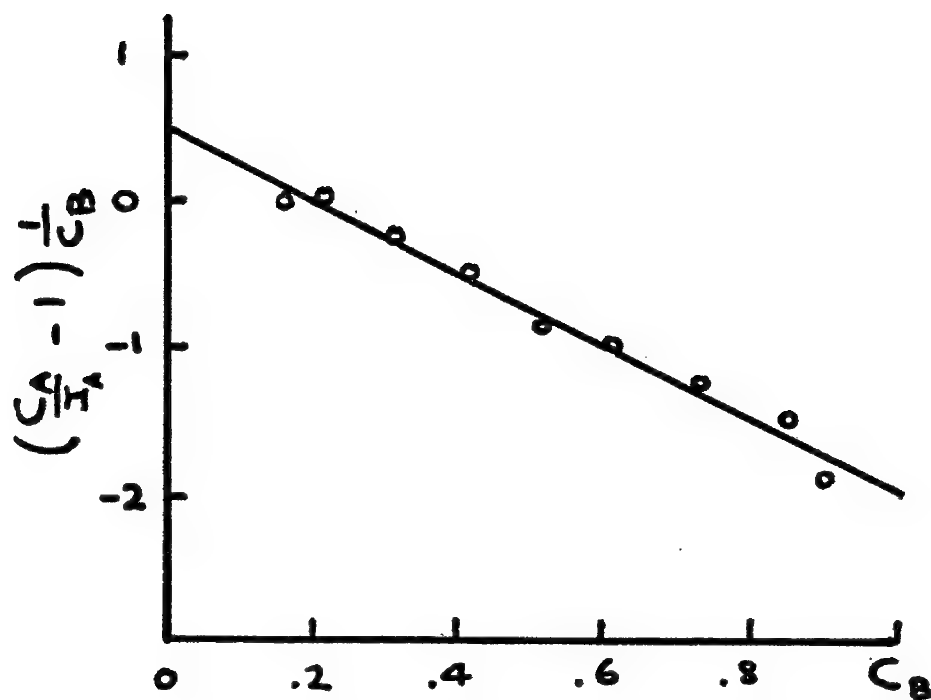
Fig. 2 - Graphical determination of the α_{AB} and α_{ABB} coefficients in the Claisse - Quintin relation.
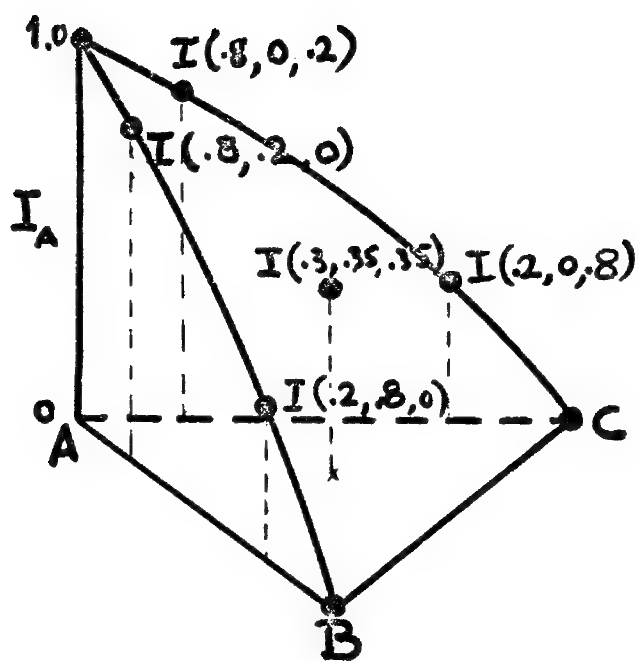
Fig. 3 –   X-ray intensity of element A as a function of composition
in a ternary system. Compositions chosen for the determination
of α coefficients in the Claisse-Quintin relation.

PRODUCTION OF ELECTRON PROBES A FEW ANGSTROMS IN DIAMETER

Albert V. Crewe
The University of Chicago
Chicago, Illinois 60637

Abstract

The advent of the field emission source of electrons has allowed the production of electron probes in the Angstrom range with meaningful electron currents. Specifically, we are now able to produce a diffraction limited probe with a radius of 2-2.5 Å with a beam current of 10^{-10} amps. While this is the current state of the art, it appears possible that in the future one should be able to produce the electron probe 1 Å in radius with approximately the same or slightly larger current. The present use of these probes is in transmission electron microscopy, but probes of slightly larger diameter are also being used for secondary emission microscopy.

BACKSCATTERED AND LOW-LOSS ELECTRON IMAGES IN THE SEM

by

Oliver C. Wells
IBM Thomas J. Watson Research Center
Yorktown Heights, NY   10598

The appearance of the backscattered electron image in the SEM will depend on the angle of incidence and on the position of the detector. There are two main possibilities:

(1) <u>Backscattered electron image with normal incidence.</u> In the microanalyzer, the specimen is usually mounted at right angles to the beam. This facilitates the calculation of x-ray corrections. The back-scattered electron detector system is then usually either a single solid-state diode mounted close to the beam, or is a pair of such diodes Fig. 1). The sum of the two diode outputs will depend on the local Z of the specimen, while the difference signal is related to the topography.[1]

A Monte Carlo calculation[2] of the penetration of electrons into a solid target is shown in Fig. 2. The probability function[3] of the maximum penetration depth of a backscattered electron into the target before it is turned back towards the surface is shown in Fig. 3. It is seen that this function is approximately constant between 0% and 30% of the penetration depth. If a diagram of the type which is shown in Fig. 2 is examined, it is found that the incident electrons are, in general, spread out to a significant extent during the initial 30% of the penetration path. This leads to the conclusion that the resolution will be limited at an appreciable fraction of the total penetration depth.

An exception to the above arises if the specimen consists of high-Z objects embedded in a low-Z matrix. Thus, according to the measurements of Gentsch and Reimer[4], a 40 kev electron beam, for example, will be enlarged by only ∿170 Å due to small-angle scattering after penetrating for 0.5 μm in carbon. This will be the degree of defocussing while examining a high-Z inclusion at this depth. This principle was used to examine biological materials stained with heavy metals by Abraham and DeNee.[5]

Electron channeling patterns can also be obtained using solid-state detectors as shown in Fig. 1.

(2) <u>Backscattered electron image with oblique incidence.</u> If the specimen is tilted relative to the beam, then the backscattered electron detector can be positioned so as to receive the electrons which have suffered a deflection of typically between 30° and 45° in the specimen (Fig. 4). The angular distribution of backscattered electrons shows a

pronounced forward lobe in this direction, which contains electrons which have lost typically less than 20% of the incident energy, and which have therefore travelled in the specimen for distances which are substantially less than the usual penetration depth.[6] The images[7,8] show the surface topography with a point-to-point resolution between the ridges in a GaAs test sample of 220 Å. We can refer to this as a "low deflection" back-scattered electron image because of the smaller deflection angle of the electrons in the specimen.

Low-loss image. The resolution can be improved by rejecting the slower backscattered electrons with an energy filter.[9] In the simplest approach, the energy filter is mounted in the specimen chamber of a surface SEM having a pinhole lens of the usual design, which is to say, the specimen is mounted outside the magnetic field. Either a secondary electron image or a low-loss image can then be obtained by suitably choosing the potentials on the filter grids and on the scintillator.

Some recent results are shown in Fig. 5. The sample is an aluminum film, which has been damaged by electromigration. The original layer of atmospherically oxidized alumina remains in position across the holes. It was reported earlier that the underlying holes cannot be seen in the low-loss image.[9] This particular sample has surface stains from the oil which was used to cool the sample during the electromigration. The secondary electron image (Fig. 5a) shows three types of contrast: from the surface topography, from the underlying holes, and from the suface stains. The low-loss image in Fig. 5b was obtained with a loss of 200 ev at 20 kv. This corresponds to a total pentration path of ~750 Å. The escape depth has been shown to be typically 10% of the total pentration path because, with a low take-off angle, the major part of this distance must be allocated to the electron trajectory in the material after it has suffered a wide-angle scattering event (Fig. 4).[10,11] This image does not show the underlying voids, and the surface stains are only shown very faintly. The major contrast is caused by surface topography, and there are some bright regions caused by penetration.

The new result is shown in Fig. 5c. Here, the loss voltage has been reduced to 25 v. The sizes of the bright regions caused by penetration have been greatly reduced. Also, the stains are much more visible, because of the reduced effective escape depth, which is now estimated to be less than 10 Å. The low-loss image with the lower values of loss voltage are now being investigated.

Some further results are shown in Fig. 6. The full-line shows the angular distribution of low-loss electrons calculated on the basis of the single wide-angle event model.[10,11] The bars show experimental values obtained by swinging an energy filter around the specimen. The agreement is encouraging, except that the observed peak is further away from the surface than the calculations indicate. The model is now being modified to see if this can be explained by additional small-angle scattering.

The final area of investigation of the low-loss image, which is being done in cooperation with A. N. Broers and E. Munro, is to examine solid specimens by the high-resolution low-loss method, in which the specimen is put into the high-field region of a condenser-objective lens.[11,13] The best resolution obtained so far is 30 Å center-to-center between gold dots, which corresponds to a dark fringe width between the dots of less than 15 Å. The advantage of this method is that it will give good topographic contrast from a solid sample, provided that it has been metallized with a suitable high-Z material.

I would like to thank C. G. Bremer for technical assistance.

REFERENCES

1. S. Kimoto and H. Hashimoto, pp. 480-489 in "The Electron Microprobe", Proc. Symp. Washington, D. C., Oct. 1964. T. D. McKinley et al, Eds., Wiley, N. Y.

2. K. Murata, T. Matsukawa and R. Shimizu, Japan., J. Appl. Phys. 10, 678-686 (1971).

3. G. Shinoda, H. Kawabe, K. Murata and T. Shirai, Techn. Rpts. Osaka Univ., 16, 423-429 (1966).

4. P. Gentsch and L. Reimer, Optik, 37, 451-454 (1973).

5. J. L. Abraham and P. B. DeNee, Proc. Seventh Ann. SEM Symp., IITRI, Chicago, 251-258; also, P. B. DeNee, J. L. Abraham and P. A. Willard, ibid, 259-266, (1974)

6. H. Kanter, Ann. Phys., 20, 144-166 (1957).

7. O. C. Wells, Appl. Phys. Lett., 16, 151-153 (1970).

8. O. C. Wells and C. G. Bremer, pp. 463-466 in Proc. Sixth Int. Conf. X-Rays Optics Mic., Osaka, Sept 1971, G. Shinoda et al Eds., Univ. Tokyo Press.

9. O. C. Wells, Appl. Phys. Lett., 19, 232-235 (1971).

10. O. C. Wells, Proc. Fifth Ann. SEM Symp., IITRI, Chicago, 169-176, (1972).

11. O. C. Wells, "Scanning Electron Microscopy", McGraw Hill, N. Y., (1974). (in press)

12. O. C. Wells, A. N. Broers and C. G. Bremer, Appl. Phys. Letter, 23, 353-355 (1973).

13. A. N. Broers, Proc. 7th Ann. SEM Symp., Chicago, 9-18, (1974).

Distance ρX (mg/cm²)

-1.5   -1.0   -0.5   0.0   0.5   1.0   1.5

Al   30KV
     0°
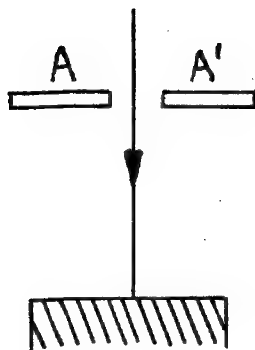
Fig. 1. Position of backscattered electron detectors with normal electron incidence (from ref. 1).
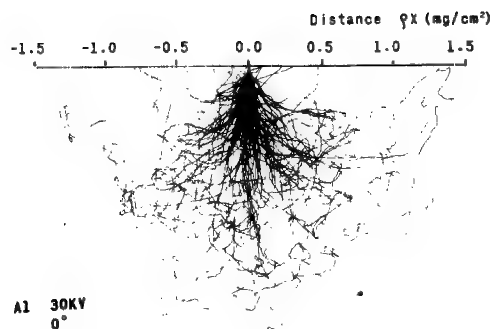
Fig. 2. Monte Carlo calculation to show the penetration of 30 kv electrons into Al (from ref. 2).

30kv

0.10 0.05 0 0.05 0.10

INCIDENT ELECTRONS

SPECIMEN SURFACE

BACK-SCATTERED ELECTRON

z_m

z_m
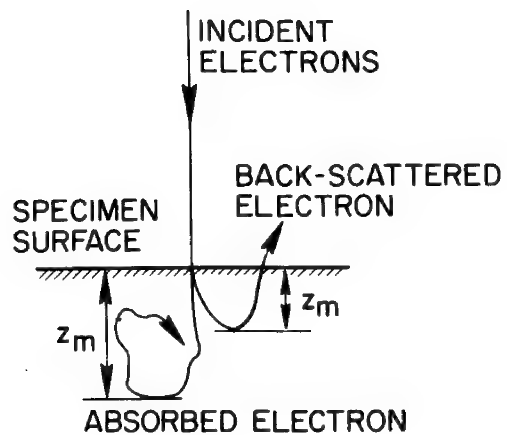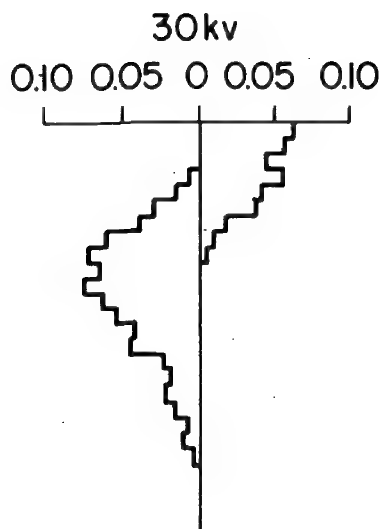
ABSORBED ELECTRON

Fig. 3. (a) Distribution of maximum penetration depth for backscattered electrons (right-hand side) and absorbed (left-hand side) electrons in copper specimen as calculated by the Monte Carlo method. (b) Definitions of depth. (From ref. 3.)

Fig. 4. With oblique incidence, a significant fraction of back-scattered electrons are deflected by a single wide-angle event, together with small-angle scattering and energy loss.
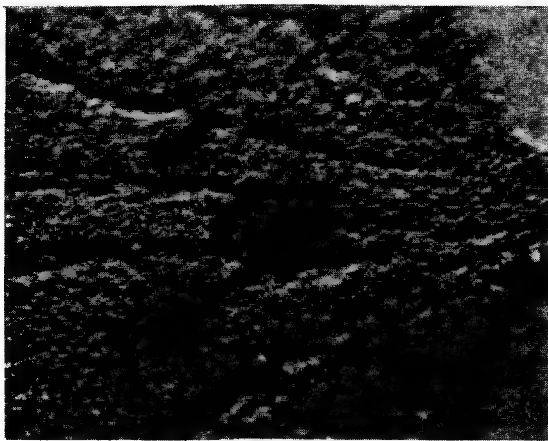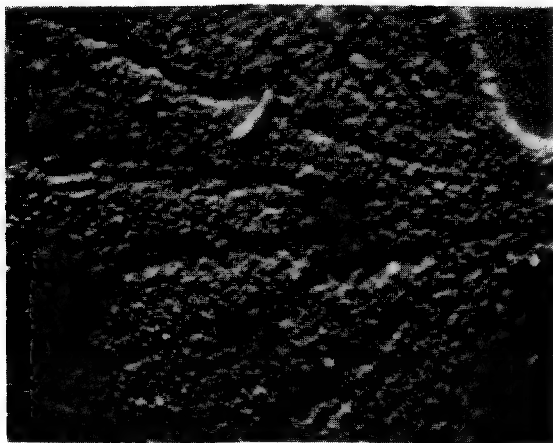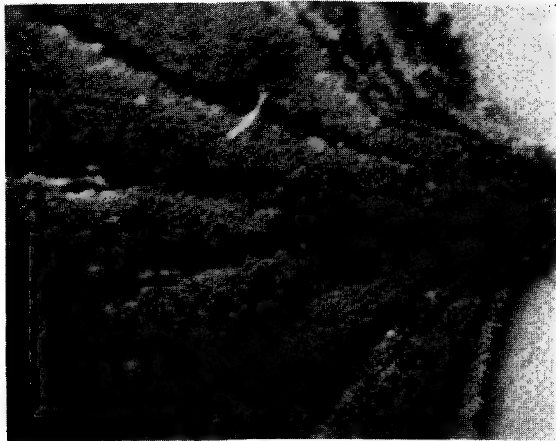
Fig. 5. Al Film, Stained over certain areas, and damaged by electromigration: (a) secondary electron image. (b) Low-loss image (200 ev loss at 20 kv). (c) as (b), but with 25 ev loss (see text).
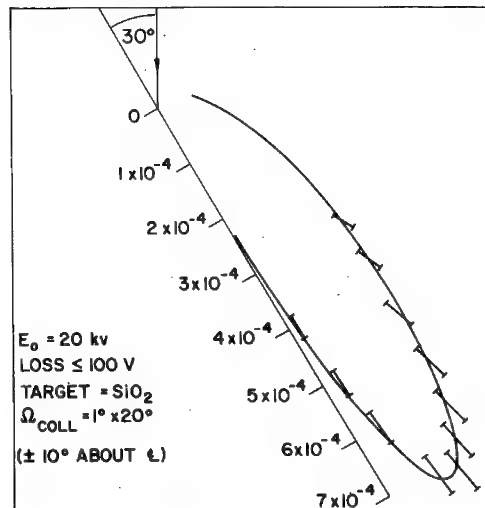
Fig. 6. Angular distribution of low-loss electrons. Full line = theory. Bars = experiments.

DUAL GUN ELECTRON MICROSCOPE FOR HIGH RESOLUTION TEM AND SEM

Poen S. Ong[1] and Curtis L. Gold[2]
The University of Texas System Cancer Center[1]
M. D. Anderson Hospital and Tumor Institute
Houston, Texas 77025

Technical Equipment Corporation[2]
Denver, Colorado 80204

The two types of electron microscopes, i.e., the conventional stationary beam and the scanning electron microscope (SEM), have developed into instruments with completely different fields of application. While the first type is used mainly for transmission electron microscopy (TEM), the major application of the second type has been for studying surfaces in the reflective mode.

Tradiationally, the TEM is characterized as a high resolution ($<5\overset{\circ}{A}$) instrument for observation of thin ($\simeq 700\overset{\circ}{A}$) samples in transmission. To obtain the high resolving power, a short focal length (1 mm) magnetic immersion lens is required. As a result, this instrument can be used only for study of small (3 mm) and nonferrous samples. The typical SEM in many aspects has just the opposite characteristics. The capability of handling large samples (25 mm) requires use of a long focal length lens (10 mm). Since low energy electrons are used for image formation, the sample space must be free of interfering magnetic fields. These requirements dictate the use of an asymmetrical 'pinhole' lens. The associated large spherical and chromatic aberrations result in a probe size which is at least one order of magnitude larger than that obtained with an immersion objective. The use of this type of lens has been found to be justified since the resolution of a SEM in reflection is limited to about $100\overset{\circ}{A}$ due to electron diffusion in the sample. However, recently, interest in a high resolution scanning transmission microscope

(STEM) is growing since it was shown that high quality pictures can be obtained by this mode of operation on samples which are considered too thick for conventional TEM. This may offer an alternate approach to high voltage microscopy and is within reach of many investigators.

The resolution in a STEM of a thin sample is mainly determined by the probe size and may therefore be reduced to a few Å. This is also true for the resolution of a layer within the first few Å of the sample. Since any existing TEM has all the required electron optical components to produce a small electron probe, a minor modification and the addition of a scanning system would transform this into a combination instrument for a high resolution SEM and STEM. Such an approach had been realized earlier by Ong[1] and resulted in an accessory which became commercially available.[2] In that approach, the objective pole pieces were modified in such a manner that the sample is located midway between them. The objective became a symmetrical double lens as originally described by Ruska.[3] The magnetic field above the sample acts as an immersion type probe forming lens. The field below acts as regular imaging objective for transmission. microscopy. The condensor system forms part of the total electron optical demagnifying system. The main limitations of this approach are the limited fields of view, the lack of spot size reduction by the system to obtain a resolution below 20Å, and the rather rigid requirement for aligning of the optical system to make the instrument useful for regular TEM as well as for SEM.

This report will describe the approach to overcome these limitations and to fully exploit the potential capabilities of any existing electron microscope for use as a high resolution (3 to 5Å) STEM without compromising in any way the operation of a conventional TEM.

To achieve a high resolution, it is desirable that the high resolution imaging system of the microscope be fully used by the probe forming electron beam for STEM, i.e., the electrons are to follow essentially the same optical path as the image forming electrons for TEM, even though in opposite directions. Therefore, a separate electron source is used for each of the two modes of operations. (A double gun instrument was proposed earlier by Nixon[4] for an electron microscope-microprobe combination.)

The similarity of the two modes of operation is illustrated in Fig. 1. Figure 1A shows schematically the optical path of a transmission microscope. In Fig. 1B, the scanning coil in a dual gun microscope is located below the projective system and the resulting SEM may be operated quite similarly to a conventional TEM. The peak current through the scanning coils may remain fixed; the magnification is controlled by the projective system which also automatically adjusts the electron optical reduction to the proper value and results in an optimum probe size and current for each magnification. The probe current is inversely proportional with the square of the magnification. Additional magnification changes are also possible by control of the scanning coil current. The similarity of the operation can be carried a step further; the transmitted beam will eventually focus in the vicinity of the electron gun. Basically, any crossover point of the condensor system allows location of an annular detector for dark field illumination followed by a complementing detector for bright field illumination.

Figure 1C shows an alternative approach, where the scanning system is located between the objective lens and the projective system. In this configuration, the magnification in the SEM mode is controlled by the peak value of the scan coil current. The limiting aperture may be located near

"TEM" Gun

Bright Field Det.

Image of Aperture

Annular Det. for Dark Field

Transmission Detector

Backscatter Detector

Scan Coils

Aperture

Aperture

Scan Coils

Fluorescent Screen

"SEM" Gun

A   B   C

Fig. 1

Bright Field Detector

Dark Field Detector

Diffracted Beam

Sample

Scan Coil

Objective Lens Off

Objective Lens On

A   B   C   D   E
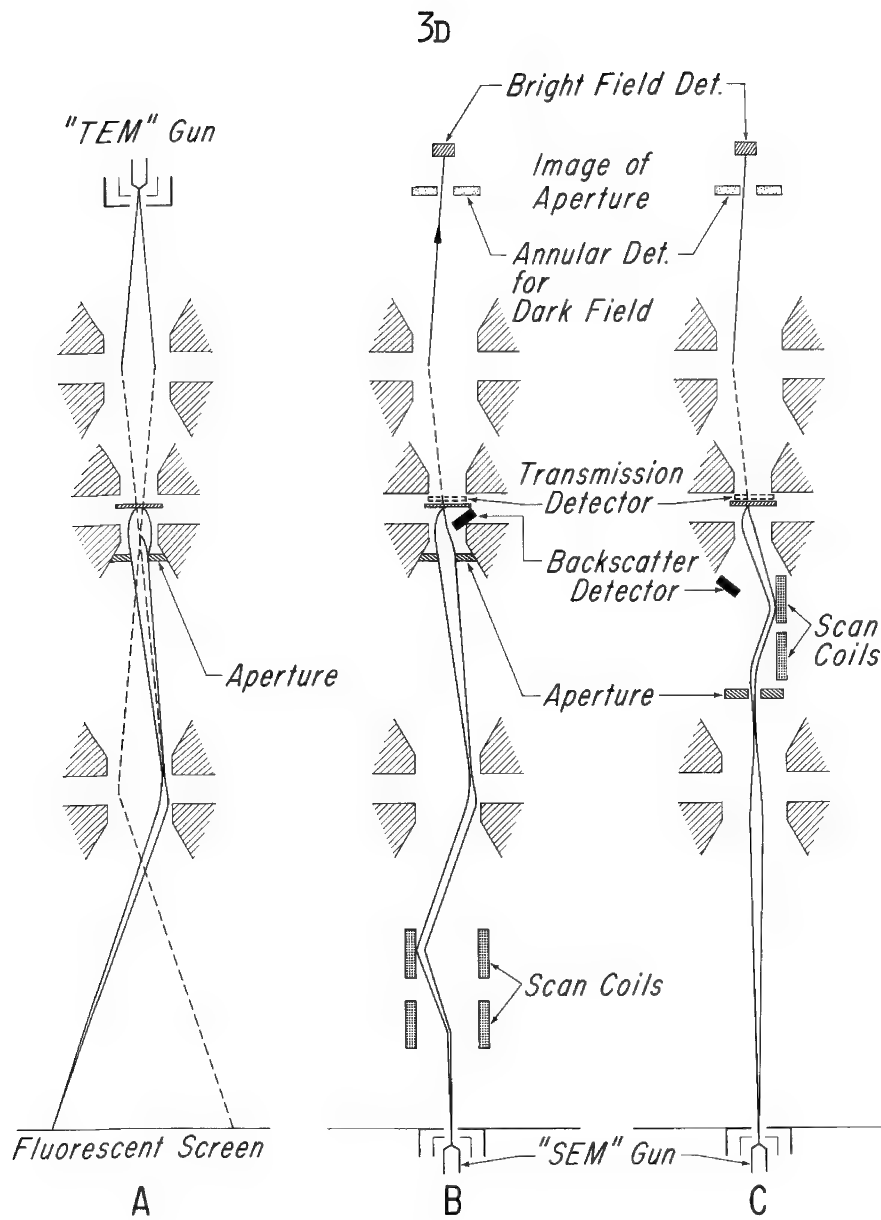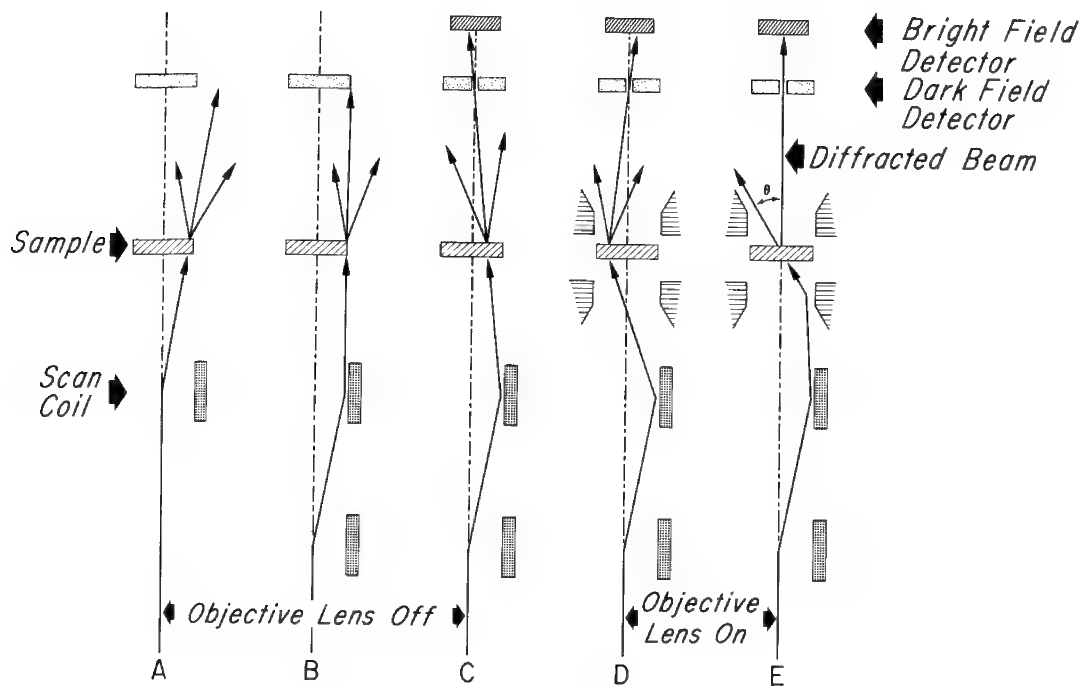
Fig. 2

the projector lens to permit more freedom in the location of a backscatter and/or secondary electron detector. Of particular importance for this version is the fact that it allows full control of the angles at which the beam strikes the sample. This is accomplished by adjusting the ratio of the current in the top and bottom coils, as shown in Fig. 2.

Figure 2A shows the situation where only one coil is used to obtain a large field of view with the objective lens off. Focusing is accomplished by the projector system. The transmitted beam is 'divergent' and it may never reach the detector at large deflection angles. This condition is avoided while maintaining the same field of view by using a double deflection as shown in Fig. 2B. In this case, the beam strikes the sample at normal incidence. A further increase of the top scan coil current results in a 'converging' beam as shown in Fig. 2C, where the pivot point of the deflection is 'focused' into a point image. When an annular detector is placed at the point image, it will produce a dark field image. The corresponding bright field image is obtained by the complimenting detector located behind.

For high resolution, the objective lens has to be used for further reduction of the spot size. In this case, the effect of the strong lens has to be taken into consideration in controlling the angle of incidence as shown in Fig. 2D.

Finally, Fig. 2E illustrates the situation where the pivot point of the beam deflection is 'focused' on the sample by an appropriate adjustment of the scanning system. In this case, the bright field detector will detect only the beam which is scattered or diffracted at an angle θ, in which θ varies with time. The electron diffraction pattern is therefore displayed on the SEM viewing screen.

A Philips EM200 electron microscope has been modified into a dual gun microscope of the type shown in Fig. 1C. Inclusion of an additional set of scanning coils will allow the instrument to be operated in the mode shown in Fig. 1B.

Both the TEM gun and the SEM gun are connected to a single high voltage power supply. A switch allows the selection of operating either the TEM or the SEM gun. Aligning of the microscope column is done in the normal TEM mode and is also correct for the SEM mode.

As was shown by Ong and LePoole[4], the image rotation of a magnetic lens causes the optical path to be different for electrons traversing through the lens in two opposite directions. It would therefore be virtually impossible to determine with certainty the *point* of impact of the beam emitted by the SEM gun by means of the image produced by the TEM gun, as was proposed by Nixon[5] in a double gun electron probe microanalyzer. It is possible, however, to cover essentially the same field of view in the TEM and SEM operation.

<div align="center">REFERENCES</div>

1. Ong, P.S.: A high resolution electron microscope for conventional imaging and scanning mode of operation. 5th Intl Cong X-ray Optics and Microanal. Tubingen 1968, Eds., G. Mollenstedt and K. H. Faukler, p329.

2. Philips Electronic Instruments, Inc.: EM 300-SEM (scanning electron microscope) attachment. Commercial paper, No. ST27 3M, August 1970.

3. Ruska, E.: Deutsche Patenschrift No. 875555 (29-5-1942).

4. Nixon, W.C.: A double gun electron microscope for selected area analysis. Proc European Reg Conf Elec Microscopy, Delft 1960, Eds., A.L. Howink and B. J. Spit, Vol. 1, p62.

5. Ong, P.S. and J.B. LePoole: A focusing aid for the x-ray projection microscope. Appl Sci Res B7:265, 1958.

SEM Backscattered Electron Imaging -- An Aid To Dust And Particulate Characterization

by

Phillip B. DeNee, Ph.D.
Jerrold L. Abraham,M.D.

Appalachian Laboratory for Occupational Respiratory Diseases
National Institute for Occupational Safety and Health
P. O. Box 4292
Morgantown, West Virginia   26505

Dust in our industrial workplaces, mines and environment is an ever increasing problem[1]. It is necessary, from the industrial hygiene standpoint, to identify and characterize these materials. One instrument used in particulate character-ization is the scanning electron microscope(SEM)[2-4]. If the dust is all of one type, it is a simple matter to size and analyze the dust using the SEM. Serious problems arise when the dust is of mixed character, part organic, carbonaceous, or other low atomic number material; and part inorganic, mineral or other higher atomic number material. This is a common problem in coal mine dust analysis[3,4] since coal mine dust contains from 5 to 50% ash[5]. It is also a common problem in environmental pollution analysis because of large quantities of soot in the environment. The analyst simply can not dis-criminate coal (carbon) from silica, pyrite, clay, calcite or other minerals by secondary electron imaging (Fig. 1). Energy dispersive X-ray analysis (EDXA) can be performed on each particle or X-ray mapping can be used for specific elements, but this is somewhat inconclusive because of the Bremsstrahlung, and quite time consuming if the particles are small (less than one micrometer).

A very simple method for rapidly identifying the mineral material in the SEM is through the use of backscattered electron imaging, Fig. 2. Since there is an increased backscattered electron yield with atomic number increase, the mineral par-ticles appear much brighter than the coal. EDXA confirmed that particles A and B were silicates (contained both Si and Al) while particle C was a silica (contained Si).

An interesting mixed dust particle is shown in Fig. 3. This particle contains both silicates and presumed coal. Essentially no differentiation is possible in the SE image (Fig. 4).

Fig. 5 and 6 illustrate a preparation of enzymatically digested lung[6] from a coal dust exposed mouse. Only one particle of higher atomic number than carbon is identified in the BSE image, Fig. 6.

An important application of this technique is to automatic image analysis systems. The BSE signal could be used to trigger the X-ray detection in the system used by E. W. White[7]. Since the example in White's Table 2[7] showed only 1 in 54 particles which was non-coal, considerable scan and analysis time would be saved by using a BSE-triggered system.

In recent publications[8,9] we used BSE imaging to identify dusts and heavy metals in situ in human tissues.

In conclusion, with the advent of improvements in the detection of backscattered electrons, BSE imaging has been rediscovered as an important aid to the rapid identification of inorganic dust in mixed samples which contain much organic material.

Acknowledgments:

References:

1. Hatch, T.F., Dust and Disease, Ch. 8, in The Air We Breathe, Farber, S.M. and Wilson, R.H.L. (Eds.), Charles C. Thomas, Springfield, Ill., 1961, p. 115-125.

2. Johari, O., and DeNee, P.B., Handling, Mounting and Examination of Particles for Scanning Electron Microscopy, in SEM/1972. Proceedings of the 5th Annual SEM Symposium, IIT Research Institute. Chicago, Illinois, April, 1972, p. 209-216.

3. DeNee, P.B., Mine Dust Characterization Using the Scanning Electron Microscope and Dust Samplers, SEM/1971, IITRI, p. 209-216.

4. DeNee, P.B., Mine Dust Characterization Using the Scanning Electron Microscope, Am. Ind. Hyg. Assoc. J., 33, 1972, p. 654-660.

5. M. Jacobson, U.S. Bureau of Mines, Wash., D.C., personal communication.

6. Nenadic, C.M. and Crable, J.V., Enzymatic Digestion of Human Lung, Am. Ind. Hyg. Assoc. J., 31, 1970, p. 81-86.

7. White, E.W. and DeNee, P.B., Characterization of Coal Mine Dust by Computer Processing of Scanning Electron Microscope Information, Ann. N.Y. Acad. Sci., 200, Dec. 29, 1972, p. 654-660.

8. DeNee, P.B., Abraham, J.L. and Willard, P.A., Histochemical Stains for the Scanning Electron Microscope -- Qualitative and Semi-Quantitative Aspects of Specific Silver Stains, SEM/1974, IITRI, p. 259-266.

9. Abraham, J.L. and DeNee, P.B., Biomedical Applications of Backscattered Electron Imaging--One Year's Experience With SEM Histochemistry. SEM/1974, IITRI, p. 251-258.
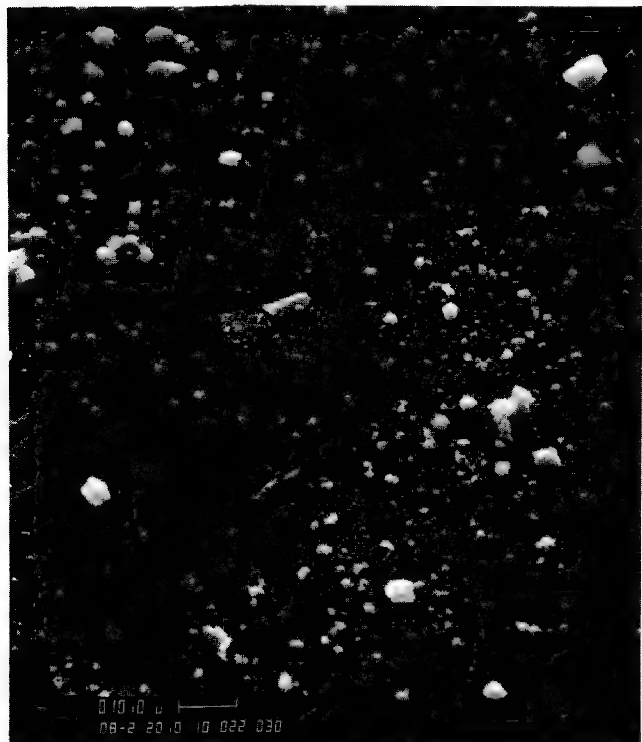
Fig. 1 SEM secondary electron image (SE) of coal dust. This figure illustrates the variety of shapes and sizes of particles present. No striking differences are noted. (See Fig. 2)

Fig. 2 Backscattered electron image (BSE) of the same area as Fig. 1. Particles A, B, and C now appear brighter than the others. Note that the remaining particles (presumably carbon) have about the same brightness as the background (carbon). Particles A and B are silicates and particle C is a silica.

Fig. 3 SEM-BSE of a coal dust particle showing a distinct band of bright (silicate) material.
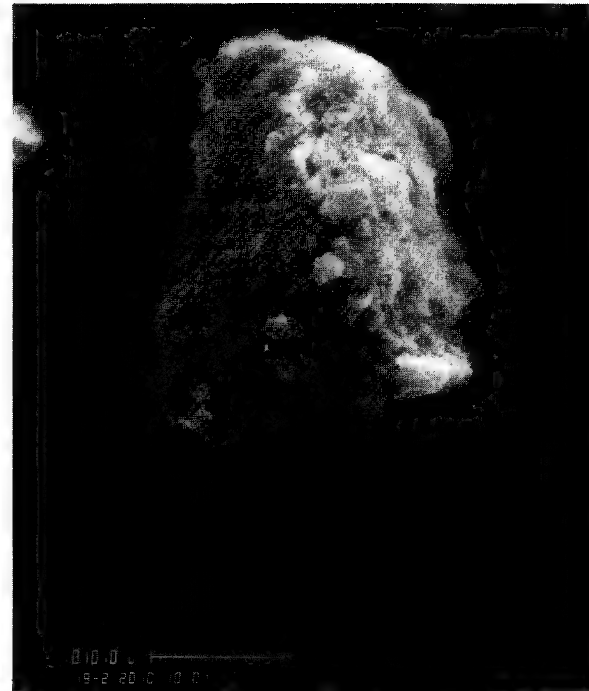
Fig. 4 SEM-SE of the same particle as seen in Fig. 3. No distinct band is detectable.
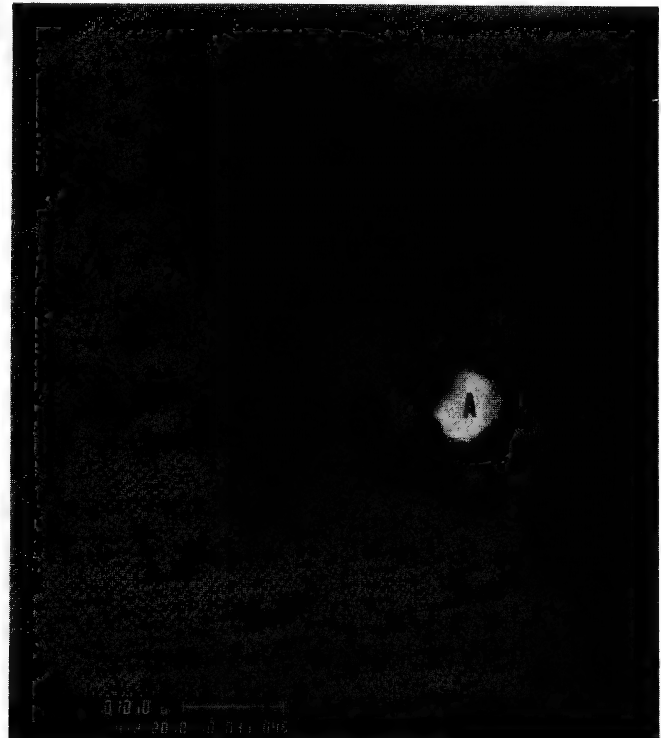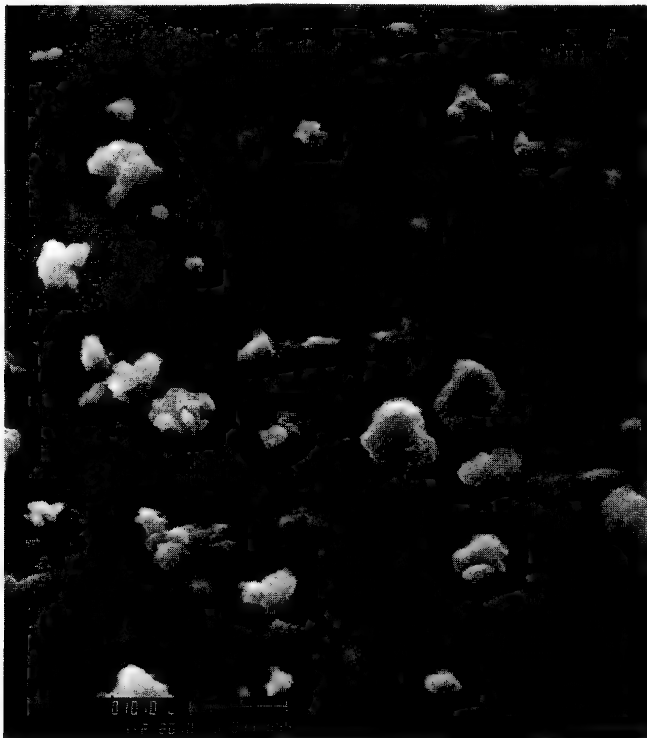
Fig. 5 SEM-SE of enzyme digested lung tissue. No difference seen in the particles.

Fig. 6 SEM-BSE of same material as Fig. 5. One particle (A) is brighter, owing to higher backscatter yield (silica particle).

Technical Note

Dust was dispensed from an ethanol suspension onto a carbon planchet and coated with 100-200Å of carbon[2,3]. Samples were examined in an ETEC Autoscan SEM*, equipped with a standard solid state backscattered electron detector[9], at 45° tilt and 20 keV. The marker "u" on each micrograph is in micrometers.

*Mention of a commercial product does not constitute endorsement by the Public Health Service.

Use of Time Derivative Transformations for Electron Micrograph Signal Processing

C. E. Fiori, D. E. Newbury, H. Yakowitz,
and K. F. J. Heinrich
Institute for Materials Research
National Bureau of Standards
Washington, D. C. 20234

In scanning electron microscopy, the microscopist usually has available image transformations which give high contrast-sensitivity over a small range of signals (black level or gamma transformations).

Derivative signal transformations can provide enhancement of fine details from specimens which produce large signal variations in the field of interest, i.e., high contrast images. These operators can also provide or modify the apparent oblique or vertical illumination of the specimen surface as well as crispen (sharpening in edge detail) [1] the image. Results of signal processing by the first time derivative, the absolute value of the first time derivative and the second derivative will be presented. Such time dependent signal processing can be carried out since the image signal is, in fact, written onto the CRT phosphor as a function of the line and frame times chosen to build up the image.

The basic purpose for using derivative operators is to provide an effective expansion of small sharp signal variations in the presence of large slow signal variations [2]. The net result is a spreading of the grey levels exposed on the recording medium by the small signal variations; the large signal variations are compressed into fewer grey levels by the derivative process. Properly applied, derivative processing can eliminate badly overexposed or underexposed regions in the final image.

Time Derivative Transformations

By modulating the CRT with the first time derivative of the signal, high contrast-sensitivity can be obtained over the entire range of signal intensity. Constant signals yield the same grey level regardless of the intensity of the constant signal. High frequency components of the image, i.e., the "fine detail" and noise (random signal fluctuations) are preferentially enhanced. Pure first time-derivative images, however, do not give the impression of depth usually conveyed by SEM images, because the static signal levels

which are responsible for shadowing are lost. This shortcoming can be avoided by mixing, in variable proportions, the original signal with the derivative signal, thus partially restoring these static signal levels while retaining enhancement of fine details.

Other time derivatives are potentially useful. We have investigated the absolute value of the first time derivative (which inverts those signal variations near the black end of the grey scale range to the white end) and the second time derivative. It must be recognized, however, that use of all time derivatives with conventional scanning intro- duces an undesirable form of anisotropy to the image [3].

In conventional beam scanning (rastering), the beam is displaced rectilinearly with horizontal and vertical velocity components, V_x and V_y. Normally, the line scan speed, V_x, is 500 to 2000 times greater than the frame scan speed, V_y. The intensity of the time derivative is related to the line scan speed. When time-derivative images are produced from this scanning method, all detail parallel to the scan line is lost (information loss line). Detail at an angle θ relative to the scan line is attenuated by a factor of $\sin\theta$ from the value produced when the scan line is perpen- dicular to the detail.

In the present work, a different technique of scanning has been employed. A 10-bit digital scan generator capable of highly precise and reproducible beam addressing has been built. With this scan generator, two sequential scans are superimposed on the recording film, with the values of V_x and V_y interchanged after the first scan. This has the effect of causing the beam to pass through each picture point in two orthogonal directions (orthogonal scanning).

When the first time derivative is scanned orthogonally, the loss of information along the line is not eliminated, but rather it is rotated relative to the orthogonal scan lines. Mathematically, the orthogonally scanned first time deriva- tive is proportional to the space gradient of the image function $f(x,y)$,

$$V\nabla f \tag{1}$$

where the constant of proportionality is the line scan velocity. Orthogonal scanning of the absolute value of the first derivative completely eliminates the information loss along any direction. The intensity of the derivative signal is still dependent on the angle relative to the scan lines and, hence, the operator is anisotropic.

Orthogonal scanning of the second time derivative results in a perfectly isotropic image transformation, i.e., the image is independent of orientation relative to the scan lines. Mathematically, the orthogonally scanned second time derivative is proportional to the space Laplacian of the image function f(x,y)

$$V^2 \nabla^2 f \tag{2}$$

where the constant of proportionality is the square of the line scan velocity. Note that the image transformation given by equation (2) is isotropic, but the image function f(x,y) is frequently anisotropic. An isotropic operator will not eliminate anisotropy already present in the image function!

An example of the various orthogonally scanned operators on the same image is given in Figure 1 (a), (b), (c), (d). Figure 1(a) is a normal secondary electron image of fly ash particles. Figure 1(b) is the first time derivative transformation of 1(a). Figure 1(c) is the absolute value of the first time derivative; a strong outlining effect is obtained. Figure 1(d) is the second time derivative of 1(a); a uniform, sharp outlining results.

The second time derivative is extremely sensitive to noise, and a high signal-to-noise ratio is necessary to produce a satisfactory image. The square of the first derivative, which when scanned orthogonally is also mathematically isotropic, is currently under study. Although the sensitivity to noise of this operator is the square of the noise of the first time derivative, it is still considerably less than the noise sensitivity of the second derivative.

References

[1]   Goldmark, P. C. and Hollywood, J. J., Proc. IRE 39, (10), 1314 (1951).

[2]   Heinrich, K. F. J., Fiori, C. E., and Yakowitz, H., Science 167, 1129 (1970).

[3]   Fiori, C. E., Yakowitz, H., and Newbury, D. E., SEM/1974, Proc. 7th SEM Symposium, (Johari, O., ed.) IITRI, Chicago, 1974.
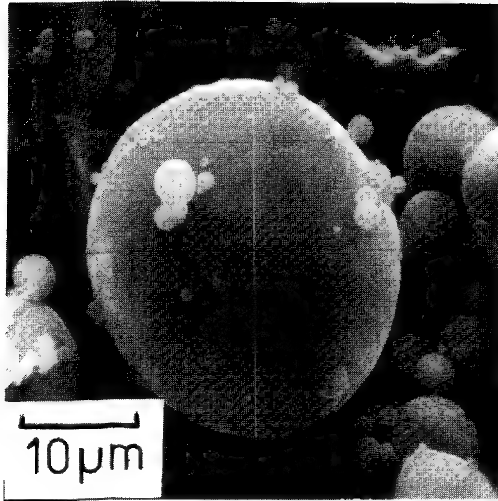
1a
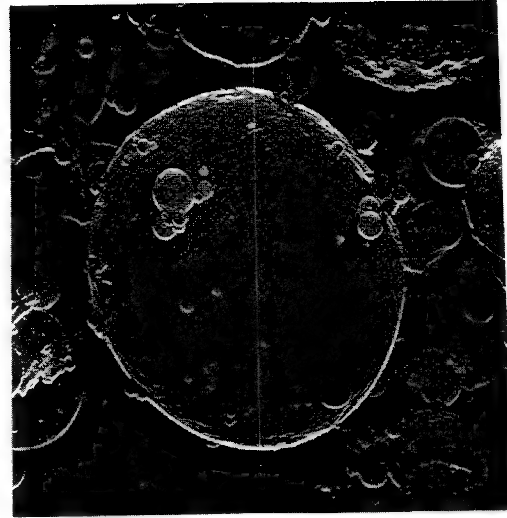
1b
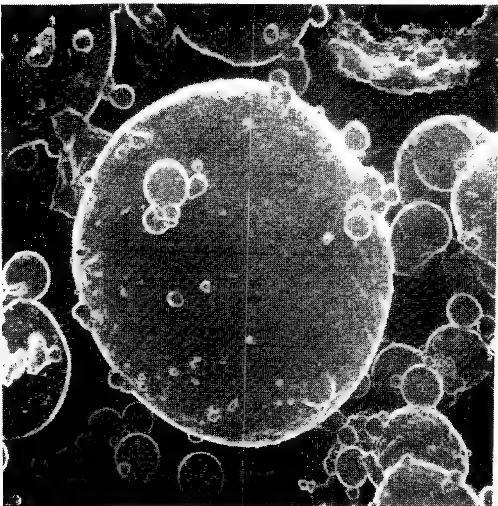
1c

1d

Figure 1(a)   Fly ash particles; secondary electron image.

Figure 1(b)   First time-derivative transformation of image of 1(a); orthogonally scanned.

Figure 1(c)   Absolute value of first time-derivative transformation of 1(a); orthogonally scanned.

Figure 1(d)   Second time-derivative transformation of 1(a); orthogonally scanned.

Monte Carlo Calculations of Type II
Magnetic Contrast in the SEM

D. E. Newbury, H. Yakowitz, and R. L. Myklebust
Institute for Materials Research
National Bureau of Standards
Washington, D. C.   20234

The magnetic field of a ferromagnetic solid can influence the interaction of energetic electrons with that solid. In the scanning electron microscope, such effects can be used to observe the magnetic domain structure of materials. Two types of magnetic contrast in the SEM have been recognized. In Type I magnetic contrast, leakage magnetic fields above the surface cause the deflection of secondary electrons which have been emitted from the specimen (for a review, see ref. [1]). Type I magnetic contrast can only be obtained from materials with strong leakage fields, such as the uniaxial materials, cobalt and $YFeO_3$.

A distinctly different contrast mechanism from that of Type I has been found to produce contrast in cubic materials, such as iron, which do not have large leakage fields [2,3,4]. Type II magnetic contrast results from the magnetic deflection of primary beam electrons during scattering within the specimen [3,5,6,7]. A typical example of domains in Fe-3 1/4%Si observed with Type II contrast is given in Fig. 1.

For this paper, the Type II contrast mechanism has been investigated by modeling the electron-solid interaction in the presence of the magnetic field with Monte Carlo calculations. The particular Monte Carlo program used in this work is described in detail in these proceedings [8]. The program calculations have been found to give good agreement with experimentally measured electron backscatter and transmission coefficients for a variety of conditions [8]. The trajectories of the primary electrons in the presence of the magnetic field are calculated in the following way: With the electron at a given point, P_i, the usual calculation is made to find the point, P_{i+1}, to which the electron would be scattered in the absence of an internal magnetic field. The electron velocity, flight direction, and the vector magnetic field are used to calculate the deflection due to the Lorentz force of the electron during flight. The point P_{i+1}, at which the deflected electron actually arrives, is thus determined. The amount of backscattered electrons for domains of opposite magnetization are calculated, and the contrast, C, is given by $(I_1-I_2)/I_{ave}$, where I is the intensity.

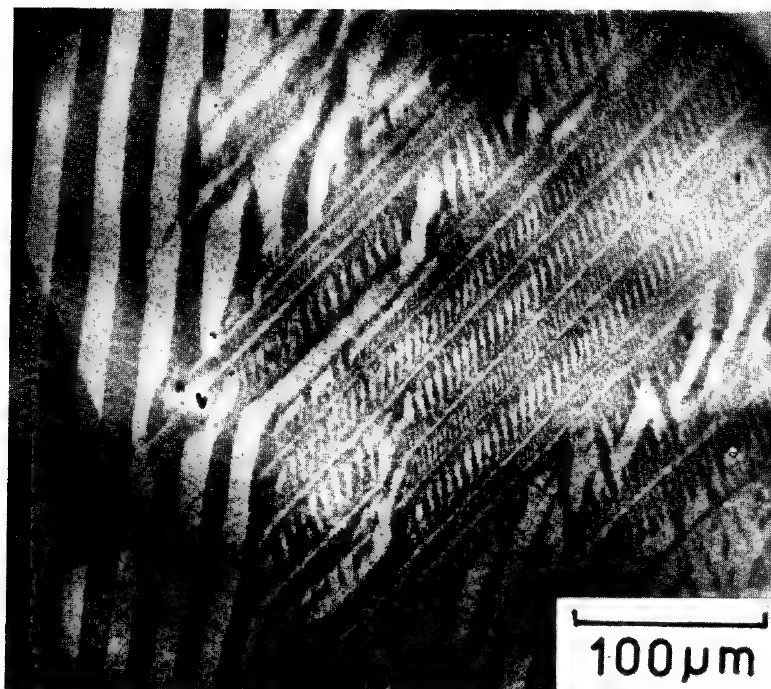Figure 1. Type II magnetic contrast. Specimen: electro-
polished Fe-3 1/4% Si; tilt: 55°; accelerating
voltage: 30 kV; specimen current: 2 X 10^{-7} amps;
signal: backscattered electrons.

Type II contrast has been measured experimentally as 0.3%
for iron at 30 kV and 55° tilt. In order to achieve
statistically valid results with the Monte Carlo calculations
at the 0.3% contrast level, a very large number of trajec-
tories, typically 10^5, would be necessary. To avoid such
costly calculations, it was first determined that the cal-
culated contrast value was linearly dependent on the mag-
netization, B, to values of B at least 75 times greater
than the saturation magnetization of iron. The various
calculations were then made with a large value of B in
order to give a statistically valid result with only 10^4
trajectories for each magnetization direction. The contrast
values were then normalized to the appropriate magnetization
for iron.

The following results have been obtained: (1) The contrast
at constant tilt is observed experimentally to increase with
increasing electron accelerating voltage [5], and this is
confirmed by Monte Carlo calculations, Fig. 2. The calcu-
lations predict a voltage dependence of the contrast of
$C \propto V^{1.44}$. (2) The contrast at constant accelerating voltage
is found experimentally to pass through a maximum with
increasing tilt relative to the beam. The Monte Carlo
calculations confirm this observation, predicting a maximum
at a tilt of about 55° from normal incidence, Fig. 3.
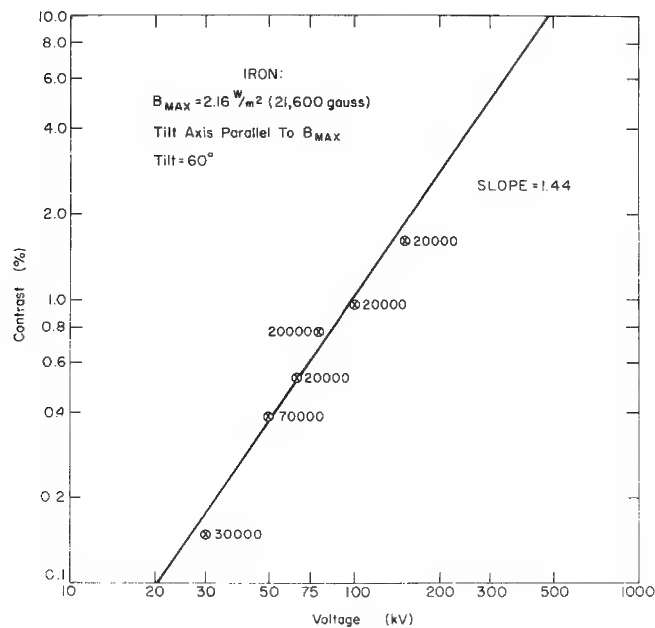
Figure 2. Dependence of Type II magnetic contrast on electron accelerating voltage. The number at each point gives the number of trajectories calculated.
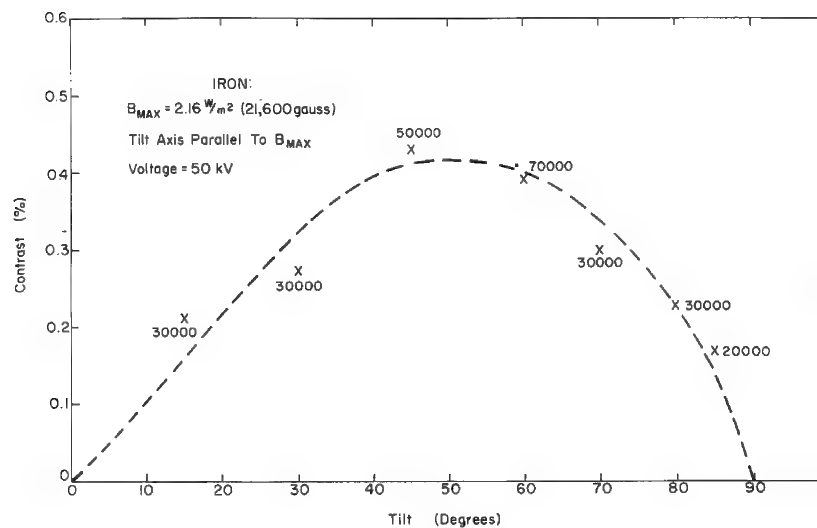
Figure 3. Dependence of Type II magnetic contrast on tilt relative to beam. Normal incidence = 0° tilt.

(3) At constant tilt and accelerating voltage, the contrast depends on the component of magnetization resolved along the tilt axis. This observation is confirmed by the Monte Carlo calculations. (4) The contrast value measured experimentally for given conditions is close to that calculated with the Monte Carlo program, e.g., a measured value of 0.35% and a calculated value of 0.25% at 30 kV, 55° tilt. Further improvements in the interaction model used in the program might reduce the difference between observed and calculated values. (5) The Monte Carlo program produces a table of the frequency distribution of backscattered electron energies. When this distribution is compared for domains of opposite magnetization, Fig. 4, the largest difference is found for electrons which have lost 0-20% of their initial energy.

IRON:
30,000 Incident
Electrons at 50 kV
Specimen Tilt = 60°
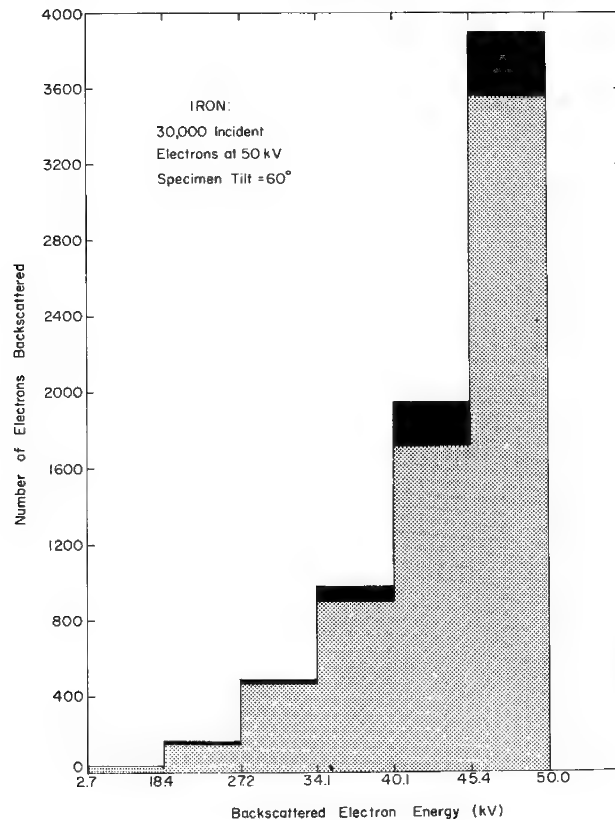
Figure 4. Energy distribution of backscattered electrons for domains of opposite magnetization. Note non-linear abscissa.

This suggests that the observed contrast could be increased by energy filtering so that those electrons which have lost more than 20% of their incident energy are excluded. The signal-to-noise ratio would be improved by excluding those electrons which contribute primarily to the background or noise. A crude energy filtering experiment has, in fact, confirmed this Monte Carlo prediction (5,7). The Monte Carlo calculations are thus useful in understanding the properties of Type II magnetic contrast and are indispensable for deducing and confirming the contrast mechanism.

References

[1]   D. J. Fathers, D. C. Joy, and J. P. Jakubovics, SEM/1973, Proc. of the 6th Annual SEM Symposium, O. Johari, ed. (Chicago, IITRI, 1973) pp. 259-266.

[2]   J. Philibert and R. Tixier, Micron $\underline{1}$, p. 174, 1969.

[3]   D. J. Fathers, J. P. Jakubovics, and D. C. Joy, Phil. Mag. $\underline{27}$, p. 765, 1973.

[4]   A. Gervais, J. Philibert, A. Riviere, and R. Tixier, Proc. 8th Natl. Conf. on Electron Probe Analysis (New Orleans, EPASA, 1973) p. 52A.

[5]   D. E. Newbury, H. Yakowitz, and R. L. Myklebust, Appl. Phys. Lett. $\underline{23}$, p. 488, 1973.

[6]   D. J. Fathers, J. P. Jakubovics, D. C. Joy, D. E. Newbury, and H. Yakowitz, phys. stat. sol. a $\underline{20}$, p. 535, 1973.

[7]   D. J. Fathers, J. P. Jakubovics, D. C. Joy, D. E. Newbury, and H. Yakowitz, phys. stat. sol. (in press).

[8]   R. L. Myklebust, D. E. Newbury, H. Yakowitz, and K. F. J. Heinrich, these proceedings.

SCANNING ELECTRON MICROSCOPY AND
MICROANALYSIS OF BIOLOGICAL MATERIALS

by

A. J. Tousimis
biodynamics Laboratories
TOUSIMIS RESEARCH CORPORATION
6000 Executive Boulevard
Rockville, Maryland   20852

Electron microbeam analysis of biological samples requires in addition to their proper preparation, the following from a well-integrated electron - light - X-ray optical system; (a) an electron optical system that is capable of producing electron microbeams of diameters smaller than the biological subcellular structure examined, of stable (better than a few parts per million) diameter and electron flux for more than thirty minutes; (b) a universal type sample stage that can conform to the precise requirements of a high quality light microscope (for localizing tissue components and aligning the X-ray optics with those of the electron-optical system); (c) both an X-ray "energy dispersive" and "wave length dispersive" characteristic and continuum detection systems and; (d) scanning modes of the electron microbeam so that, secondary and primary backscattered electrons from the specimen, transmitted electrons, specimen current and photon detectors can be recorded along with the X-ray characteristic/continuum data. Only an integrated system capable of the functions described is useful for most biological studies where not only the highest possible topographic resolution is desired but also that detection of the lowest (less than 1% wt) elemental concentration is usually the case.

The sample preparation procedures are normally dictated by the experimental parameters. In general tissues prepared by chemical "succession" are limited to studies involving localization of known-diffusable cellular components while physical "fixation" has serious limitations in the preservation of ultrastructural details, it has the advantage of preserving ionic or diffusable species in situ. In some cases both procedures are used. Thin film or solid (beryllium, carbon, silica glass) substrates for the tissue sections are used, depending on topographic and/or analytic information desired. All specimens-with some exception - are to be quoted uniformly with carbon in a rotating tilting device. This 50Å coating does not interfere with neither microanalysis nor microscopy in any mode and it is necessary to avoid local charging effects.

A typical study involving normal human volunteers in an intestinal absorption experiment, involves the excission of small pieces (0.5 mm^3) of tissue (figure 1) which is prepared by both physical and chemical fixation for either frozen section drying (figure 2) or critical point drying (figure 3) or embedding in epoxy for standard TEM. The integrated information obtained by the instrumentation outlined above furnishes one with both the topographic and analytic information desired in this type of studies.
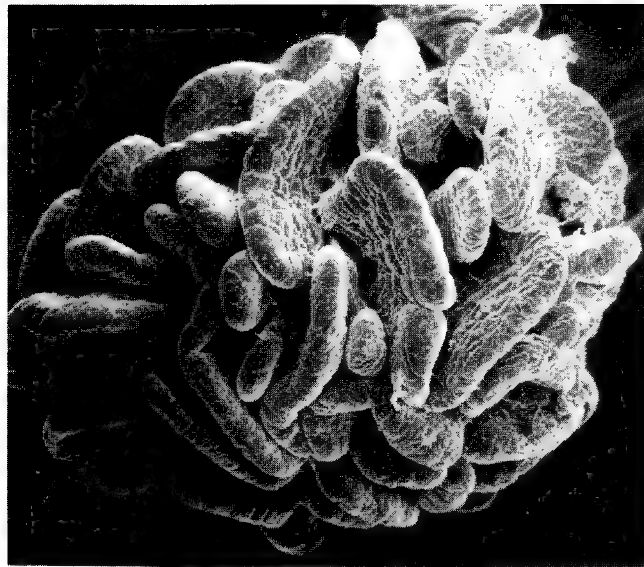
Figure 1
Scanning electron micrograph of one
of several tissue pieces obtained
during biopsy of human small intestine
(normal).
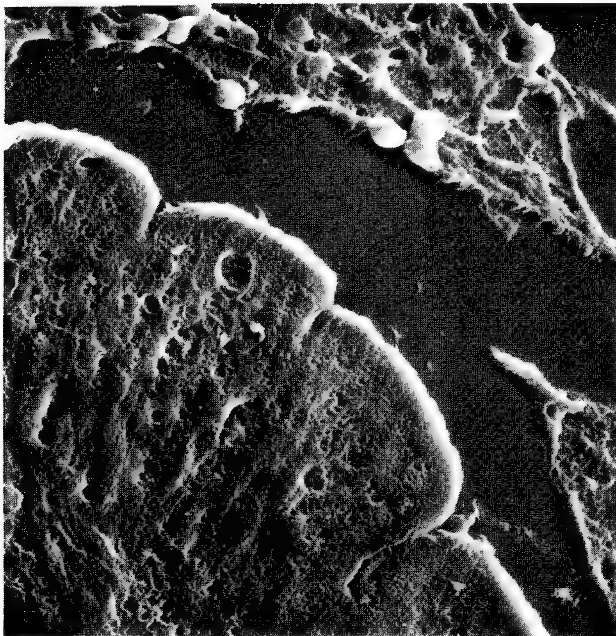
Figure 2
Frozen dried - frozen thin
section of a portion of human
small intestinal villus, prepared
for electron microbeam analysis.
SEM - secondary electron.
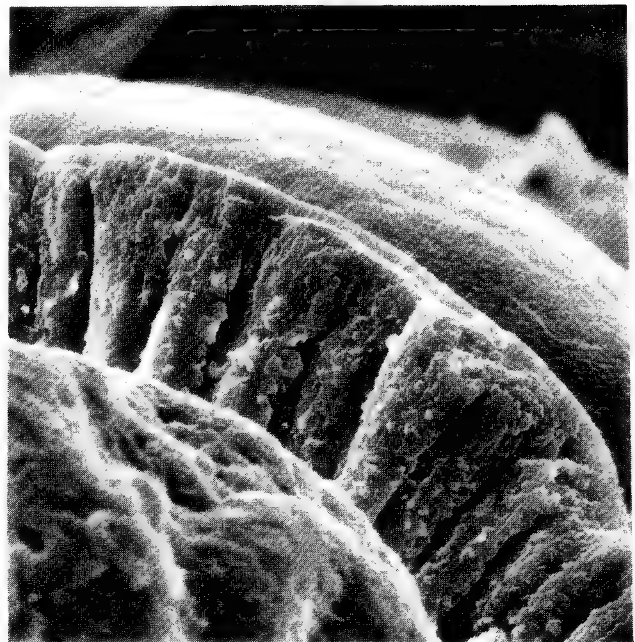
Figure 3
Free fracture of the normal
human intestinal villus,
epithelial cells (microvilli
on outer surface) are closely
packed on top of lamina
propria. SEM - second
electrons.

A METHOD FOR
ELECTRON PROBE MICROANALYSIS OF ORGANIC COMPONENTS IN PICOLITER SAMPLES

J. V. Bonventre and C. Lechene

Biotechnology Resource in Electron Probe Microanalysis,
Laboratory of Human Reproduction and Reproductive Biology
and Department of Physiology
Harvard Medical School
Boston, Mass. 02115

The method developed to use the electron probe to quantitate the elemental content of picoliter biological liquid droplets (1, 2) can be extended to organic analysis, permitting the organic components of biological samples as small as 20 picoliters to be measured. The method is based on the principles of chemical analysis whereby a sample containing an unknown amount of an organic component of interest is combined with a reagent which will specifically and quantitatively react with the organic component to form a precipitate. In order to apply this precipitation procedure to electron probe microanalysis, the reagent and thus the precipitate, must contain an element which can be quantitatively analyzed by the electron probe. The sample and the reagent must be combined quantitatively in a system where no evaporation is permitted. The precipitate must then be washed of all non-reacted reagent and sample components. Finally, the precipitate must remain insoluble and when counted by the electron probe must produce counts directly correlated with the amount of organic component of interest in the original sample.

The picoliter samples are handled in specially calibrated micropipettes under stereo microscopic control and are manipulated with a micromanipulator (1, 2). They are placed under paraffin oil onto a vitreous carbon disc that has been ashed in an oxygen plasma for 5 seconds and washed with acetone. An identical volume of reagent is then introduced into each of the sample droplets. The reagent is chosen so that the organic component of interest is specifically and quantitatively precipitated. The preparation, carbon disc with the droplets covering the precipitates, is then placed in a centrifuge tube and the disc is supported by a fitted Lucite base at a distance of 5.5 cm from the bottom of the tube. The disc is then placed in a swinging bucket and centrifuged at 3,000 r.p.m. for one hour in a Sorvall GLC-2 centrifuge. The centrifugation results in the flattening of the precipitates against the carbon disc at the bottom of the sample drops, fixing them in position (fig. 1). The preparation is then removed from the centrifuge tube and washed with m-xylene to remove the oil. Care is taken during this washing procedure not to expose the drops to the air at any time. The carbon disc with the droplets, now covered with m-xylene, is quenched in isopentane at -160°C. It is then removed and placed in a constant temperature bath of absolute alcohol at -60°C for 2 - 5 minutes until the frozen droplets sublimate in the liquid alcohol and the alcohol soluble components of the drops diffuse away. As a result only the precipitates, washed of the reagent and of the other ionic components of the original sample droplet, remain on the carbon disc. The absolute alcohol is then removed from the bath and the carbon disc is allowed to dry. Precipitates appear as thin (1 - 2 μm thick) spots on the disc. They are comparable to each other in size and shape and

their surface area is equal to or smaller than the surface area of contact between the original droplets and the carbon support (fig. 2). The washed and dried precipitates are now ready to be examined by electron probe microanalysis.

In order to evaluate this precipitation procedure a model system has been used. Sample droplets are taken from standard mixed solutions containing various known concentrations of NaCl, KH_2PO_4, $CaCl_2$, and $MgSO_4 \cdot 7H_2O$. A solution of $AgNO_3$ is used as the reagent and a volume equal to that of the sample is added to each droplet. The concentration of Ag in the reagent is higher than the maximum concentration of Cl in the standard solutions. Therefore the Cl concentration will be the limiting factor in the interaction with the Ag ion, resulting in the precipitation of all of the Cl out of the solution in the form of AgCl. The excess $AgNO_3$ and the other ions remain in solution. The samples are then processed in the manner described above. The precipitates, identical in size for a given experiment, may range from 60 to 90 μm depending on the volume of the sample droplets used in the particular experiment (10 - 120 picoliters). They are analyzed with a Cameca MS 46 electron probe. The electron beam diameter is set to cover a complete precipitate spot and is maintained at a constant diameter for the entire analysis. The accelerating voltage is 20 Kv. The characteristic Ag Lα and Cl Kα X-ray lines are measured with PET crystals and the Na Kα1 line is measured with a KAP crystal. The fourth spectrometer is set to monitor the background continuum at a wavelength of 2.36 Å, arbitrarily chosen because it results in a sufficiently high count rate and because there is no other element of interest near this wavelength. As it is not practical to measure the background off-peak on each spot, the background for each element is measured on-peak on the carbon disc. The background on each characteristic line, as measured off the spots on the carbon disc, is empirically corrected for the small change in continuum which is a function of the atomic number and amount of precipitate. This correction factor is determined by the fraction of rise in background measured in the fourth spectrometer between the carbon and the AgCl precipitate.

The results show that the amount of Ag and Cl that is counted in the final precipitate is directly correlated with the amount of Cl in the original sample (fig. 3). In addition the Na counts are extremely low (representing less than .5% of the original amount in the sample). This indicates that the $AgNO_3$ reagent reacted specifically and quantitatively with the Cl ion in the sample droplet to produce a precipitate of AgCl which was subsequently washed of excess reagent and all other original component ions. The precipitate is maintained homogeneous and when probed for Ag and Cl the counts are precisely indicative of the amount of Cl in the original sample.

In conclusion it is thus possible to obtain, with the electron probe, calibration curves from a precipitation reaction at an ultramicro level. By choosing specific precipitation reactions in analytical organic chemistry for components of interest one can now extend the biological application of the electron probe to include the quantification of organic components in picoliter samples.

References

1) Lechene, C. The use of the electron microprobe to analyse very minute amounts of liquid samples. Proc. Fifth Nat. Conf. on Electron Probe Anal. 32A - 32C, 1970.

2) Lechene, C. Electron probe microanalysis of picoliter liquid samples. In <u>Microprobe Analysis of Cells and Tissues</u>, edited by Theodore Hall, Patrick Echlin, and Rudolf Kaufmann, pp. 351 - 368. Academic Press, London, in press.

Acknowledgment
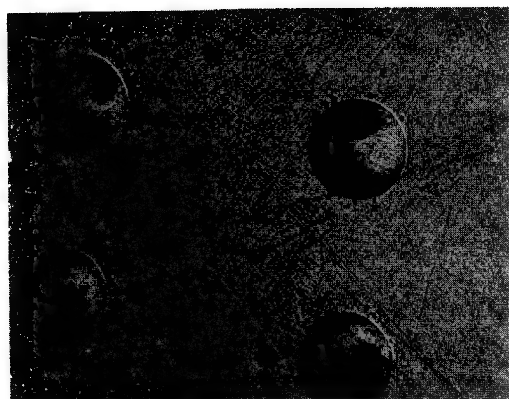
Figure 1 Photomicrograph of prep-
aration after centrifugation. The
droplets have a total volume of
168 pl (84 pl of sample and 84 pl
of $AgNO_3$ reagent) and are 80 μm in
diameter. The AgCl precipitate
sits at the bottom of each droplet,
flattened against the disc by the
centrifugation.
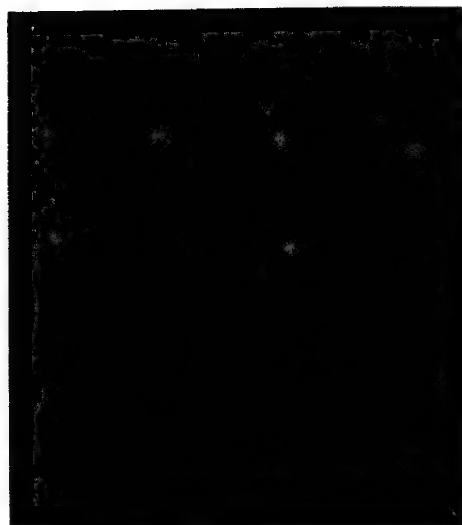
(mM/L)

21

220

150

105

42

Figure 2 Photomicrograph of precipitates
after freeze-substitution and drying.
The precipitates, 10 - 20 μm in diameter,
are ready to be analyzed with the electron
probe. The concentration of chloride in
the sample droplets is given at the right
of each row.

Vol = 84 pl

Ag (Cts)

15000

10000

5000

r = .995

Cl (mM/L)

0   100   200

Vol = 84 pl

Cl (Cts)

7500

5000

2500

r = .998

Cl (mM/L)

0   100   200
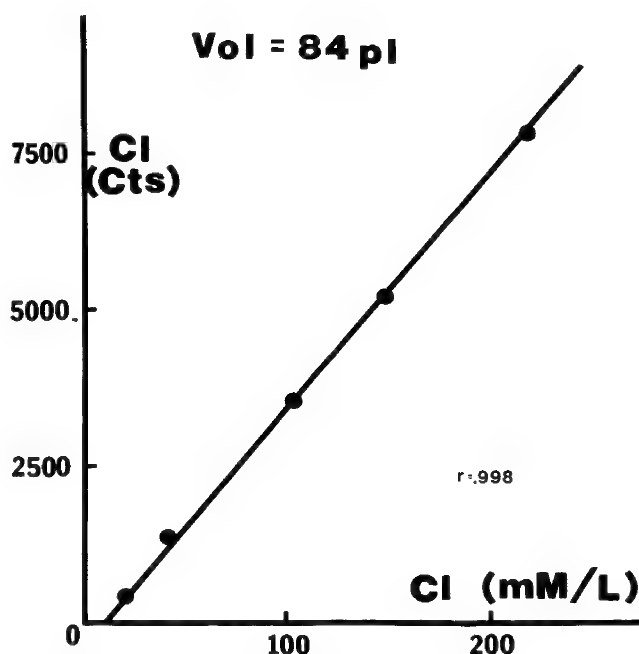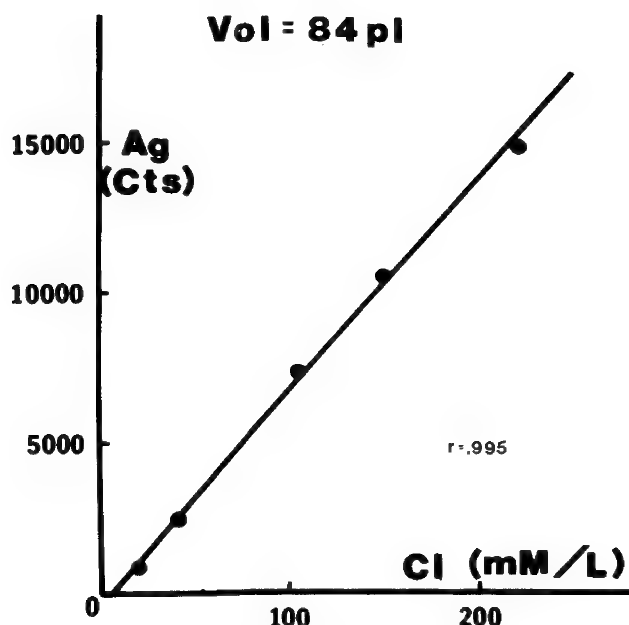
Figure 3 Calibration curves obtained from the micro-precipitation method.
The original sample volume (Vol) is 84 pl.
Cl (mM/L) represents the concentration of chloride in the standard solutions.
Ag (Cts) represents the total silver X-ray counts recorded in 10 seconds from
the AgCl precipitate formed. Cl (Cts) represents the total chloride X-ray
counts recorded in 10 seconds for the AgCl precipitate formed.
[r is the correlation coefficient]

ELECTRON PROBE MICROANALYSIS OF ISOLATED CELLS: RED BLOOD CELLS

C. Lechene, C. Bronner[*], and R. G. Kirk[*]

Biotechnology Resource in Electron Probe Microanalysis,
Laboratory of Human Reproduction and Reproductive Biology
and Department of Physiology
Harvard Medical School
Boston, Mass.   02115

Electron probe microanalysis (EPA) could be a powerful tool to quantitate the chemical elemental content of isolated cells. Its extensive use in biology to study such a general and unknown field is not limited by the technical operation of the probe, but by the preparation of the biological samples. The mounting support must provide a good electrical and thermal conductivity and a low bremsstrahlung. The cells must be well-isolated from each other on the support in order to measure their total elemental content without overlapping. They must be analysed in great numbers to allow for statistical study of the elemental distribution. Above all, the mounting procedure must preserve the cellular ionic content, avoiding any redistribution of the ions between the cells and the suspension medium.

Red blood cells constitute an ideal model system for establishing a method of preparation of single cells for EPA; they are easy to obtain, their transport properties have been extensively studied, they can be loaded with known concentrations of Na and K (1) and could thus possibly provide calibration curves for EPA (2).

Of the several preparation techniques we attempted, the most reliable is the spraying of the cells onto a vitreous carbon support. The method we present results in homogeneous and reproducible measurements by EPA of a great number of cells, well-isolated on their supports.

General Method

The cells were prepared from fresh blood. The blood was centrifuged and the packed cells diluted by a factor of ten, either in acid sucrose or in plasma. The method described by Kirk et al (2) was used for loading the cells with different concentrations of Na and K.

We compared preparations mounted on vitreous or polygraphite carbon (E. Fullam) and on beryllium foil (Ventron Alfa), polished and cut in our laboratory.

We compared identical batches of cells mounted on the support by:
   i)   smearing
  ii)   centrifugation with dibutylphthalate with subsequent draining (2)
 iii)   spraying; the Bernouilli effect for the spray was created with
        nitrogen gas, delivered under 25 - 30 lbs pressure through a
        22 gauge needle. The needle was positioned with a micromanipulator
        to the free end of a .8 mm (I.D.) glass tube dipped in the cell
        suspension; the nitrogen jet provoked the spray to which the support

---

[*]Department of Physiology, Duke University Medical Center, Durham, N. C.   27710

was exposed for one to two seconds.

In all three cases the cells were air-dried on the support and then kept under vacuum until analysed by the electron probe.

The analysis was performed with a Cameca MS 46 electron probe. The accelerating voltage was 11 Kv; the beam diameter was kept constant at approximately 10 μm, enlarged to cover one cell; the beam current was 50 nA; the characteristic X-ray lines were analysed for Fe Kα with an LiF crystal, for S Kα, Cl Kα, and K Kα with a PET crystal and for Na Kα1 with a KAP crystal. Four elements were counted simultaneously. The background was measured on-peak, off cells, on the support. Hundreds of cells were analysed, using either the manual stage or the special automated stage, step motor driven. Up to 500 cells could then be counted automatically (3).

Results

1. Quality of the support –
    Compared to beryllium, the vitreous carbon (VC) gave a background lower for K (VC:18.00 $\pm$ 4.8 S.D., N = 126; Be:22.5 $\pm$ 9.3 S.D., N = 23; t = 8.3, p << 0.001), and identical for Na (VC:7 $\pm$ 2.59 S.D., N = 125; Be:6.61 $\pm$ 3.14 S.D., N = 23; t = 1.03, p > 0.2). As the net signal to background ratio was better for all elements on the vitreous carbon, this support was retained for subsequent preparations.

2. Quality of the preparation –
    It was found that:
    i)   On one batch of cells, the preparation with dibutylphthalate gave, during the same probe run, a potassium signal lower than on the smear or the spray preparation. Moveover, the mean K counts were significantly variable from one support to another, mounted during the same centrifugation.
    ii) The mean K signals of smeared preparations were significantly different on different areas of the same support. [It should be noted that the variations are correlated with the appearance of the cells in these areas]. In one smear, mean K counts/ 10 sec. were 58.0 $\pm$ 11.6 S.D. for circular and clear cells, 75.6 $\pm$ 9.9 S.D. for clear cells which looked biconcave (fig. 1:a_1,a_2), and 106.9 $\pm$ 22.9 S.D. for biconcave and dark cells. All means are significantly different, with p < 0.01.
    iii) The sprayed cells (fig. 1:b) provided reproducible EPA for the same batch of cells from one spray to another, and their intensity signals were similarly distributed. There were no differences between 1/10 dilution of cells in acid sucrose (RS) or in plasma (RP). Mean K count/10 sec. for RS = 119.5 (N = 143), for RP = 118.5 (N = 209), t = .219, p > .5 . There was a strong correlation between the potassium and iron signal. In the RS group the correlation coefficient (r) = .88, and in the RP group r = .87.

It should be noted that under our EPA conditions there was no variation of the intensity signals after a prolonged beam bombardment on one cell; there was no significant difference for K between the initial mean of ten

times 10 sec. counts on one cell and that obtained after 5 min. of beam bombardment (t = .052, p >>.5).

3. Calibration curves –
By loading the cells under treatment with nystatin (Mycostatin ® Squibb) with different concentrations of Na and K (2) it was possible to get calibration curves (fig. 2). It is unnecessary to emphasize the possible application of such curves to measure the elemental content of single cells by EPA.

Discussion

The variable intensity signals observed in the smeared and dibutylphthalate preparations is likely due to the redistribution of ions. It should be noted that the lower the K intensity signal on the cells, the higher it was in the medium beside the cells. The reason for the segregation of groups of cells with different mean K signals in different, definite areas on the smears of whole blood is unknown. Another factor affecting the intensity of the signals could be the absorption of characteristic X-rays by variable thicknesses of plasma or dibutylphthalate covering the cells. Conversely, in the spray preparation the cells are not "embedded" in a layer of their medium of suspension and the support around the cells remains clean; the volume in which the ions could redistribute could not be more than a film of the suspension medium around the cells and thus does not allow for significant redistribution of ions or for crystal growing during the air drying.

Several empirical criteria are retained to assert the quality of the preparation: the homogeneous distribution of the characteristic X-ray lines in the analysed cells; the intensity of the K signal in the preparation; the equivalence between this intensity in the normal cells which have been manipulated (by washing, centrifugation, standing, etc.) and control cells from whole blood or diluted in plasma, immediately prepared for EPA; the absence of any segregation of elemental salt crystals for the elements of interest, as it could be revealed by exploring the surface of the preparation with a focused beam; the presence in great number of isolated cells on the support in order to cover them with an enlarged electron beam (without overlapping) which is necessary for absolute and accurate measurements of the X-ray intensity signals of their elemental content.

EPA is the only tool which makes possible the correlative analysis of the elemental content of single cells; the number of cells analysed could be large enough to study the distribution of elements of interest. The method we describe permits easy preparation of cells in large number and which keep their ionic content; it will thus allow for significative measurements by EPA in populations of single cells.

References

(1) Cass, A. and M. Dalmark. Equilibrium dialysis of ions in nystatin-treated red cells. Nature New Biol. 244:47 – 48, 1973.

(2) Kirk, R. Gary, Miles A. Crenshaw, and D. C. Tosteson. Potassium content of single human red cells measured with an electron probe. J. Cell Physiol., in press.

(3) Moher, T., C. M. Aden, R. Beeuwkes, A. Sanderson, and C. Lechene. Automation of an electron probe for biological analyses. These proceedings.
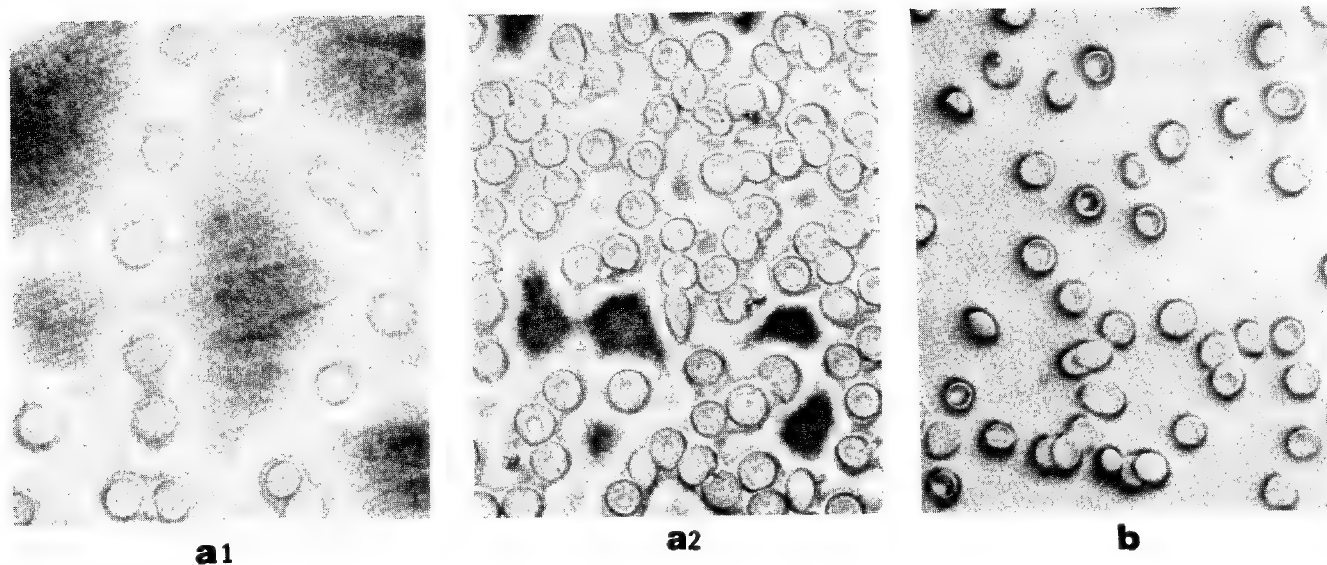
Acknowledgment

Figure 1
Photomicrograph (G700) of red blood cells mounted for EPA
a_1: smear, clear cells, flat; few cells; K signal is low
a_2: same smear, other area, clear cells, likely biconcave; numerous cells, but very few isolated; K signal higher than a_1 but lower than in spray
b: spray, large number of cells, well-isolated; K signal homogeneously high
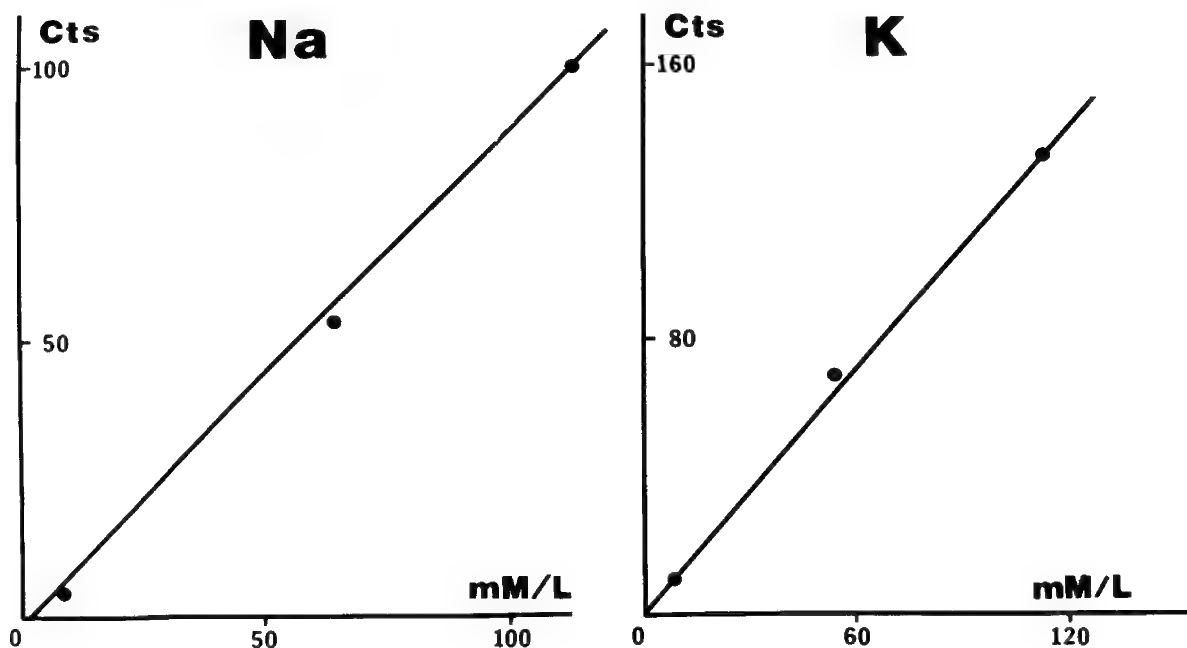
Figure 2
Calibration curves obtained by EPA of red blood cells
mM/L: cell concentration (as measured by spectrophotometry) after loading under nystatin; for Na: 8.26, 62.2, and 112 mM/L and for K: 112, 53, and 8 mM/L.
cts: counts/10 sec measured on individual cells by EPA. Each point is the mean count on 10 cells only.

SEM Identification of Biogenic Silica in Jute:

Silica in Human Lung Following Exposure to Burning Jute

by

Phillip B. DeNee, Ph.D.
Jerrold L. Abraham, M.D.
Albert H. Gelderman, M.D.

Appalachian Laboratory for Occupational Respiratory Diseases
National Institute for Occupational Safety and Health
P. O. Box 4292
Morgantown, West Virginia 26505

and

G. Boyd Shaw, M.D.
Suite 703, Medical Tower
Jackson, Mississippi 39216

In this study, the scanning electron microscope (SEM) has been applied to the identification of respired dust resulting from an industrial accident. This accident involved the inhalation of smoke from burning jute-bagged cotton bales. Our results indicate that at least some of the silicon-containing particles found in the lung may have originated from the burned jute. Available evidence does not yet allow conclusion as to the etiologic role of the particles in the patient's disease, as cases have been described following exposure to fume inhalations, respiratory infections and inhalation of foreign bodies[1].

The patient, a 56 year old manager of a cotton compress warehouse, was exposed for approximately fourteen hours to dense smoke from burning cotton bales in his warehouse. Progressive shortness of breath developed over the next few months. A chest X-ray four months after the fire showed bilateral lung infiltrates. The clinical history, X-rays and pulmonary function tests were consistent with an interstitial pulmonary inflammation as reviewed by Gosink et al.[1]. Routine pathological examination of the lung tissue biopsied 18 weeks after the exposure showed an uncommon disorder known as bronchiolitis obliterans[1]. In this condition the small airways of the lung (terminal and respiratory bronchioles) become obstructed by granulation tissue (early scarring)(Fig. 1). This results in severe impairment of the lung function. The patient spontaneously recovered in several months, as did less than a third of Gosink's series[1].

Since polarizing light microscopy revealed birefringent material associated with soot particles in the lung (Fig. 2), we attempted characterization of these particles with the SEM. Most SEM studies of biological samples use only the secondary electron imaging mode for study of surface morphology[2]. We have developed techniques to characterize biological samples further, using some of the several types of information simultaneously available in the SEM[3-7]. In situ X-ray micro-analysis in tissue sections and use of the backscattered electron imaging mode are used in conjunction in the example presented here.

Five micrometer thick paraffin sections of lung were mounted on 2 mm thick carbon planchets, deparaffinized, critical point dried and carbon coated. The planchets were then glued to aluminum SEM stubs and studied in the SEM. Figure 3 is a secondary electron image of one of the areas. Much surface morphology is seen but no particles are readily detectable. When the same area is viewed in the backscattered electron mode (Fig. 4), a large number of particles are noticed. These particles are ones which have a higher average atomic number than the surrounding tissue. Several particles were identified by energy dispersive X-ray analysis as containing only silicon. Other particles showed, in addition to silicon, lesser amounts of magnesium, aluminum, calcium, potassium, titanium, and iron. We examined samples of jute bagging material from the same lot burned in the warehouse fire. Figures 5 and 6 show the secondary and backscatter image, respectively, of one such sample. Numer-ous particles of average atomic number higher than that of the background organic tissue are apparent in Figure 6. Analysis of these was similar to those found in the lung tissue.

Sampling of a larger volume of the jute bagging was facilitated by low temperature ashing (below 150° C for 24 hrs.) followed by spray dispersion of the particles on carbon plan-chets[8-9] Figures 7 and 8 illustrate typical particles. Once again, analysis of the particles was similar to that of the particles in the lung tissue.

The silica material from the jute is probably biogenic silica[10-12] which is commonly found in plant material. It is similar in character to that found in other dicotyledonous plants such as white ash, sugar maple and American Linden. The morpho-logy of the particles, Figures 7 and 8, are typical of that found in the dicots. The cellular architecture of the plant is often preserved in biogenic silica[10], as can be seen in Figures 7 and 9.

Biogenic silica can exist in many forms; rod, sphere, scrolls, convoluted sheets and cups. It can exist in the

amorphous phase as opal, or in the crystalline phases alpha quartz and cristobalite[11]. It has also been found associated with aluminum, magnesium, calcium and iron as a silicate or group of silicates[13]. The particle size range for the biogenic silica includes the respirable range and thus could be the source of the material found in the lungs.

In conclusion, through the application of the SEM to human pathology, we are aided in identification of material found in the human lung and in the search for possible sources for this material. In addition, we have been able to identify a toxic material, biogenic silica (alpha quartz, cristobalite and opal), which has previously been known only to soil agronomists.

Acknowledgements:

References:

1. Gosink, B.B., Friedman, P.J. and Liebow, A.A., Bronchiolitis Obliterans: Roentgenologic-Pathologic Correlation, Am. J. of Roentgenol., Rad. Therapy and Nuc. Med., 117(4), Apr., 1973, p. 816-832.

2. Hollenberg, M.J. and Erickson, A.M., The SEM: Potential Usefulness to Biologists, J. Histochem. Cytochem., 21, 1973, p. 109-130.

3. DeNee, P.B., Abraham, J.L. and Gelderman, A.H., Methods for a SEM Study of Coal Workers' Pneumoconiosis, in SEM/1973, Proceedings of the 6th Annual SEM Symposium, IIT Research Institute. Chicago, Illinois. April, 1973, p. 411-418.

4. Abraham, J.L. and DeNee, P.B., SEM Histochemistry Using Backscatter Electrons and Metal Stains, Lancet, 1, 1973, p. 1125.

5. Abraham, J.L., DeNee, P.B. and Gelderman, A.H., Specific Metal Staining of Biological Tissues for the SEM Using Backscatter Electron or Specimen Current Imaging, Proc. Electron Probe Analysis Soc. of Amer., New Orleans, Aug., 1973, Abstract 67.

6. Abraham, J.L. and DeNee, P.B., Biomedical Applications of Backscattered Electron Imaging--One Year's Experience With SEM Histochemistry. SEM/1974, IITRI, p. 251-258.

7. DeNee, P.B., Abraham, J.L. and Willard, P.A., Histochemical Stains for the Scanning Electron Microscope -- Qualitative and Semi-Quantitative Aspects of Specific Silver Stains, SEM/1974, IITRI, p. 259-266.

8. DeNee, P.B., Mine Dust Characterization Using the Scanning Electron Microscope and Dust Samplers, SEM/1971, IITRI, p. 209-216.

9. Johari, O., and DeNee, P.B., Handling, Mounting and Examination of Particles for Scanning Electron Microscopy, SEM/1972, IITRI, p. 249-256.

10. Wilding, L.P., and Drees, L.R., Scanning Electron Microscopy of Opaque Opaline Forms Isolated from Forest Soils in Ohio, Soil Science Soc. of Amer. Proc., 37(4), 1973, p. 647-650.

11. Wilding, L.P. and Drees, L.R., Contributions of Forest Opal and Associated Crystalline Phases to Fine Silt and Clay Fractions of Soils, Clays and Clay Minerals, 22(3), 1974, in press.

12. Wilding, L. P., and Drees, L.R., Biogenic Opal in Ohio Soils, Soil Science Soc. of Amer. Proc., 35(6), 1971, p. 1004-1010.

13. Wilding, L.P., Dept. of Agronomy, Ohio State University, Columbus, Ohio 43210, Personal Communication.

Figure Legends*

Fig. 1

Light micrograph of lung biopsy (elastic tissue stain). Much loose fibrotic tissue (F) is seen filling a small bronchiole (B). The bronchiolar epithelium (EP) is intact above the terminal bronchiolar elastic lamina (EL). Note also the more normal area of lung with thin alveolar septae (➔) and alveoli containing numerous macrophages (➤➔).

Fig. 2

Polarizing light micrograph of lung biopsy (hematoxylin and eosin stain, partially polarized). Several bright birefringent particles can be seen associated with soot particles in macrophages, located interstitially near respiratory bronchioles (RB).

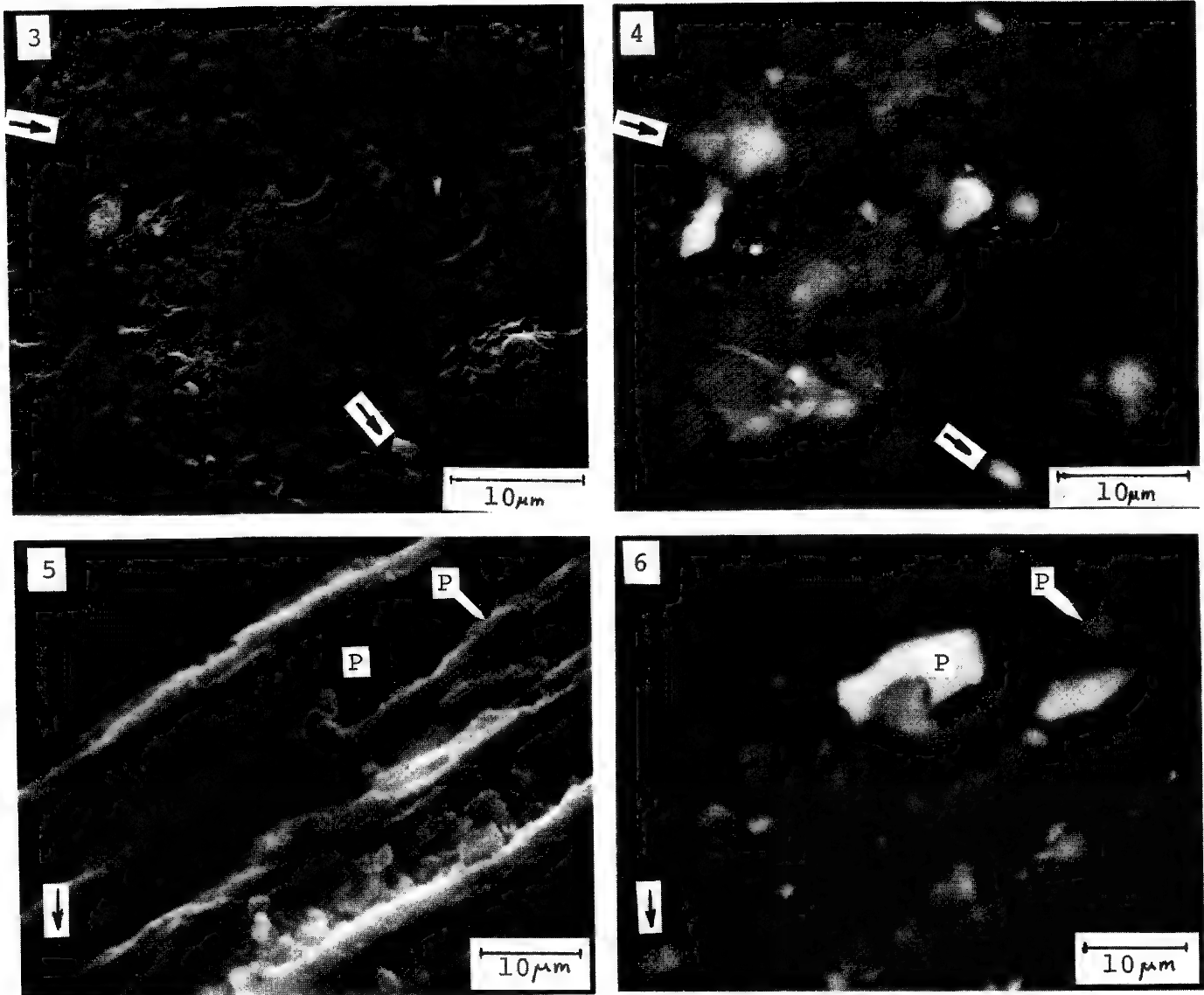* - All SEM micrographs were taken at 20 keV and 45° tilt.
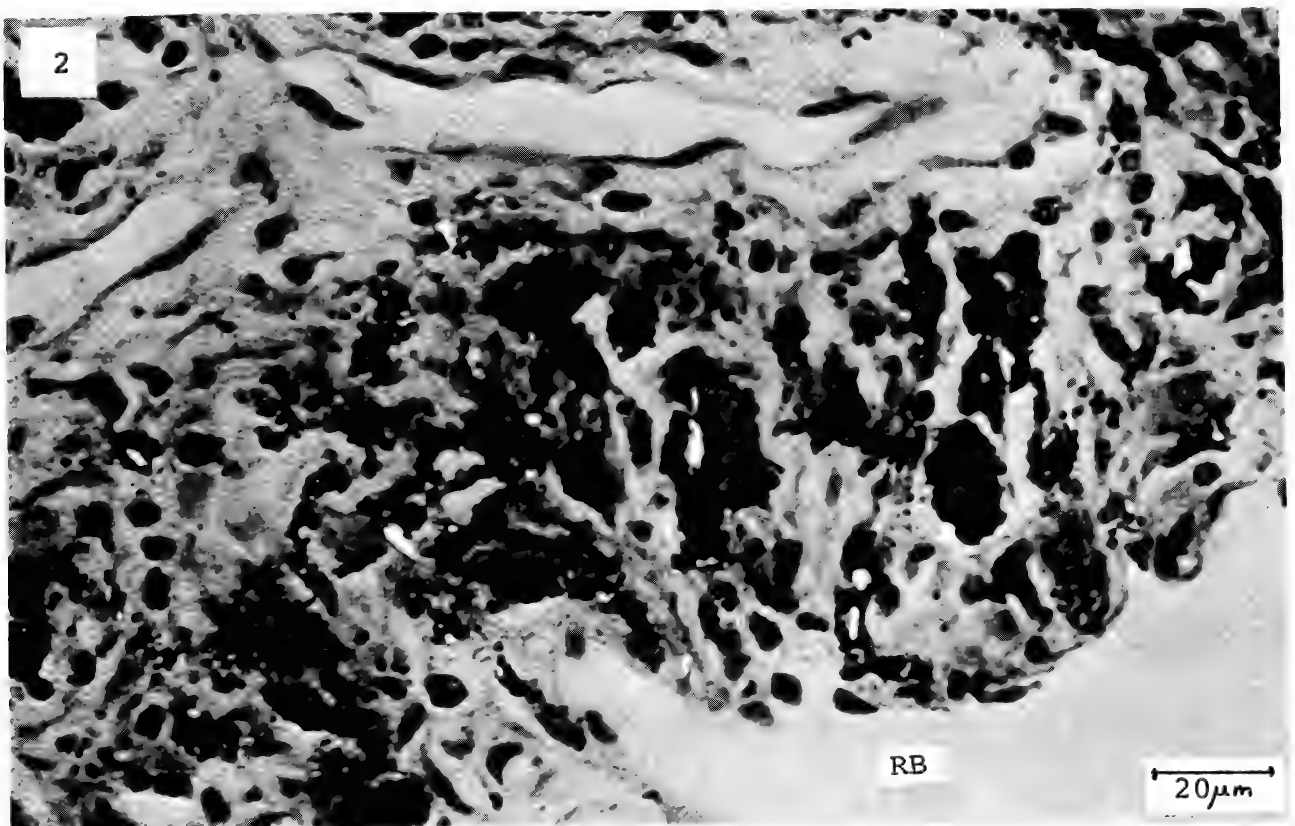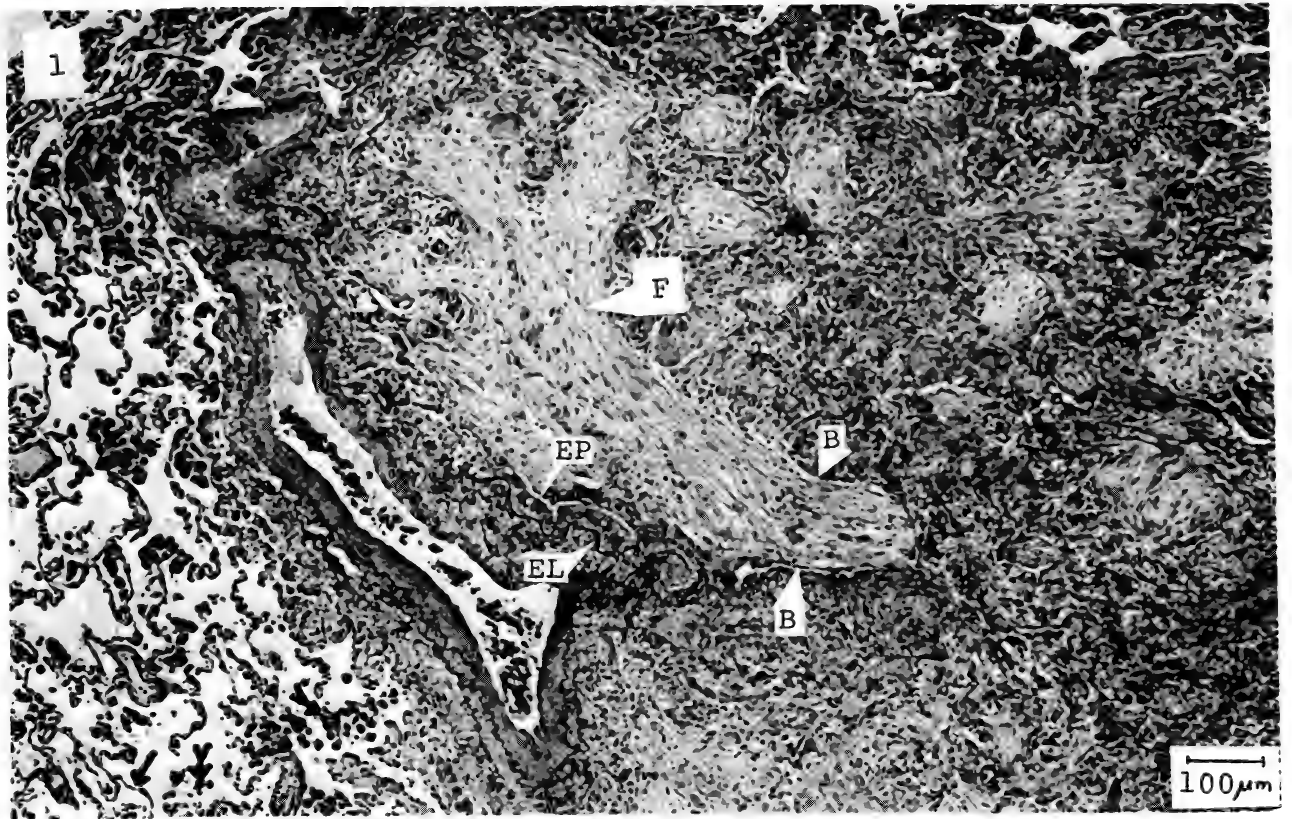
Fig.3

SEM, secondary electron image of section of lung mounted on carbon planchet. No remarkable detail is recognizable in the surface morphology.

Fig. 4

SEM, backscattered electron image of identical area seen in Fig. 3. Several bright areas indicate particles having higher backscatter coefficient than the surrounding organic tissue and supporting carbon. Note that particles of higher atomic number than carbon located beneath as well as on the surface (→) are revealed.

Fig. 5

SEM, secondary electron image of jute showing its fibrous character and the many associated particles (P).

Fig.6

SEM backscatter electron image of fiber shown in Fig. 5, illustrating the material of higher atomic number than the surrounding tissue. Note that one particle (→) is below the surface of the fiber when comparing Fig. 5 and 6.
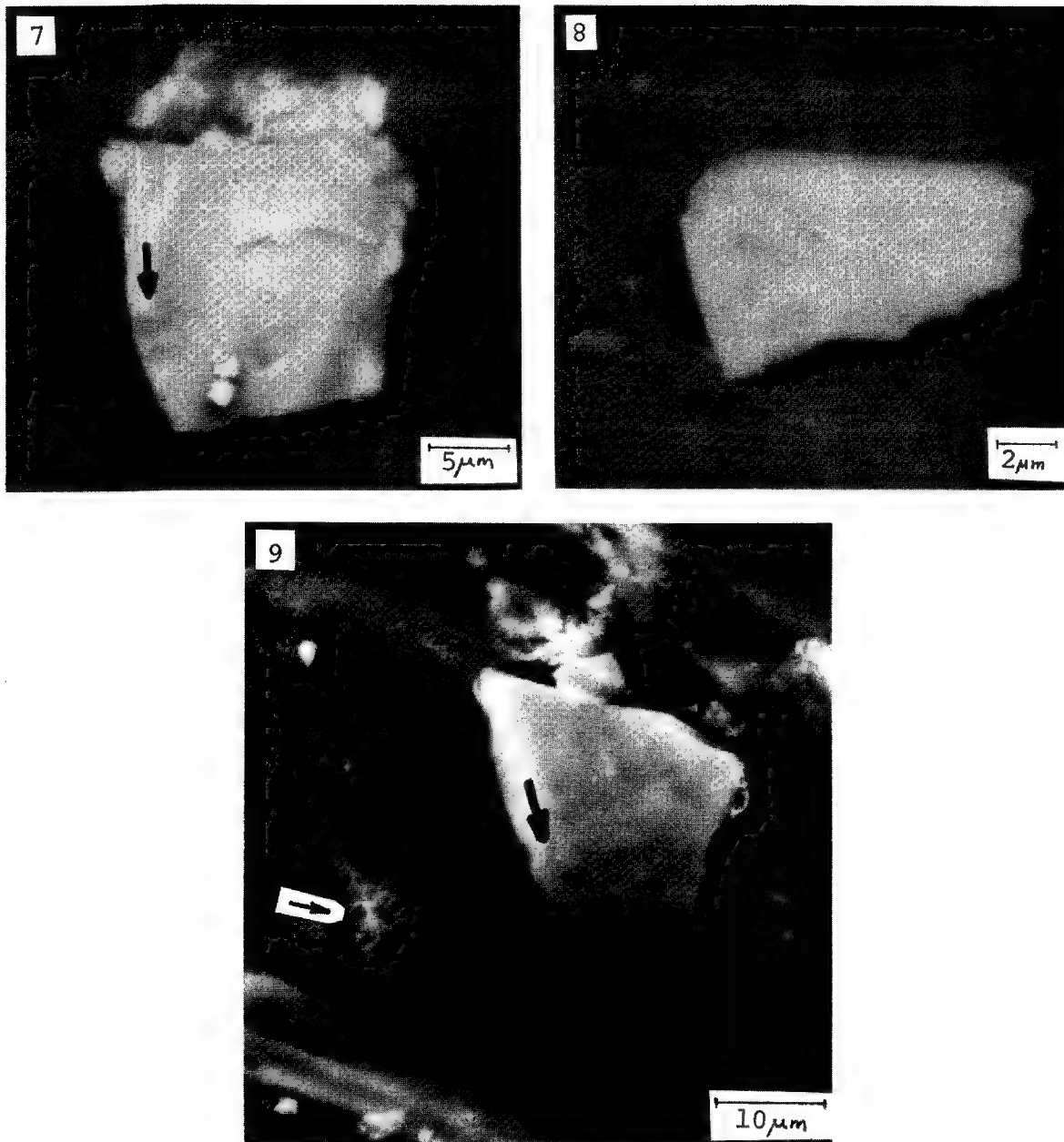
Fig. 7

SEM, secondary electron image of a particle remaining from low-temperature ashed jute, spray dispersed onto a carbon stub. Note its porous cellularity (➡).

Fig. 8

SEM, backscatter electron image of another particle prepared as in Fig. 7.

Fig. 9

SEM secondary electron image of particle on the same jute fiber as shown in Fig. 5. Note the porous cellularity of the jute and the similar cellular nature of the particle.

BACKSCATTERED ELECTRON SIGNAL FOR BACKGROUND MONITORING WITH BIOLOGICAL TISSUE SAMPLES

F. Duane Ingram and Mary Jo Ingram
Department of Physiology and Biophysics
University of Iowa
Iowa City, Iowa 52242

Quantitative electron probe analyses of soft biological that have been freeze-dried, fixed with osmium vapor and embedded in Epon are complicated by lack of homogeniety of the samples (1,2). The contrast rendered the sample by selective staining of protein structures by osmium is indispensible for precise localization of the electron beam in the tissue. However, concomitant with varying density to the electron beam is nonuniform production of background radiation in various locations. Electrolyte measurements which are often near the minimum detection limits of the electron probe can be made only if this background is known for each point of analysis.

When required measurements are few and high precision is mandatory, the appropriate method of obtaining background is to rock the spectrometers off peak and collect information both above and below peak for each location analyzed. A more efficient method is either to leave one spectrometer detuned to monitor background continuously, or to place an additional detector in the electron probe for continuum monitoring. For situations and conditions in which the above methods are either impractical or unavailable it is possible instead to obtain information which can be converted to a number representing background by monitoring the backscattered electron signal. It has not been established that this method is desirable or even applicable for samples of substantially varying compositions; however, the data indicate that acceptable accuracy is obtainable with biological specimens which are about 80% epoxy.

Essentially, the procedure consists of measuring the off-peak background at a number of locations on the specimen and simultaneously monitoring the backscattered electron signal with a digital voltmeter. Data points so obtained are fitted with a straight line by the method of least squares. Throughout this procedure it is necessary from time to time to check the beam current and backscattered electron signal for stability. By duplicating the beam and electronics conditions, the on-peak data points may be corrected for background by reference to the backscattered electron signal.

The electronics gain adjustment is effected by reference to the backscattered electron signal from a quartz sample, and the zero level is established with no sample under the electron beam. Quartz has been selected to check for beam and electronic drift because of its stability, reproducibility of measurements and omnipresence when working with plastic sections mounted on quartz slides. A 10 kV, 50 nA beam on quartz has been adopted as a standard electron beam. With a properly zeroed amplifier, a gain is established for the electronics that will produce a 0.5 volt signal with quartz. This results in signals ranging from about 0.3 volt on pure plastic to just over 1.0 volt on the most intensely stained portions on the tissue samples. The off-peak background on such tissue sections typically spans the range from 13 to 36 mEq/kg for K, 13 to 24 mEq/kg for Cl and 10 to 25 mEq/kg for Na.

Data is collected by means of an on-line LINC-8 computer with an ARL-EMX electron probe (3). The information is stored as line-scan profiles of up to 256 points each. These line-scan profiles are obtained simultaneously for each of the three spectrometer signals and the backscattered electron signal. From a calibration of the backscattered electron signal obtained by scanning a few areas with the spectrometers off-peak, information is available to correct each point for background as explained above. The resulting counting rates are converted into numbers representing concentrations by reference to secondary standards as described elsewhere (4).

An example of the precision to be expected from this method of treating the background is presented in Table I. Although the uncertainty in the intercept is large compared with the magnitude of the intercept, it results in only a second order correction. The important uncertainty is in the slope. This is found to be an 8% to 14% uncertainty which is acceptable for background measurement.

By calibrating and using the available backscattered electron signal for a determination of the Bremsstrahlung background, a convenient and practical system presents itself for examining high contrast plastic-embedded biological tissue samples. Although the relative uncertainty of the background measurements obtained in this manner is substantial, the magnitude of the uncertainty is only one to three mEq/kg, an entirely acceptable uncertainty for routine biological studies.

TABLE 1

A Calibration of the Backscattered
Electron Signal for Determining
Off-Peak Background

X-ray Line	Diffraction Crystal	Number of Data Points	Slope ± Est. of S.D. (Cnt/24 sec/mv)	Intercept ± Est. of S.D. (Cnt/24 sec)	Regression Coefficient
K-Kα	LiF	34	0.1069 ± 0.0096	6.4 ± 7.1	0.89
Cl-Kα	NaCl	34	0.0875 ± 0.0097	46.3 ± 7.1	0.85
Na-Kα	KAP	34	0.0486 ± 0.0070	8.3 ± 5.1	0.77

References:

1) Ingram, Mary Jo and C. Adrian M. Hogben. Procedures for the study of biological soft tissue with the electron microprobe. In: Developments in Applied Spectroscopy, W.K. Baer, A.J. Perkins, E.L. Grove, Eds., Plenum Press, New York, Vol. 6, 1968, p 43-64.

2) Ingram, F. Duane, Mary Jo Ingram and C. Adrian M. Hogben. Quantitative electron probe analysis of soft biological tissue for electrolytes. Journal of Histochemistry and Cytochemistry. 20:716-722, 1972.

3) Ingram, F. Duane. A small computerized on-line data gathering system for the electron microprobe. Proc. Fourth Natl. Conf. on Electron Microprobe Analysis, 27A-27D, 1969.

4) Ingram, F. Duane, Mary Jo Ingram and C. Adrian M. Hogben. Pure crystals as secondary standards for quantitative electrolyte studies of soft biological tissue. Proc. Eighth Natl. Conf. on Electron Probe Analysis, 62A-62E, 1973.

THE USE OF FROZEN SECTIONS IN THE ANALYSIS OF BONE

by

James R. Coleman, Paul Batt, Patricia Moran and Ronald R. Warner*

Department of Radiation Biology and Biophysics
University of Rochester School of Medicine and Dentistry
Rochester, New York 14642

*Present Address: Department of Physiology
Yale University School of Medicine
New Haven, Connecticut

Electron probe analysis of bone has been hampered by difficulties associated with the methods used to prepare this dense, mineralized tissue for analysis. For example, air drying has been shown to convert the amorphous calcium phosphate component of bone to calcium hydroxy-apatite and conventional fixation, dehydration and sectioning procedures permit the loss of soluble materials (1,4,8,9,10). The technique of frozen sectioning (2) promised to circumvent such difficulties. This technique depends on rapid freezing to very low; e.g., -80° C, temperatures in order to immobilize diffusible elements in a matrix of ice. The tissue is maintained at this low temperature to prevent the formation and growth of different phases in the ice which can produce translocations of materials. Thus sectioning is carried out in a cold chamber, and the section is either dried while in the frozen state, or dried slowly at increasing temperatures (2). We employed the technique of frozen section-ing to prepare thin sections of bone for electron probe analysis in order to measure the potassium content of the mineralized region of the bone and to determine the calcium to phosphorous ratios that occur in various portions of growing bone. Both of these parameters are important to theories of bone mineralization and calcium homeostasis but have proven difficult to determine (5,12). The purpose of this report is to present the methods employed and sufficient analytical data to demonstrate the utility of the method.

Chick calvaria were rapidly removed from decapitated 2-day-old chicks, and quickly plunged into a bath of liquid propane or liquid freon cooled by liquid nitrogen, or directly into liquid nitrogen. The calvaria, while

in a pool of liquid nitrogen, were fractured into small pieces about 2-5 mm on a side using chilled forceps. A small drop of 25 per cent serum was placed in a slotted copper chuck sitting in a liquid nitrogen bath. Just as the albumin began to freeze, a piece of frozen calvarium was inserted into the albumin containing slot, rapidly freezing the calvarium to the chuck. The whole assembly was then transferred to a liquid nitrogen bath for storage, and later placed in the pre-cooled microtome cold chamber.

Sectioning was performed with a Servall Porter Blum MT2 microtome and Cryokit (2). Sections were cut at $-100°$ to $-120°$ C, with nominal thickness of one of three microns, and were transferred by means of a fine tungsten wire attached to a glass rod to a clean silicon disc. The sections were dried in a stream of cold dry nitrogen usually for one hour, then slowly brought to room temperature while still in an atmosphere of dry nitrogen. Rapid drying by transferring the sections and silicon disc to a $100°$ C hot plate was occasionally employed. Operating conditions were as previously described (3) and X-ray intensities were corrected according to the BASIC program (11). The results of a typical analysis can be seen in Table 1. The analysis was performed by moving the beam in approximately 5 μ steps across the section from the periosteal to the endosteal surface. The mean weight per cents of calcium and phosphorus are greater than that obtained by bulk analysis. This is due to the fact that the tissue envelopes of the bone as well as the mineral were analyzed in the bulk analysis, lowering the mean values of calcium and phosphorous; while probe analysis included only mineralized regions. This is confirmed by the fact that the Ca/P ratios for the two analyses are quite similar. There is no significant difference in the content of sodium and potassium found by each method. This is due to the fact that the sodium and potassium content of the tissue is approximately the same as the mineral (5). Table 1 also shows that the calcium content of the conventionally prepared specimen is significantly lower than the frozen section ($p < 0.001$), the phosphorous content is significantly lower ($p < 0.001$), and the Ca/P ratio is significantly lowered ($p > 0.001$) as well. This is consistent with findings of a large loss of

of calcium and phosphorous due to exposure to aqueous solutions during
preparation, and suggests preferential loss of calcium, or a portion of
mineral with a high Ca/P ratio (1).

The mean Ca/P ratio of 1.52 for the frozen section, and the conven-
tionally prepared specimen are both substantially higher than the 1.0 ratio
(wt.% converted to atomic %) reported in thin sections of bone mineral
previously (6). The cause of this discrepancy is not immediately obvious,
but the phosphorous content reported by Remagen (6), 24 wt.%, is about
1.9x the value usually reported for bone mineral, e.g., 12.5% (5), suggest-
ing that phosphorous may have been gained during the preparative procedure
or that some error may have crept in due to the correction procedure.

It is of note that the Ca/P ratios form an orderly progression from
one side of the bone to the other. When these values are used to plot a
least squares linear regression against relative distance, they produce a
line with a Ca/P intercept of 1.3 and a slope of 4.2×10^{-3}, and there is
an 87.5% goodness of fit between the observed points and the regression line.
Since the periosteal surface contains the most recently deposited mineral,
and the endosteal surface consists of older mineral, this suggests there is
a progression from mineral with a Ca/P characteristic of amorphous calcium
phosphate to a mineral with a Ca/P characteristic of calcium apatite. This
confirms a previous observation of Wergedal and Baylink (12), using thick
samples, that the Ca/P ratio characteristics of new bone was similar to that
of amorphous calcium phosphate. It has been shown that amorphous calcium
phosphate can be a major component of bone, and is also a necessary inter-
mediate in the formation of calcium hydroxyapatite from calcium phosphate
solutions (8,9,10). Thus it appears likely that the first form of bone
mineral is an amorphous calcium phosphate, and this transforms to an apatite
form with time.

The presence of substantial amounts of potassium in the bone is also
significant. Since bone mineral incorporates almost no potassium, this
element must be distributed throughout the aqueous phase of the mineralized
regions, and at much greater concentrations than exist in the extracellular

spaces (5). This finding suggests the existence of some barrier which prevents the equilibration of bone potassium with extracellular space, but provides no insight as to the morphological counterpart of this barrier.

References

1) Boothroyd, B., 1964, The problem of demineralization in thin sections of fully calcified bone. J. Cell Biol. 20, 165.

2) Christensen, A.K., 1971, Frozen thin sections of fresh tissue for electron microscopy, with a description of pancreas and liver. J. Cell Biol. 51, 772.

3) Coleman, J.R. and A.R. Terepka, 1972, Electron probe analysis of the calcium distribution of cells in the embryonic chick chorioallantoic membrane. I. A critical evaluation of techniques. J. Histochem. Cytochem. 20, 401.

4) Harper, R.A. and A.S. Posner, 1966, Measurement of non-crystalline calcium phosphate in bone mineral. Proc. Soc. Exptl. Biol. (N.Y.) 122, 137.

5) Neuman, W.F., 1969, The milieu interieur of bone: Claude Bernard revisited. Fed. Proc. 28, 1846.

6) Remagen, W., H.J. Hohling, T.A. Hall and R. Caesar, 1969, Electron microscopical and microprobe observations on the cell sheath of stimulated osteocytes. Calc. Tiss. Res. 4, 60.

7) Sabatini, D.D., K. Bensch and R.J. Barnett, 1963, Cytochemistry and electron microscopy. The preservation of cellular ultrastructure and enzymatic activity by aldehyde fixation. J. Cell Biol. 17, 19.

8) Termine, J.D. and E.D. Evans, 1972, Comparative chemistry of amorphous and apatitic calcium phosphate preparations. Calc. Tiss. Res. 10, 171.

9) Termine, J.D. and A.S. Posner, 1966, Infrared analyses of rat bone: age dependency of amorphous and crystalline mineral fractions. Science 153, 1523.

10) Termine, J.D. and A.S. Posner, 1967, Amorphous crystalline relationships in bone mineral. Calc. Tiss. Res. 1, 8.

11) Warner, R.R. and J.R. Coleman, 1972, A computer program for quantitative microanalysis of thin biological material. Proc. VII Natl. Conf. Electron Probe Analysis, San Francisco, Calif., 41A.

12) Wergedal, J.E. and D.J. Baylink, 1973, Electron microprobe measurements of bone mineralization in vivo. Am. J. Physiol. 226, 345.

Acknowledgements

TABLE 1

	wt %				Ca/P At %
	Ca	P	K	Na	

1. Electron Probe Analysis of Frozen Section

	Ca	P	K	Na	Ca/P At %
Site #1	27.82	15.65	0.12	0.66	1.37
2	27.62	15.08	0.07	0.74	1.42
3	29.60	15.47	0.08	0.77	1.48
4	28.94	15.39	0.05	0.77	1.45
5	28.92	14.92	0.05	0.71	1.50
6	28.21	14.92	0.07	0.86	1.46
7	28.50	14.40	0.07	0.84	1.53
8	30.71	15.40	0.04	0.71	1.54
9	31.97	15.91	0.01	0.42	1.55
10	30.70	14.58	0.01	0.33	1.63
11	30.21	14.37	0.01	0.33	1.62
12	27.99	12.88	0.01	0.28	1.68
Mean	29.27	14.91	0.05	0.62	1.52
S.D.	1.38	0.81	0.04	0.21	0.09

2. Electron Probe Analysis of Conventional Preparation (N =8)

	Ca	P	K	Na	Ca/P At %
Mean	21.22	12.39	0.03	0.11	1.33
S.D.	1.27	0.88	0.02	0.05	0.05

3. Bulk Analysis*

	Ca	P	K	Na	Ca/P At %
	25.0	12.4	0.06	0.55	1.56

*Pooled values of 16 calvaria, courtesy Dr. William F. Neuman.

APPLICATION OF ELECTRON PROBE ANALYSIS AND SCANNING ELECTRON
MICROSCOPY TO THE STUDY OF SILICA IN PLANTS

S.L. Soni*, D.W. Parry (a) and P.B. Kaufman (b)

School of Plant Biology, University College of North Wales, Bangor,
U.K. (a) and Department of Botany, University of Michigan, Ann Arbor,
Mich. 48104, U.S.A. (b)

Silica in plants has been investigated by a dry-way method (spodo-
gram)[1], using different chemicals and mounting media[2], by means of
wet-way and dry-way ashing and analyzing silica in the ash by chemical,
X-ray, and thermal procedures[3], using stains such as toluidine blue[4]
and safranin-phenol[5], employing autoradiographic technique[6,7],
transmission electron microscopy[8], and the phase-contrast microscopy[2].
In the present studies, the deposition of silica in plants at the
cellular and tissue levels has been analyzed through the use of
the electron probe microanalyzer (model EMX-SM, ARL at Ann Arbor
and model JXA-3A, JEOL at Bangor) and the scanning electron micro-
scope (JEOL, JSM-U3 at Ann Arbor and Cambridge Stereoscan Mark II
at Bangor).

Epidermal peels of internodes (Fig. 1), leaves (Figs. 2,7,8) and
inflorescence bracts (Fig. 3) from fresh and dried plants are
prepared using a razor blade and jeweller's forceps.

Chromated preparations (Fig. 4) of fragments of different parts of
the plant are made by treating with 25% ammonia for 24 hrs, washing
in distilled water and soaking in 6% H_2O_2 for 1-6 days to decolorize
the material. The decolorized specimens are placed in solutions
consisting of dilute chromic or perchloric acids, nitric acid,
sulfuric acid and hydrochloric acid. The dish is placed on a copper
plate and heated at one corner to provide the necessary heat for the
reaction. When the green coloration disappears, the specimens are
repeatedly washed with distilled water. Such treatments enable the
silica deposits to be studied in detail.

The epidermal peels and chromated preparations are placed in alumi-
nium foil envelopes 2 cm^2, immediately frozen in liquid nitrogen
(-194°C). These are then dried at 0°C in a Virtis automatic freeze
dryer (no. 10-010) for 2 hrs or freeze-dried in a deep freeze at
-30°C for 24 hrs. The dried epidermal peels and chromated preparations
are mounted on aluminium stubs (JEOL microprobe and Cambridge ster-
eoscan) or copper squares (ARL microprobe) or copper grids (JEOL,
SEM) with electrically conductive silver paint for microanalysis
and with celloidin for SEM studies.

The macerated tissues and isolated silica deposits (Figs. 5,11,12)
are prepared by using Jefferey's solution[9] or by boiling in solutions
of the acids cited above. The solution containing the macerated

---

tissues or isolated silica deposits is centrifuged and washed
several times with distilled water and finally preserved in absolute
methanol. Drops of methanol containing the silica deposits are
placed on aluminium stubs or copper squares with a micropipette;
the methanol quickly evaporates leaving the macerated tissues or
silica deposits for microprobe analysis or SEM studies.

For the study of silica deposition in the internal tissues (Figs.
6,9,10), longitudinal and transverse sections (5-10 μm thick) are
cut with the cryostat (SLEE) according to the technique of Knox[10].
Such sections are mounted directly on aluminium stubs or copper
squares.

To reduce any charge build-up, the specimens are coated with con-
ducting material. Gold/Palladium (Figs. 3-6) and chromium films
(Figs. 1-2) prove satisfactory, in contrast to carbon films, for SEM
studies. The specimens prepared by these different techniques are
coated with carbon films for microprobe analysis (Figs. 7-12).
These are coated in a vacuum-evaporator fitted with a rotating device
for uniform coating, then stored in a desiccator until ready for
analysis or SEM studies.

The electron probe microanalyzer is operated at 15-25 KeV and an
absorbed electron current of 0.05-0.08 μamps. The higher currents
severely damage the specimens, particularly the frozen sections and
highly hydrated tissues. The X-ray spectrometer is peaked for the
first order silicon Kα line, using a potassium phthalate (KAP) crystal
in the ARL microprobe and an ammonium dihydrogen phosphate crystal
in JEOL microprobe. Absorbed or secondary electron images are employed
to examine the tissues and to select cells for analysis. Qualitative
determinations of silicon distribution were made by recording inten-
sities, in counts per second (cps), at selected sites. The counting
time was 10-50 seconds and averaged. Usually five separate obser-
vations were made per cell or site, permitting statistical tests for
elemental detection to be made by the procedure of Lipps and Ribbe[11].

For the analysis of other elements, the spectrometers are peaked
for the first order Kα wavelengths using a potassium acid phthalate
(KAP) crystal for Mg, P, and Na, a mica crystal for Rb, a lithium
fluoride (LiF) crystal for Fe, and a quartz crystal for Ca, Mn, Cu
and K in JEOL microprobe and a lithium fluoride (LiF) crystal for
Ca, K, Fe, and Mn and an ammonium dihydrogen phosphate crystal for
P in the ARL microprobe.

In this study, the scanning electron microscope (JEOL model) was
operated at 25 KeV, the sample current was 0.3×10^{-11} amps. The
Cambridge stereoscan was operated at 20 KeV, and the beam current
was 150-200 μamps.

The presence of knobs (small, S; large, T), papillae (Fig. 3), and
pores of depressions (Fig. 1) on the surface of the silica cell is
revealed using the SEM[12]. The analysis shows the presence of silica
in the spherical knobs on the surface of leaves of Scapania (liver-
wort)[13], on the surface of aerial shoots of Equisetum[14,15], on the
surface of the aerial parts of rice (Oryza)[16,17].

The analysis has confirmed the presence of a silica layer external to the epidermis of the aerial parts of the rice plant[16,18]. The details of this silica layer has been investigated further by light microscopy and by the use of the SEM (Figs. 3,4)[19].

The analysis at the cellular level has shown that particular types of epidermal cells (e.g., stomatal apparatuses, trichomes, short or long epidermal cells) may accumulate significant quantities of silica ($SiO_2 \cdot nH_2O$) in one part or on one surface of that part, and that these same types of cells do not accumulate detectable amounts of silica on the other surface of the part or organ of the same plant[20].

Electron probe analysis shows that either significant amounts of silica are accumulated in the entire epidermal system[14,21] or deposited in localized specific structures such as discrete knobs and rosettes on the epidermal cells[14] or in silica cells, trichomes, in the walls of long epidermal cells, and in stomatal apparatuses[20,22-25].

The analysis indicates that silica must be accumulated rapidly in the specialized cells such as silica cells in oat, rice and scouring rushes or horsetails[24]. In contrast, in umbrella plant (Cyperus), the accumulation of silica by long epidermal cells and silica cells appears to occur in two stages: the first is gradual and takes place in the basal portion of the internode in regions within the inter-calary meristem; the second is rapid and occurs at sites well above the intercalary meristem[26].

Employing the electron probe microanalyzer, the study of the accumulation silica in oat (Avena) intercalary meristem stem segments treated in GA_3 (gibberellic acid), sucrose, GA_3 + sucrose, and water suggests that sucrose and gibberellin may play a role in regulating the silicification process in developing internodes[27].

The analysis to determine whether the accumulation of significant quantities of silica (as in silica cells) affects the accumulation of other elements in developing cells shows that there appears to be a decrease in the accumulation of potassium and an increase in calcium[20,28,29].

The analysis of rice roots shows the deposition of silica to be specific to the endodermis with the greatest deposition associated with the inner tangential walls of the endodermal cells[30].

In conclusion, our studies and those of others have shown that the electron probe microanalysis and scanning electron microscope[31,32] have added a new dimension to the study of the silica accumulation process in plants. These instruments may also prove to be useful in order to obtain a better understanding of the role of silicon deposition in animals including man[33,34].

References

1. Netolitsky, F. In Linsbauer, K. (ed.). Handbuch der Pflanzenanatomie. Band 3/la, 1-80, Berlin (1929).
2. Parry, D.W. and Smithson, F. Ann. Bot., 22, 543 (1958).
3. Jones, L.P.H. and Milne, A.A. Pl. Soil, 18, 207 (1963).
4. Sangster, A.G. Ann. Bot., 34, 245 (1970).
5. Yoshida, S., Ohnishi, Y., and Kitagishi, K. Soil Sci. Pl. Nutr., Tokyo, 8, 30 (1962).
6. Rothbur, L. and Scott, F. Biochem. J., 65, 241 (1957).
7. Mitsui, S. and Takatoh, H. Soil Sci. Pl. Nutr., Tokyo, 9, 54 (1963).
8. Kaufman, P.B., Petering, L.B. and Soni, S.L. Phytomorphology, 20, 281 (1970).
9. Johansen, D.A. Plant Microtechnique. McGraw-Hill, New York (1940).
10. Knox, R.B. Stain Techn., 45, 265 (1970).
11. Lipps, J.H. and Ribbe, P.H. J. Paleontol., 41, 492 (1967).
12. Kaufman, R.B., Soni, S.L., Bigelow, W.C., and Ghosheh, N.S. Phytomorphology, in press.
13. Duckett, J.G. and Soni, S.L. The Bryologist, 75, 583 (1972).
14. Kaufman, P.B., Bigelow, W.C., Schmid, R., and Ghosheh, N.S. Amer. J. Bot., 58, 309 (1971).
15. Laroche, J. Rev. Gen. Bot., 76, 483 (1969).
16. Soni, S.L. and Parry, D.W. Amer. J. Bot., 60, 111 (1973).
17. _____, Kaufman, P.B. and Jones, R.A. Bot. Gaz., 133, 66 (1972).
18. Parry, D.W. and Soni, S.L. JEOL NEWS 10e, 23 (1973).
19. _____, _____, In preparation.
20. Soni, S.L., Kaufman, P.B. and Bigelow, W.C. Phytomorphology, 20, 350 (1970).
21. Kaufman, P.B., Soni, S.L., LaCroix, J.D., Rosen, J.J. Planta (Berl.), 104, 10 (1972).
22. Soni, S.L., Kaufman, P.B. and Bigelow, W.C. Pl. Soil, 36, 121 (1972).
23. Hayward, D.M. and Parry, D.W. Ann. Bot., 37, 579 (1973).
24. Kaufman, P.B., Bigelow, W.C., Petering, L.B. and Drogosz, F.B. Science, 166, 1015 (1969).
25. _____, LaCroix, J.D., Rosen, J.J., Allard, L.F., Bigelow, W.C. Amer. J. Bot., 59, 1018 (1972).
26. Soni, S.L., Kaufman, P.B. and Bigelow, W.C. Micron., 3, 348 (1972).
27. _____, _____, _____. J. Expt. Bot., 23, 787 (1972).
28. _____, _____, _____. Ann. Bot., 36, 611 (1972).
29. _____, _____, _____. Amer. J. Bot., 59, 38 (1972).
30. Parry, D.W. and Soni, S.L. Ann. Bot., 36, 781 (1972).
31. Sangster, A.G. Ann. Bot., 32, 237 (1968).

32. Scurfield, G., Segnit, E.R. and Anderson, C.A.   Proceedings of the 7th Annual SEM Symposium IIT Research Institute, Chicago, 389 (1974).
33. Carlisle, E.M.   Science, 167 (1970).
34. Voronkove, M.G.   Chemistry in Britain, 9, 411 (1973).
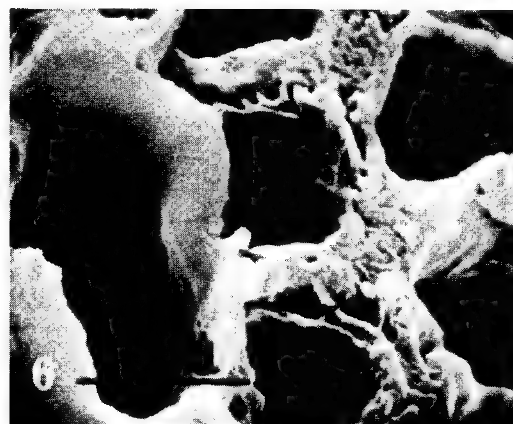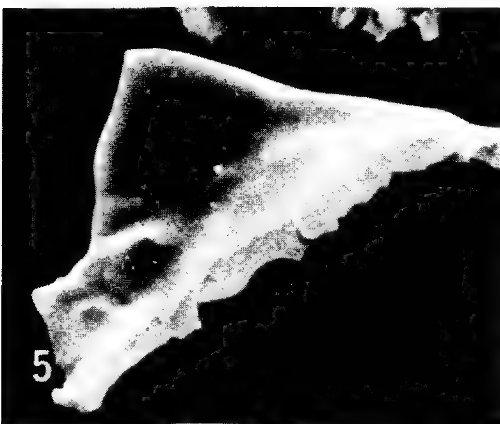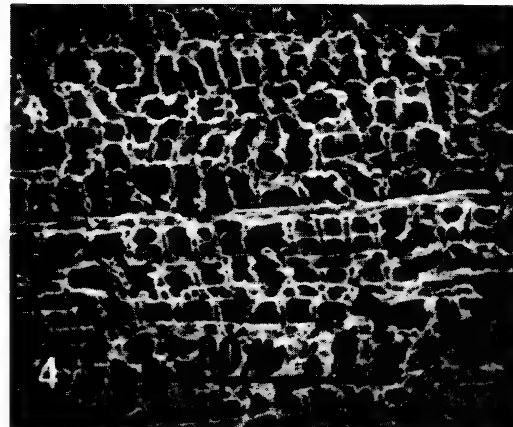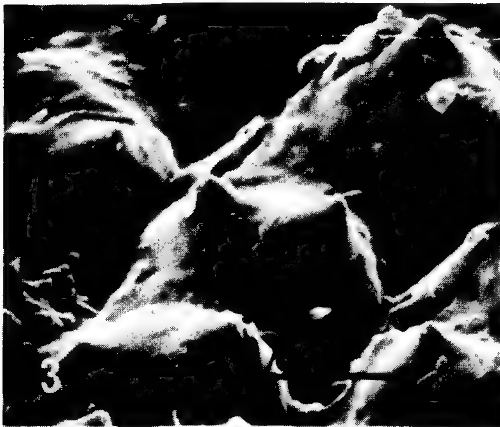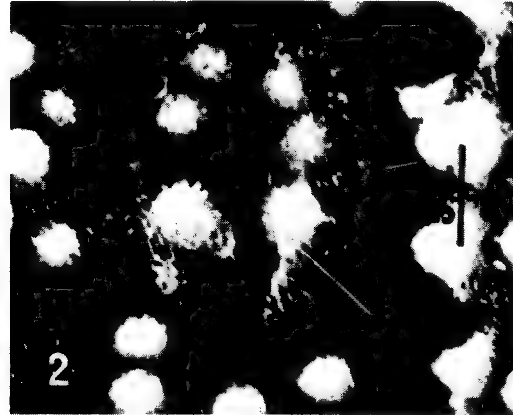
Figs. 1-6.   Scans from an area of rice internodal epidermis (1,2), lemma epidermis (3), chromated preparation of lemma (4), isolated papilla (silica deposit) from the surface of lemma (5), and transverse section of rice root showing endodermal cells.
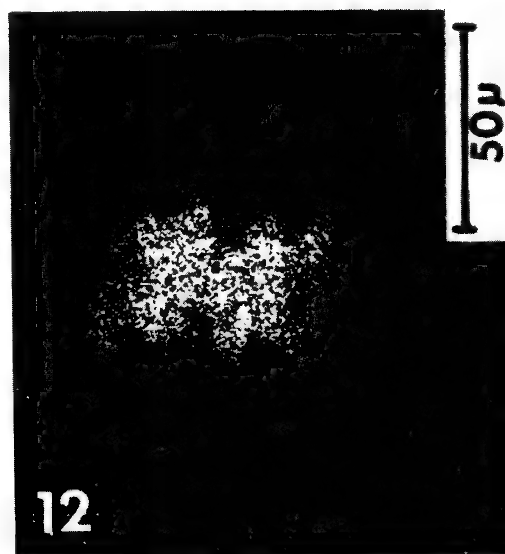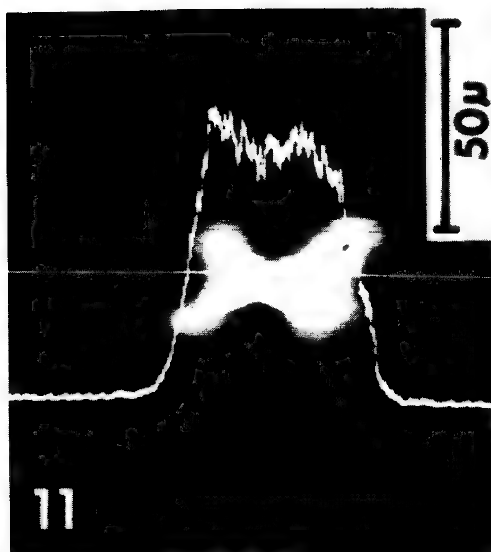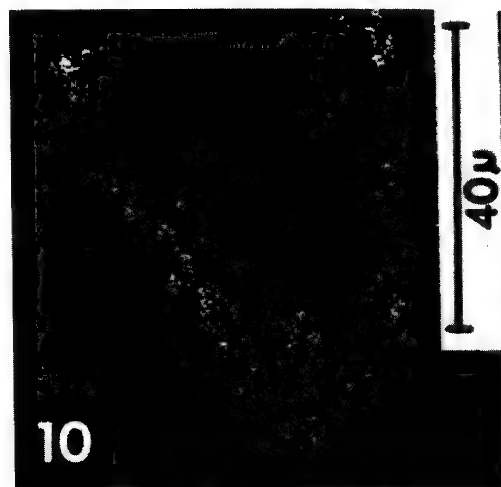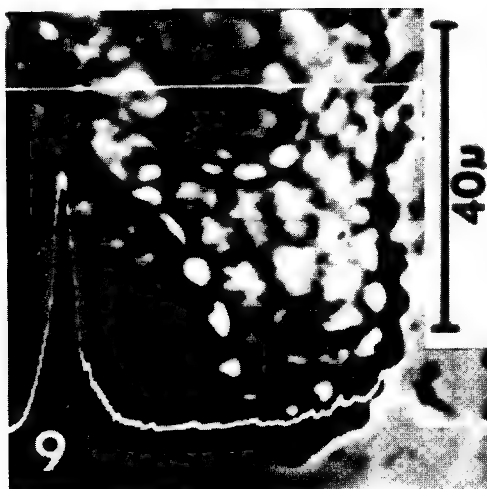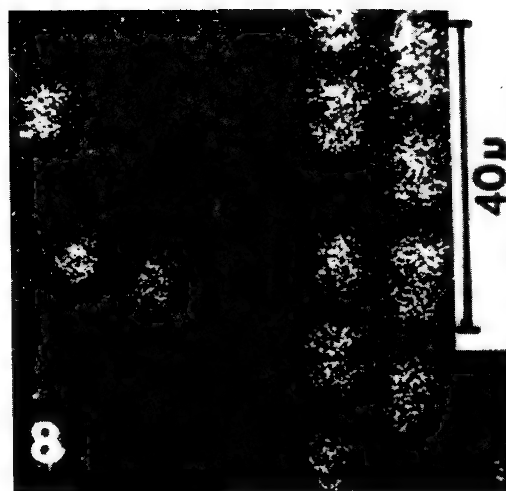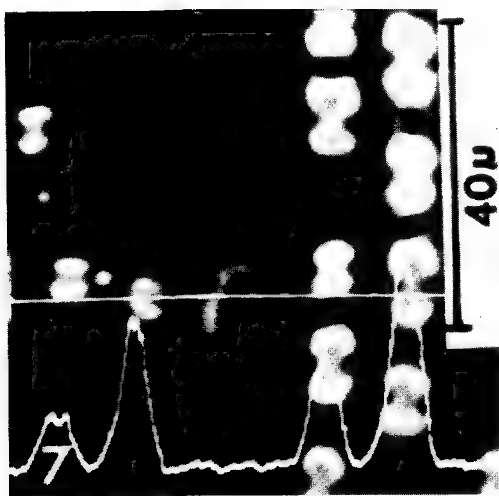
Figs. 7-12. Absorbed electron images (7,9,11) with line scans for silicon and X-ray images (8,10,12) for Si (K) of: leaf epidermis of heath grass (dried) plant (7,8); the transverse section of rice leaf blade (9,10); isolated silica cell from rice leaf blade (11,12).

Applications for High Power Electron Beams

J. Goldak, M. Bibby
Carleton University, Ottawa, Canada

The current "state of the art" for applications of high power electron beams is reviewed. The emphasis is placed on the unique advantages of electron beams in melting, welding, machining, heat treatment and flying spot radiography. In each case those aspects requiring further study particularly where SEM and probe research would be helpful, are discussed.

In striking contrast to the microbeams that are the focal point of this conference is a 4500 KW electron beam furnace capable of producing 120 tons of stainless steel per day (Figure 1). The relatively high vacuum and high degree of superheat in EB melting produces steels with unique properties and problems. In particular, extremely low levels of gases, high vapor pressure residuals and inclusions provide exceptional corrosion resistance and ductility (1). This is, however, also the source of a problem – the susceptibility to grain growth in welding and heat-treatment. In addition to large crucible electron beam melting a new concept of electron beam scan melting has recently been introduced. This is potentially useful in eliminating defective surface areas of cast ingots and rolled billet; slab and plate forms. Essentially an electron beam is scanned across a surface remelting the surface defects. This eliminates oxy-acetylene scarfing or machining these areas before subsequent forming (2).

Electron beam welding is a much more important commercial process that was originally developed by the nuclear and aerospace industries (3). It is now well established in the automotive and other high volume industries because its high welding speed and low operating cost often make it the least expensive welding process for large production runs.

Oddly enough electron beam welders are classified by the level of vacuum used. In the hard vacuum type, the workpiece is mounted in a vacuum chamber that is evacuated to 10^{-4} torr. Hard vacuum electron beam welders usually have production cycles of the order of one hour and are suitable for development, prototype and job shop work but not production. In order to increase the production rate, the pump down time must be reduced. This is done by minimizing the free volume of the work chamber and performing the weld at a pressure of 0.1 torr. The electron beam gun must, of course, be held at 10^{-4} torr and is differentially pumped. These units are called partial pressure electron beam welders and are frequently used in the automotive industry (4). For the highest production rates the evacuated work chamber is eliminated entirely. These are called "in-air" welders. Electron gas scattering reduces the power density, increases the weld width, decreases welding speed and limits working distances to about one centimeter (5). Radiation shielding must be carefully designed for a typical unit operates at 175 KV and about 30 KW. Production rates as high as four pieces per second are reported.

In spite of a number of serious attempts the detailed mechanism that enables a high power density electron beam to penetrate as much as 200 mm (8 inches) of steel is not well understood (6). Basically a power

density in excess of 10^6 watts/cm^2 vaporizes the metal. The vapor pressure of evaporating atoms exerts a downward pressure on the liquid forming a keyhole or cavity (Figure 2). As a result metal melts in front of the moving electron beam, flows behind the cavity and freezes forming the weld. Beyond this little is known. The temperature in the cavity has been estimated at 5000°K by Schwartz from measurements of evaporation rates (7). Plasma effects due to electron-ion interactions including gas focussing have not been measured experimentally or calculated from theory.

A start on the fluid dynamics of the molten puddle has been made by Tong and Giedt who took high speed radiographs of the cavity (8). They claim that the movement of the weld pool surface is analogous to that of a sphere dropped into a fluid (Figure 3). The motion of the weld pool surface is thought to lead to weld defects called cold shuts and spiking (Figure 4) which seriously degrades the performance of the weld (9). These defects can be avoided by judiciously selecting certain welding speeds and by beam oscillation (10). However, since these defects pose a serious limitation to the quality of thick welds for pressure vessels, a better understanding of their behavior and cause would be useful.

While Tong investigated the behavior of the cavity, he did not consider the motion of the liquid metal. The extent of mixing in the molten zone is not clear. Schwartz found a homogeneous fusion zone in dissimilar metal welds (7). However Figure 5 shows a highly heterogeneous fusion zone in a titanium-nickel lap weld. Just what fluid motion takes place in an electron beam weld is unknown. Furthermore the top and bottom (root) surface of the finished weld can form notches (under cutting) which degrades the weld. It is likely that these notches are formed by the motion of the liquid metal. A better understanding in this area should lead to improved welds.

The solidification of conventional welds has long been studied particularly by Savage (11). However the cooling rates, growth rates and temperature gradients in electron beam welds are all large. This usually leads to a fine fusion zone structure which is frequently beneficial. For example, electron beam welding is one of the few ways of equalling the base metal strength and toughness in the weld and HAZ (heat-affected zone) of a new microalloy steel (Figure 6) (12). These steels combine the high strength and low temperature toughness needed for gas pipelines in the Arctic and the integrity of base material is maintained in the weld at least in part by the fine grain structure. It should be pointed out, however, that the whole question of toughness in welds is not well understood. Many of the answers lie in micro-structure, crack morphology and chemical segregation. In the micro-alloy steels higher toughness values can be produced in the cast fusion zone than in the wrought plate which is contrary to conventional wisdom. The underlying cause will only be deciphered when the microsegregation of carbon, niobium, molybdenum and manganese has been fully established. Weld solidification and subsequent cooling is always complicated by thermal stresses. The prediction and control of residual stress is not at all well understood. The high thermal gradients, restraint and time dependent plastic flow present in and around the weld zone present a real challenge to the theorist. A better understanding in this area would greatly assist welding engineers. If there is not sufficient strength and ductility in and around the weld zone to accommodate this stress, hot cracking can occur (Figure 7). Microsegregation in the weld zone can aggrevate this problem. In many metals, including steels,

phase transformations occur both in the fusion and HAZ occur as the weld cools. If the transformed phase is brittle as it often is in steels, so called cold cracking can occur when the yield strength is exceeded. There is no doubt that SEM and microprobe analysis will play a major role in our understanding and the elimination of cracking.

The phases that appear in the weld depend on the thermal history of the material. This can be determined from heat flow calculations (13). Once the time-temperature thermal history of a point either in the fusion or HAZ is known, the microstructure can be predicted from continuous cooling transformation curves (14). This is not a useful concept in arc welds where there is such a wide spectrum of temperature profiles that virtually all possible microstructures occur in every weld. However, calculation and experience shows that in EB welds there is very little difference in the cooling curve of a point at the center of the fusion zone and of a point at the outside edge of the heat-affected zones. Thus EB welds have surprisingly uniform microstructures.

Electron beam machining is less well developed than electron beam welding (15). To machine a material the power density of the beam is increased and the beam is pulsed at rates as high as 10^4 hertz. Essentially a small amount of material is vaporized with each pulse and the amount of melting minimized. Electron beam machining is frequently used for machining non-metals including the production of artificial leather.

Electron beam annealing and heat treating is another area of increasing interest (16). Electron beam annealing of strip has the advantage of fast start up and shut down times, high thermal efficiency, and the capacity to change strip thickness without delay or high scrap loss. This technique is expected to become more important as energy shortages grow. At the same time electron beam heat-treating has been found to increase the cutting life of some tools many times. The electron beam heat-treats only the very surface of a cutting tool rendering it hard and wear resistant while the main body of the tool remains soft and tough.

Looking back in history, the first application of high power electron beams was probably medical radiography. Conventional radiography is now a well established technology. However the potential for flying spot scanning radiography lies in the future. The principle of flying spot scanning radiography is simple. It uses a scanning electron beam - like a SEM - to generate a moving point source of x-rays. A fixed aperture acts as a pinhole lense to produce a scanning collimated x-ray beam typically 0.2 mm in diameter. Like the SEM various signals can be used to generate images displayed on a CRT. The intensity of the x-ray beam transmitted through a specimen can be used as in conventional radiography. Alternately fluorescent x-rays emitted from the specimen can be used as an x-ray probe.

The disadvantage of scanning radiography is its relatively long exposure time. Its advantage lies in its low radiation dose. A typical medical x-ray photograph absorbs approximately 10^{11} photons, has a resolution of 6500 lines and an exposure time of a fraction of a second. Obviously flying spot scanning with 800 line CRT imaging offers little direct competition to established conventional radiography. However it can be used to advantage whenever radiation dose is critical. A good example is pelvimetry (Figure 8) where conventional radiography is used

to measure the dimensions of pelvic girdle and thus assess the difficulty of the delivery in childbirth. In this case flying spot radiography could reduce the radiation dose by five to six orders of magnitude.

The technique consists of measuring eleven dimensions from two radiographs containing approximately 13000 lines of information. The radiation dose is approximately one rad. Scanning radiography would permit the eleven lines to be scanned directly with a dose reduction of three orders of magnitude due to the reduced number of lines. A scintillation detector is two to three orders of magnitude more efficient than film. Combining these effects leads to a dose reduction of 5 to 6 orders of magnitude. A very important factor considering the sensitivity of the fetus to radiation.

A second potential application is flying spot x-ray fluorescence spectroscopy using naturally occurring or injected dyes such as iodine. In this case a non dispersive energy detector is used to detect iodine K_α and K_β radiation emitted from iodine in the thyroid, circulatory system, kidneys or placenta.

Conventional techniques use radiography with high dye contents or radioactive isotopes. The first provides high spatial resolution at high radiation doses. The second provides some time resolution, for example in kidney diagnosis, and modest spatial resolution at a significant local and full body radiation dose.

Flying spot spectroscopy would minimize the radiation dose with good spatial and time resolution. For example it is critical to the life of the expectant mother that the placenta be delivered after not before the baby. Since the placenta consists largely of blood, a small concentration of natural iodine could be injected into the blood stream and the iodine content measured at a few points to establish the position of the placenta.

We have taken radiographs with radiation doses as low as 10^{-9} rads with useful information and radiation doses of 10^{-6} rads are routine. Conventional radiography are usually 10 mrad to 1 rad per exposure. Background radiation exposes each of us to doses of approximately 100 mrads per year. Five hours in a jet at 35,000 feet adds 5 mrad to our exposure. Thus scanning radiography offers the opportunity for certain types of radiography to be performed with radiation doses that are negligible with respect to background radiation levels.

References

(1)   Harrington, T.H., The Electron Beam Continuous Hearth Refining Process, CIM Conference of Metallurgists, Toronto, August 24/26, 1970.

(2)   Goldak, J., Burbidge, G., Bibby, M.J., Electron Beam Billet Conditioning, CIM Conference of Metallurgists, Toronto, August 24/26, 1970.

(3)   Stohr, J.A., Fuel Elements Conference, Paris, 1958, TID7546 Book 1, p. 917.

(4)   Solomon, J., James, H., Proceedings Second International Conference
      on Electron and Ion Beams in Science and Technology, AIME,
      1966, p. 553.

(5)   Meier, J.W., Welding Journal, 1964, p. 925.

(6)   Meulemans, M., Second International Conference on Electron and Ion
      Beams in Science and Technology, 1966, p. 357.

(7)   Schwartz, H., Journal of Applied Physics, Vol. 35 (7), 1964, p. 2020.

(8)   Tong, H., Giedt, W., Welding Res. Supplement 6, 1970, p. 259s.

(9)   Anderson, J.D., Electron Beam Welding High Strength Low Alloy (HSLA)
      Steels, M.Eng. Thesis, Carleton University, March 1974.

(10) Eichhorn, F. and Schuhmacher, IIW Document IV-122-73.

(11) Savage, W.F., Lundin, C.D., Aronson, A.H., Welding Journal Research
      Supplement, Vol. 44 (4), 1965, p. 175s.

(12) Bibby, M.J., Goldak, J., Electron Beam Welding High Strength Low
      Alloy (HSLA) Steels - manuscript in preparation.

(13) Goldak, J.A., Burbidge, G., Bibby, M.J., Can. Met. Quart., Vol. 9 (3),
      1970, p. 459.

(14) Goldak, J.A., Burbidge, G., Bibby, M.J., Can. Met. Quart., Vol. 9 (3),
      1970, p. 467.

(15) Steigerwald, K.H., Meyer, W.E., Konig, J., Tenth Symposium on
      Electron Ion and Laser Beams Technology, 1969, p. 87.
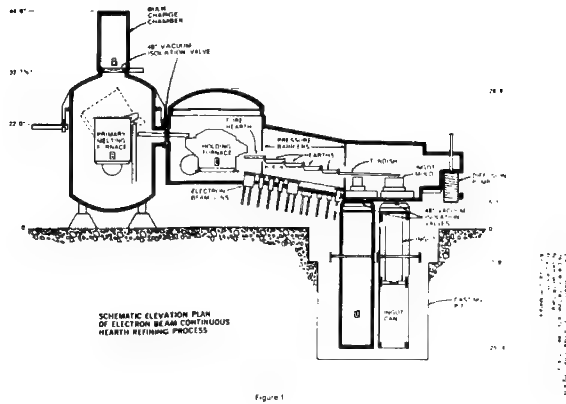
(16) Shah, R., 1AM1, 1973, p. 20.
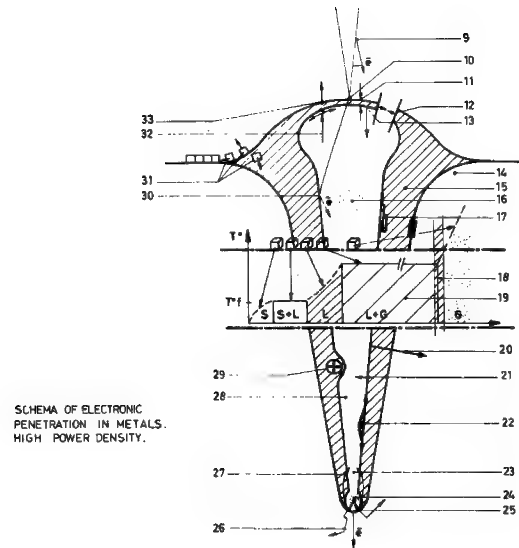
Figure 1 Airco Temescal Electron
Beam Furnace

SCHEMA OF ELECTRONIC
PENETRATION IN METALS.
HIGH POWER DENSITY.

Figure 2 Electron Beam Weld Cavity
(Meulemans)

STATIONARY EB, WORKPIECE MOTION

304 STAINLESS STEEL

BEAM VOLTS—35 KV

BEAM CURRENT
—175 ma
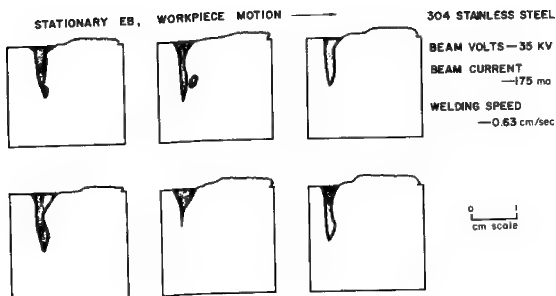
WELDING SPEED
—0.63 cm/sec

cm scale

Figure 3 Electron Beam Weld
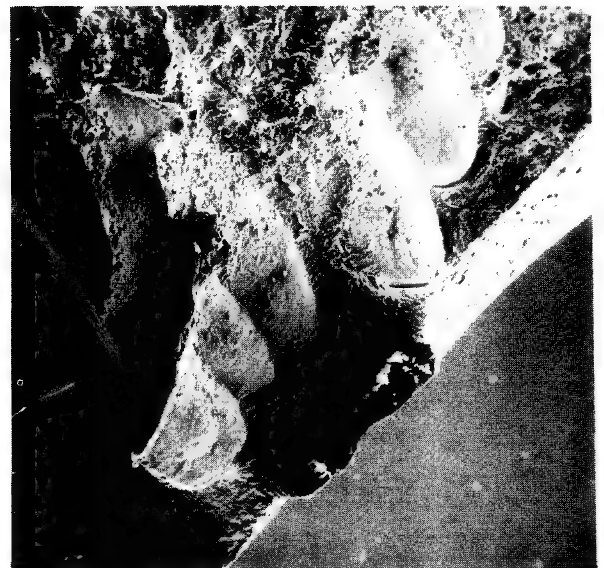Cavity Oscillation
(Tong and Giedt)

Figure 4 Electron Beam Fusion Zone
Cold Shuts X125
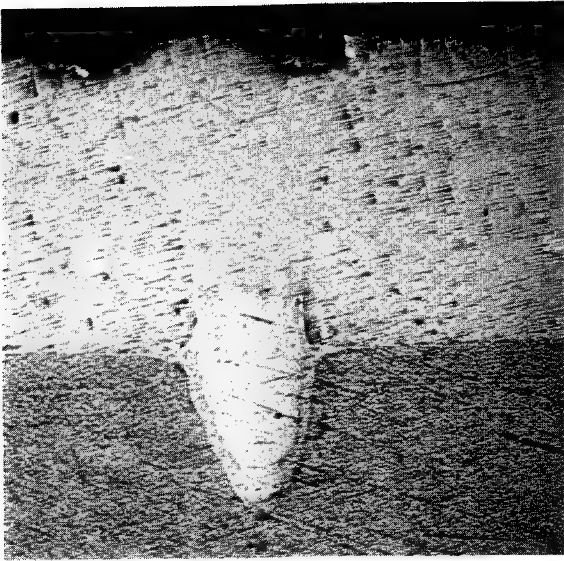
Figure 5   Lapp Weld Showing
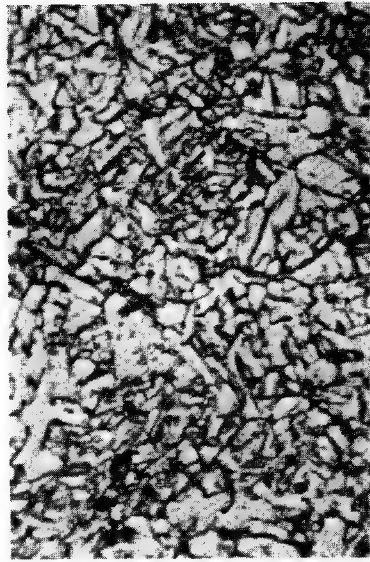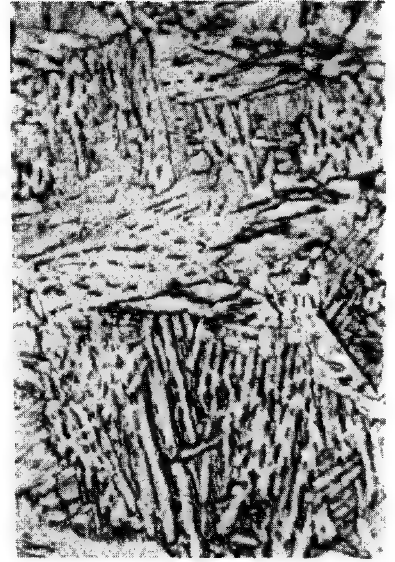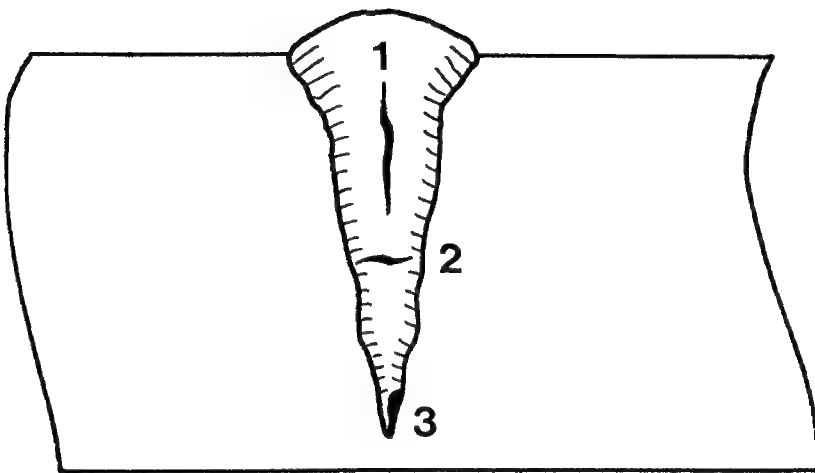   Heterogeneous Weld
            Zone Mixing

(a)   (b)

Figure 6   HSLA Steel Microstructure
            (a) Parent Material
            (b) Fusion Zone Material X1000

1. **CENTERLINE CRACK**
2. **HORIZONTAL CRACK**
3. **COLD SHUT**

Figure 7   Electron Beam Fusion Zone Defects

TRANSVERSE

Inlet

Mid Cavity (Interspinous)

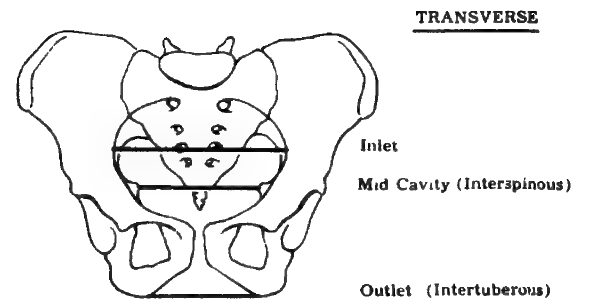Outlet (Intertuberous)

Figure 8   X-Ray Scanning
            Pelvimetry

THIN FILMS AND BULK SPECIMEN X-RAY MICROANALYSIS IN THE ELECTRON MICROSCOPE

A.Armigliato (a), P.Bergamini (b) and L. Morettini (c)

(a) CNR-LAMEL, 40126 Bologna (Italy) (b) CISE, Segrate, Milano (Italy)

(c) Istituto di Metallurgia, Università di Bologna (Italy)

The present research activities of our LAMEL Laboratory include the study of the precipitates of Boron and Phosphorus induced into Silicon wafers thermally diffused as well as heat treated in bulk. The identifi cation of such particles is considerably helped by a quantitative anal ysis of the elements involved, which can be carried out by an X-ray spectrometer associated to an electron microscope. In this way, the composition of a precipitate in a thin film can be related to its crys tal structure, which can be deduced from the study of the electron imag es and the corresponding diffraction patterns.

The instrument we used was a Siemens Elmiskop 101 TEM, equipped with a wavelength dispersive semifocusing X-ray spectrometer (RMAS 101). As a preliminary test of its analytical performances we have carried out quantitative analyses on two binary alloys (Cu-Zn and Cu-Au) both in bulk and in thin films, and in thin Silicon specimens, heavily doped with Boron and Phosphorus.

a) Copper-Zinc alloys. A few specimens some hundreds microns thick of Cu-Zn alloys of different compositions were prepared, and the ZnKα and CuKα X-ray intensities were measured with our spectrometer,together with the corresponding ones generated by pure standards. The accelerat ing voltage was 40 kV. The same specimens were also analysed with a Jeol 50 A scanning electron microscope, equipped with a fully focusing crystal spectrometer. In both cases the composition of these alloys were calculated by using a MAGIC IV computer programme by Colby (1) and compared with the ones resulting from physico-chemical polarographic analysis. In Table I the Cu wt% in three different alloys are reported.

Some Cu-Zn specimens were thinned for TEM observation and the X-ray intensities were recorded as before. The compositions of these thin films were calculated by the computer according to the Philibert-Tixier equation (2), and also by hand, substituting to the stopping power correc tion in the standards, the approximation of Bishop (3). In Table II are reported the concentrations of Cu, computed with these two procedures, in three thin specimens, obtained from the same thick alloy. The composition of this alloy, as deduced from polarographic analysis, is also shown. The agreement between the two sets of data is within about 1%.

b) Gold-Copper alloys. The same measurements described above were made also on specimens of Cu-Au alloys some hundreds microns thick. The characteristic X-ray lines analysed were AuLα and CuKα . The con centrations of Gold, in three alloys of different composition,were cal culated from the RMAS 101 and Jeol 50 A spectrometric data and are rep orted in Table III, together with the ones deduced from coulombometric analysis. Some of these thick specimens were thinned for electron micro scopy, but the resulting thickness uniformity was not satisfactory: generally, however, there was a good agreement between the values obtained from the equation of Philibert-Tixier, with and without the Bishop's approximation.

c) Phosphorus and Boron doped Silicon thin films. As a further check of the analytical performances of our instrument, we have done X-ray intensities measurements on bulk doped Silicon wafers: the corresponding dopants concentrations, as determined by resistivity measurements, rang

ed from 8.5×10^{18} to 7.5×10^{19} P at/cm^3, and from 7.2×10^{19} to 4.5×10^{20} B at/cm^3. These figures were checked by neutron activation analysis (P doped wafers) and by colorimetric analysis (B doped wafers). The specimens were thinned for the microscope and analysed with our spectrometer. The SiKα, BKα and PKα lines were measured at 50 kV for the P doped thin films and at 20 kV for the B doped ones. The intensity ratios I(PKα)/ /I(SiKα) and I(BKα)/I(SiKα) were calculated and plotted versus the concentration of the dopant in the films. The resulting calibration curves are straight lines, as can be seen from Figs. 1 and 2.

We have also tried to determine the films composition by calculation using high resistivity Si, pure B and GaP as thick standards, and working at 20 kV. The results obtained in the various samples by using the Philibert-Tixier formula are given in Tables IV and V, together with the corresponding values deduced from resistivity measurements.

If the Bishop's approximation is used, the dopants concentrations differ from the ones quoted in Tables IV and V by less than 5%, which is tolerable, at least within the degree of analytical accuracy attainable with our technique.

The choice of the mean ionisation potential J is very critical in the case of Boron. In fact, the computer programme MAGIC IV derives the J values from the equation of Berger and Seltzer (4), while other authors uses the formula of Duncumb (5). In Boron, the equation of Berger and Seltzer gives J = 92 eV, while Duncumb gives J = 156 eV. The resulting computed Boron concentration of the film labelled SiB2 in Table V (C_B = = 0.238 wt%) is 0.199 wt%, if the J of Berger and Seltzer is used, and 0.223 wt% with the J of Duncumb. This latter figure is in closer agreement with the true concentration: for this reason we have used the J of Duncumb in computing the concentrations reported in Table V.

In the case of Phosphorus, however, the J values are 183 eV (Berger and Seltzer) and 166 eV (Duncumb): this difference does not lead to an appreciable discrepancy between the computed P concentrations.

Finally, the minimum detectability limit C_{DL} for B and P can be calculated, according to the equation (6):

$$C_{DL} = \frac{2C_{std} \sqrt{I_B}}{I_P - I_B}$$

were C_{std} is the concentration of the element considered in a specimen of known composition, I_P and I_B are the peak and the background intensities respectively. For the beam current and the counting time we used in our experiments, one obtains 3×10^{18} at/cm^3 and 2×10^{19} at/cm^3 for P and B, respectively.

1) J.W.Colby, Adv. in X-Ray Analysis, 11, p. 287, Plenum Press, 1968.
2) R.Tixier and J.Philibert, Proc. 5th Int. Congress on X-Ray Optics and Microanalysis (Tübingen 1968) p. 180.
3) H.E.Bishop, Brit. J. Appl. Phys. Ser. 2, 1, 673 (1968).
4) M.J.Berger and S.M.Seltzer, NASA Report N65-12506 (1964).
5) P.Duncumb, P.K.Shields-Mason and C.Da Casa, Proc. 5th Int. Congress on X-Ray Optics and Microanalysis (Tübingen 1968) p. 146.
6) John C.Russ, Proc. Symposium on Thin-Section Microanalysis (St.Louis Missouri 1972) p. 134.

Table I

SPECIMEN	Cu Wt %		
	RMAS 101	POLAROGRAPHY	MICROPROBE
z c 2	96,2	95,7	95,2
z c 5	70,0	70,4	70,6
z c 8	10,5	11,2	10,1

Table II

Film	Cu wt%		
	Polarography	RMAS 101	
		Bishop	Phil. Tixier
4A	80,5	81,5	80,6
4B	80,5	81,0	80,1
4C	80,5	80,6	79,5

Table III

Specimen	Au wt%		
	RMAS 101	Coulomb.	Microprobe
1	0,99	1,2	1,6
5	52,2	52	49,8
7	92,3	92,2	92

Table IV

specimen	Phosphorus wt.%	
	resistivity	RMAS 101
Si P 1	0.16	0.12
Si P 2	0.084	0.076
Si P 3	0.019	0.021

Table V

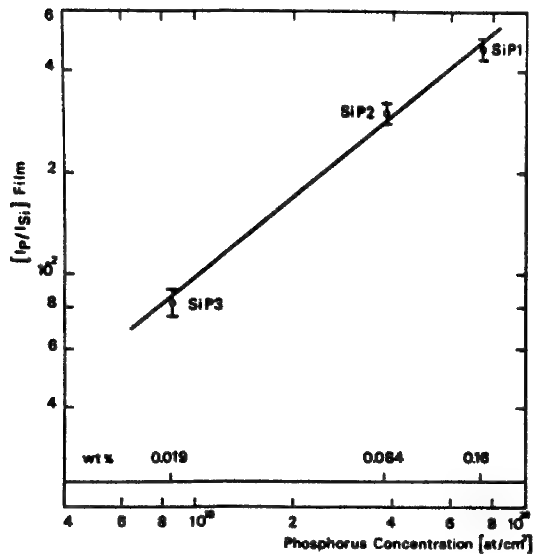| specimen	Boron wt.%	
	resistivity	RMAS 101
Si B 1	0.349	0.385
Si B 2	0.238	0.223
Si B 3	0.162	0.155
Si B 4	0.056	0.048

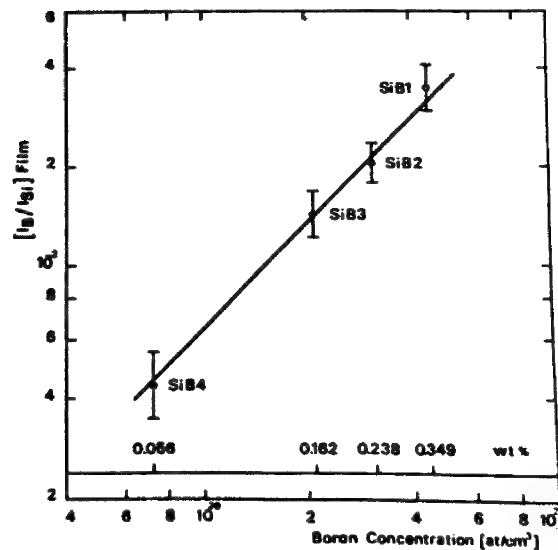Fig. 1. Calibration curve
for P doped Si thin films.

Fig. 2. Calibration curve
for B doped Si thin films.

AN INVESTIGATION OF NATURAL DETERIORATION OF ABORIGINAL ROCK PAINTINGS BY SCANNING ELECTRON MICROSCOPY AND X-RAY MICROANALYSIS

R. M. Myers and J. M. Taylor

Analytical Research Services,
Canadian Conservation Institute,
Ottawa, Canada, K1A OM8

Before establishing conservation treatments for the thousands of Indian rock paintings or pictographs scattered across Canada a scientific study was initiated to examine the causes of natural deterioration of the paintings. This deterioration, which includes fading, surface paint loss and exfoliation of large pieces of rock has been largely attributed to physical and chemical weathering of the rock face on which the pictographs are inscribed. Our studies show that, with the exception of exfoliation, this is not the case.

Several small rock chips removed from paintings at the Agawa Bay site north of Sault Ste. Marie were examined in detail using an optical stereo-microscope and minute particles ($\sim$75 μm in dia.) were removed from the surface and the interior rock for XRD analysis. The remaining samples were mounted in polyester resin, sectioned and polished to produce opaque cross-sections which were photomicrographed in colour and then coated and examined in a Hitachi SEM equipped with an EDX analyzer. Single point, line scan and isometric element mapping modes of analysis were used to characterize the composition of the samples. Comparisons of composition between samples were made by ratioing the counts for major constituents.

In examining Figs. I, II and III it is evident that all samples consist of a four layer structure (generally 14 - 80 μm thick), the base rock, an under-layer, a pigment layer, and a surface overlayer and not just the rock-pigment layer structure expected. The underlayer was generally visible with an optical microscope and was originally thought to be a chemically weathered crust. However, the overlayer was only detectable using the SEM (except in specific cases where there was a high Ca content producing a thicker opaque layer).

The composition of the layers proved to be of critical importance in determining their origin. Figure II shows that both the overlayer and under-layer are an identical aluminum silicate and their composition bears no relation-ship to the underlying particle of base rock. No concentration gradients of soluble ions (Na, Ca, K) could be found in the line scans. Even more import-ant, the Al/Si count ratio always decreased when going from the base rock to the surface layers, except of course if the base rock was a grain of pure quartz. (The ratio for a grain of K feldspar was .25/1 whereas for the surface layers it averaged .05/1).

In geochemical weathering, silica is constantly leached out of the rock and alumina accumulates in the clay type residue (1). Thus, the weight per cent Si per unit volume in any sample of feldspar always decreases with

increasing weathering regardless of variations in the parent rock mineralogy, climatic conditions or local physio-chemical parameters (2). If chemical weathering was occurring, the Al/Si count ratio would always be smaller in the interior of the rock than on the surface but as stated before, the opposite was found. In addition to this, the XRD patterns of surface layers showed only an amorphous band with no evidence of any weathering products and petrographic analysis of larger rock samples showed an unweathered granite substrate. Thus we can safely say that chemical weathering of the rock face beneath a painting is not a major factor in the destruction of the paintings.

From the experimental results a model has been worked out which not only explains the formation and composition of the surface layers but also provides answers to some of the questions put forward at the start of the project. Groundwater seepage (usually acidic) from above the site percolates down through the soils and rock extracting soluble ions such as Na, Ca, K, Si and to a lesser extent Al by a process of chemical weathering. As the water reaches the rock face and trickles down, it evaporates, resulting in the less soluble ions (Al, Si, Ca) reaching their saturation limit and depositing out on the rock face. This deposit would be much richer in silicon than aluminum and over a period of years a thin layer would develop. The shaman artist then arrived at the site, executed his paintings with a red pigment (identified by XRD as αFe_2O_3) and groundwater seepage again covered the face with a thin transparent mineral layer.

Undoubtedly the surface layers helped bind the pigment to the rock and both SEM and XRD results show the pigment to be intimately mixed with them. They also acted as a protective coating impervious to water, and prevented the chemical weathering that would have destroyed the faces long ago. Unfortunately this structure also provides a means of degradation. In all samples studied a minute crack (1-5 μm) appeared between the surface layers and the base rock (Figs. I and III), probably due to differing coefficients of thermal expansion between the two. Thus with extreme temperature variations small surface particles are breaking off and the paintings are gradually being lost. The conservation problem then is not with pigment flaking (i.e. a weak pigment bond) as was previously thought but rather complete surface layer loss due to a weak underlayer to rock bond. The apparent "fading" of the paintings is also a result of the surface layer formation which becomes thick enough to partially obscure the paintings.

References:

1. Carrol, D. "Rock Weathering", Plenum Press, New York, p. 100 (1970).

2. Hariss, R.G. and Adams, J.A. "American Journal of Science" 264 p.151 (1966).
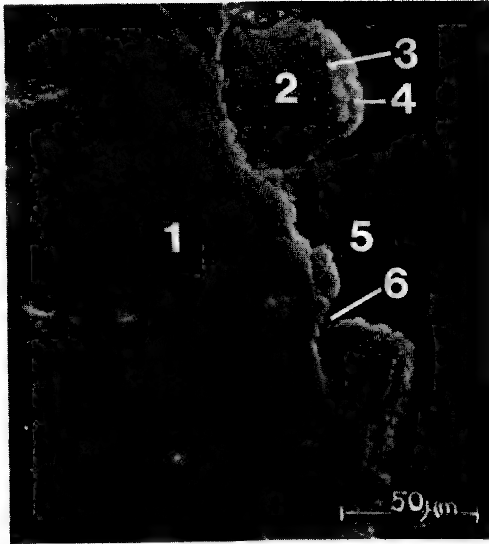
Fig. I

A polished cross section removed
from Agawa Face 111b showing
(1) base rock, (2) underlayer,
(3) pigment layer, (4) overlayer,
(5) area of layer loss, (6) crack
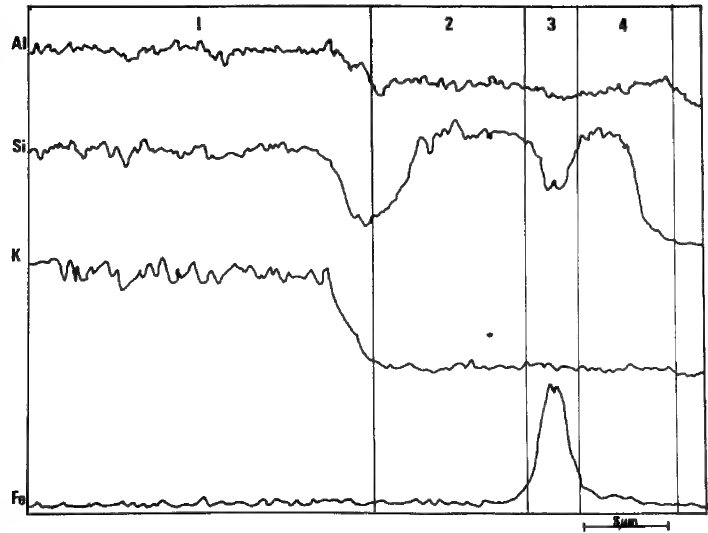between layers and base rock.

Fig. II

Element line scans of a typical Agawa cross
section showing the four layer structure,
(1) base rock (K feldspar), (2) underlayer
(3) pigment layer, (4) overlayer and the
high Si content of the surface layers. The
signal intensity of all elements drops at the
1-2 interface due to a crack.

Fig. III

A polished cross section from Agawa
Face 111b demonstrating isometric
element mapping of (1) Fe, and (2)
Si. Isometric element mapping is
carried out by operating the SEM at
a slow scan speed and using a rate
meter output from a selected region
of interest in the EDX to modulate
the y deflection of the display screen.
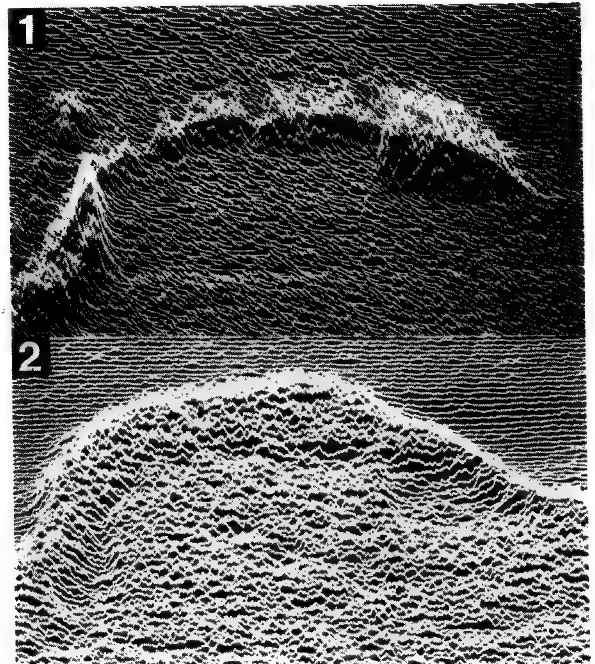
ELECTRON ENERGY DEPOSITION PROFILES IN THIN POLYMER FILMS

D. F. Kyser and K. Murata*

IBM Research Laboratory
San Jose, California 95193

Monte Carlo simulation of kilovolt electron beam scattering and energy loss in targets which consist of thin films on thick substrates has been developed. The use of such calculations for quantitative electron probe analysis of thin films with X-ray fluorescence has been reported previously [1]. Such calculations also have direct application to the physics and technology of electron beam lithography with polymer films on thick substrates [2]. Profiles of energy density (eV/cm^3) deposited in the thin film by an impinging electron beam are calculated with parameters which include beam voltage and angle of incidence, film thickness, film composition, and substrate composition. These profiles are thought to control the geometry of the chemically-etched electron resist patterns. The contribution of substrate backscattering to the spatial distribution and magnitude of the profiles is automatically included within the Monte Carlo simulation, and is shown to be a significant effect for particular combinations of the various parameters. The substrate backscattering effect has also been demonstrated by experiment [3, 4].

In the Monte Carlo simulation, angular electron scattering is calculated with the screened-Rutherford model for cross-section, and energy loss between scattering events is calculated with the Bethe approximation in this single-scattering model. To achieve good statistics, typically 20,000-50,000 trajectories are calculated on an IBM S/360 model 195 computer within our laboratory.

Point, line, and plane source electron beams have been simulated to identify the limiting effects on lateral spatial resolution and depth profiles of energy deposited. Laterally distributed or periodically spaced electron beams can be simulated by superposition. Comparison of this Monte Carlo calculation is made with other analytic models [5, 6] and the limited experimental data available [7].

*On sabbatical leave from Osaka University, Osaka, Japan.

1. D. F. Kyser and K. Murata, Proc. 8th National Conference on Electron Probe Analysis (New Orleans, 1973), paper no. 28. Also see IBM J. Res. Develop. (July, 1974), in print.

2. G. R. Brewer, IEEE Spectrum 8, 23 (1971). Also see IEEE Trans. Electron Devices ED-19 (May, 1972) and J. Vac. Sci. Technol. 10 (Nov./Dec., 1973).

3. T. O. Sedgwick, A. N. Broers, and B. J. Agule, J. Electrochem. Soc. 119, 1769 (1972).

4. N. Saitou, C. Munakata, and Y. Honda, Jap. J. Appl. Phys. 11, 1061 (1972).

5. R. J. Hawryluk and H. I. Smith, Proc. 5th Int. Conf. on Electron and Ion Beam Science and Technology, ed. by R. Bakish (The Electrochemical Society, Princeton, 1972), p. 51.

6. J. S. Greeneich and T. Van Duzer, J. Vac. Sci. Technol. 10, 1056 (1973).

7. E. D. Wolf et. al, Record of 11th Symp. on Electron, Ion and Laser Beam Technology, ed. by R. F. M. Thornley (San Francisco Press, 1971), p. 331.
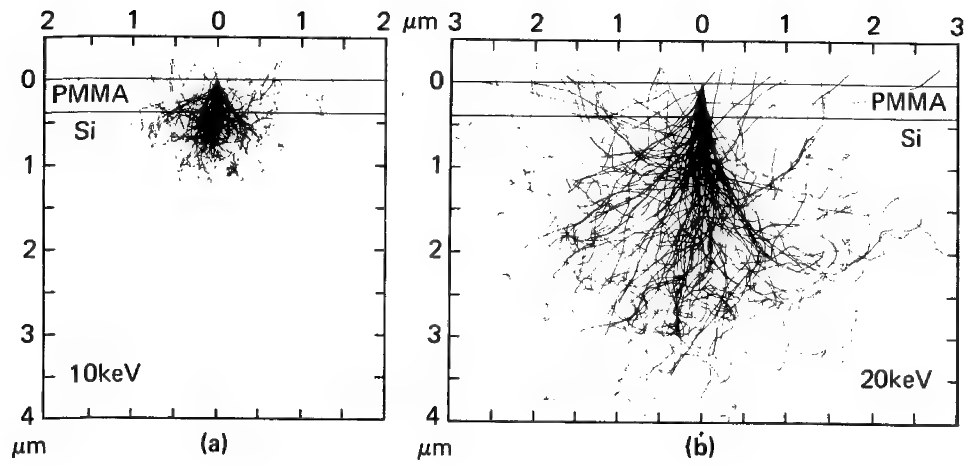
Figure 1. Simulated trajectories of 100 electrons impinged at the origin in a 0.4 μm PMMA film-Si substrate at (a) 10keV and (b) 20keV.
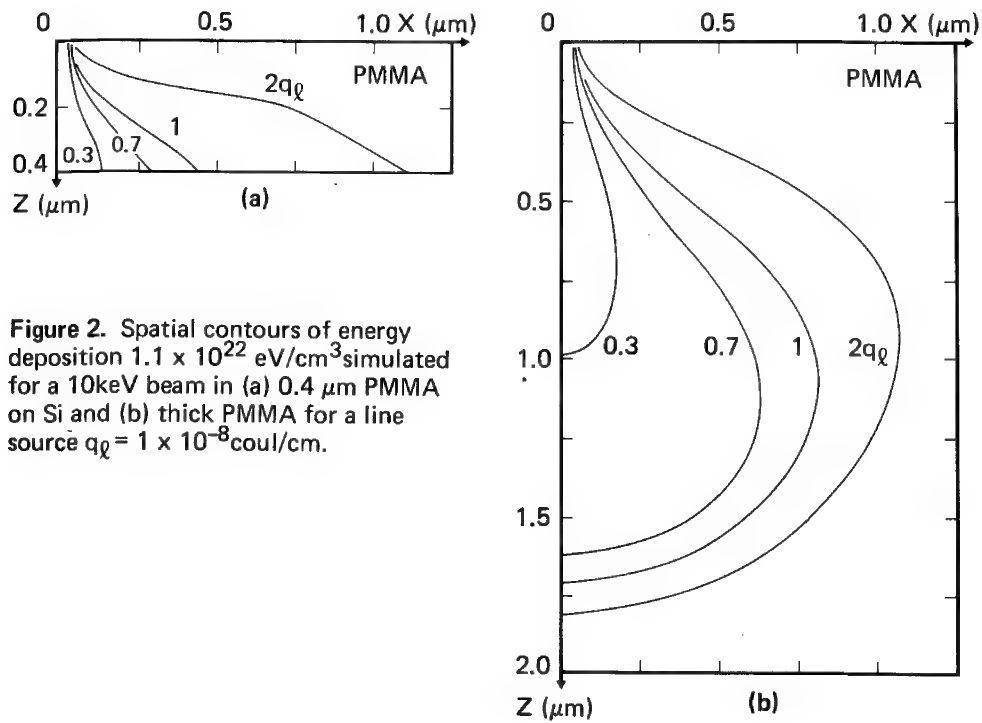

Figure 2. Spatial contours of energy deposition 1.1×10^{22} eV/cm^3 simulated for a 10keV beam in (a) 0.4 μm PMMA on Si and (b) thick PMMA for a line source $q_\ell = 1 \times 10^{-8}$ coul/cm.

REAL-TIME CATHODOLUMINESCENT SPECTROSCOPY

C. Michel and A. Sicignano
Philips Laboratories
Briarcliff Manor, N.Y. 10510

Real-time spectroscopic analysis of visible and infrared (3000 - 12,000Å) cathodoluminescent (CL) radiation has been performed using a silicon vidicon tube[1] (Sivicon TM). The typical instrument set-up consists of a spectrometer mounted with a Sivicon tube, as shown in Fig. 1. In this arrangement, the CL radiation emitted through the exit port (window) of a conventional scanning electron microscope[2] (SEM) is focussed on the entrance slit of the spectrometer. The CL channel is composed of collimating lens, diffraction grating, imaging lens, and deflecting mirrors. The mirrors deflect the CL spectrum onto the upper half of the vidicon tube. Using a proper mirror-lens arrangement, the other portion of the tube can be used as a direct view channel. With the mirror option (M-3) described in Fig. 1, conventional SEM pictures in CL mode of detection can also be simultaneously analyzed.[3]

In this work, evaluation of a real-time CL wavelength dispersive technique capable of analyzing transient phenomena is demonstrated. GaAs and GaP LED material was selected for this study in the visible and the near-infrared region. Particular attention was focussed on the analysis of transient phenomena such as the capture of a CL (or EL) pulse shown in Fig. 2, or the change in the CL spectral distribution due to sample (or beam) heating, as shown in Fig. 3. The CL radiation was

simultaneously detected and spectrally analyzed with a resolution of 30Å and a sensitivity of 10^{-11} watt/cm^2. Preliminary results show that this system is particularly suitable for the spectral analysis of CL radiation of transient phenomena. The unique feature of simultaneously achieving real-time, spatial and spectral analysis with a relatively high sensitivity and resolution will be discussed, together with potential applications and future improvements[4, 5] of this spectroscopic system.

(1) This spectroscopic system was designed and built at Philips Laboratories.

(2) The SEM used in this study was an AMR-900.

(3) With this system, CL signal can be displayed on the SEM CRT screen, or a strip chart recorder.

(4) A SIT-tube should be more efficient because it provides, with a coating of suitable fluorescent substance, an electron gain of about 2000 over the silicon vidicon.

(5) Data storage devices combined with a computerized system would be highly desirable for handling rapidly changing CL signals.

18c

SEM ELECTRON BEAM

SAMPLE

HOT/COOL STAGE

LENS

WAVELENGTH CALIB. FILTER

REFERENCE LIGHT SOURCE

DEFLECTION MIRROR M-1

ENTRANCE SLIT

COLLIMATOR LENS

GRATING

SPECTROMETER LENS

SPECTROMETER CHANNEL

MIRROR

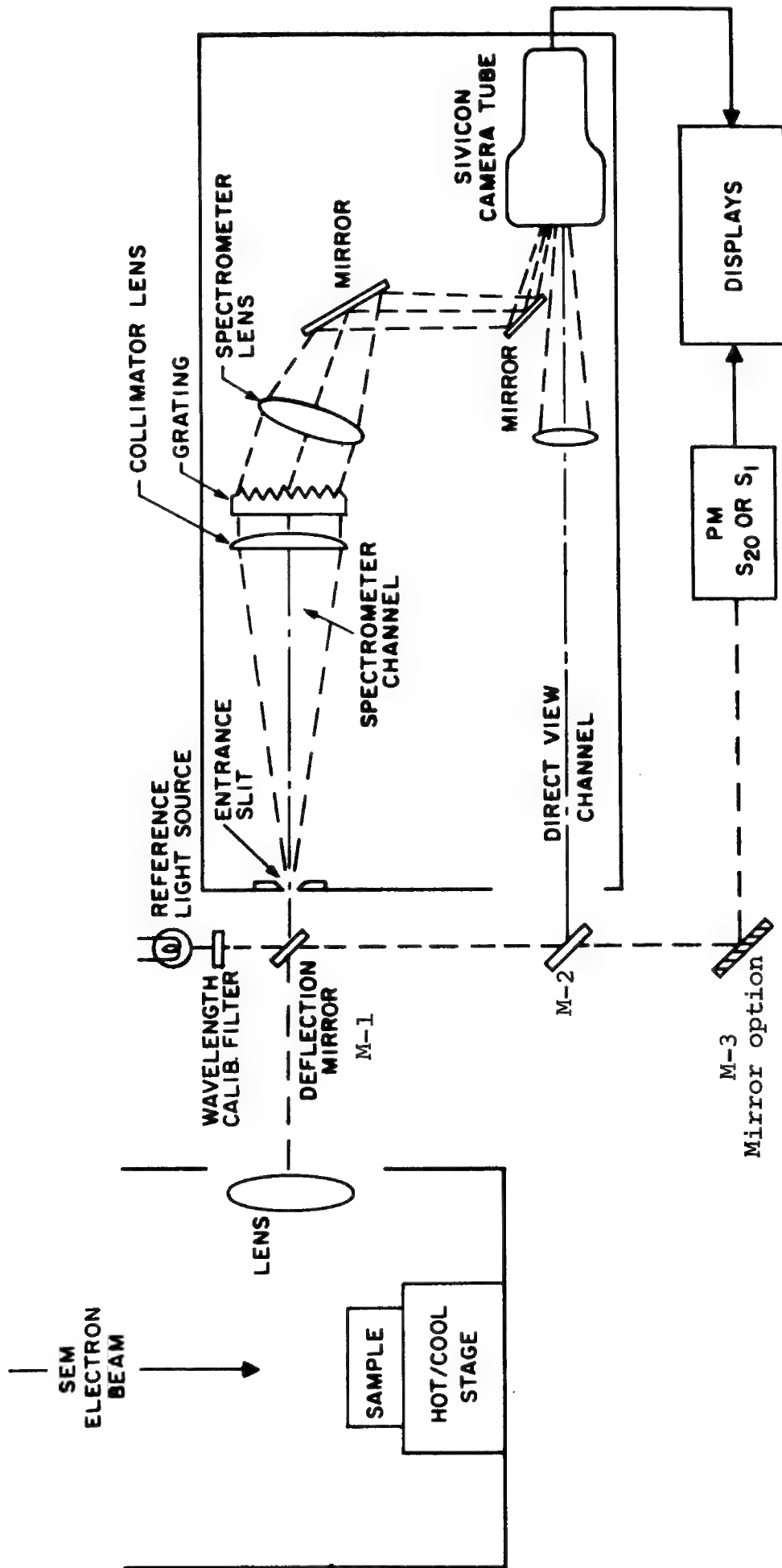SIVICON CAMERA TUBE

MIRROR

DIRECT VIEW CHANNEL

M-2

M-3
Mirror option

PM S₂₀ OR S₁

DISPLAYS

FIG. 1

Schematic of the CL dispersive system

λ (μm)

a.

c.
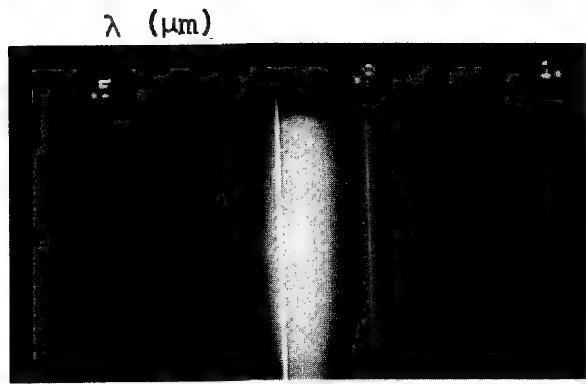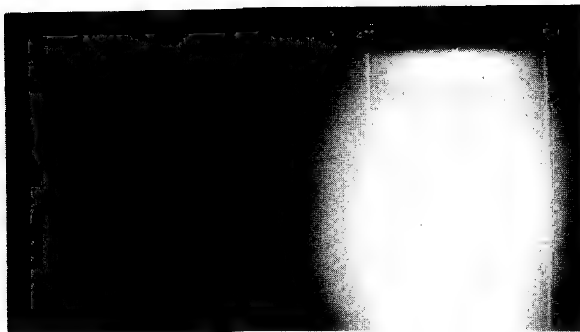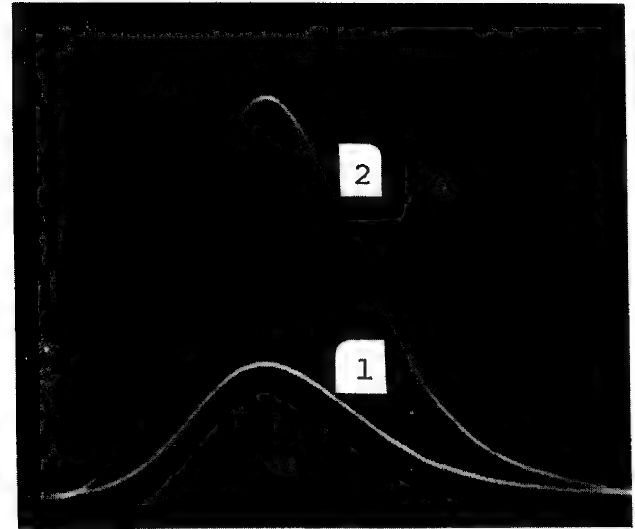
b.   I(CL) vs λ

FIG. 2

a.   Photograph of TV monitor display showing the
     real-time spectrum emitted by a red GaP diode.
     Wavelength calibration scale (μm) and markers
     are shown at the top.

b.   The spectral distribution of the diode displayed
     on an oscilloscope screen simultaneous with (a.).
     Curve (1) shows the electroluminescent (EL) spectral
     distribution; a CL pulse superimposed on this d.c.
     signal and captured in Curve (2).

c.   Spectral response due to junction breakdown of the
     same diode.
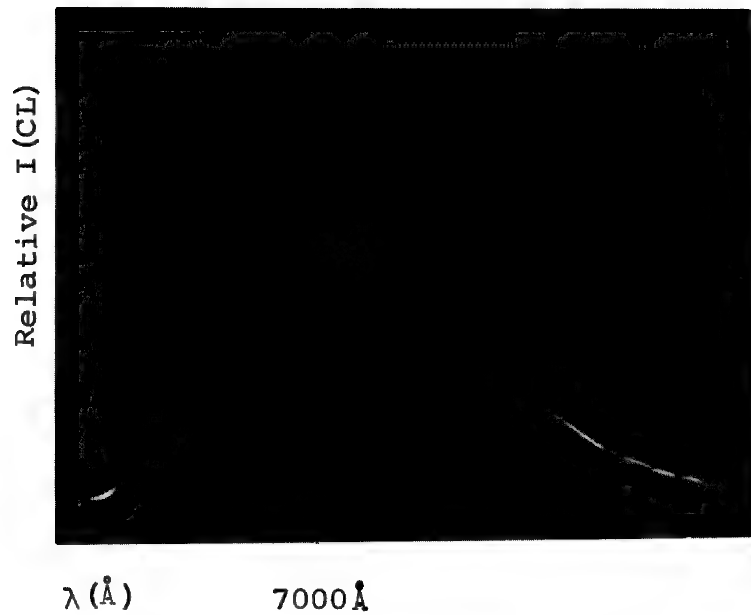
FIG. 3

a. Effect of localized beam heating on the CL
spectral response for GaP (red) material.

b. Peak wavelength shift and broadening effect on
the CL spectral distribution curve due to con-
trolled temperature variation. These curves
were obtained using a hot and cool stage on
GaAs material.

EXPERIMENTAL X-RAY MASS ATTENUATION COEFFICIENTS
BETWEEN THE M_I AND M_V ABSORPTION EDGE OF GOLD

Wayne J. Steele

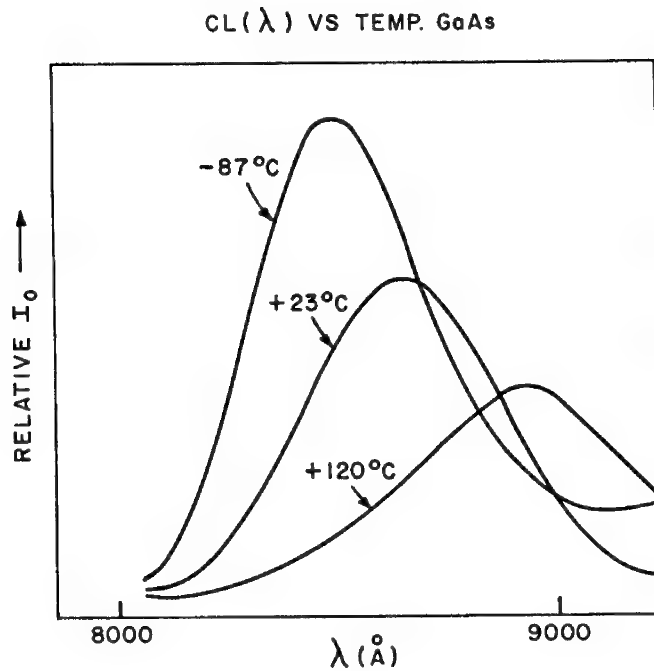Lawrence Livermore Laboratory, University of California
Livermore, California 94550

ABSTRACT

Experimental values obtained for X-ray mass attenuation coefficients between the M_I and M_V absorption edges of gold are presented below. Also presented is a brief discussion of the experimental procedure.

Introduction

Situations frequently arise during microprobe analysis of alloy systems in which it is desirable to use certain M-characteristic lines to avoid interfering line problems. Examples would be the advantageous use of the Mβ gold characteristic line in a gold-platinum alloy or gold-zirconium alloy. In both cases, Mβ Pt and Lβ Zr interfere with the Mα gold characteristic line. Since mass attenuation coefficients are not well known between the gold M_I and M_{IV} absorption edges and very little data exist between the M_{IV} and M_V edges, and since published values vary as much as 50%, we found it necessary to verify these values experimentally.

Procedure

Thirty-three characteristic radiations between Lβ₁ antimony (3.08 λ) and Mα iridium (6.26 λ), were used. These were generated from the pure element standards at 20 keV and ~30 nA specimen current with gold foils (varying in thickness from 5,000 to 12,000 Å) used as absorbers.

Gold foils of nominal thickness were made at the Lawrence Livermore Laboratory using vapor deposition techniques. After weighing, they were examined by scanning electron microscopy to establish surface morphology. Less than half the foils produced were considered satisfactory for our experiment because of the presence of surface defects and voids.

Acceptable foils were then mounted on an adapter ring. The adapter was spring loaded to an arm extending through one of the ports on the microprobe. This configuration made it relatively easy to move the foil between the x-ray source

and the electron trap on the spectrometer. When securely
in place, the adapter fits over the electron trap. To mini-
mize drift effects, three 10 s counts were taken for each
characteristic radiation of interest with the foil removed,
and immediately following, another three 10 s counts were
taken with the foil in place. This was repeated five times
for each characteristic radiation of interest. To minimize
possible effects of the electron beam on the pure element
standards, and hence the x-ray source, the specimen stage
was translated ~2 μm following each 10 s counting period.
　　　Foil thicknesses were verified experimentally by
measuring the absorption of each of twelve different charac-
teristic radiations of nine different elements below the M_I
absorption edge and above the M_V absorption edge. Foil thick-
nesses were then calculated by the equation

$$I = I_o \, e^{-\mu\rho x}$$

using the average μ of Heinrich,[1] Frazer,[2] and Bracewell[3]
for each of these characteristic radiations.
　　　The measured thicknesses were then used to calculate
the mass attenuation coefficients for four foils of signifi-
cantly different thickness. These (μ) values were then
averaged for each radiation and are listed in Table 1. Also
listed in Table 1 are appropriate σ values for each radiation
as calculated from the (μ) values of each foil. The σ were
calculated using the expression

$$\sigma = \sqrt{\frac{\sum_{i=1}^{n} [\mu - \overline{\mu}]_i^2}{n - 1}}$$

　　　Figures 1 and 2 illustrate the scatter of μ values pub-
lished by different authors along with the values obtained by
this experimental method.

Table 1. Summary of derived mass attenuation coefficients.

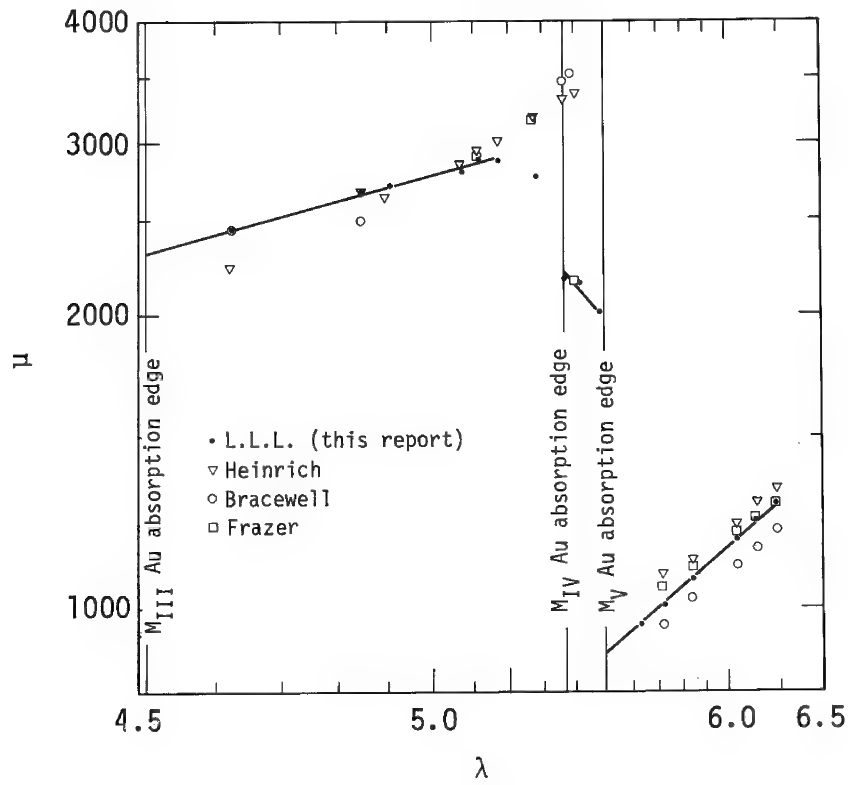|	λ (Ref. 4)	μ	σ
$\mu(Au,SbL\beta_1)$	3.23	1422	20
$\mu(Au,TeL\alpha)$	3.29	1469	38
$\mu(Au,SnL\beta_1)$	3.38	1589	14
$\mu(Au,SbL\alpha)$	3.44	1628	34
$\mu(Au,InL\beta_1)$	3.56	1788	10
$\mu(Au,SnL\alpha)$	3.60	1819	34
Au M_I absorption edge	3.60_9		
$\mu(Au,UM\beta)$	3.72	1898	11
$\mu(Au,CdL\beta_1)$	3.74	1926	8
$\mu(Au,InL\alpha)$	3.77	1964	10
$\mu(Au,UM\alpha)$	3.91	2113	9
$\mu(Au,AgL\beta_1)$	3.94	2106	8
Au M_{II} absorption edge	3.92_8		
$\mu(Au,ThM\beta)$	3.94	2070	20
$\mu(Au,CdL\alpha)$	3.96	2091	17
$\mu(Au,ThM\alpha)$	4.14	2268	18
$\mu(Au,AgL\alpha)$	4.15	2304	17
$\mu(Au,PdL\alpha)$	4.37	2550	27
Au M_{III} absorption edge	4.50_9		
$\mu(Au,RuL\beta_1)$	4.62	2445	27
$\mu(Au,RuL\beta)$	4.85	2676	25
$\mu(Au,BiM\beta)$	4.91	2711	14
$\mu(Au,BiM\alpha)$	5.12	2887	30
$\mu(Au,MoL\beta_1)$	5.18	2895	22
$\mu(Au,PbM\alpha)$	5.29	2788	16
$\mu(Au,SK\alpha)$	5.37	2187	30
Au M_{IV} absorption edge	5.36_3		
$\mu(Au,MoL\alpha)$	5.42	2171	28
$\mu(Au,HgM\beta)$	5.43	2172	16
$\mu(Au,NbL\beta_1)$	5.49	2009	30
Au M_V absorption edge	5.57_2		
$\mu(Au,AuM\beta)$	5.62	964	21
$\mu(Au,NbL\alpha)$	5.73	1008	11
$\mu(Au,AuM\alpha)$	5.84	1071	21
$\mu(Au,PtM\alpha)$	6.05	1168	27
$\mu(Au,PK\alpha)$	6.16	1227	30
$\mu(Au,IrM\alpha)$	6.26	1275	26
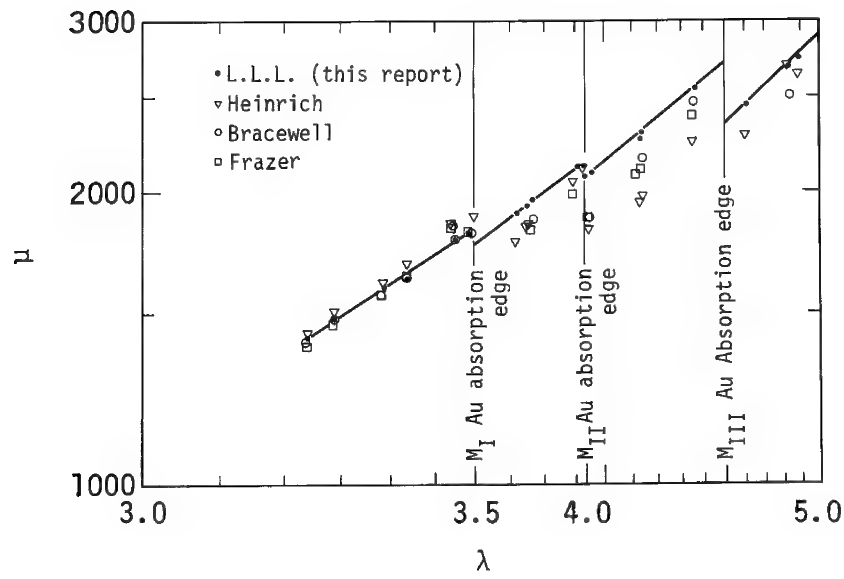
Fig. 1. Scatter of μ values from λ = 3 to λ = 5.

Fig. 2. Scatter of μ values from λ = 4.5 to λ = 6.5.

19E

Acknowledgments

The author wishes to thank Jack Johnson for his very helpful contributions and advice, Charles Hugenberger for designing and fabricating the necessary hardware, and Perry Studt for statistical evaluation of the data.

This work was performed under the auspices of the U.S. Atomic Energy Commission.

REFERENCES

1. T.D. McKinley, K.F.J. Heinrich, and D.B. Wittry, Eds., *X-Ray Absorption Uncertainty, The Electron Microprobe* (John Wiley and Sons, Inc., New York, 1966).
2. J. Frazer, *A Computer Fit to Mass Absorption Coefficient Data*, Institute for the Study of Matter, University of California, La Jolla, SIO Ref. No. 67-29 (1967).
3. B.L. Bracewell and W.J. Veigele, "Tables of X-Ray Mass Attenuation Coefficients for 87 Elements at Selected Wavelengths" in E.L. Grove and A.J. Perkins, Eds., *Developments in Applied Spectroscopy*, Vol. 9, p. 357-400 Plenum Press (1971).
4. J.A. Bearden, *X-Ray Wavelengths*, Johns Hopkins University, NYO-10586 (1968).

SIMULTANEOUS MICROPROBE ANALYSIS OF SILICATES FOR NINE ELEMENTS USING WAVELENGTH DISPERSIVE SYSTEM

E. Jarosewich, C. Obermeyer and J. Nelen
Department of Mineral Sciences
Smithsonian Institution
Washington, D.C. 20560

The microprobe analysis of silicates is an established and well-developed technique. Recent advances in this field center primarily on automation and non-dispersive techniques, both particularly useful for complete analysis of a single spot. Each of these techniques is favored by different workers depending on the application, available hardware and available funds, and in addition, to personal preference. The automated system is favored by many as being more precise, the disadvantage being that longer dwelling on the same spot may degrade the sample; also total time for analysis could be from 2-6 minutes. The non-dispersive system, with its advantage of simultaneous analysis, requires careful handling of data and need of stripping programs because of higher background counts and still somewhat limited resolution, especially in higher wavelength regions.

The system used in our laboratory for simultaneous analysis of 9 elements is a rather simple and rapid one. There are six fixed spectrometers: Si, Al, Fe, Mg, Ca and K and three scanning spectrometers. The latter are used for Na, Ti and Mn or P. This arrangement allows simultaneous analysis of 9 elements in a single counting period of 10 or 20 seconds. A pulse height curve is generated for each element and an appropriate baseline and window permanently set. This permits optimization of peak to background count, without the need for the user to adjust these when going from one element to another. The background is very low, typically 0.5-1 c/s for Al, Mg, Ca and K when using quartz as the standard.

This arrangement gives a complete and rapid analysis, particularly for the samples which degrade under the beam, and is especially useful in zoning studies. The print-out is arranged in the conventional form of a chemical analysis of silicates: SiO_2, Al_2O_3, FeO, MgO, CaO, K_2O, Na_2O, TiO_2 and MnO or P_2O_5, giving the user an immediate overview in chemical variation from one element to another.

A COMPARISON OF SOME QUANTITATIVE TECHNIQUES FOR
TREATING ENERGY   DISPERSIVE X-RAY SPECTRA.

Peter J. Statham

Department of Mineralogy and Petrology, University

of Cambridge.

The energy-dispersive X-ray spectrum is subject to defects
which arise from the solid-state detector and the processing electronics.
However, with adequate collimation of the X-rays, a pile-up rejector
and high integrity electronics, the major defects can be corrected by
straight-forward computation on the digitised spectrum. The problem is
thus reduced to the mathematical deconvolution of a number of gaussian
peaks which lie upon the continuous-radiation background with super-
imposed statistical channel-to-channel fluctuations or noise. It is
fundamental to any method of data reduction that the quality of the
result depends on the amount of relevant information used by the technique
and the statistical accuracy of the experimental data supplied. The
only solution for poor statistical accuracy is to obtain more counts.
There are several, superficially different, techniques for treating spectra
but they all implicitly use similar information. In this work comparisons
have been made between existing and some new methods of treating energy-
dispersive spectra.

Background subtraction may be accomplished by the following
procedures.

1.   Interpolation of the background beneath the peaks using linear,
quadratic or more specialised analytical curves.

2.   Extrapolation of the background beneath the peak from the low
energy side.

3.   Fourier-transform techniques involving the removal of low-
frequency components from the spectrum.

4.   Physical calculation of the background shape with empirical
adjustment and fitting to the spectrum.

5.   Use of a stored background curve obtained from an element of
medium atomic number followed by fitting.

6.   Stripping of peaks until no peaks can be detected in a search
routine. (The amount stripped off each peak will, of course, itself,
be the background-subtracted value).

All these methods use the information that the background is generally a
smooth function of energy. Method 2 uses the additional information that
the absorption-edge for a given element lies at a higher energy than its
major line but cannot be usefully applied where several overlaps occur.
Method 3 uses the increased high-frequency content of the peaks to separate
them from background but generally distorts the spectral lines because of
supression of low-frequency components which are common to both peak and background.

Absorption edges are convoluted by the same instrumental function as
the peaks and thus have a similar frequency distribution, making
separation difficult by simple aperturing in frequency space. Physical
calculation, as in Method 4, has the advantage of introducing information
on absorption edges and detailed information on the shape especially at
low energies. However, there are uncertainties in the theory and,
although the method is possibly the most powerful, a complete treatment
involving convolution of the calculated bremstrahlung curve with the
correct instrumental function, followed by fitting to the spectrum, is
very extravagant on corespace and computing time for a small dedicated
computer. Use of a stored background curve as in 5 can supply useful
information at low energies in the region of appreciable absorption by
the beryllium window but no account is taken of absorption edges. The
stripping technique in 6 uses the additional information that the peaks
are gaussian in shape and the accurate centroid and width of each curve.
With suitable choice of peak-detection criterion, peak heights can
generally be accurately ascertained even in the presence of absorption
edges. However, in this technique it is very important to use the correct
parameters for each peak and the electronic performance must necessarily
be highly predictable.

The problem of overlapping peaks can be approached as follows.

1.   Integrate peaks over a fixed number of channels and perform
theoretical or empirical calibration for overlaps.

2.   Use linear or non-linear regression techniques to fit the data
to the sum of a number of analytical curves, one for each peak.

3.   Use matrix or Fourier techniques to enhance the resolution until
peaks are separated.

4.   Strip peaks piece-wise until all peaks are removed.

5.   Strip minor peaks (e.g. K_β) by using the major peak height
(K_α) and a scaling factor (or using any suitable combination of related
peaks).

Methods 1 to 4 are all theoretically restricted in that they cannot resolve
accurately peaks which are closer than a limit determined by the peak width
and the number of sample points. Method 1 is worst in this respect as it
effectively provides only one sample point for each peak but is essentially
just a special case of Method 2 which is better because it includes more
information concerning the peak shape. If the instrumental function is
accurately known (in this case a gaussian) it is possible to reverse the
convolution process by suitable weighting in Fourier frequency space as in
Method 3. The problem is, however, ill-conditioned and constraints are
necessary in the presence of statistical noise but it is possible to obtain
about 70% improvement in resolution with low distortion. This improvement
is only possible because knowledge of the instrumental function has been
utilised. The complete deconvolution to single line intensities is made
possible by including information concerning the peak position and width,
as well as shape. This is provided in Method 4 which has an advantage over
2 in that a matrix-inversion package is not required and it can be incorporated

simultaneously with background subtraction Method 6. When peaks are too close together (e.g. TiK_β /VK_α), Method 5 can be employed provided a related line is available. However, such stripping must be incorporated in conjunction with the X-ray intensity correction procedure to take account of differential absorption in the specimen of the X-rays of major and minor lines. The accuracy of the stripping ratio is critical in the case of severe overlap since there is then no indication when stripping has been carried out incorrectly.

In an automated quantitative system it is desirable to minimise subjective operator intervention. Ideally, therefore, the combination of techniques incorporated in the data-processing program will provide for the analysis of the widest possible range of sample compositions. The remaining demands made upon an unskilled operator are then essentially governed by the nature of the equipment used. In this work a system has been developed with these aims in mind, making use of the facilities afforded by the Harwell "Highspec" analyser interfaced to a D.G.C. Nova 1220 computer.

QUANTITATIVE MICROANALYSIS WITH MINIMUM
PURE ELEMENT STANDARDS

John C. Russ
EDAX Laboratories
Raleigh, North Carolina   27612

INTRODUCTION

The conventional starting point for quantitative microanalysis is the determination of the K-ratio for each element by measuring the x-ray intensity of the element on the unknown and on a standard, commonly a pure element or oxide. This value is then used as the input to a ZAF or other type of correction calculation from which emerges elemental concentrations. The advantage of the use of standards is that it automatically corrects for a variety of instrumental effects, the most important being the total efficiency of the crystal spectrometer which is hard to reproduce from measurement to measurement, and in addition varies from instrument to instrument. The disadvantages include the inconvenience of obtaining all of the needed standards, the time required to make all of the measurements, and the need for instrument stability during that time.

The energy-dispersive x-ray analyzer has now come into very broad usage-- numerically exceeding wavelength-dispersive units by about 4 to 1--and is being increasingly used for quantitative as well as qualitative work because of the obvious advantages of speed and simultaneous detection of all elements. To date, however, the programs used for quantitative correction have been the classical ones, with a method identical to that for wavelength-dispersive spectrometers -- i.e., the use of standards for each element. The energy-dispersive spectrometer measures and counts the x-rays from each of the elements present simultaneously, and it is the potential for rapid analysis that makes the time needed to measure standards particularly objectionable. Since the energy-dispersive spectrometer has a constant total spectrometer efficiency that can be expressed as a simple function of energy, we have devised a method to eliminate the requirement for elemental standards and calculate relative K values directly.

Spectrometer Efficiency

The lithium-drifted silicon semiconductor detector is 100% efficient over a considerable part of the useful energy range. At high x-ray energies, there is an increasing probability that the photon may penetrate through the detector without being stopped, and at low energies the photon may be absorbed in the beryllium entrance window or the "dead" silicon on the front of the detector. There is also a possibility that a silicon x-ray may escape the detector volume causing an escape peak and thus reducing the measured peak height; this possibility is greatest for low energy x-rays since they interact with the detector near its front surface.

The overall shape of the spectrometer efficiency vs. energy curve thus is basically flat with drop-offs at high and low energies which are simple exponentials, as would be expected for a process involving x-ray absorption, and can be fit with high accuracy to an expression of the form

$$T = e^{-(C_1/E^{2.8})} \left\{ 1 - e^{-(C_2/E^{2.8})} \right\}$$

where the constants describe the window thickness and detector thickness of the spectrometer being used. The dependency on $E^{-2.8}$ models the dependence of the mass absorption coefficients on x-ray energy.

Relative Elemental Intensities

The relative intensities of x-rays from two different pure elements depends on the relative probabilities that electrons of a given energy excite the shell of interest, that x-ray photons are emitted, that they escape the surface without absorption, and that they are detected. This can be expressed by an equation of the form

$$\frac{P_1}{P_2} = \frac{R_1}{R_2} \frac{(U_1-1)^{5/3}}{(U_2-1)^{5/3}} \frac{W_1}{W_2} \frac{L_1}{L_2} \frac{A_2}{A_1} \frac{F_1(\chi)}{F_2(\chi)} \frac{T_1}{T_2}$$

where

R is the effective current factor
U is the overvoltage ratio E_0/E_c
W is the fluorescence yield for the shell being used
    for analysis
L is the relative intensity of the line being used
A is the atomic weight
$F(\chi)$ is the absorption function evaluated for self
    absorption of x-rays, with
    $\chi = \mu_{self} \cos \psi / \sin \theta$
T is the spectrometer efficiency

Experimental Data

We have measured intensities from a variety of pure elemental standards for K, L, and M lines, various accelerating voltages and geometries (electron incidence and x-ray takeoff angles). Figure 1 shows a representative set of data (26.4 kV, 40° specimen tilt, 48° takeoff angle) with the intensities all normalized to the Fe Kα intensity. The agreement between the predicted and actual values is evident.
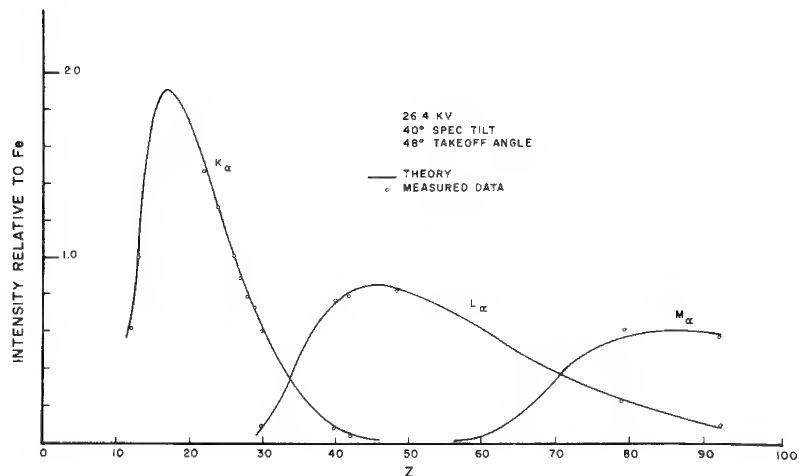
Figure 1.   Agreement between measured intensities of
            various elements (expressed as relative
            to iron Kα) and theory.

Routine Quantitative Analysis

Since the model for predicted pure element intensities is readily cal-
culated for any given geometry and accelerating voltage, it is only
necessary to measure the intensity from some convenient element. We
customarily use Al Kα for low voltage analysis of minerals, Ni Kα for
most routine work with moderate accelerating voltages, and occasionally
Mo Kα or Lα or Au Lα or Mα when appropriate. The net intensities from
each element are then converted to K values and input to a conventional
ZAF routine, giving final accuracies similar to the conventional method,
but with a great savings in time.

QUANTITATIVE ANALYSIS OF SULPHIDES AND SULPHOSALTS

USING AN ENERGY DISPERSIVE SPECTROMETER

M.I. Corlett and Margo McDonald
Department of Geological Sciences,
Queen's University,
Kingston, Ontario,
Canada.

Some interesting quantitative analytical work using energy-dispersive spectrometry has been done by summing intensities over a few channels immediately surrounding a characteristic emission peak channel for each element in the spectrum. Background values are obtained by interpolation between peak-free regions and by corrections for contributions by neighbouring peaks to the total measured intensities in the channels used for the analysis. This method (see, for instance, Plant and LaChance (1)) has several advantages:

1. simple spectra can be rapidly resolved, given a limited chemical system such as the common rock-forming silicates;

2. since only small parts of the emission spectrum are used, the apparent concentrations obtained can be corrected for absorption, fluorescence, and atomic number effects using standard ZAF programs developed for wavelength-dispersive analysis using the same parts of the spectrum.

There are disadvantages to such methods, however. The intensities, and thus the precisions, are necessarily rather low, since only a portion of the spectrum is used in the analysis. Also, the accuracy of the method is inherently dependent on electronic stability, since any drift will shift the distribution of the emission spectrum from channel to channel. If no internal standard is used, such a shift will be seen as a change in concentration. In addition, the problems of background measurement, soluble in the relatively simple common rock-forming silicate spectrum, seem insoluble for the complex sulphide and sulphosalt spectra. Finally, only spectra with known components may be analysed with confidence; any additional component likely necessitates a revision of the background correction for at least part of the spectrum.

A multiple least-squares fitting technique (program ML) developed by F.H. Schamber (2) overcomes these disadvantages. First, complete spectra of up to six standards within any given region of interest may be fitted to the unknown spectrum. Since all of the emission spectrum in this region is used, the intensities obtained (given the same operating conditions as above) are increased. Second, because the fit is made only in peak regions it is not background-sensitive; simplistically, background is ignored, and "peak above background" for the standard is fitted to "peak above background for the unknown. Third, a chi-squared value is computed for the fit within the region

of interest. This value, a measure of "goodness of fit", is extremely
sensitive to (a) peak shift due to electronic drift; (b) spectral line
broadening due to changes in detector resolution; and (c) the presence of
any foreign spectral line in the region of interest.

Various problems were anticipated using energy-dispersive
techniques. Basically the difficulties seemed to centre about three points:

1. the variable differential absorption of α and β* spectral
lines due to interposed absorption edges of other elements.
Since the complete K, L, or M spectrum of an element may
be used in analyses based on multiple least-squares fitting,
a change in the α:β ratios may introduce a significant
error in the apparent concentration. For example, the FeK
absorption edge lies between Co Kα and CoKβ emission lines;
the emission ratio CoKα:CoKβ is thus a function of, among
other things, the iron concentration. This case – an absorption
edge falling between pairs of spectral lines – is the worst
possible one; if the effect of this on the α:β ratio is
negligible, then the effect of the proximity of an absorption
edge may also be ignored.

2. the resolution of these complex spectra;

3. the obtaining of interference-free standard spectra.

Each of these difficulties has been studied in our laboratory,
and we believe that they have been resolved.

A. Variable differential absorption

The emission lines and absorption edges of the elements occurring
in sulphosalts are shown in Fig. 1. Several interferences between major
absorption edges and principal emission lines can be seen; these are listed
in Table 1.

The magnitude of the effect of these interferences was checked by
calculating the absorption correction for the α and β emission lines of
element E (the emitter), given a matrix of (a) 99.9%A (the absorber), 0.1%E;
(b) 50.0%A, 50.0%E; and (c) 0.1%A, 99.9%E. These calculations were performed
using a large, general-purpose ZAF correction program, a distant relative of
Frazer, Fitzgerald and Reid's (3) program EMX2. Results of these calculations

---

*γ lines have not been considered; their intensities are always low compared
to α and β lines, and thus changes in their absorption are of little
significance.

are also given in Table 1.

The effect of the interposed absorption edge can be seen in each case; the ratio $\alpha:\beta$ decreases as the composition ranges toward pure E. However, the relative generation of α and β radiation affects the importance of variable differential absorption for the analysis. For example, cobalt will show a change (predicted from the $f(\chi)$ values in Table 1) in the detected $\alpha:\beta$ ratio of roughly 5%. But since the $\alpha:\beta$ ratio is high, and it is the emission of β radiation that is more strongly affected by the change in iron content of the material, this change results in less than a 1% relative decrease of cobalt emission in nearly pure iron. Thus for computational purposes the cobalt radiation can be considered as being monochromatic, with a hypothetical blended wavelength reflecting the $\alpha:\beta$ ratio.

In contrast, bismuth and tellurium have not only a larger change in the detected $\alpha:\beta$ ratio but also a lower $\alpha:\beta$ ratio. Significant analytical discrepancies could therefore be expected if a single blended wavelength, calculated from emission ratios for the pure element, were used in ZAF calculations. Two alternatives are suggested. First, the regions in which the fits are performed could be narrowed to exclude the β radiation of these two elements. The wavelength used in computations would then be that for α radiation. Second, the $\alpha:\beta$ ratio could be included as a variable in the correction programs designed for energy-dispersive data; its value would depend on the concentrations of the interfering elements.

Fortunately, for the immediate problem being investigated (a copper-mercury sulphantimonide occurrence), the elements bismuth, tellurium, and silenium could be ignored; as an additional desirable side effect, the memory space needed for constants in the mini-computer used in on-line computation was thus cut by 36%.

Two additional points should be noted. First, this attenuation of $\alpha:\beta$ ratios might be more crucial if one were using only a few peak channels for analysis and were attempting to make a background correction on a second peak, near the β line of the first peak, by subtracting a fixed proportion of the first measured peak. Second, for elements with very high $\alpha:\beta$ ratios the different constants for β radiation can be ignored and all the measured radiation treated as α radiation. In such cases simple standard ZAF corrections, designed for wavelength-dispersive spectrometry, may be applied to the apparent concentrations.

B. Resolution of complex spectra

The program ML has proved to be a powerful tool in such resolution; reasonable analyses have been obtained from such difficult spectra as PbS and

HgS (compare Figure 1 and Table 3).

C. Reference standards

The relatively poor resolution of energy-dispersive spectrometers
compared to wavelength-dispersive spectrometers means that it is difficult
to obtain a reference peak or spectrum which is free from interference by
other peaks. Wherever possible metal standards have been used in these
analyses. The exceptions are mercury, lead and sulphur standards. For
these elements natural montroydite, HgO, natural witherite, $PbCO_3$, and
synthetic pyrrhotite, Arnold B (60.4% Fe, 39.6%S) were used because of
their spectral purity in the regions containing HgM, PbM and SK emission
lines. The natural minerals are unanalysed; a study of analyses in the
literature indicates that they are always stoichiometric and that they
rarely contain significant impurities. The latter observation is supported
by microprobe studies of the standards chosen.

Analytical considerations

Reference spectra were collected over a short period of time
(about 1 1/2 hours) and stored on a magnetic tape. Copper was used as an
internal standard to monitor for drift during standard spectra collection.
Specimens were then analysed at leisure and compared, using a series of
multiple least squares fits, with the reference spectra. Analytical
conditions are given in Table 2. The proportion of each element's reference
spectrum needed to obtain the best possible fit to the unknown spectrum is
equivalent to that element's "apparent concentration", in wavelength-
dispersive analysis terminology, and can be processed using normal ZAF
programs, provided they are modified to take into account the mixed character
of the spectra used in analysis (i.e. $\alpha+\beta$, rather than α radiation). Such
a modified program is SULPHOCORR, adapted from a larger general wavelength-
dispersive analytical program to handle energy-dispersive analysis of
sulphosalts. This program is now being converted to run as a magnetic
tape-stored routine for on-line analysis.

One attraction of the tape cassette system is the possibility of
storage of reference and specimen data for comparison at any time. This
powerful feature requires very stringent control of operating conditions.
To check this we standardize each day on copper metal making sure that Cu Lα
and Cu Kα are being detected in the same channels as they were when the
reference standards were analysed (this is done by routine ML, checking
the goodness of fit by monitoring χ^2 values). Copper is used because it has
peaks near the ends of the analysed spectrum. This provides a rapid check
on the gain and zero settings of the amplifier and ADC respectively. In
addition the relative peak areas of Cu Lα and Cu Kα are monitored as a
check on high voltage stability; if necessary, the high voltage is adjusted

to obtain the same Lα/Kα ratios that were obtained when the reference
standards were analysed. Copper metal is further used as an internal
standard to reference back to standard conditions; for example, if an
analysis during a run gives 110% copper in copper metal, then all the
results for the unknown spectra must be divided by 1.100 to give "apparent
concentrations".

With these precautions we find that we can operate for weeks
without re-collecting standard reference data.

Analytical results

A miscellaneous group of sulphide and sulphosalt minerals have
been analysed to test these operating procedures. These minerals cover
a wide compositional range and thus provide a good test of the analytical
method.

It was found after preliminary testing that spurious Hg and Pb
values were being recorded. Presumably these readings are due to the
very irregular background in this region of interest and to the low
intensities of the reference spectra. To confirm this, the specimens and
mercury and lead standards were reanalysed at 25 KV, and the spectra
investigated in the region which contains the Hg L and PB L spectra. If
no mercury or lead was found by analysis in this spectral region, they
were left out of the multiple least-squares fits from 0 to 10 KeV.

Analytical results are given in Table 3. They show good "totals",
a common measure of the success of a spectrochemical analysis. Reduction
to mineral formulae gives a second check on the accuracy of an analysis.
With one exception, cinnabar, the deviation from ideal formulae is less
than 7%. This compares favourably with deviations calculated for wet
chemical analyses in the literature; see, for example, Deer, Howie and
Zussman (4). In part these deviations may represent real departures from
stoichiometric compositions. The larger deviation in the cinnabar analysis
may possibly be due to uncertainties in the ZAF corrections themselves.

REFERENCES

(1) G. Plant and G. LaChance, "Quantitative electron microprobe analysis
           using an energy-dispersive spectrometer". Proc. Eighth
           Nat. Conf. on Electron Probe Analysis, New Orleans,
           Paper 13 (1973).

(2) F.H. Schamber, "A new technique for deconvolution of complex X-ray energy
           spectra". Proc. Eighth Nat. Conf. on Electron Probe Analysis,
           New Orleans, Paper 85A (1973).

(3) J. Frazer, R.W. Fitzgerald, and A.M. Reid, "Computer programs EMX and
           EMX2 for electron microprobe data processing". Scripps
           Institute of Oceanography Report 66-14 (1966).

(4) W.A. Deer, R.A. Howie, and J. Zussman, "Rock-forming minerals. Volume 5:
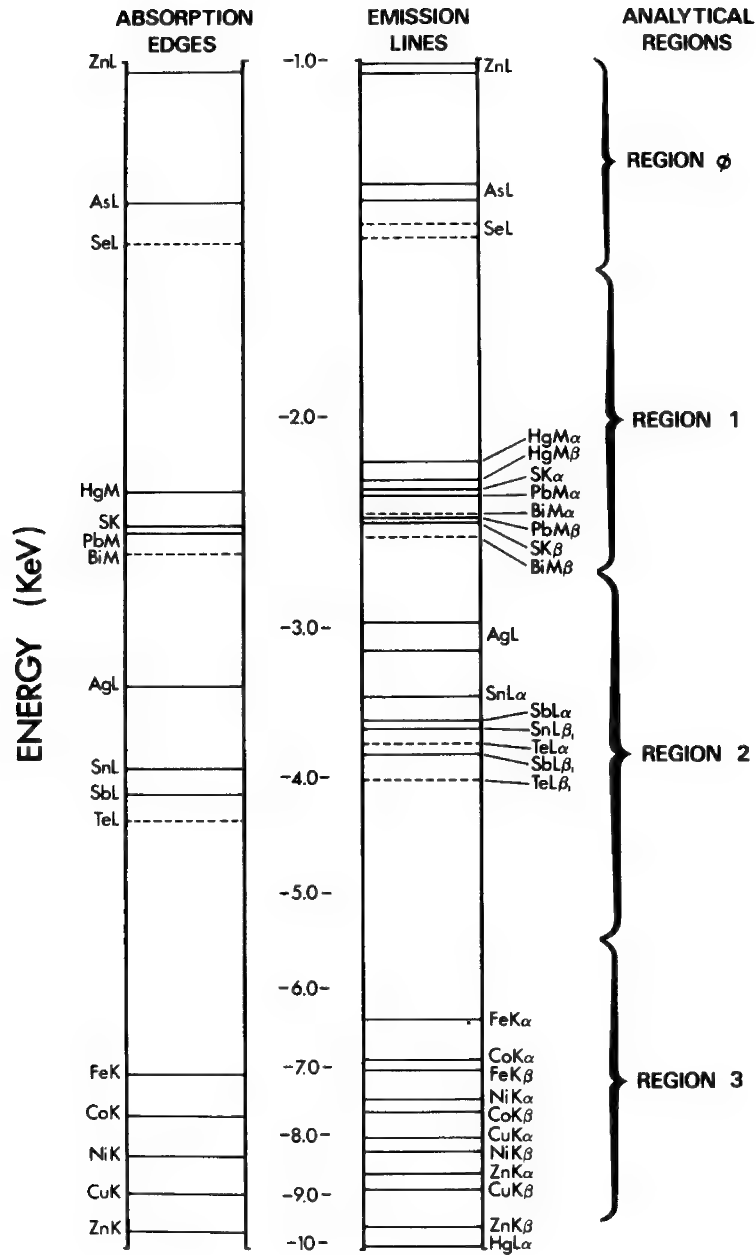   Non-silicates". J. Wiley and Sons, New York (1962).

Figure 1. Positions of major absorption edges and emission lines, 0 to 10 KeV range. The "regions of interest" within which multiple least-squares fits were made are shown at the right.

TABLE 1

Absorption edge - emission line pairs which may give rise to variable differential absorption. A and E refer to absorber and emitter respectively, and are used in the text discussion of variable differential absorption. Calculations for E_O = 15 KeV.

A	Edge	KeV	E	Line	KeV	approximate α:β ratio	$f(\chi)$ (a) 99.9%A, 0.1%E	$f(\chi)$ (b) 50.0%A, 50.0%E	$f(\chi)$ (c) 0.1%A, 99.9%E
S	K	2.470	Bi	Mα / Mβ	2.421 / 2.526	1	.9864 / .6293	.9645 / .7049	.9727 / .8449
Pb	M_V	2.502	Bi	Mα / Mβ	2.421 / 2.526	1	.9433 / .6998	.9430 / .7660	.9419 / .8451
Sn	L_{III}	3.927	Te	Lα / Lβ	3.768 / 4.029	2	.9301 / .8377	.9259 / .8830	.9217 / .9332
Fe	K	7.109	Co	Kα / Kβ$_1$	6.922 / 7.648	7	.9900 / .9396	.9894 / .9649	.9888 / .9914
Co	K	7.707	Ni	Kα / Kβ$_1$	7.473 / 8.265	7	.9915 / .9497	.9911 / .9709	.9906 / .9928
Ni	K	8.329	Cu	Kα / Kβ$_1$	8.040 / 8.906	7	.9929 / .9586	.9925 / .9760	.9921 / .9940
Cu	K	8.978	Zn	Kα / Kβ$_1$	8.627 / 9.566	8	.9941 / .9662	.9938 / .9806	.9935 / .9951

TABLE 2

Analytical conditions for sulphosalt analyses. $E_O = 15$ Kev, 100 µA
emission current, ~1.5 nanoamperes specimen current. Cu metal used as
internal standard. 200 seconds counting time.

Element	Standard	Region of interest (KeV)	Other spectra used in ML fit
As	As metal	1.000 - 1.510	Co, Ni, Cu, Zn
Hg	HgO	1.510 - 2.700	Pb, S, Ag, Sn
Pb	$PbCO_3$	1.510 - 2.700	Hg, S, Ag, Sn
S	Arnold B	1.510 - 2.700	Hg, Pb, Ag, Sn
Ag	Ag metal	2.700 - 5.500	Sn, Sb, Hg, Pb
Sn	Sn metal	2.700 - 5.500	Ag, Sb, Hg, Pb
Sb	Sb metal	2.700 - 5.500	Ag, Sn, Hg, Pb
Fe	Fe metal	5.500 - 9.500	Co, Ni, Cu, Zn
Co	Co metal	5.500 - 9.500	Fe, Ni, Cu, Zn
Ni	Ni metal	5.500 - 9.500	Fe, Co, Cu, Zn
Cu	Cu metal	5.500 - 9.500	Fe, Co, Ni, Zn
Zn	Zn metal	5.500 - 9.500	Fe, Co, Ni, Cu

TABLE 3

Energy-dispersive analysis of sulphides and sulphosalts

	1	2	3	4	5	6	7	8	9	10	11	12	13
S	53.95	35.40	40.89	.30	.07	18.21	-	24.51	22.19	12.23	14.20	33.58	18.78
As	.10	-	.16	77.45	54.06	47.45	71.22	2.03	44.57	-	-	-	1.82
Sb	.05	-	-	.33	3.83	.34	.40	26.49	.12	.01	.26	-	22.66
Fe	44.93	30.86	59.40	.34	-	.21	.30	5.46	34.73	.41	.02	.29	-
Co	-	-	.12	19.61	.20	29.23	18.61	.19	-	.09	.21	-	-
Ni	-	-	.35	.47	43.26	5.39	10.13	.29	-	.01	.17	.05	.26
Cu	-	33.61	-	.10	.03	.03	.07	33.46	-	.42	.04	.02	.25
Zn	.04	-	.15	-	.33	-	-	-	-	.01	.54	64.87	.44
Ag	-	-	.18	.18	-	1.55	.23	2.58	-	.10	-	-	-
Sn	-	-	-	.43	.37	-	-	-	-	.55	-	-	-
Hg	-	-	-	-	-	-	-	4.81	-	87.49	-	-	-
Pb	-	-	-	-	-	-	-	-	-	-	83.12	-	55.92
Total	99.08	99.88	101.28	99.22	102.16	102.42	100.97	99.83	101.61	101.32	98.57	99.01	100.12

No.	Mineral	Ideal composition	Formula basis	Mineral formula
1.	Pyrite	FeS_2	S = 2.00	$Fe_{.95}S_{2.00}$
2.	Chalcopyrite	$CuFeS_2$	S = 2.00	$Cu_{.96}Fe_{1.00}S_{2.00}$
3.	Pyrrhotite	$Fe_{1-x}S$	S = 1.00	$Fe_{.83}S_{1.00}$
4.	Skutterudite	$CoAs_{3-x}$	$\Sigma Co = 1.00$	$(Co_{.94}Ni_{.02}Ag_{.01}Cu_{.01})_{1.01}(As_{2.91}S_{.03}Sb_{.01})_{2.95}$
5.	Niccolite	$NiAs$	$\Sigma As = 1.00$	$(Ni_{.98}Zn_{.01})_{.99}(As_{.96}Sb_{.04})_{1.00}$
6.	Cobaltite	$CoAsS$	$\Sigma Co = 1.00$	$(Co_{.82}Ni_{.15}Ag_{.02}Fe_{.01})_{1.00}As_{1.04}S_{.94}$
7.	Safflorite	$CoAs_2$	$\Sigma As = 2.00$	$(Co_{.66}Ni_{.36}Ag_{.01})_{1.03}(As_{1.99}Sb_{.01})_{2.00}$
8.	Tetrahedrite	$Cu_{12}As_4S_{13}$	S =13.00	$(Cu_{8.95}Fe_{1.66}Hg_{.41}Co_{.05}Ni_{.08})_{11.56}(As_{3.70}Sb_{.46})_{4.16}S_{13.00}$
9.	Arsenopyrite	$FeAsS$	Fe = 1.00	$Fe_{1.00}As_{.96}S_{1.11}$
10.	Cinnabar	HgS	S = 1.00	$(Hg_{1.14}Sn_{.01}Fe_{.02}Cu_{.02})_{1.19}S_{1.00}$
11.	Galena	PbS	S = 1.00	$(Pb_{.90}Co_{.01}Ni_{.01}Zn_{.02})_{.94}S_{1.00}$
12.	Sphalerite	ZnS	S = 1.00	$Zn_{.95}S_{1.00}$
13.	Boulangerite	$Pb_5Sb_6S_{11}$	S =11.00	$(Pb_{5.07}Ni_{.08}Cu_{.08}Zn_{.13})_{5.36}(Sb_{3.49}As)_{3.94}S_{11.00}$

ABSTRACT

COMPREHENSIVE QUALITATIVE AND QUANTITATIVE
ANALYSIS OF ENERGY DISPERSIVE X-RAY SPECTRA

T. D. Kirkendall
Communications Satellite Corporation
COMSAT Laboratories
Clarksburg, Maryland 20734

This paper describes a new analytical program for the complete qualitative and quantitative analysis of energy dispersive X-ray spectra generated either by electron or X-ray excitation. The spectra are generated by a unique hardware system, previously described in part,[1] consisting of an automated electron probe using a PDP-8 mini-computer which may also be configured as a 1000 to 4000 channel pulse height analyzer. Figure 1 diagrams the system. Under program control at the PDP-8, X-ray spectra may be accumulated in the computer memory from a lithium drifted silicon X-ray detector mounted either on an electron probe or on an X-ray excited energy dispersive spectrometer. The spectra may then be transmitted via a direct high speed communications line to a dataset on disc at the in-house IBM 360/65 computer. While the PDP-8 is collecting the next set of data, the qualitative and quantitative analysis of the spectra may be performed in the 360 in an interactive time sharing environment using a standard 2741 terminal.

The qualitative/quantitative pulse height analyzer (PHA) program is written in Fortran, and in this installation, shares the direct access datasets along with the PDP-8. The spectrum is introduced as a one dimensional array of measured intensities at a finite number of equally spaced energy values, typically 1024 channels of 20 eV/channel covering the energy region of 0 to 20 KeV. Each spectrum is identified by a four character alphanumeric name at the time of its transmittal to the dataset. Magnetic tape, cards or paper tape may also be used as alternative means of data input.

The performance of operations in the PHA program is controlled by a sequence of user-input commands, providing the same qualitative treatment of both X-ray and electron generated spectra up to the point when the operator desires a quantitative analysis. For the qualitative analysis, the program contains four regions of live storage for the spectra on which various functions may be performed. Several categories of commands are provided:

1. Data Handling Commands for displaying the contents of the data file, for retrieving, storing and deleting information from the file, and for printing and plotting selected data.

2. Arithmetic Commands for performing simple operations on one or more sets of data including: addition, subtraction, scaling, copying and taking absolute values.

3. Spectrum Handling Commands for smoothing, determining background and identifying peak locations in the spectrum.

4. Element Identification Commands for identifying the most probable elemental lines associated with each peak.

Smoothing of the spectra is performed by minimizing the least squared error of an approximating third-degree polynominal over 5, 7 or 9 points, at the operator's option. The background algorithm defines each local minimum as any point whose intensity is less than that of all four neighboring points and makes twelve passes through the spectrum, each time assigning an amplitide to the minima equal to the average of the adjacent amplitudes. The resulting values are passed through a low pass smoothing filter with a cut-off frequency of 0.05 cycles/channel to generate the background "spectrum."

Peak locations are determined by locating the extrema via the second derivative. Unfolding of overlapping peaks is accomplished assuming Gaussian shapes and accounting for the dependence of half width resolution on peak energy.

An example of the analysis of the NBS 1156 maraging steel
standard by X-ray fluorescence is shown in Figure 2. Figure 3
is a double plot of the smoothed spectrum, scaled 1 and 10 X.

The result of the qualitative analysis of a spectrum is
the identification of all peak locations, their net intensities
and areas and the listing of the four closest X-ray emission
lines and their deviations for each peak. This is determined by
searching a complete table of the K, L and M emission lines of
the elements. From this list the analyst, by applying his
knowledge of the sample composition, selects the elements and
lines to be analyzed quantitatively. The selected data are then
transmitted to the appropriate corrections program which is
called as a subroutine to the master PHA program. The analyst
may invoke as a subroutine either MAGIC IV[2] for the standard
ZAF corrections of electron probe data or a program using the
fundamental parameter method of Criss and Birks[3] for calcu-
lating compositions from data obtained by X-ray excitation.

Invariably, pure element standards are used for both probe
and X-ray fluorescence analysis; for consistency, their spectra
are smoothed and treated for background removal in the same
manner as those of the unknowns. The total time for a complete
qualitative and quantitative determination is typically five
minutes. Relative accuracy is virtually always within 10% for
concentrations above about 1%, using counting times on the
order of 60 to 100 seconds. The Si(Li) detector resolution of
180 eV FWHM at 5.9 KeV, in conjunction with the curve resolving
algorithm, appears to be adequate to separate K_β/K_α line inter-
ferences where the interfering elements differ in atomic number
by at least 2. Precision over the long term (several months) is
better than 5%.

This Si(Li) detector, mini/maxi-computer system offers the
analyst a convenient, reliable and efficient means of accurate

macro and micro X-ray analysis without the usual sacrifice of rewriting and cramming a large corrections program into an already overburdened laboratory computer.

ACKNOWLEDGMENTS

The author would like to thank Messrs. L. Birks, J. Criss, J. Gilfrich and D. Brown of the Naval Research Laboratory, and Messrs. J. Hannsen and W. Cook of Comsat Laboratories for their assistance.

REFERENCES

1. T. D. Kirkendall and P. F. Varadi, "An Automated Microprobe Under PDP-8 Control Using an IBM 360/65 for Program and Data Storage," Sixth National Conference on Electron Probe Analysis, July 27-30, 1971, Pittsburgh, Pennsylvania.

2. J. W. Colby, "Magic IV - A Computer Program for Quantitative Electron Microprobe Analysis," Bell Telephone Laboratories, Allentown, Pennsylvania.

3. J. W. Criss and L. S. Birks, "Calculation Methods for Fluorescent X-ray Spectrometry - Empirical Coefficients vs Fundamental Parameters," Analytical Chemistry, Vol. 40, No. 7, June 1968.
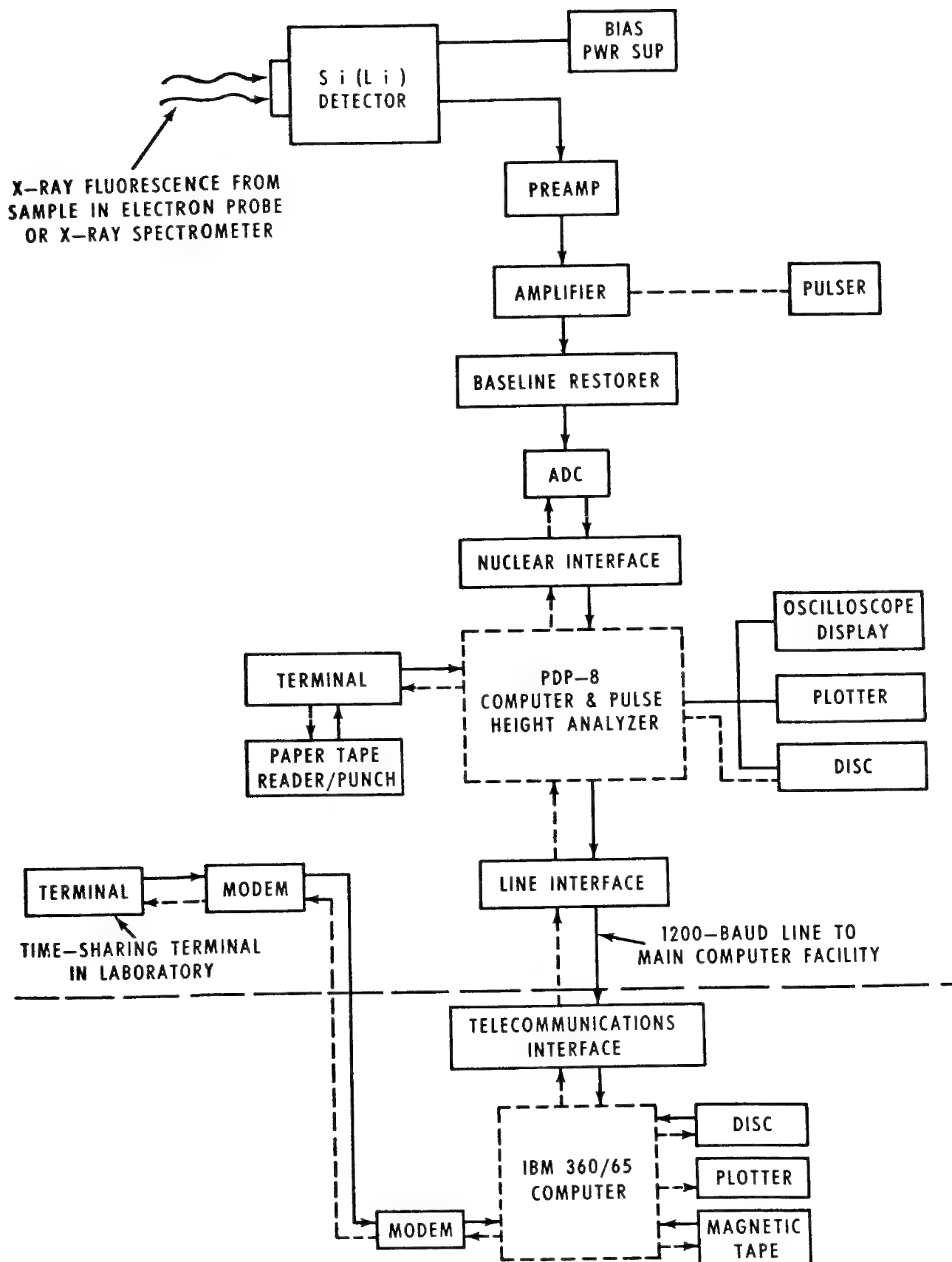
Figure 1 Multichannel Pulse Height Analysis System Using a PDP-8 for Data Collection and an IBM 360/65 for Data Reduction.

Figure 2. <u>Qualitative/quantitative analysis of N B S 1156 steel</u>.

```
get n156 1
OK
smooth 1 2 7
OK
background 2 3
NO BACKGROUND FOUND IN SPECTRUM
OK
copy 2 3
OK
scale 3 10.
OK
title nbs 1156 steel
OK
plot 2 3        (See Fig. 3.)
OK   -    PLOT COUNT=   1
peaks 2
OK   -        9 PEAKS HAVE BEEN FOUND
identify 0.02
```

NBS 1156 STEEL

PEAK IDENTIFICATION

CHANNEL	ENERGY	INTENSITY	LINE	ERROR	LINE	ERROR
320.89	6.418	3409.00	FE-KA1	0.017		
345.26	6.905	410.00	CO-KA1	-0.022		
352.02	7.040	682.00	FE-KB1	-0.015		
375.68	7.514	448.00	NI-KA1	0.038		
874.40	17.488	79.00	MO-KA1	0.016		

```
OK
confirm fe ka1 co ka1 ni ka1 mo ka1
OK
OK
OK
OK
analyze
 ENTER ELAPSED TIME IN SECONDS
50.
 ENTER INTENSITY (C/S) OF STANDARD FOR:
 FE  KA1
92.8
 CO  KA1
91.0
 NI  KA1
92.9
 MO  KA1
33.0
```

NBS 1156 STEEL

QUANTITATIVE ANALYSIS

ELEMENT	WEIGHT %	N B S ANALYSIS	
FE	68.71	69.67	(by difference)
CO	8.21	7.3	
NI	19.57	19.0	
MO	3.51	3.1	
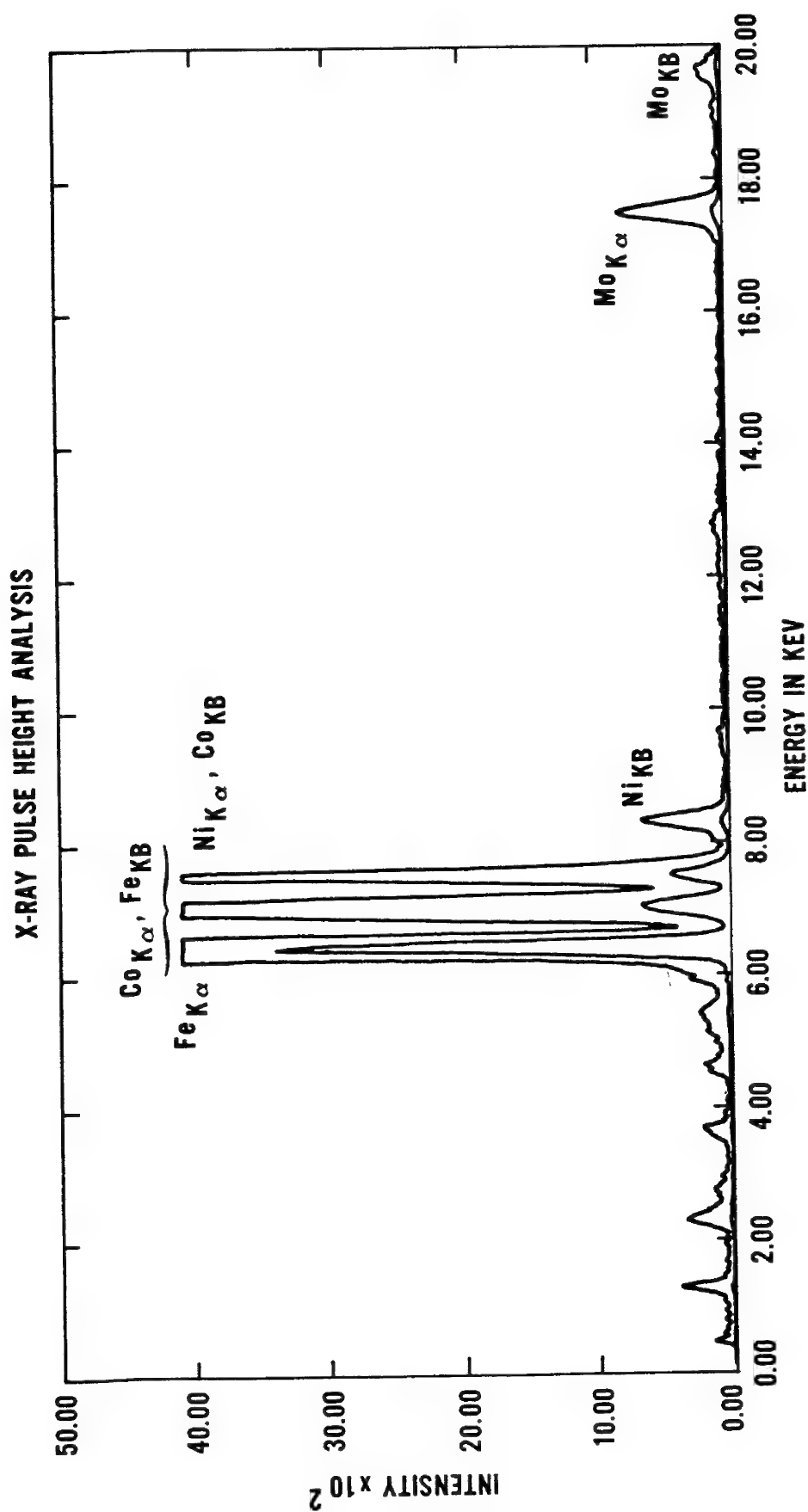
Figure 3   NBS Std. Ref. Mat. #1156 Smoothed Data, Scaled 1X, 10X

COLLIMATOR FOR ENERGY DISPERSIVE X-RAY ANALYSIS OF
RADIOACTIVE MATERIALS IN A SCANNING ELECTRON MICROSCOPE

Ursula E. Wolff
General Electric Company, Vallecitos Nuclear Center, Pleasanton, Calif. 94566

and

Richard C. Wolf
Microspec Inc., 999 Commercial Street, Palo Alto, Calif. 94303

Energy-dispersive x-ray analysis of radioactive materials is limited by the continuous background produced by the β and γ radiation of the irradiated specimen. Since the solid state detector of the x-ray analyzer in a scanning electron microscope (SEM) is located close to, and in the direct line-of-sight from the specimen, shielding is impossible. Without some sort of protection the x-ray detector will be swamped by radiation from specimens which are not too radioactive for the secondary electron detector in the SEM. To reduce the unwanted background a collimator for the x-ray detector was designed and built, and its effectiveness determined.

Collimator Design

The collimator consists of a piece of heavy metal, 2.8 cm thick, fitted to the front of the regular detector arm. A Ta-10% W alloy was chosen because of its non-magnetic properties, high x-ray absorption coefficient, and good machinability. The collimator has a conical hole with the cone base centered on the Si detector. The cone apex is located at the intersection of the electron optical axis with the specimen surface. Figure 1 shows a schematic of the arrangement. The collimator does not interfere with the normal stage movements.

Experiments

The effectiveness of the collimator was tested with six Zircaloy-2 specimens representing a critical range of radioactivity as listed in Table 1. The specimens were sections of irradiated reactor fuel cladding from which the fuel had been removed. Secondary electron images could be obtained from all specimens even though the noise was rather high for the specimens with the highest radioactivity. X-ray energy spectra were accumulated and the detector dead time observed for all specimens without and with the collimator in place, and for each of these configurations without electron beam and with the electron beam exciting the specimen. The instrument dead time for each of the four combinations is recorded in Table 1. It was found that a usable spectrum could be obtained with a dead time up to about 90%. Beyond that the detector was swamped for all practical purposes.

Observations

As seen in the table, the collimator significantly reduced the dead time for all specimens. The table also shows that for the highly radioactive specimens tested most of the contribution to dead time was made by the β and γ activity of the specimen: the dead time with electron beam excitation was only slightly higher than without the electron beam.

Because of the geometry of the collimator hole, an elliptical surface area of $<75mm^2$ contributes to the signal received by the detector. Consequently, the relative effectiveness of the collimator should increase for larger specimens. For specimens that occupy only a fraction of the area of the "active ellipse" the effectiveness of the collimator should be slight or nil. This in fact was observed. Compare, for example, Specimens E and F. Both had a total β plus γ activity of 11 R/h at 2 inches. However, Specimen E had 6 times the area of Specimen F. The area of the latter was considerably smaller than the "active ellipse" while the area of E was larger. Consequently, all of F contributed to the dead time, but only a fraction of E. As a result the collimator had reduced the dead time of E considerably whereas Specimen F still swamped the detector even with the collimator. Similarly Specimens C and D can be compared. Specimen C was tested in two directions, with the long dimension parallel and at right angles respectively to the long axis of the "active ellipse". The results make it clear that in the second position a greater part of the specimen was outside the ellipse and the dead time was lower than with the specimen in the first position. Similarly, the dead time was even lower for the still larger Specimen D. What really determines the effect on dead time is not the absolute value of the β plus γ activity but rather the specific activity weighted and integrated over the area of the "active ellipse". Although exact calculations of this integral were not made the results of the dead time measurements suggest this actually to be the case.

In addition to high-activity specimens the collimator is useful also for low-activity specimens for a different reason. The β and γ radiation and probably also the back-scattered electrons excite x-rays in the other materials of the specimen chamber, notably the specimen holder and the final lens pole piece. These x-rays will be detected by the solid state detector unless they are screened out by the collimator. This effect was observed with Specimen A. All spectra obtained without the collimator contained Cu and Zn lines from secondary excitation of the brass specimen holder. These lines were absent when the collimator was installed.

Summary

A heavy metal collimator in front of the solid state detector of an energy-dispersive x-ray analyzer serves two functions for the analysis of radioactive materials:

1. The detector is shielded from the β plus γ background radiation except from that radiation originating from a small ($<75mm^2$) elliptical specimen region. The system is most effective, therefore, for larger specimens of high total but intermediate specific activity.

2. The detector is shielded from characteristic x-rays excited within the specimen chamber in materials other than the specimen, notably the specimen holder and the final lens pole piece. This effect is present even in low-activity specimens.

Acknowledgements

The collimator principle was suggested by H. S. Rosenbaum, and his encouragement of this work is greatly appreciated.
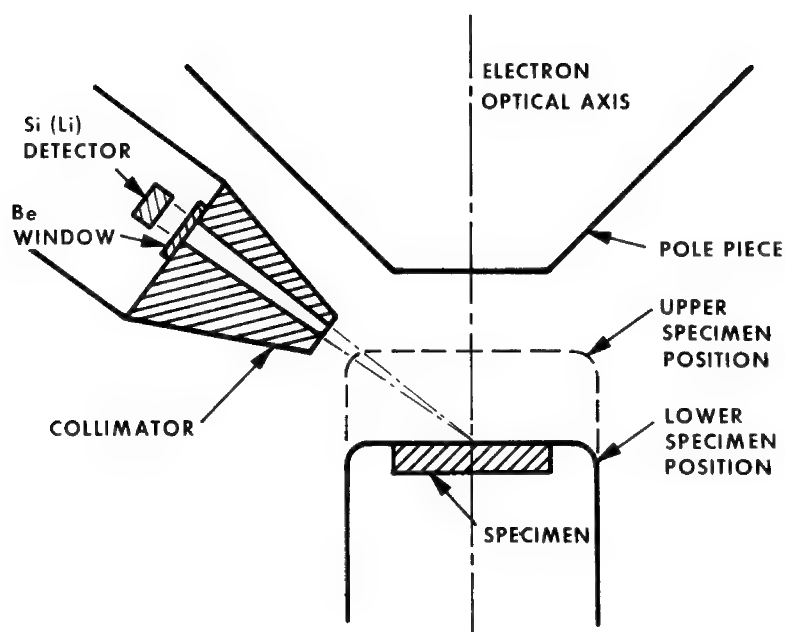
Figure 1.   Schematic of Collimator Arrangement

Table 1.

Spec. Id.	Size (mm)	Activity at 2"(mR/h) β plus γ	Specific Activity (mR/h/mm^2) β plus γ	Dead Time in % (2 μs shaping time)			
				Without Collimator		With Collimator	
				No Beam	With Beam	No Beam	With Beam
A	8½x3	180	7		70		55
B	5x4	1,300	65	84	89	65	65
C	11x3½	5,000	130	96	98	72	73
	3½x11			96	98	68	68
D	10x10	5,000	50	94	97	60	73
E	11x9½	11,000	115	100	100	76	78
F	5½x3	11,000	670			95	100

ADVANCES IN QUANTITATIVE ENERGY DISPERSIVE SPECTROMETRY

D. R. Beaman and L. F. Solosky

The Dow Chemical Company
Midland, Michigan 48640

Seventy-nine elemental analyses were performed with a state-of-the-art energy dispersive spectrometer (EDS) in an attempt to determine if the quantitative capabilities of these systems had improved since the last investigation (1). The following improvements were incorporated in the new system relative to the system discussed previously (1). The detector revolution was 165ev at 5.9Kev and 1000 cps total spectral count rate. A pulse pile-up rejector was used. The amplifier gave less than 10ev line broadening and 5ev peak shift for spectral count rates up to 30000 cps. The spectral data were stored in a computer where the background correction was made using a deconvolution technique described by Schamber (2) in which a multiple least squares fit is made to the unknown spectrum using stored spectra from pure standards. The improvement in detector revolution coupled with the deconvolution program significantly reduced the errors introduced through peak overlap.

All the analyses were performed in an electron probe on well-characterized materials. The spectral count rate was maintained at 2000 cps or less, therein requiring counting intervals ranging from 100 to 400 seconds. Analyses were compiled on the following alloys, compounds, and minerals: Ti-Nb, Mg_2Si, Fe-Ni, Fe-Cr, Cr_2C_3, Fe-Si, Cu-Au, Cr-Co-Mo, Fe-Ni-C, W-Mo, Cu-Zn, Au-Ag, $CaMgSi_2O_6$, $CaSiO_3$, and Hess 39. Compositions, C_{calc}, were calculated from the measured x-ray intensity ratios, k, using programs by Schamber (2), Colby (3), Yakowitz, Myklebust and Heinrich (4), and Beaman (5). The relative errors, $\Delta C/C$, were calculated using

$$\Delta C/C = (C_{calc} - C_{true})/C_{true}$$

and the data are summarized on the histogram. In the case of the

EDS, the statistical parameters were calculated excluding concentrations below 5%. The statistical data include only those systems which were common to all three investigations.

A definite improvement is evident with the improved EDS used in the present work. The histogram and accompanying statistical quantities show a distinct reduction in the width of the distribution, i.e., the standard deviation has decreased from 7.2 to 4.3%. Based on the data it was concluded that a relative error of better than ±4% of the amount present could be expected at concentrations above 10 wt. %. This is in contrast to the previously reported (1) value of ±6% for concentrations above 20%. The performance of the wavelength dispersive spectrometer (WDS) is still superior where an error of ±1% is expected (1). An important consideration is the need for highly-accurate results since, in most cases, a relative error of 4% may be entirely satisfactory. On the other hand, the materials studied here are relatively simple systems in which the EDS gave some rather large errors.

At concentrations above 20% no significant dependence of the relative error on concentration was observed; however, for analyses in the composition range of 5 to about 20%, one can expect a relative error of ±7% with 43% of the analyses within ±4%. For six concentrations below 5% the standard deviation and arithmetic mean were 16% and 13%, respectively, with no error less than 6%.

The results of the present investigation were degraded slightly when the background correction was made by interpolation from portions of the spectrum free of characteristic peaks. The standard deviation and arithmetic mean were then 4.9% and 3.8%, respectively, as compared to 4.3% and 3.1% when using the fitting procedure. This implies that the fitting procedure of Schamber (2) improves the background correction.
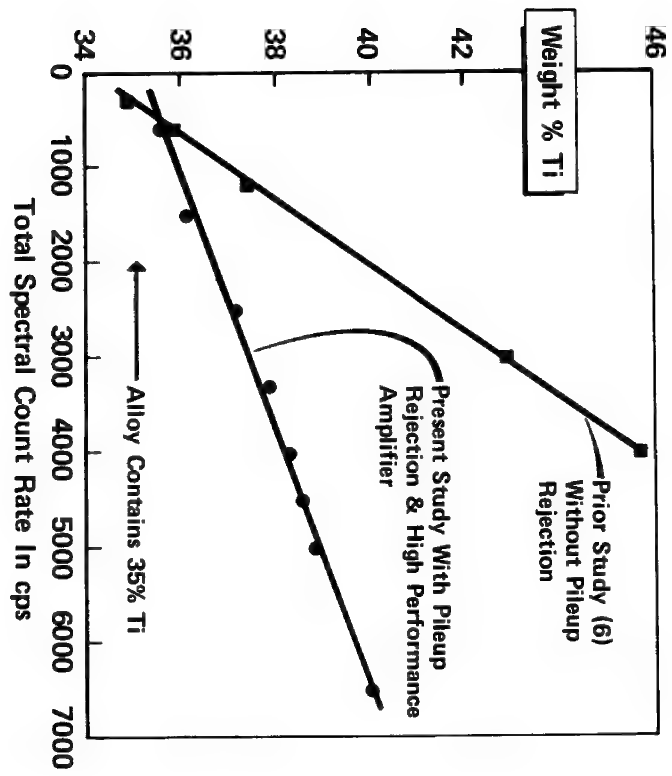
The primary problem encountered in this work was the dependence of the measured intensity ratio and concentration on the total spectral count rate. The figure shows the Ti concentration in a Ti-Nb alloy containing 35% Ti as a function of the spectral count rate measured on pure Ti. The upper curve, exhibiting very high count rate sensitivity, is for the older system (6, 7) which was not equipped with

a pile-up rejector or high-performance amplifier. The performance
of the system used herein (lower curve) is considerably better but
still inadequate unless the spectral count rate is maintained at
undesirably low levels. To achieve a relative error of less than
2% in the Ti concentration would require a spectral count rate of
less than 1000 cps. The improvement in count rate sensitivity is
presumed to be responsible for the reduction in positive bias
(algebraic mean) from +1.9 to +1.0%. The problems related to
count rate sensitivity may be circumvented by measuring the concen-
tration as a function of count rate over a limited range and extra-
polating to zero count rate to determine the measured concentration
or intensity ratio. We have been unable to develop a deadtime
correction that provides consistently good results when applied
to all measured intensities. Operation at low count rates for
quantitation is usually feasible because qualitative work can be
carried out at high count rates in a system with negligible peak
broadening and shift. In future systems one would hope to have a
live-time correction that would eliminate this problem.

REFERENCES

1. D. R. Beaman and L. F. Solosky, Anal. Chem., 44, 1598 (1972).
2. F. H. Schamber in Proceeding Eight National Conference on
   Electron Probe Analysis, 85 (1973).
3. J. Colby in Advan. X-Ray Anal., 11, 287 (1968).
4. H. Yakowitz, R. L. Myklebust and K. F. J. Heinrich, NBS Tech.
   Note 796 (1973).
5. D. R. Beaman, Microkhim. Acta, 1969, 117 (1969).
6. D. R. Beaman, L. F. Solosky, and L. A. Settlemeyer in Tutorial
   Proceedings Eight National Conference on Electron Probe Analysis,
   73 (1973).
7. D. R. Beaman and T. Nagatani in The Electron Microanalyzer and
   Its Applications; Proceedings of a meeting sponsored by the
   National Science Foundation and the Japan Society for Promotion
   of Science (1973).

WDS
Prior Study (1)

$$\frac{\Delta C}{C} = \frac{C\ (CALC) - C\ (TRUE)}{C\ (TRUE)}$$

	EDS		WDS
	Present Study	Prior Study (1)	Prior Study (1)
No. Analyses On Histogram	54	55	55
No. Omitted From Mean	4	4	0
Algebraic Mean	1.0	1.9	−0.2
1 Standard Deviation, σ	4.3	7.2	1.2
Arithmetic Mean	3.1	5.2	0.9
RMS Error	5.3	8.9	1.6
% Of Errors Within ± 1%	32	20	62
% Of Errors Within ± 2%	48	41	87
% Of Errors Within ± 4%	70	59	100
No. Of Positive Errors	33	32	31
No. Of Negative Errors	21	23	24

No. Of Analyses

EDS
Present Study

EDS
Prior Study (1)

Negative %   Positive %

$100 \times \Delta C/C$

Weight % Ti

Total Spectral Count Rate In cps

Alloy Contains 35% Ti

Present Study With Pileup
Rejection & High Performance
Amplifier

Prior Study (6)
Without Pileup
Rejection

TELEVISION SCANNING ELECTRON MICROSCOPY OF DYNAMIC EVENTS

W.C. Nixon

Engineering Department, Cambridge University, England

A special two lens scanning electron microscope has been optimised for television scanning rates and used with a video tape recorder to observe dynamic specimen changes. The instrument uses either a tungsten or lanthanum hexaboride electron emitter and can produce an electron probe of 300 A with a beam current of 100 nA which is necessary for a low noise TV image. Many changing specimens have been studied including materials under tension, compression and shear, rotating ball bearings under operating conditions and changing voltage contrast on microcircuits. Three different examples are presented below.

1) A sand grain compressed to fracture showing strain charging

In Figure 1 a sand grain is held between the jaws of a vise in (a) and the electrical charging pattern on the surface follows the outline of the grain. Compression starts and in (b) the grain has fractured. A different charge pattern now exists and this charging changes rapidly as the grain is compressed. The pattern is repeatable and seems to be related to the local stress concentration. In (c) part of the grain has rotated and in (d) only the tall pillar is left which is starting to dig into the steel jaws of the vise on the upper side. In (e) this penetration has gone much further and in (f) the field of view is changed to show the removed steel cutting. The charging pattern appears to be similar to the photoelastic stress patterns seen in plastic models when compressed and viewed in polarised light. Some piezoelectric effect may also be occuring. Dr. N.K. Tovey supplied the micro vise used in these experiments.

2) Human skin observed in situ

This microscope can operate with poor vacuum in the specimen chamber and biological material seen with no preparation. The author's thumb was placed over a half inch hole in the chamber wall in line with the electron beam and the results are seen in Figure 2. In (a) at 100x the ridges are seen and also a charging paper fibre. In (b) at 200x the surface of one ridge and the valleys between the ridges are shown and in (c) at 1000x the rough line between ridges is recorded.

3) Dynamic microcircuit voltage contrast

In Figure 3 a microcircuit is shown with a square wave voltage signal producing a broad band that is synchronised with the scanning rate. By slight frequency adjustment this band will move slowly over the circuit giving a sharp edge at any point. Switching surges that are not repetitive have also been recorded.
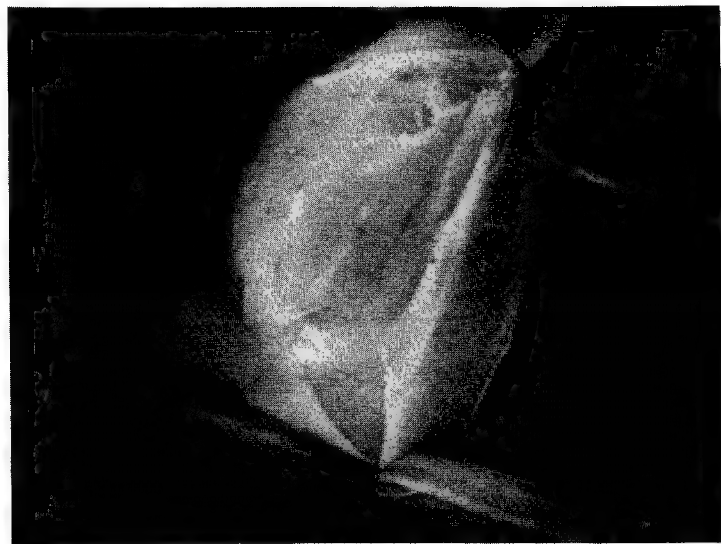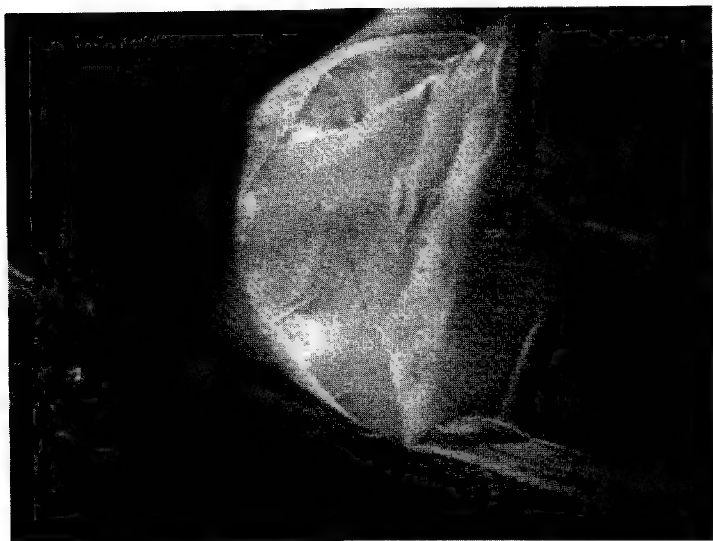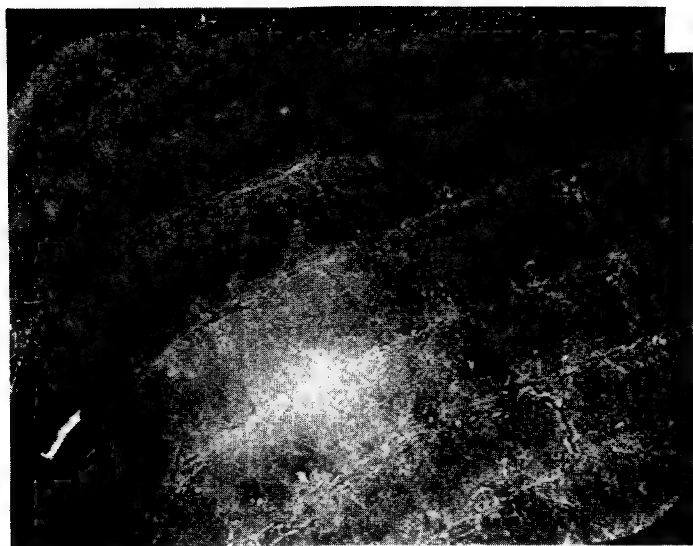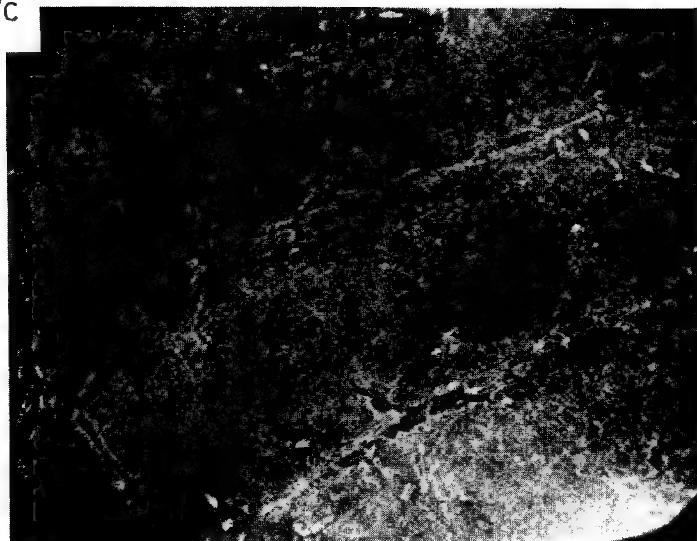
(a)
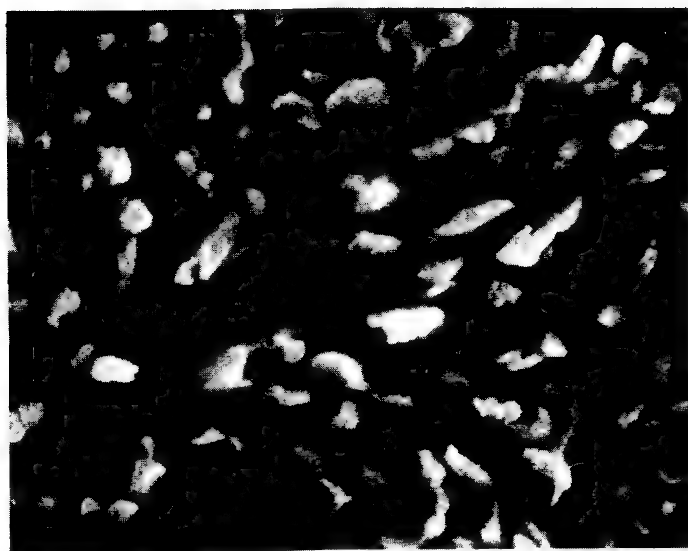
(b)

(c)

(d)

(e)

(f)
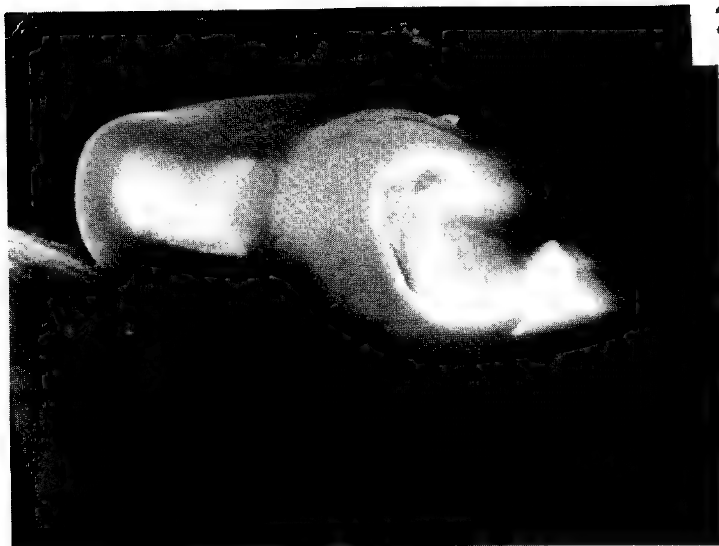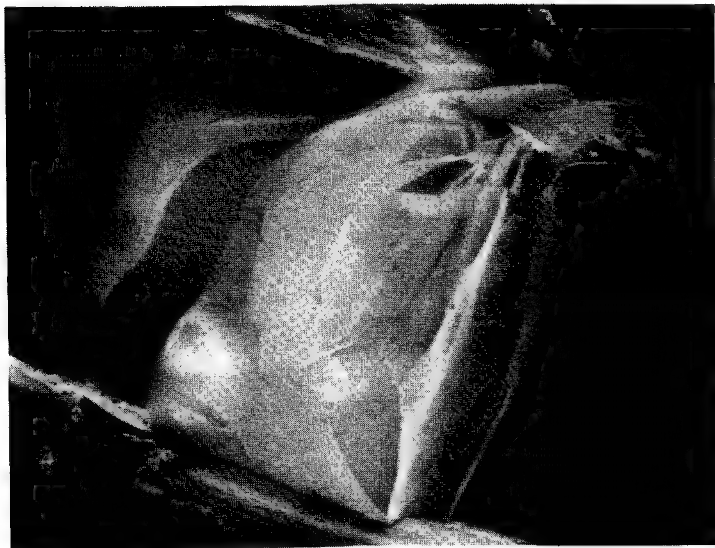
20μm

FIGURE 1

(a)

100µm

(b)

50µm

(c)

10µm

FIGURE 2

20µm

FIGURE 3

A NEW SYSTEM FOR DYNAMIC STEREO OBSERVATION IN THE SEM

E. J. Chatfield and V. Nielsen
Department of Applied Physics
Ontario Research Foundation
Sheridan Park, Mississauga
Ontario, Canada

Introduction

The large depth of focus in the SEM often leads to errors or difficulties in interpretation of micrographs.[1] For this reason, stereo pairs are often prepared by tilting the specimen through a few degrees between two exposures. Use of a stereo viewer will then permit a three dimensional image to be seen. The technique, however, is exacting and time consuming, particularly at high magnifications. A beam deflection technique has been described by Dinnis,[2,3] which used a double deflection of the electron beam below the final lens to produce the two directional views required for observation of a stereo image. The system also operated at slow scan rates only, and used side-by-side CRT displays which were viewed by the operator through a mirror stereoscope.

In this paper a system is described which operates at TV scan rates, and displays the image as an anaglyph on a colour TV monitor.[4]

Instrument Design

Figure 1 shows the principle of operation. The first stereo deflection is given using the conventional double deflection scanning coils, and the deflection back to the optical axis is given by an after lens deflection (ALD) coil. The ALD coil assembly shown in Figure 2 is located on the final lens plate. By switching the two deflections, the beam obtains two angular views of the central point on the specimen. The ramp waveform is applied to the double deflection system in the usual manner, and is synchronised with the switching of the stereo

deflections. At TV scan rates, the stereo deflection has one polarity for the first field (odd scan lines) and the opposite polarity for the second field (even scan lines). In Figure 1 it can be seen that the beam remains on axis during passage through the final lens: this is in contrast to the similar system described by Boyde.[5]

The video output signal from the instrument is switched alternately to the red and green electron guns of a colour TV monitor. The dual image is viewed through red and green filter stereo glasses. An obvious advantage is that several observers can see the image simultaneously.

Astigmatism is introduced by the additional deflection system below the final lens, and it is necessary to increase the drive supplied to the normal stigmator assembly. The astigmatism is different in both angle and magnitude for the two deflection angles; this has been accommodated by a dynamic stigmator circuit which permits separate correction of the two images. After this has been accomplished, it is possible to achieve a resolution of better than 1000Å on stereo pairs directly photographed from the TV screen.

System Performance

Figure 3 and 4 are stereo pairs of a marine animal (bryozoan) at a stereo separation of 8°, and Figure 5 shows a stereo pair which illustrates the system resolution. These resolution micrographs were obtained using one second exposures directly from the colour TV screen, and at a direct magnification of 40000, illustrating that the image quality is limited by noise. A Taylor[6] quartz light guide is already in use, which increases the signal-to-noise ratio significantly; a lanthanum hexaboride gun would improve this still further. Distortion of the image has been investigated, and it has been found that no significant distortion of a square copper mesh is observed as a result of the stereo deflections; the distortion that is present is a limitation of the original TV scanning circuits, some of which is inherent in the

production quality TV receiver.

Videotape Recording

The dynamic events viewed in stereo can be recorded using an unmodified monochrome videotape recorder. The bandwidth requirement is identical with that of a monochrome system; the only requirement is for alternate fields to be switched to the appropriate colour during replay. In practice, the TV set was modified internally so that any stereo video signal, either live or pre-recorded, is automatically switched so that the right eye image is displayed in red and that for the left eye in green.

Applications

The system is sufficiently simple in use that a wide range of applications can be foreseen, particularly in fractography and biological work. Micromanipulation within the instrument will also become much simpler with the addition of the depth perception which this accessory provides.

References

1. A. Boyde, Proceedings of the 4th SEM Symposium, IITRI, Chicago, (1971) 1-8.

2. A. R. Dinnis, Ibid, 43-48.

3. A. R. Dinnis, Scanning Electron Microscopy: Systems and Applications 1973, Conference Series No. 18, Institute of Physics, London, 178-179.

4. E. J. Chatfield, J. More, and V. Nielsen, Proceedings of the 7th SEM Symposium, IITRI, Chicago, (1974) 117-124.

5. A. Boyde, Ibid. (in publication).

6. M. E. Taylor, Rev. Sci. Instrum., 43, No. 12, (1972) 1846-1847.
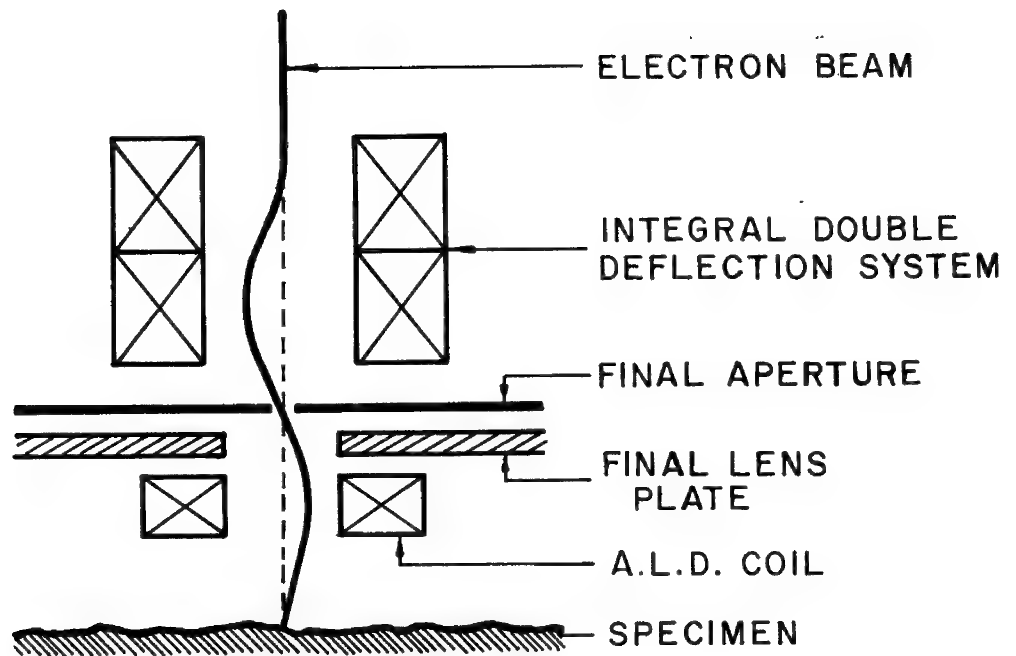
Figure 1. Triple stage deflection system used for dynamic stereo imaging. The beam path shown corresponds to the normally undeflected position, with one polarity of stereo deflection applied.
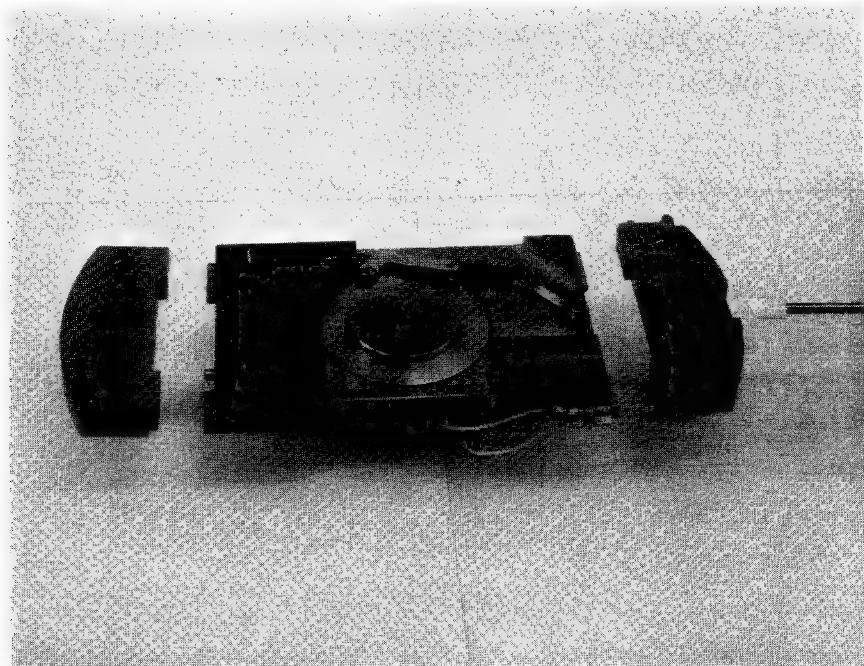
Figure 2. After lens assembly. Rotation of ALD coil is effected by a push rod installed in the side plate. The centre component can be removed easily during specimen exchange.
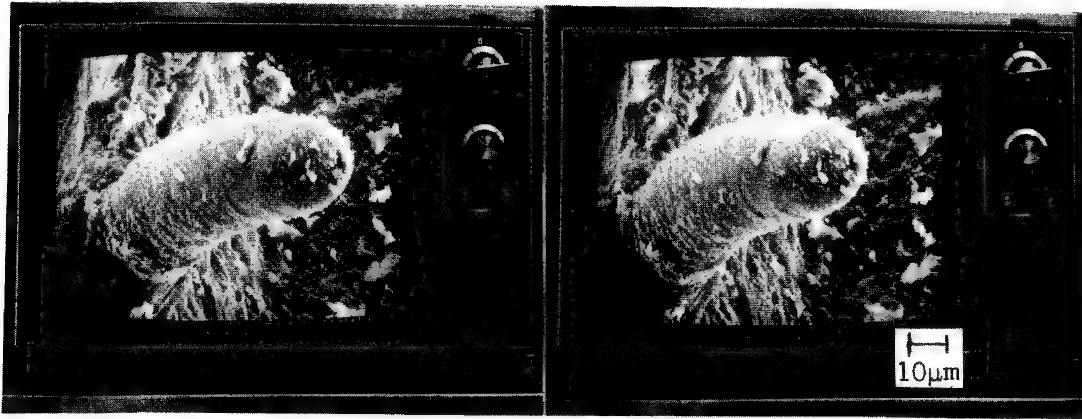
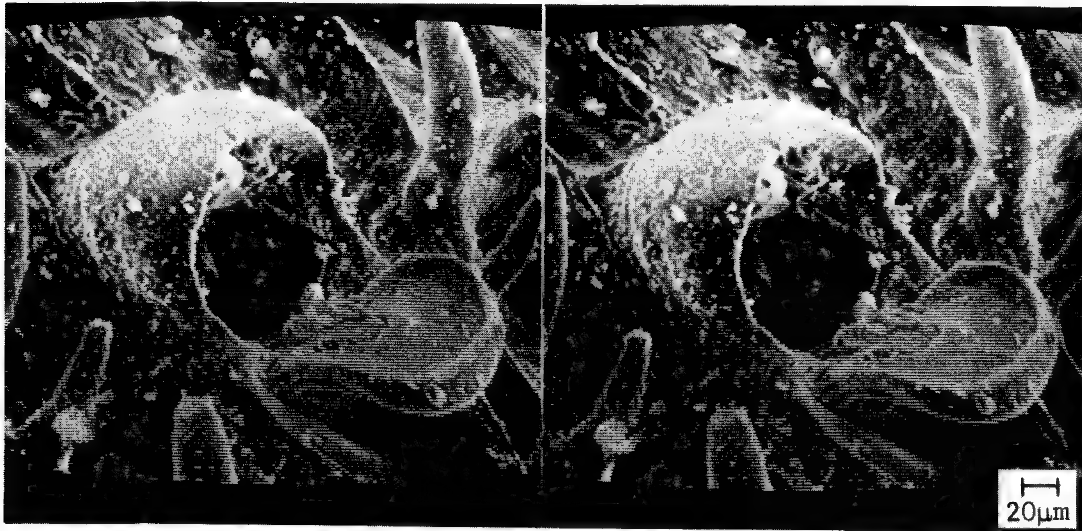Figure 3. Bryozoan, Colonial Marine Animal (Maritimes) Stereopair, 8° separation.

Figure 4. Bryozoan, 8° separation

Figure 5. Dendritic Silver Mesh, 8° separation, showing resolution of 1000Å

A RAPID ASSESSMENT OF MERCURY ION IMPLANTATION DAMAGE IN BORON-DOPED SILICON USING THE SCANNING ELECTRON MICROSCOPE

by

E.M. Schulson and D.A. Marsden[+]

Atomic Energy of Canada Limited
Chalk River Nuclear Laboratories
Chalk River, Ontario, Canada

The purpose of this paper is to demonstrate an SEM method of assessing mercury ion implantation damage in boron-doped silicon, and to compare the SEM assessment with that derived from the well-established technique of Rutherford Scattering. The Hg^+/Si system was considered to be suitable for SEM analysis because the peak in the radiation damage occurs near the surface; i.e. at a depth of $\sim$130 A. The Hg^+/Si combination was also considered to be of interest to the study of radiation damage, because Della Mea et al.(1) reported that high concentrations of boron suppress the damage rate.

The experiments were performed as follows. Etch-polished, <111>-oriented silicon wafers of two boron concentrations, 10^{17} atoms/cm^3 and 10^{20} atoms/cm^3, were implanted with mercury ions. The implants were made at room temperature using 40 keV ions, and the crystals were tilted a few degrees to avoid ion channeling. Following the implantations, the specimens were examined, first with a JSM-II SEM and then by the Rutherford Scattering (RS) method. The SEM study was performed by using the electron channeling pattern (ECP) technique (reviewed elsewhere 2,3), and the image was formed by collecting the back-scattered electrons. The RS study was carried out with a beam at 1 MeV He ions from a Van de Graaff accelerator, and the yield of the back-scattered ions as a function of ion energy was obtained and analyzed as described elsewhere(4).

Figure 1 shows the effect of irradiation on the SEM-ECP's from silicon of the two boron concentrations. For Hg^+ doses above 1×10^{14} ions/cm^2 electron channeling contrast could not be detected above background. The main point to note is the decrease in pattern contrast with increasing dose. This feature is due to the progressive decrease in the crystallinity

---

[+]Now at Ontario Dept. of Health, 360 Christie St., Toronto, Ontario

of the silicon rather than to the presence of mercury per se. It occurs because as the degree of crystallinity decreases, the Bloch wave character of the electrons becomes lost, thereby leading to reductions in the orientation dependent back-scattering of electrons. Another point to note is that the boron concentrations of the levels examined appear to have no effect on the susceptibility of silicon to radiation damage, as deduced from the similarity in pattern contrast from both types of silicon. This observation is interesting in the light of earlier work. Della Mea et al.(1) reported that silicon crystals doped with 10^{20} atoms/cm^3 of boron were more resistant to room temperature radiation damage by 42 keV Hg$^+$ implants than were crystals doped with 10^{17} and 10^{18} atoms/cm^3 of boron. On the other hand, Hirvonen and Eisen(5) in a similar study found no evidence for this effect. Our work, therefore, confirms that the anomalous annealing effect noted by Della Mea et al. is not due entirely to the high boron concentration.

To express quantitatively the degradation in pattern contrast, the procedure followed was to measure the decrease in contrast for the {220} lines relative to that from an unirradiated crystal of the same orientation, and then to express this in terms of a contrast reduction parameter R, described earlier(6). This is the critical-beam-current method(7). Accordingly, the beam currents for which the {220} lines could just be detected above background were measured, care being taken to darken the SEM room and to standardize the SEM frame scan at 5 seconds before taking readings. The table lists the critical currents from which the R_{220} values, also listed, were computed.

ECP Contrast Degradation, R, Versus Does for 40 keV Hg$^+$ Implantations in Silicon at Room Temperature

Hg$^+$ Dose (ions/cm^2)	Critical Beam Current (n Amps) - $i_{c,220}$	$R_{220} = 1 - (i_c^r/i_c^t)^{1/2}$
0	0.3 (ref.) = i_c^r	0
1.0×10^{13}	0.7 = i_c^t	0.34
1.3×10^{13}	1.1 = i_c^t	0.45
1.9×10^{13}	4.0 = i_c^t	0.72
3.0×10^{13}	5.5 = i_c^t	0.76
4.0×10^{13}	12 = i_c^t	0.84
5.0×10^{13}	10 = i_c^t	0.83
1.0×10^{14}	20 = i_c^t	0.88

Figure 2 compares the SEM assessments with RS assessments. The latter measurements are presented in terms of relative disorder parameters. These were obtained, first by normalizing the back-scattered He ion yield generated within the first 300 A of the surface with respect to the yield from specimens irradiated to a dose of 5×10^{14} ions/cm^2, and then by assuming that the most heavily irradiated sample was completely amorphous within the damage zone. Presented in this way the RS measurements agree quite closely with the SEM results. Both detect the break in the damage/dose curve which occurs at a dose of $\sim 4 \times 10^{13}$ ions/cm^2, and both confirm that boron concentrations in the range 10^{17} to 10^{20} atoms/cm^3 have no significant effect on the damage rate in silicon.

It should, perhaps, be emphasized that the good agreement between the two methods in the present case is not a basis for concluding that agreement should always be expected. In general, we believe that agreement can only be expected when the main scattering processes which give rise to the respective signals occur within the same region of the crystal, or when the crystal is uniformly damaged such that the same overall damaged structure characterizes the electron and the He ion scattering zones. In the 40 KeV Hg$^+$/Si case, both signals come from roughly the same regions: the SEM-ECP contrast originated within the first few hundred angstroms of the surface(8), and the RS data was obtained from the first 300 A.

Also, it should be recognized that the SEM information cannot be interpreted in terms of the structure of the damaged zones, but merely as a measure of the overall or gross level of damage. The RS data, on the other hand, can be used to obtain the total number of displaced atoms, for shallow implants such as these, or the fraction of lattice atoms displaced as a function of depth for deeper implants.

ACKNOWLEDGEMENTS

REFERENCES

1. G. Della Mea, A.V. Drigo, P. Mazzoldi, G. Nardelli and R. Zannoni, Appl. Phys. Letters, 16 (1970) 382.

2. G.R. Booker, "Modern Diffraction and Imaging Techniques in Material Science", Ed. S. Amelinckx, R. Gevers, C. Remant and J. van Landuyt, North-Holland Co., 1970, p. 613.

3. E.M. Schulson, "Electron Microscopy and structure of Materials", Ed. G. Thomas, R.M. Fulrath and R.M. Fisher, University of California Press, 1972, p. 286.

4. J.A. Davies, J. Denhartog, L. Eriksson and J.W. Mayer, Can. J. Phys., 45 (1967) 4053.

5. J.K. Hirvonen and F.H. Eisen, Appl. Phys. Letters, 19 (1971) 14.

6. E.M. Schulson, Proc. Fifth European Congress on Electron Microscopy, Manchester 1972, p. 480.

7. E.M. Schulson, Rev. Sci. Instruments, 44 (1973) 348.

8. J.P. Spencer, C.J. Humphreys and P.B. Hirsch, Phil. Mag., 26 (1972) 193.
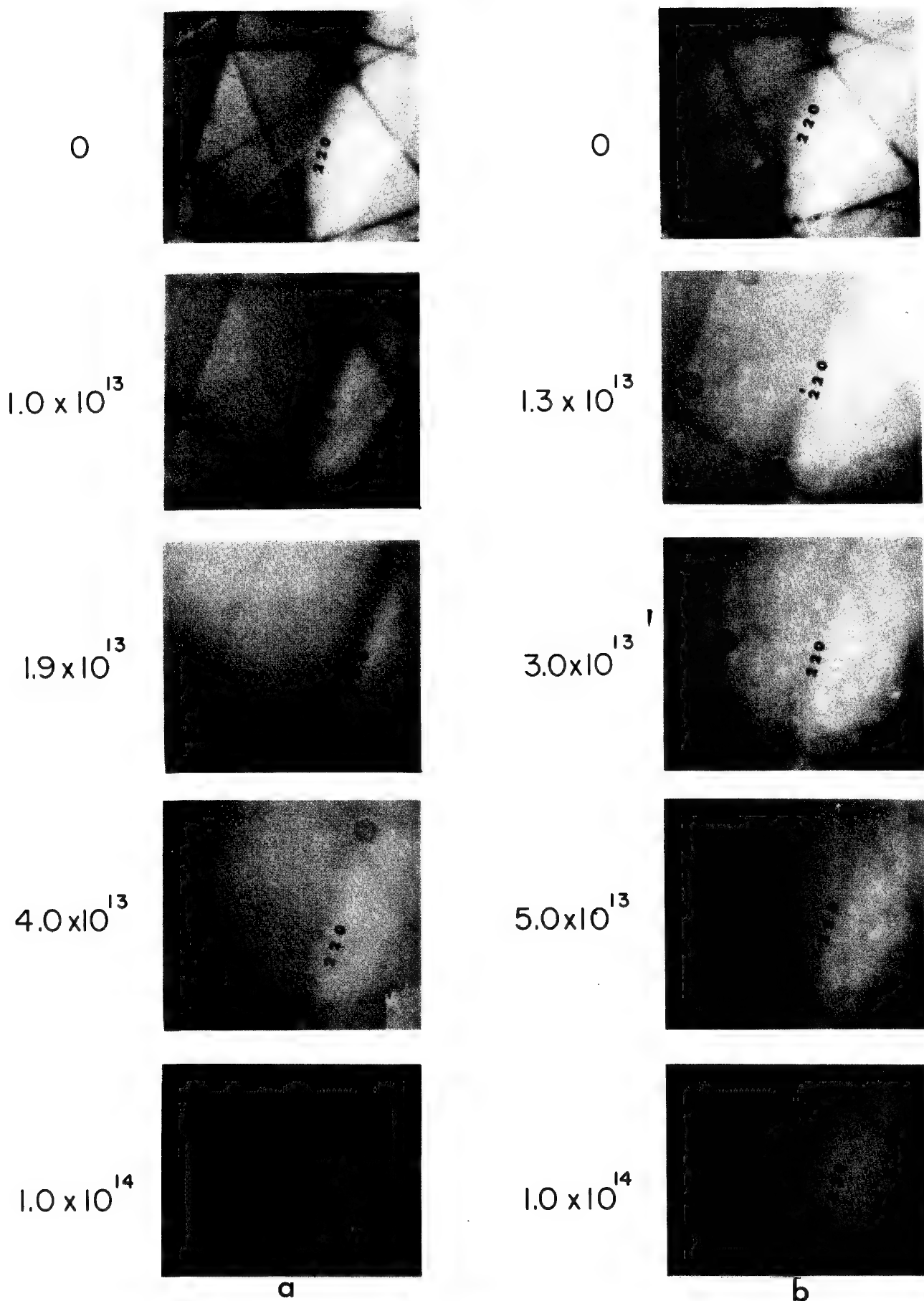
Figure 1   Showing the degradation of SEM-ECP contrast versus dose (ions/cm^2) from silicon crystals implanted with 40 KeV Hg$^+$ at room temperature, for crystals containing (a) 10^{17} B atoms/cm^3 and (b) 10^{20} B atoms/cm^3. B appears to have no effect. SEM beam conditions: 25 KV; 3 x 10^{-4} radians divergence; 0.1 µA max. current at the specimen; unfocussed scanning beam.
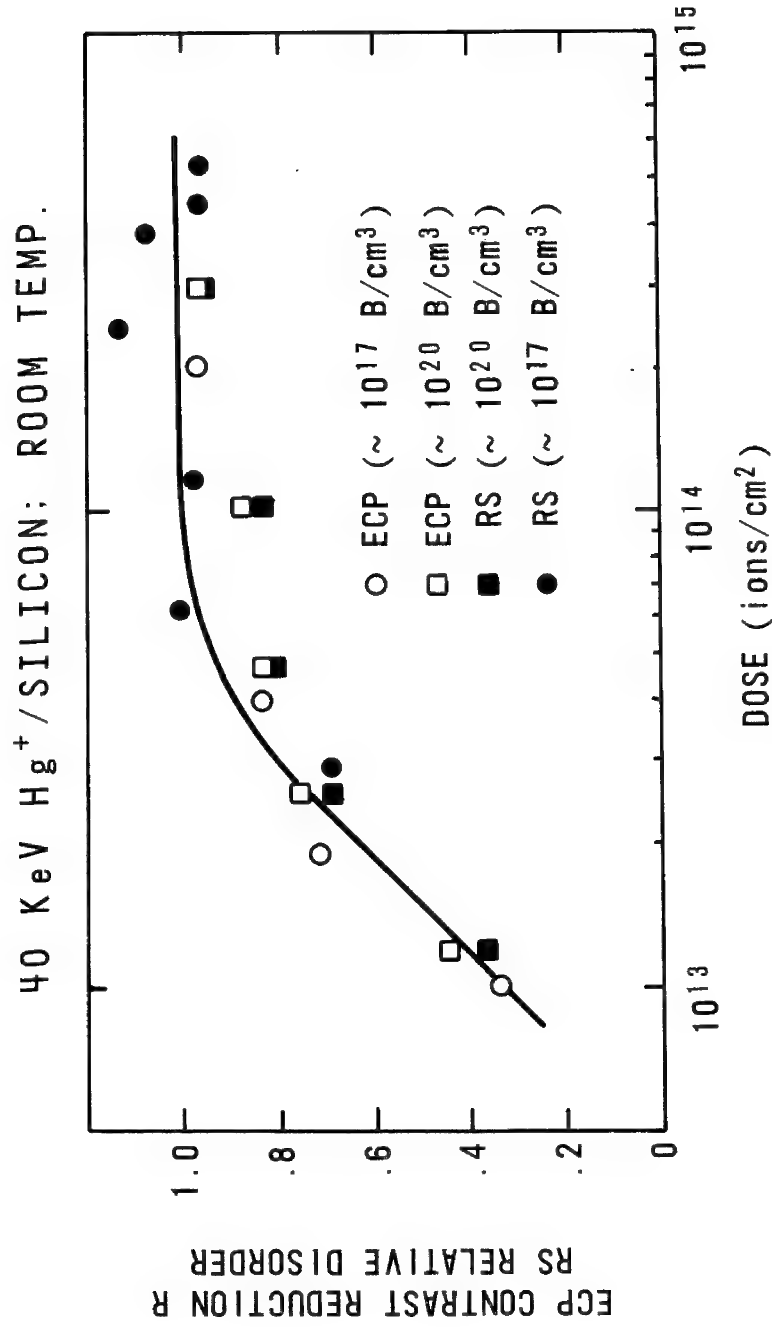
Figure 2 SEM-ECP and RS assessments versus dose of gross ion implantation damage in silicon due to 40 Mev Hg+ bombardment at room temperature. Note the agreement between the two methods of assessment. Both methods detect a break in the curve at a dose of ∿4 x 10^{13} ions/cm².

FIELD EMISSION MICROSCOPY USING HIGH PROBE CURRENT DENSITIES

L. M. Welter
Coates & Welter Instrument Corporation
777 N. Pastoria Avenue
Sunnyvale, Ca. 94086

The field emission electron source has long been recognized to have a higher brightness, lower electron energy spread, and smaller effective source size than thermionic type sources. These characteristics of the field emitter can result in superior instrument performance producing the highest resolution with a good signal to noise ratio in a variety of microbeam applications.[1 and 2] However, the ultimate resolution of the field emission system has, in some instances, been sacrificed to obtain larger total probe currents. Auger analysis, microbeam fabrication, and X-ray analysis are some applications where this trade in performance is sometimes made.

Fig. 1 shows the relative performance of an electron probe forming system using various types of electron sources.[2] For example, the presently available field emission system can always focus more current into a smaller probe than the thermionic tungsten filament system can as long as the required probe diameter is less than about 1500Å (solid curves). The thermionic emitters are limited by the maximum operating temperature of the source material. However, since the field emitter can operate at ambient temperature because electrons are extracted from the source material by applying very large electrostatic fields, an increase in probe current of more than 100 times is possible at any given probe diameter (dashed curves for field emission in Fig. 1). This performance improvement of the field emission system would move the "current crossover" to a probe diameter of about 1μ when compared with the thermionic tungsten filament. Experimental results for a field emission system operating at these high probe current densities (amps/cm^2) will be presented.

REFERENCES

1. A. V. Crewe (1971), "High Intensity Electron Sources and Scanning Electron Microscopy", _Electron Microscopy in Material Science_, Academic Press, New York, N. Y., 162-207.

2. L. M. Welter (1974), "Application of a Field Emission Source to Scanning Electron Microscopy", _Principles and Techniques of Scanning Electron Microscopy_, Vol. 3, Van Nostrand Reinhold Co., New York, N. Y. (to be published).

FIELD EMISSION

PROBE CURRENT (A)

10^{-5}
10^{-6}
10^{-7}
10^{-8}
10^{-9}
10^{-10}
10^{-11}
10^{-12}
10^{-13}

TUNGSTEN FILAMENT
LANTHANUM HEXABORIDE
FIELD EMISSION (GUN ONLY)
FIELD EMISSION (GUN AND LENS)

10^1 10^2 10^3 10^4
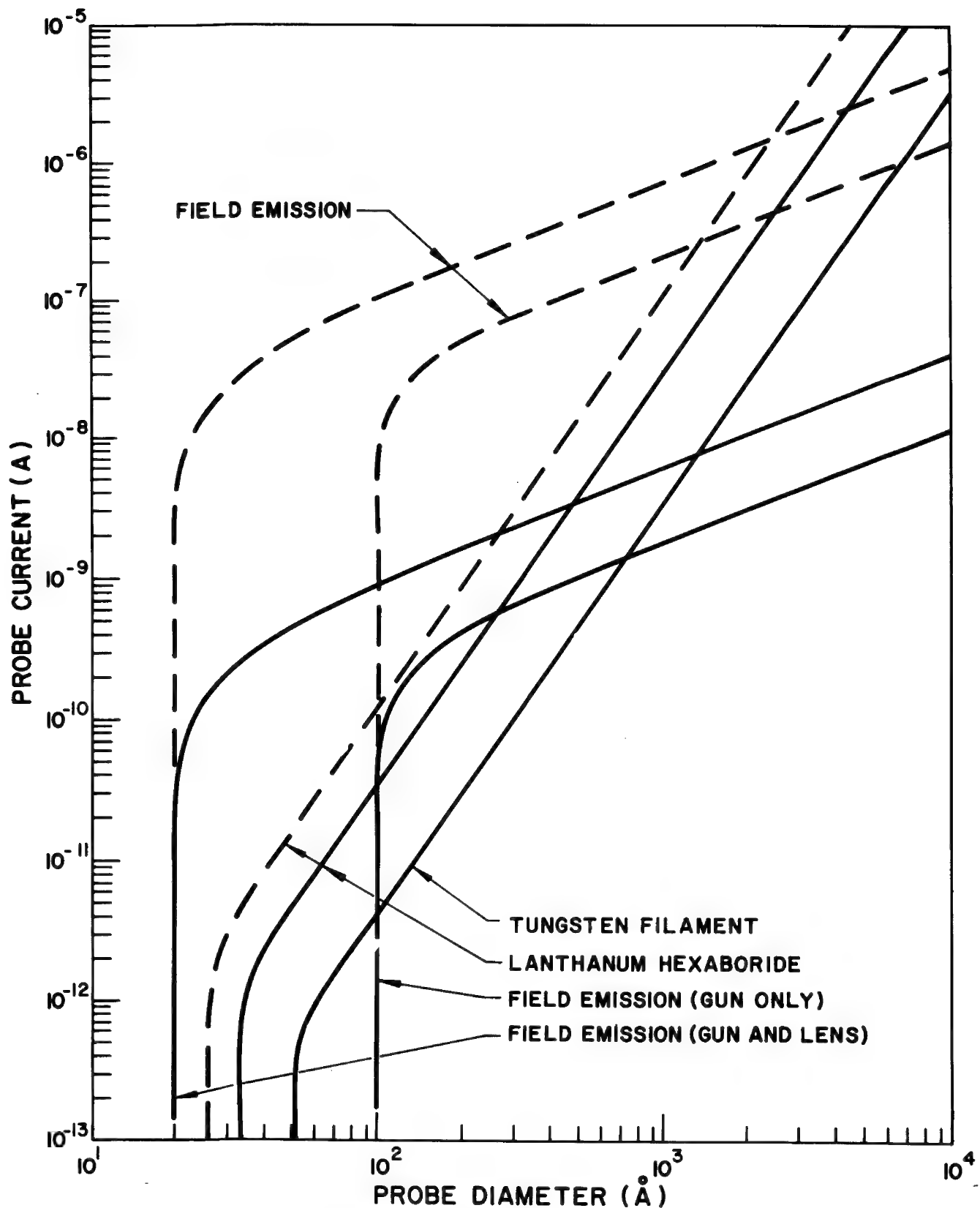
PROBE DIAMETER (Å)

Fig. 1. A comparison of field emission and thermionic electron sources indicating the amount of current which can typically be concentrated into a given probe diameter by each type of source. The solid curves indicate present day values. The dashed curves for field emission represent the new state of the art which is the subject of this paper, and the dashed curve for the lanthanum hexaboride thermal emitter indicates increased current possibilities using Schottky emission.

Plasma Etching for SEM and EMP
Examination of Microelectronic Devices

Authors: A. M. Sheble, T. P. Teel, and J. R. Devaney

SUMMARY

In the waning days of the 60's, a significant change in integrated
circuit processing began to emerge. This change was the addition of a
low temperature glass passivation layer over the entire die surface. The
glass layer performes two useful functions, (a) it protects the interconnect
metallization from mechanical damage during manufacturing and, (b) it prevents
shorts between the metallization runs by loose encapsulated conductive
particles. In order to perform quality control or failure analysis functions,
it is necessary to remove this glass layer. In the past, this process has
been accomplished with a fluorine based wet acid etchant. Although this
technique is quite effective in removing the glass, it is possible for
undesirable reactions between the glass etch and underlying metal runs to occur.
Since hydrofluoric acid solutions attack aluminum as readily as they do
glass, great care must be taken or the glass revmoval can result in damaged
metallization.

Plasma etching or low temperature ashing with an RF field has recently
found numerous applications in semi-conductor processing and production.
The advantage being a dry procedure with the introduction of no wet solutions.
For example, low termperature ionized oxygen gas plasmas have demonstrated
their practical utility, in the removal of organics such as photo resist.[1]
By the same effect, if a gas containing fluorine such as CF_4 is introduced
into the RF field, a reaction occurs which removes glass and silicon but
does not attack aluminum or nichrome.

The necessity for removing this glass passivation layer for failure
analysis and quality control inspections of the underlying metallization
is a direct result of the many various scanning electron microscope
specifications which require the inspection of the interconnect metal
continuity and quality over oxide steps on the circuit surface.[2,3,4,5]
It is impossible to analyze the quality of step coverage with the
glass passivation intact. Wet chemical removal with an ammoniumfluoride
buffered HF solution is a popular and effective technique, but, as
mentioned previously, the possibility of damaging the alumiuum metallization
does exist. It will be shown that with an ionized fluorine gas plasma
passiviation glass is effectively removed with no damage to the aluminum
metallization, and in the particular application to glassivated PROM'S
(Programable Read Only Memories) the plasma etch produces information and
results which are not obtained with chemical etches alone.

PROCEDURE

Both the scanning electron microscope and the electron microprobe have been utilized in the study of the effectiveness of plasma etching in the study of: (1) metallization step coverage, (2) aluminum silicon interactions in semi-conductor contact window, and (3) the reaction products and fusion gap in programable read only memories. In each case, great care was taken to analyze the exact same area before and after glass passivation removal and not just representative areas. In every case where possible, alternate methods such as wet chemical methods and replication techniques were also used for comparison.

GLASS PASSIVATED PROM'S

Most circuits of the memory type such as the ROM or PROM contain many closely spaced components which require a minimum of separation between the metallization segments. Thus, there is a need for glass passivation to protect the circuit from small extraneous particle-induced shorts. This glass passivation alters the reactions which occur when a nichrone link is fused. Also, it reacts with the nickel and chromium which becomes molten during the fusing (programming) operation. To study the result of this "fusing" reaction, several parallel efforts were effected which were designed to determine the location of nickel and chromium after fusion, and to demonstrate the applicability of plasma etching to the problem.

I. Scanning Electron Microscope (SEM) study.

    (a) Correlate optical images to SEM images after plasma etch.
    (b) SEM study of fusible links after plasma etch.
    (c) SEM study of links after wet chemical etch and then the same links after plasma etch.

II. Electron Microprobe (EMP) study.

    (a) Determine spacial distribution of nickel and chromium before and after passivation glass removal by plasma etching.
    (b) X-ray line scan of fused links for nickel and chromium after chemical etch and then the same links after plasma etch.

GLASS PASSIVATED INTEGRATED CIRCUITS

The selection of aluminum as the conductive material in integrated circuits and transistors, while in some ways one of convenience, did involve serious metallurgical considerations, In the case of integrated circuits, of major importance, on the positive side is the fact that aluminum readily adheres to silicon dioxide but will not rapidly diffuse through it. In addition, aluminum forms ohmic (non-rectifying) contacts with silicon. Other more obvious properties of importance are its ease of deposition and patterning with chemical etches.

On the negative side of the list is its susceptibility to chemical attack and low current density capacity. In addition, aluminum will readily alloy

with highly stressed or heavily doped silicon. This phenomenon has been
extensively studied by Black and Hall at Motorola, Incorporated. [6,7]
Excessive alloying of aluminum into silicon in the contact windows can result
in poor manufacturing yields. This is particularly true in the case of
shallow junctions which are becoming more and more popular in todays high
speed circuitry.

Examination of the continuity of aluminum metallization run over oxide
steps has become an important QC function for devices to be used in hi-rel
application, since these areas are prime targets for metallization failure.
In order to delineate the nature and amount of aluminum silicon interaction
in IC contact windows, and to examine the effects of passivation glass
removal on the continuity of metallization over oxide steps; the following
methods were performed.

I. Examination of metallization step coverage

    (a) SEM examination of good and bad metallization step coverage
        after glass removal by both wet chemical and plasma etching
        techniques.

II. Aluminum silicon reactions in contact windows

    (a) Removal of aluminum and replication of pitted surface
    (b) Removal of silicon die by plasma etching and direct examination
        of under surface with the SEM
    (c) Metallurgical cross section of effected window contact
        followed by optical and SEM examination.

RESULTS & CONCLUSIONS

The use of an ionized fluorine plasma is an effective technique for the removal
of glass passivation from the surface of both aluminum and nichrome in
programable read only memories. In addition to the removal of the deposited
glass from the nichrome link surface, it also acts as a selective etch for
the removal of the chromium doped glass in the area of the fusion gap, thus,
revealing the true shape and size of the reacted region.

It has also been shown that a fluorine gas plasma may be used to completely
remove the silicon die from beneath its interconnect aluminum metallization, this
allowing direct observation of the aluminum reaction volume in the contact window.

The plasma etcher has been shown to be a particularly useful tool for
examination of microelectronic devices. This is particularly true when it is
used in conjuction with other more established techniques such as chemical etching
and surface replication.

1. R. S. Thomas, J. R. Hollahan, "Use of Chemically Reactive Gas Plasmas in Preparing Specimens for Scanning Electron Microscopy and Electron Probe Microanalysis", proceedings of the 1974 Symposium of Scanning Electron Microscopy pulbished by IITRI Chicago, Illinois.

2. Scanning Electron Microscope Inspection of Semiconductor Device Metallization, Specification. S-311-p-12 Goddard Space Flight Center Greenbelt, Maryland.

3. Scanning Electron Microscope Procedure for Microcircuits. Jet Propulsion Laboratory, Pasadena, California.

4. Inspection Standards – Semiconductor Devices, Scanning Electron Microscope, STC 0008, McDonnell Douglas, Long Beach, California.

5. Scanning Electron Microscope Inspection of Semiconductor Device Metalization, Specification 908053, Hughes Aircraft Company, Culver City, California.

6. E. Hall, "Silicon RF Power Transistor Metallization", Research and Development Technical Report ECOM – 0164F, October, 1971. United States Army Contract DAAB07-70-C-0164, Motorola, Inc., Semiconductor Products Division, Phoenix, Arizona.

7. James R. Black and Edward L. Hall, "Semiconductor Wearout – Its Analysis and Prevention", Solid State Technology, Vol. 2, No. 1, 1972

A CAMAC Automated Electron Microprobe

W. T. Kane

Research and Development Laboratories
Corning Glass Works
Corning, New York   14830

Automation of the electron microprobe has come a long way in the last few years due primarily to: 1) the very rapid development of minicomputer technology, and 2) the preemption of qualitative and semiquantitative microanalysis by the relatively inexpensive EDS-equipped SEM. These developments have simultaneously made possible and forced microprobe development toward the area of rapid and accurate quantitative microanalysis where, despite overblown advertising to the contrary, it retains a decided edge.

At the present time, high-level computer languages such as FORTRAN and BASIC, capable of real time data acquisition and control, are available for a number of excellent minicomputer systems and have reduced the programming difficulties for automation by at least an order of magnitude. A third generation of instruments have been designed incorporating the rugged and precise crystal spectrometers and sample stages which are required in automated operation and rather good SEM capability as well. Several manufacturers supply completely integrated microprobe systems which include the computer software, interface, and the automated instrument. Such systems can be operational within a reasonable time after installation.

The major difficulty with the current state of the art is the interface, the black box which allows the computer and the microprobe to exchange information and instructions. In most of the systems supplied by the manufacturers, the interface is hard-wired and specific to the computer and instrument configuration supplied. Although some of these interfaces are housed in NIM bins and have the appearance of modularity, a look at the back of the electronics rack reveals non-NIM power supplies and soldered-in intermodule data busses. At least one NIM-based modular interfacing package has been available for over 5 years but the modules are proprietary to a single supplier and special power supplies are required. In short, as the interface is installed in the majority of currently available systems, changes in either the computer or in the instrument control configuration will necessarily involve real difficulty, inconvenience and expense.

Although the future is difficult to predict, change is inevitable. In the eleven-year history of our microprobe, an average of

seven thousand dollars a year has been spent on modification and upgrading the hardware. With the exception of the sample stage all the major subsystems have been replaced or significantly modified and the instrument is currently operated exclusively in ways which were not envisioned when it was delivered in 1963. Our laboratory is by no means unique in this respect as a review of the instrumentation sessions of this meeting over the years will indicate. Currently available proprietary interfaces will clearly present a substantial obstacle to necessary changes in systems configuration in the future.

As was the case with the NIM standard for modular instrumentation, the most promising solution for this interfacing problem comes to us from the Nuclear Physicists in the form of a standard for interfacing called CAMAC which could be an acronym for computer-automated measurement and control.[1,2,3] It should be clear that CAMAC is not a trade name for equipment but rather a very detailed set of specifications for the electrical, mechanical, and functional characteristics of instruments which handle data exchanged between a system controller and a process. It is a modular interfacing system involving plug-in units mounted in a standard chassis or crate. Each plug-in unit occupies one or more mounting stations in the crate. At every station there is an 86-pin socket which provides access to buss lines for data, control, and power. The stations are 17.2 mm wide which is exactly half the width of the NIM single width module and an adapter plug will allow a NIM module to be installed in a CAMAC crate. Each plug-in in the crate is individually addressable with provisions for addressing up to 16 registers within each. Thirty-two functions may also be controlled in each plug-in. The attempt to fully utilize this ample data and command structure will tax the ingenuity of the designers of micro-circuits for some time to come. Data is transmitted in separate 24-bit read and write busses making possible data transmission rates substantially exceeding the rate at which current minicomputers receive it even in DMA mode. It is not my purpose to give a comprehensive description of CAMAC other than to indicate that it is compact, fast, not likely to become obsolete, non-proprietary, and most important an international standard for interfacing.

The CAMAC system for our ARL-SEMQ will perform the following functions:

1. Control 4 crystal spectrometer stepping motors.
2. Control 3 sample stage stepping motors.
3. Control 3 magnetic lens power supplies.
4. Control the high voltage supply as well as the filament current and bias voltage.
5. Control the base line and window width for 6 pulse height analysers.
6. Provide scalers for 6 spectrometers and a beam or sample current integrator.

7. Control 10-bit accuracy deflection for both x-y raster generation and beam location.

8. Provide system timing.

9. Provide inputs for all necessary limit switches.

All these control and data acquisition functions will be accomplished with 14 plug-in units which will occupy 23 stations of the crate. The remaining two stations are occupied by the crate controller which is plugged directly into the PDP/11 Unibus™. Thus, one standard 14-inch rack position will house the entire control and data acquisition for a rather completely automated system.

However, space was not a primary consideration when this system was planned. Our purpose in selecting CAMAC was: 1) to facilitate the system changes which we know already will be required during the life of the instrument, 2) to simplify our system maintenance problems since the plug-in units are simple to trouble-shoot, and 3) start to eliminate the "Tower of Babel" syndrome which has already set in for other automated instruments in our laboratory.

At present in one department we have five different computer-automated instruments. The computers are PDP/8's and PDP/11's but each of the five interfaces is different and four are hardwired and proprietary units. Both system modification and maintenance has become a headache and often a nightmare. CAMAC's fixed specifications will do much to eliminate both problems since only one set of rules for data transmission and control needs to be learned. As a matter of laboratory policy, whenever it is feasible, CAMAC will form the basis for all future laboratory automation efforts.

In summary, the automation of microprobes has come of age and with it the need for the standardization of interfacing has become clearly apparent. CAMAC appears to fulfill this need admirably. It has a well-developed technology with over 800 products available from 60 manufacturers in 10 countries. It is an accepted inter-national standard and significant work has already been accomplished in generating standard high-level language subroutines for it. Change may well be inevitable but CAMAC gives us the tools to cope gracefully with our part of it.

References:

1. CAMAC Tutorial Issue, IEEE Trans. on Nuc. Sci., V. NS-20 No. 2, April 1973.

2. "CAMAC - A Modular Instrumentation System for Data Handling", TID-25875, U.S.A.E.C., July 1972.

3. "CAMAC - Organization of Multi-Crate System", TID-25876, U.S.A.E.C., March 1972.

APPLICATIONS WITH A COMPUTER CONTROLLED ELECTRON PROBE MICROANALYZER SYSTEM

Okudera, S., Ohyi,H., Harada,Y.

JEOL LTD. Akishima, Tokyo, 196, JAPAN.

Along with the advancement of the electron probe micro-analyzer (EPMA), its application covers a wide field and then, various analyses that are new to the EPMA have been more and more required. To meet the demand of the individual field, we have developed a new complete computer control system for the JXA-50A electron probe microanalyzer. The system consists of a JXA-50A, an interface, a minicomputer having 12k memory, peripherical devices and specially developed conversational language named "JECASS-X".

All functions including crystal position displacement, crystal exchange for the spectrometers up to three channels, counters and a timer, X,Y and Z axes position displacement for the specimen stage, an electron beem shutter and probe current digital read out, are controlled by the computer through the interface.

As the software, a special conversational computer language "JECASS-X" (JEol Computer Automatiom System Software for X-ray microanalyzer) is provided for this system. Since the JECASS -X is a high level language as the FORTRAN, users can easily compose programs for his own analyses.

One of unique features of the system is a series of instru-mental corrections that play major role to ensure the accuracy within one percent of relative error for major elements in the quantitative analysis. As the instrumental corrections, the probe current, background and dead time corrections are provided. Especially, due to the probe current correction, the fundamental data such as peak intensities of standard

specimens might be able to be used at least week to week
basis, not day to day basis with satisfactory accuracy.

The typical analyses with the computer controlled EPMA are
as follows.

1. Qualitative Analysis

Major considerations for the qualitative analysis with
wavelength dispersive spectrometers are number of elements. to
be analyzed, time required for the analysis and to set the
spectrometer right on a peak position.   In a case, measuring
time including typeout was 270 sec for 105 elements (actually
preset positions) and one second of sampling time with three
spectrometers.   The program for peak position setting is
provided.

In an application to a stainless steel specimen, 0.22% of
Co and 0.075% of Cu can be readily detected with 0.01 micro-
ampare of the probe current.   If the number of elements to
be analyzed can be limited, say 30 to 40, either the probe
currentcan be reduced with better resolution or the limit of
detectability can be improved by using long sampling time,
with fixed measuring time.

As compared with the energy dispersive system, which is
well known as a suitable instrument for qualitative analysis
because of its simplisity in operation, the computer contrlled
wavelength dispersive spectrometer is far superior to the
energy dispersive system for bulk specimens in terms of the
limit of detectability, spectrum resolution, light element
analysis for lighter than Mg, analyzing time in the case of
trace element analysis, etc..

2. Quantitative Analysis

For quantitative analysis, several correction methods are
provided.   Generally, for oxide mineral specimens, on-line
Bence & Albee method is applied and on-line or off-line ZAF
for metal and others.   On-line program for determination of

mineral molecular formular is also provided for oxide mineral specimen.

Since all procedures in the analysis such as peak searching, stage positon displacement for X, Y and Z axes, are on-line controlled, the analysis can be completed without any manual operation. Of course, debugging of data is possible at any moment in the sequence of the analysis, if necessary.

3. Others

Trace element analysis with better sensitivity than conventional method using a rate meter, empirical calibration curve method with instrumental corrections, two dimentional area analysis with Z axis calibration are also provided.

With the provision of the system language "JECASS-X", the total system is now completed as the real user's oriented system.

Details will be presented.

AUTOMATION OF AN ELECTRON PROBE FOR BIOLOGICAL ANALYSES

T. Moher, C. M. Aden, R. Beeuwkes, A. Sanderson, and C. Lechene

Biotechnology Resource in Electron Probe Microanalysis,
Laboratory of Human Reproduction and Reproductive Biology
Department of Physiology
Harvard Medical School, Boston, Mass. 02115
and Division of Engineering and Applied Physics
Harvard University, Cambridge, Mass. 02138

Quantitative analysis of the elemental content of picoliters-size liquid samples by the electron probe is becoming a powerful tool for physiologists. The method we have described (1, 2) is now being applied in renal physiology (3, 4), and reproductive biology; it will likely be expanded to other areas of biological research. Full use of the electron probe capability requires the automation of data acquisition and data manipulation. There the high price of the instrument is justified by the great number of measurements it can uniquely provide.

In many microprobe automation schemes, a mini-computer is used to handle the process-control of the probe, with data analysis taking place either at a later time on the mini-computer, or on a larger, typically time-shared, system. In this way, the mini-computer is totally "dedicated" to the task of acquiring data during the run, and is unavailable for other uses during that time.

We have developed an integrated system which combines the function of processed control of the electron probe and automated data acquisition with the capability for data manipulation. In our system these two functions operate "simultaneously," enabling the user to acquire data at the same time he is working with data already acquired on the actual run or on any previous run.

I   System Description

    A.   Components –

       Our hardware configuration is as follows:
       - Cameca MS 46 electron probe with four spectrometers and an automated specimen stage (custom-built; stepping motor-driven)
       - Hewlett-Packard 2100A mini-computer with 24 K of core memory (16-bit) and Hewlett-Packard 7901 disc drive with removable cartridges (1.25 million words/cartridge)
       - Tektronix 4012 graphics display terminal with Tektronix 4610 hard copy unit
       - Custom-built computer interface and scalers/timer (Harvard Electronic Design Center).

    B.   Hardware Features –

       We have developed the hardware and electronics to:
       i)   control the position of the specimen stage (in all three

dimensions) either manually-or from computer;
ii)   monitor the electron beam current and other signals (such
      as pulse height analyzer discriminator level); and
iii) control the setting of the four spectrometers (under final
      testing).

Two features of the hardware are particularly significant. First,
process-control and data acquisition require a minimum of computer
resources. The hardware stores the specimen stage position, and
will automatically drive stepping motors to move the stage to any
"stored" location, interrupting the computer only when the movement
is completed. Likewise, once the computer has started the scalers
counting, it is completely unencumbered until the counting time
has expired. Second, the automation does not obstruct manual
operation in any way; the operator can run the probe manually, with
the computer recording the significant data.

Finally, we would stress the importance of the automated stage to
biological work. We normally have hundreds of samples on one
specimen block (1, 2), and the savings in time and effort by the
automated stage is invaluable.

C.   Software Features –

The programs have been written to facilitate their use through
interaction with the display terminal. Some of the software features
include:
  i)   Menu-selection. This method of directing program-flow
       presents the user with a list of options from which he
       selects one item by "pointing" at it with cross-hair cursors.
       In this way, the need for typing skills is kept to a minimum,
       and the user is reminded of all the available options.
  ii) Simultaneity. The Hewlett-Packard Real-Time Executive
       multi-programming system has a foreground-background priority
       scheme which allows us to use the computer to its full
       capacity at the same time we are collecting data. Typically,
       a high-priority foreground program controls the probe, taking
       CPU time as it needs it. Since much of its time is spent
       waiting for scalers to count and the stage to move, other tasks
       with lower priorities, such as data manipulation and program
       development, can proceed in the background. The user
       operating in the background need not know that data acquisition
       is even taking place. For security, the two regions are
       hardware- and software-protected from one another.
  iii) Data structure. The data are written in files on the disc
       in a manner that lends itself easily to menu-selection. An
       experiment directory keeps track of experiment files on a
       cartridge, the experiment files keep track of their raw files,
       and, in turn, the raw files point to their reduced files and
       concentration files (see System Usage for definition). The
       user can save or delete data at will, and the system will
       remember what is on the disc cartridge at all times.

II   System Usage

A. Data Acquisition –

For the user sitting down to the display console, the procedure to initiate readings is simple. Through menu-selection (pointing with the cross-hair), the user is asked to identify the experiment and indicate the mode of operation (automated or manual stage). He then types a title and the spectrometer identification. At this point, depending on selectable options, the user may input coordinates or use previously gathered coordinates of the locations of the samples to be analyzed. If not done previously, the user must also input the labels and counting times for the samples, a process greatly simplified by a powerful editing program and menu-selection.

Once initialized, the computer can read and control the scalers and timer, monitor the beam current and control sample (to allow for on-line correction of scaler data due to drifts in current or spectrometers), and control the movement of the automated stage without further operator intervention. Moreover, since the stage coordinates of each sample are retained on the disc, these same samples can be re-analyzed for different elements or under different operating conditions without further specification. Once the automation of the spectrometers is completed, we will be able to make round-the-clock use of the electron probe.

B. Data Manipulation –

The user is able to work with any of the previous experimental data stored on the disc at any time in one of three forms:
   i)   the raw file – the actual counts as they come off the scalers, appropriately labelled;
  ii)   the reduced file – derived from the raw file, consisting of the mean and standard deviation of aliquot samples, minus background (the facility exists to save several reduced files for each raw file); or
 iii)   the concentration file – derived from the reduced file, consisting of elemental concentration in the sample given in mM/1.

The user has the ability to list files, edit files, label files, draw standard curves, plot beam current or control counts for selected samples, and move easily from one form of the file to another. A statistical package provides least squares regression, correlation, paired and non-paired comparison of means, and histograms of files or selected portions of files or of their algebraic transformations as input directly by the user, who is thus able to use the display screen as a "scratch pad" to investigate potential mathematical relationships.

III   System Performance

In liquid droplet experiments (1, 2), an analysis of 150 samples takes about five minutes from completion of the automated readings until

standard regression curves and experimentally-determined elemental concentrations are displayed.

In an analysis of red blood cells, we count 300 cells for forty seconds apiece. The run takes approximately four hours using the automated stage, with no operator intervention required. The data is "reduced" in about two minutes and selected histograms of elements and ratios of elements take about thirty seconds apiece to produce. Another run on the same samples with counting time of, for instance, 120 seconds can then be started to run all night.

In conclusion, electron probe microanalysis is a method which could provide the biologist with measurements unobtainable by other means; these measurements can be made on ultramicro volumes (picoliters); they can quantitate all the chemical elements of atomic number greater than 6; and they are physically correlated within the same samples due to the non-destructive nature of the method.

The automation of the electron probe and of the data acquisition process makes it very easy to operate for the biologist, and the automation of the data reduction provides on-line results in an immediately useable form.

References

1) Lechene, C. The use of the electron microprobe to analyse very minute amounts of liquid samples. Proc. Fifth Nat. Conf. on Electron Probe Anal. 32A – 32C, 1970.

2) Lechene, C. Electron probe microanalysis of picoliter liquid samples. In Microprobe Analysis of Cells and Tissues, edited by Theodore Hall, Patrick Echlin, and Rudolf Kaufmann, pp. 351 – 368. Academic Press, London, in press.

3) Agus, Z. S., L. B. Gardner, L. H. Beck, and M. Goldberg. Effects of parathyroid hormone on renal tubular reabsorption of calcium, sodium, and phosphate. Am. J. Physiol. 224:1143 – 1148, 1973.

4) Fernandez, Pedro C. and Jules B. Puschett. Proximal tubular actions of metolazone and chlorothiazide. Am. J. Physiol. 225:954 – 961, 1973.

Acknowledgment

AUTOMATED ELECTRON MICROPROBE
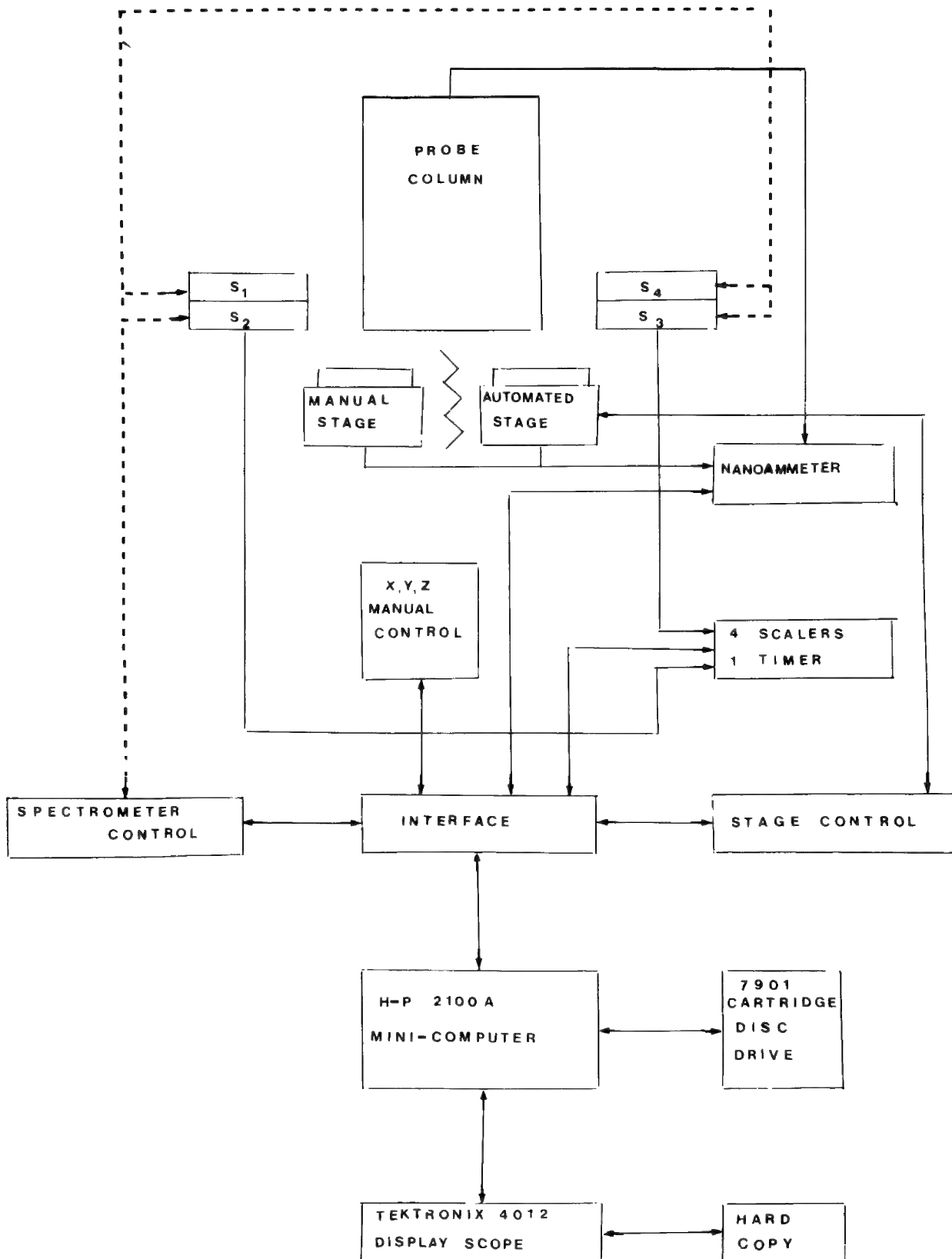
ELECTRON MICROPROBE COMPUTER IMAGING

W. B. Estill
Materials Characterization Division 8314

H. D. Jones
Numerical Applications Division 8441

D. Benthusen
Device Studies Division 8342
Sandia Laboratories, Livermore

Conventional electron microprobe X-ray images are obtained by scanning the electron beam across a sample and collecting the resulting X-ray signal. Data obtained in this manner is often noisy and has little quantitative value. A new technique, called "Electron Microprobe Computer Imaging" (EMCI) produces X-ray images that are comparatively less noisy. Moreover, the X-ray data can be analyzed quantitatively and standard image processing techniques can be used to improve resolution.

The EMCI technique is carried out by means of an ARL automated electron microprobe.[1] Typically, 1600 X-ray intensity measurements are obtained in a grid pattern covering the area of interest. The X-ray intensity grid is prepared by either moving the sample or moving the electron beam (stepwise) and counting at each location a certain amount of time (1 second is usually sufficient).

The resulting X-ray data is transferred to the CDC 6600 computer for smoothing and image enhancement. The X-ray image represented by the smooth data can be plotted on a Calcomp microfilm plotter, in which case the relative elemental concentrations are represented by the 31 grey levels available on the plotter. The data can also be plotted using the Xynetic

plotter, which produces a color image that relates elemental concentrations to one of ten colors.

If quantitative information is desired, the smoothed data can be corrected by a computer correction procedure such as MAGIC.[2] A quantitative elemental X-ray image results.

The EMCI technique is an extremely valuable tool in studying the chemistry and spatial distribution of elements in micro-inclusions and grain boundaries. For example, Figures 1 and 2 illustrate how the EMCI technique is of considerable aid in the familiar though difficult microprobe analysis of a shallow concentration gradient, particularly when the gradient extends only a short distance from its source. Figure 1 is an EMCI (CrKα) image of a 309 stainless steel sample containing a stringer of Cr_xC_y that began to dissolve during solution treatment at 2100°F, but dissolution was arrested by water quenching.[3] Figure 2 shows the sparse data available from a conventional X-ray microprobe image (CrKα) of the same sample area.

EMCI (Cr Kα)

Figure 1.

Cr Kα
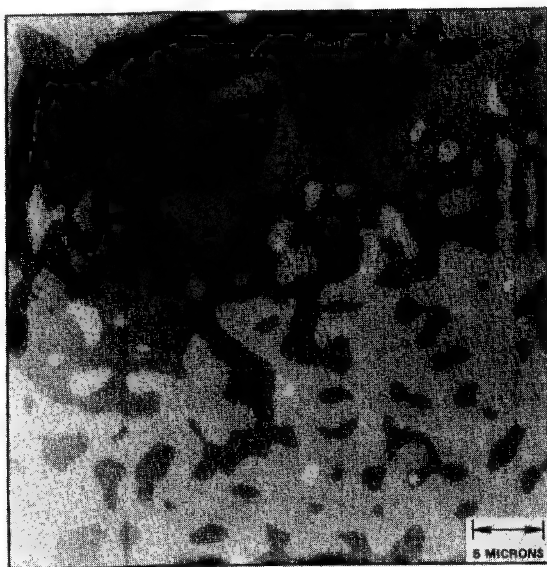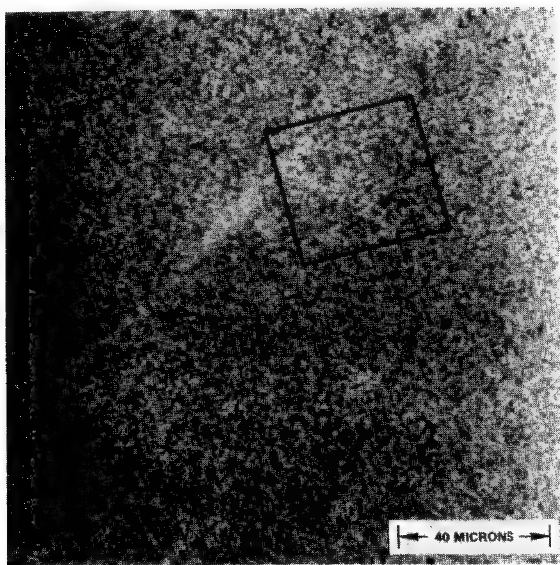
Figure 2.

[1]Estill, W. B., Benthusen, D. E., and Jones, H. D., Proc. 8th Nat'l Conf. on Electron Probe Analysis (1973).

[2]Colby, J., "A Computer Program for Quantitative Electron Microprobe Analysis."

[3]Thompson, A. W., private communication.

DATA REDUCTION SYSTEM FOR ELECTRON
PROBE MICROANALYSIS

Everett D. Glover

Department of Geology & Geophysics, Science Hall,
University of Wisconsin, Madison, Wisconsin, 53706

A data reduction and correction system for the unautomated probe
has been in operation at the Department of Geology and Geophysics for
the last three years. It features versatility in handling probe data
for most types of probe problems where there is a limitation on the
number of elements analyzed conveniently at one time on one sample
point.

It is a hybrid system designed for timer-scaler outprint to an
electric typewriter plus card punch with correction programs presently
including (1) direct comparison to a standard or to several standards
least square fitted; (2) Bence and Albee application (1) of Ziebold-
Ogilvie, Castaing empirical method; and (3) J. W. Colby's Magic IV (2).
Any other correction program desired may be grafted onto main data
reduction program as a sub-routine. Details of the data system and the
correction programs written, as well as the adaption of previously
written programs of others are briefly described.

Data System

The heart of this system is a 10-digit encoder, which can be hand
set at the probe console, to label each count set taken. The 10 digits
allow complete description of the count set (punched card) so that order
in the set of data cards is never necessary. The data on the cards is
arrayed by the software. The coding system, except for the 'complete-
ness in description' feature is similar to those of Boyd et al (3) and

Rucklidge (4). The encoder uses part of two 7-digit cycles of the 'data translator' to print the 10-digit code and is similar in construction to that of Rucklidge (5). The card punch operates through 10 relays directly off the output to the typewriter solenoids. The code comprises the following:

Digit 1, peak or background on sample or standard

Digits 2-7, atomic numbers of 3 analyzed elements

Digit 8, 9, sample number

Digit 10 'standard set' or 'standard repetition' number

This latter (Digit 10) allows accumulation of up to 9 sets (repetitions) of any group of 1-3 standard elements, with subsequent assignment of any combination of 'standard sets' (up to 5) for the analyzed elements to any block of samples. No interpolation between standard sets has been found necessary. Normal drift is compensated for by 'beam current' control of counting, while abrupt changes may be best compensated for by recording a new standard set.

Other features of the system include options for background subtraction for single or groups of samples, option for correcting a block of samples in a large data deck, option to print Fe as FeO or Fe_2O_3 when oxide analysis is done and an extensive statistical section. Among the statistics enumerated are mean and ordinary standard deviation based on up to 20 counts (for peak or background on standard or sample); calculated standard deviation of the mean values of standards and samples, background and dead time corrected counts, and the calculated standard deviation of the mean of the count ratios for each element.

The main program, dubbed 'Genie' arrays the data, does statistics listed above and delivers the count ratios to the chosen sub-routine.

Genie 1: Theoretical correction

After data reduction by the Genie main routine this program uses J. M. Colby's MAGIC IV as a sub-routine to correct up to 8 elements plus

one by difference. The output has been slightly changed to make it more useful for mineral analysis. Output are (1) estimated concentrations (count ratio multiplied by concentration of analyzed element in standard), (2) correction factors for absorption, electron penetration, backscatter and fluorescence based on the _actual_ _standard_ used. Colby's original MAGIC IV gave correction factors with respect to the pure element as standard. Thus the product of the estimated concentration and the product of the correction factors equals output concentration. In addition, concentrations appear also as oxides and formula calculation for oxide minerals is carried out if oxygen is present and if the number of oxygens in the formula for each sample is input.

Previously the Goldstein-Comella program (6) was used in the Genie 1 theoretical subroutine. This will correct 9 elements at a time rather than the 8 of MAGIC IV.

Genie 2: Empirical method

The subroutine here makes correction for up to 10 elements by the Bence-Albee empirical oxide system for 36 elements (additional $\propto$ factors for other elements are now available, Chodos, (7)). Options are (1) correction of anhydrous minerals with Fe present as Fe^{++}, (2) correction of minerals bearing H_2O, OH or Fe^{+++}. In the latter case 4 iterations are completed, then the total is subtracted from 100% and the difference assigned to "water" or "excess oxygen" before completing iterations to convergence; or, alternatively, the water or 'excess oxygen', analyzed for separately, may be input. Output includes concentrations as oxides and a mineral formula as in Genie 1.

Genie 3: Direct comparison

In this program samples are compared to a standard for each element or to several standards least square fitted. The program is set up to run 1 to 3 elements at a time with a total of up to 10 different standard concentrations. Output are concentrations and parameters of the goodness of fit of the least square fitting.

Summary

The versatile data reduction system described has been in operation successfully for several years. Using it statistical computation is applied to X-ray count data and averages are corrected.

It is open-ended in the sense that new correction programs can easily be grafted on the data reduction system as sub-routines. Disadvantages are that statistics are done on count data rather than concentrations and that concentrations usually represent averages for a sample rather than data on a specific sample point. Both of these drawbacks are inherent in the unautomated probe system with analysis done for 1 to 3 elements at a time.

The use of card punch collection of data is slow but very convenient for teaching purposes since punched cards are an easily edited form, and since they are easily prepared for computer input.

References

(1) Bence, A. E. and Albee, A. L. Empirical correction factors for the electron microanalysis of silicates and oxides. J. Geol. 76, 382-403 (1968). See also Albee, A. L. and Ray, L. Correction factors for electron probe microanalysis of silicates, oxides, carbonates, phosphates and sulfates. Anal. Chem. 42, 1408-1414 (1970).

(2) Colby, J. W., MAGIC IV – A new improved version of MAGIC. Proc 6th Nat'l. Conf. Electron Probe Analysis. Pittsburgh, Penn., July 27-30, 1971.

(3) Boyd, F. R., Finger, L. W. and Chayer F. Computer Reduction of Probe Data. Ann Reports of the Geophysical Laboratory, Carnegie Institution, 1967-8, p. 210-215. Washington, D. C.

(4) Rucklidge, J. Documentation of Program EMPADR IV SILGEMIN, 1967. Provided by Rucklidge.

(5) Rucklidge, J. Diagram and Description of encoder. Provided by
       Rucklidge.

(6) Goldstein, J. I. and Comella, P. A. A computer program for elec-
       tron probe microanalysis in the fields of metallurgy and geology.
       Goddard Space Flight Center, April, 1969, Greenbelt, Maryland.

(7) Chodos, A. A. Personal Communication, February, 1974.

Acknowledgements

A REAL TIME APPROACH TO LABORATORY AUTOMATION

W.T. Hatfield, M.F. Ciccarelli, R.B. Bolon & E. Lifshin

General Electric Corporate Research & Development

Minicomputers have been used to automate laboratory equipment for some time. In the case of the microprobe, the approach most often taken by both manufacturers and users has been to couple a dedicated machine to each instrument and build an operating system based on an interpretative language such as Basic or Focal[1-5]. While such languages offer the flexibility of interweaving instrument control commands with mathematical manipulations, the latter are inherently slow if any degree of complexity is required. Furthermore, the cost of additional core and expanded input/output peripherals necessary for rapid program development capability is often difficult to justify for a single system.

This paper describes a minicomputer system which uses a real time operating system to control several instruments simultaneously. The system is centered around an Interdata 70 computer with a 48K byte memory. It is supported by a high speed paper tape reader, two magnetic tape cassette transports, a 1.2 million word disc, a high speed printer and a number of teletypes. The various instruments which are to be controlled are interfaced through a Programmable Asynchronous Line System (PALS), which provides 8 separate lines which can be used to transmit and receive ASCII data at one of 4 software selectable band rates (Figure 1). In addition, the operating system supports a Fortran compiler which makes it possible to write the program for the various instruments in Fortran. The compiler along with a text editor can be run as a low priority task while other programs are running. This makes it possible to do on line program development.

Presently a JEOL JXA-50A combination scanning electron microscope and microprobe, a Cameca microprobe, a Northern Scientific multi-channel analyzer and a Siemens Sequential X-ray Spectrometer have been interfaced. In the near future, a Siemens pole figure goniometer, a Joyce Loebel microdensitometer and Rigaku Denki diffractometer will be added to the system.

1. P. Duncumb, Quantitative Microprobe Analysis: 5th National
    Conference on Electron Probe Analysis, New York 1970 (EPASA 1969)

2. A.A. Chodos and A.L. Albee, Quantitative Microprobe Analysis
    and Data Reduction Using an On-line Minicomputer: 6th National
    Conference on Electron Probe Analysis, Pittsburgh, Pa., 1971
    (EPASA 1971)

3. J.W. Colby, Microprobe Analysis Integrated Automation Computer
    System: 7th National Conference on Electron Probe Analysis,
    San Francisco, Calif., 1972 (EPASA 1972)

4. L.W. Finger and C. Hadidiacos, Computer Automation of an
    Electron Microprobe: 7th National Conference on Electron
    Probe Analysis, San Francisco, Calif., 1972 (EPASA 1972)

5. W.F. Chambers, The Sandia Approach to Electron Probe Auto-
    mation: 8th National Conference on Electron Probe Analysis,
    New Orleans, La., 1973 (EPASA 1973)
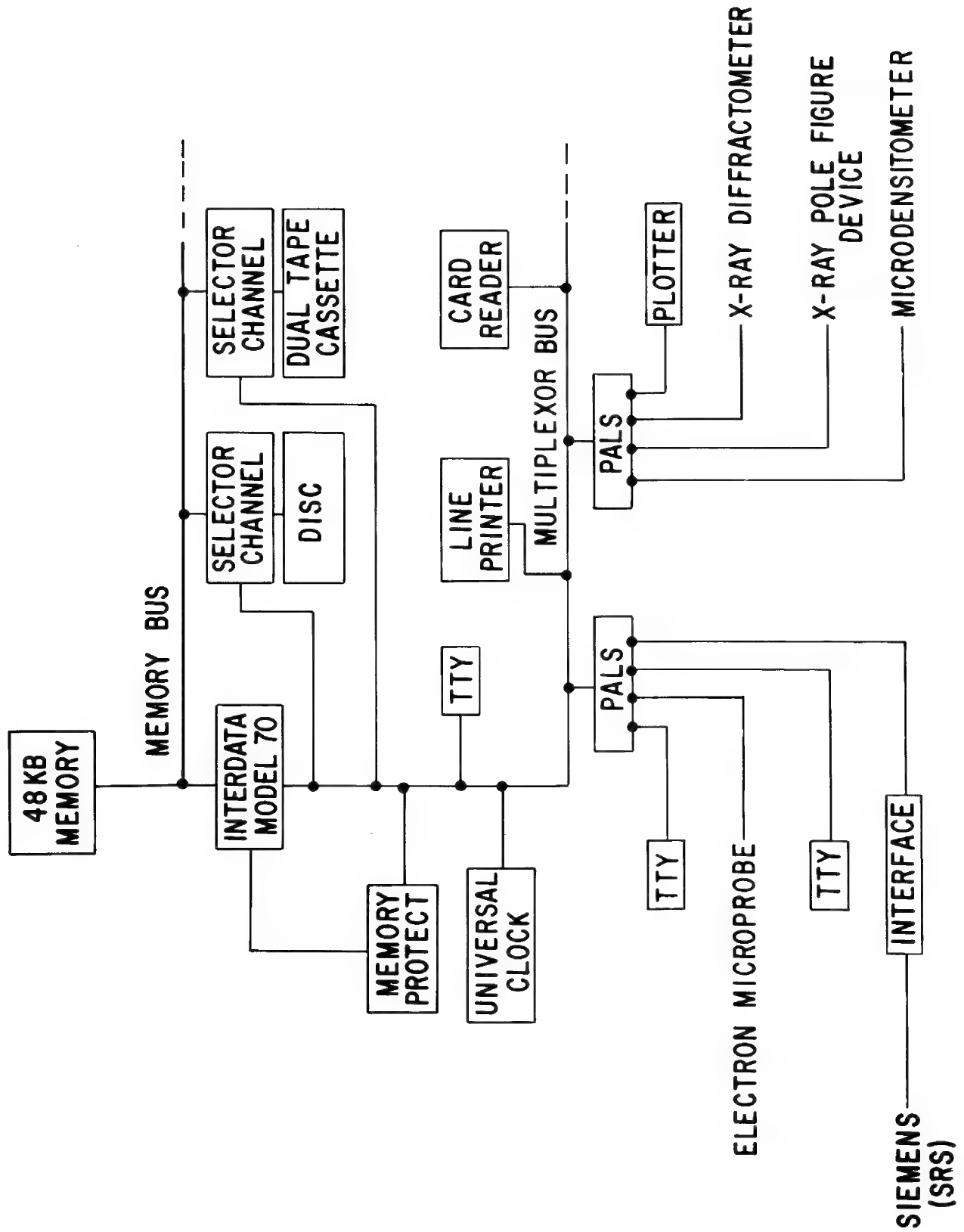
48KB MEMORY

MEMORY BUS

INTERDATA MODEL 70

SELECTOR CHANNEL — DISC

SELECTOR CHANNEL — DUAL TAPE CASSETTE

MEMORY PROTECT

UNIVERSAL CLOCK

TTY

LINE PRINTER

CARD READER

MULTIPLEXOR BUS

PALS

PLOTTER

X-RAY DIFFRACTOMETER

X-RAY POLE FIGURE DEVICE

MICRODENSITOMETER

PALS

TTY

ELECTRON MICROPROBE

TTY

INTERFACE

SIEMENS (SRS)

Quantitative Electron-Probe Analysis: Review of Iterative Procedures and Evaluation of Electron Backscattering

G. Springer
Falconbridge Metallurgical Laboratories, Thornhill, Ontario, Canada

Two topics in quantitative electron probe analysis will be discussed in detail: improvements in the iterative procedures and the evaluation of electron backscattering factors.

1. Iterative Procedures

The X-ray intensity ratios that are obtained with an electron-probe micro-analyzer are converted to concentration ratios by applying correction factors. Since these factors are dependent on the unknown concentrations iterative procedures are commonly employed to determine their true values.

A recent survey (1) of computer programs used to correct electron-probe data lists the so-called "simple" method of iteration most frequently and reflects considerable favour for the "Wegstein"(2) and "hyperbolic"(3) procedures. A "spiral" procedure for ternary systems has also been described (4). Each of these methods seems to reach convergence in virtually all practical applications and there is no clear indication which one should be given preference.

In the simple method, calculated concentrations from the proceeding iteration cycle are used as input for the new cycle. This mode of successive approximations to the solutions of a set of equations is equivalent to the well-known Jacobi or Gauss-Seidel methods in numerical analysis, but the rate of convergence is slow and, in certain instances, convergence may not be reached at all.

It can be demonstrated that both the Wegstein and the hyperbolic procedures are modifications of the renowned Newton method for finding roots of equations. The derivative of the correction function is required

in this case. According to Wegstein it is assumed that the derivative is sufficiently closely represented by a difference ratio. The same supposition holds for the hyperbolic procedure with the additional constraint that the correction factor is unity if the concentration of the analyzed element is 100%. This latter condition may not always be fulfilled, in particular if standards with compositions widely different from the specimens are used; it can be shown that quite erroneous results may be obtained in some instances.

2. Electron Backscattering

Electron-backscattering factors are required for the atomic number corrections. In general they are computed from polynomial expressions (5,1). Examination of the original, measured data and theoretical considerations show that simpler expressions can be devised without sacrifice in accuracy.

REFERENCES

1. D.R. Beaman, J.A. Isasi, Anal. Chem., 1970, 42, 1540.

2. S.J.B. Reed and P.K. Mason, Transact. Second Natl. Conf. Electron Microprobe Analysis. Boston, 1967.

3. J.W. Criss and L.S. Birks, The Electron Microprobe, John Wiley, New York, 1966.

4. K. Matsabura, Proc. 6 Intern. Conf. X-ray Optics and Microanalysis, Univ. Tokyo Press, 1972.

5. G. Springer, Fortschr. Mineral. 1967, 45, 111.

The Measurement of Depth Distribution Curves
at Electron Energies from a few to
15 keV

by

J.D. Brown and L. Parobek

Faculty of Engineering Science and
Centre for Interdisciplinary Studies in Chemical Physics
The University of Western Ontario
London N6A 3K7 Canada

Knowledge of the characteristic x-ray production as a function of depth in a specimen ($\phi(\rho z)$ curves) permits the establishment of all the corrections used in quantitive electron probe micro-analysis. These curves have been measured by a number of authors (1,2,3,4) for electron energies above 15 keV. Only one measurement has been made at lower energies and that at 13.4 keV(1). To provide data for comparison with the present correction equations as they apply at lower electron energies the present measurements of the $\phi(\rho z)$ curves were undertaken.

As electron energies decrease, the depth of x-ray production decreases and problems of film thickness uniformity and mass thickness determination increase. At 10 keV, 95% of the directly produced CuKα x-rays in copper are produced at mass depths less than 250 $\mu g/cm^2$. A quartz crystal monitor whose sensitivity was approximately 2 $\mu g/cm^2$ was used during the evaporation as a first estimate of layer thickness. The actual thickness was determined by weighing, x-ray spectrometry and atomic absorption. The three methods agreed to within the limits of experimental accuracy.

$\phi(\rho z)$ curves were measured for CuKα and SiKα x-rays in Al, Ni, Ag and Au matrices. *f(x)* curves have been obtained from these data and will be compared with the present equations. Data on the atomic number effect will be compared with other data from bulk specimens.

References

1. BROWN, J.D., "Advances in Electronics and Electron Physics", Suppl. 6, p 45 (1969).

2. CASTAING, R. and DESCAMPS, J. J. Phys. Radium 16 304 (1955).

3. BROWN, J.D. and PAROBEK, L., Adv. X-Ray Anal. 16 198 (1973).

4. VIGNES, A. and DEZ, G., Brit. J. Appl Phys., Ser 2, 1 1309 (1968).

Testing and Development of a Monte Carlo Program for Modeling Electron-Specimen Interactions

R. L. Myklebust, D. E. Newbury, H. Yakowitz
and K. F. J. Heinrich
Institute for Materials Research
National Bureau of Standards
Washington, D. C.   20234

The classical theory of quantitative electron probe analysis applies to flat, polished, infinitely thick specimens positioned normally to the electron beam. The theory is inapplicable for any other types of specimen configuration; particularly for those in which any of the specimen dimensions are less than the range of x-ray production by the electron beam. To overcome these difficulties, we have used a Monte Carlo method similar in principle to that of other investigators [1,2] to compute the electron scattering and x-ray intensities from tilted specimens and from cylindrical particles of infinite length and different diameters.

The Monte Carlo procedure used in this work uses a simple Rutherford scattering model for the primary electron-solid interaction. Since inelastic collisions cause the electrons to lose energy with little angular deflection, inelastic scattering can be described by Bethe's energy loss law without consideration of concomitant changes of direction of the electrons. The number of elastic interactions has been reduced to 60 per trajectory in order to save computer time. It should be noted that the Monte Carlo procedure is, for the most part, empirical in nature, and broad assumptions are involved in the scattering and energy loss models.

We use a variable step length between collisions in which the step length is related to the current value of the energy of the electron. The sum of the step lengths for 60 steps is equal to the Bethe range for the incident energy. The effects of a finite beam size and the distribution of electron impacts within the beam have been taken into account by using a Gaussian-distribution random number generator to model the beam (Fig. 1), for which a circle containing 80% of the electrons is defined as the beam diameter [3]. For the calculation, parameters such as the electron beam diameter, the operating potential, the position of the beam center on the specimen, and the composition, size, and orientation of the specimen can be selected.
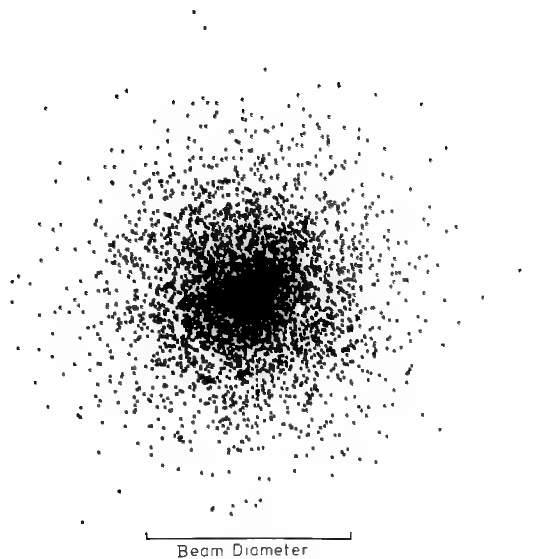
Beam Diameter

Figure 1.   Cross-section of an electron beam as predicted
            by a Gaussian random number generator.   The beam
            diameter contains 80% of the electrons.

This program has been used to study and confirm the mechan-
ism responsible for magnetic contrast of Type II in the
scanning electron microscope, as is described elsewhere in
these proceedings [4].

Several different experiments have been performed to test
the model. The backscattered electron yield from a flat,
thick piece of Fe-3.22 Si was measured in the scanning
electron microscope as a function of specimen tilt.   The
experimental results represented by the solid line in.
Fig. 2 are compared to those of the Monte Carlo calculations
which predict a very similar curve. The model we use is
also useful for the analysis of thin films which are either
on a substrate or free-standing. For example, the electron
backscatter and electron transmission through thin unsup-
ported copper films are plotted in Fig. 3. The solid lines
are experimental data from Cosslett [5], and the points are
the values predicted by the Monte Carlo program.
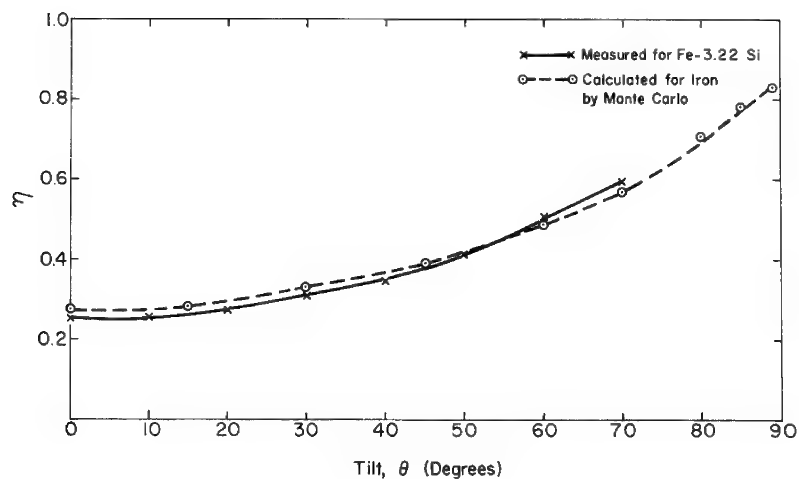
Figure 2.   Backscattered electrons as a function of specimen
            tilt from Fe-3.22 Si. Specimen biased to eliminate
            secondary electron escape.
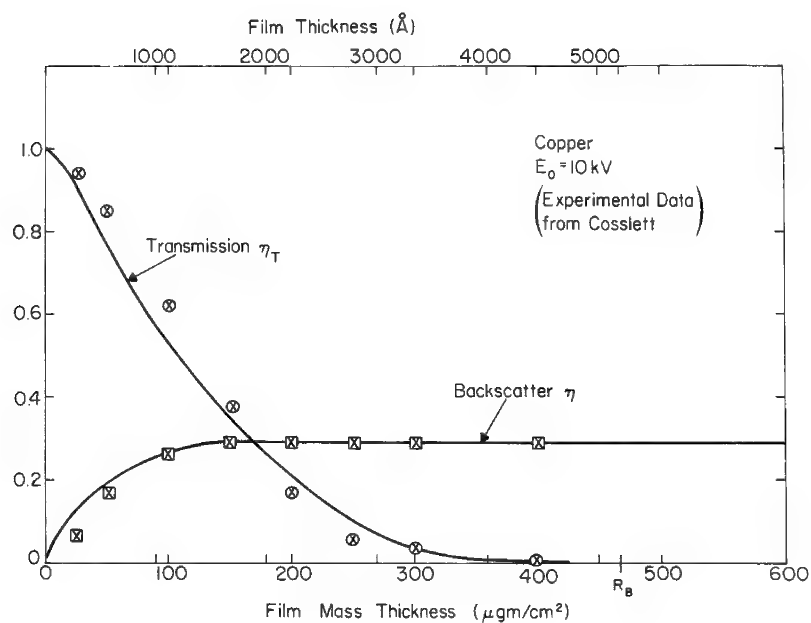
Figure 3.   Electrons backscattered from and transmitted through
            copper foils. The points are the Monte Carlo
            predictions.

Single-element metallic needles of small diameter were pre-
pared by a chemical etching method. These needles were
gradually tapered down to points on the order of 0.2 μm
tip radius. The diameter, x-ray emission, and specimen
current were measured at points along such a nickel needle.
The difference between the beam current, as measured in a
Faraday cup, and the specimen current was called the elec-
tron backscatter even though it includes electrons trans-
mitted through the needle as well as electrons that miss
it entirely. The Monte Carlo program predictions of this
electron backscatter are shown in Fig. 4 together with the
experimental measurements. The x-ray intensity ratio of
NiKα emission from the needle and from a flat specimen
agree well with the Monte Carlo results.

Further program development and experiments are currently
being carried out. In particular, the x-ray emission model
used in the program is being tested further in order to
augment and refine initial results reported by Heinrich
et al. [6].
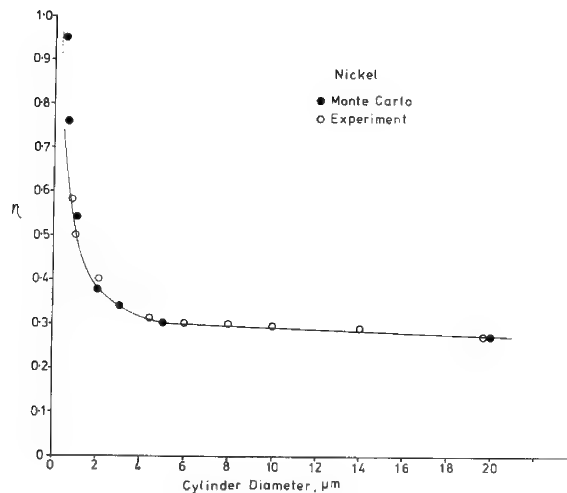
Figure 4. Backscattered electrons as a function of the
diameter of nickel cylinders.

References

[1] Curgenven, L. and Duncumb, P., Tube Investments, Ltd. Research Report No. 303, July 1971. (Available from P. Duncumb, Tube Investments, Ltd., Hinxton Hall, Essex, England.)

[2] Bolon, R. B. and Lifshin, E., in Scanning Electron Microscopy/1973, Proceedings of the 6th Annual SEM Symposium, Johari, O., ed. (Chicago, IITRI, 1973) p. 285.

[3] Brewer, A. L., in Microprobe Analysis, Andersen, C. A., ed., John Wiley and Sons, New York, p. 83 (1973).

[4] Newbury, D. E., Yakowitz, H., and Myklebust, R. L., Monte Carlo Calculations of Type II Magnetic Contrast in the SEM, these proceedings.

[5] Cosslett, V. E., in X-ray Optics and Microanalysis, Castaing, R., Deschamps, P., and Philibert, J., eds., Hermann, Paris, p. 85 (1966).

[6] Heinrich, K. F. J. H., Yakowitz, H., and Vieth, D. L., Proceedings of the 7th National Conference on Electron Probe Analysis (San Francisco, EPASA, 1972) p. 3A.

MICROPROBE TECHNIQUE USING APL FOR NONDESTRUCTIVELY DETERMINING THE CONCENTRATION PROFILE OF Si IN Al/4 Cu THIN FILMS

G. DiGiacomo
IBM System Products Division
East Fishkill Facility
Hopewell Junction, New York 12533

This technique was developed specifically for determining the concentration profile of Si in Al/4 Cu thin films (~ 1 μm); however, it is applicable to other systems. The Si profile within this alloy is created after an ultrathin film of silicon is deposited on the Al/Cu film and sintered under controlled conditions. For a given diffusion activation energy, diffusion coefficient, and film thicknesses, one can obtain desired profiles up to complete saturation by varying the diffusion time and temperature. Microelectronic Al/Cu conductors are saturated with Si intentionally to prevent the solution of silicon from the substrate into the conductor and the subsequent penetration of Al into the substrate. The technique is based on (1) the use of multiple accelerating voltage which allows selective depth analysis of the thin metal film in terms of X-ray intensity (Fig. 1); (2) comparison of the samples' X-ray intensities to a known standard to obtain average concentration vs. depth, and (3) differentiation of average concentration curves to obtain local concentration as a function of depth, namely, the diffusion profile. Profile calculation and plot is effected at an APL/360 terminal in a matter of seconds utilizing a simple program. The program is based on the range equation[1] which expresses the effective depth of X-ray production. The input data consists of the average intensity profile (for which few points need be entered) for sample and standard, accelerating voltage and element voltage threshold, and alloy density. The program
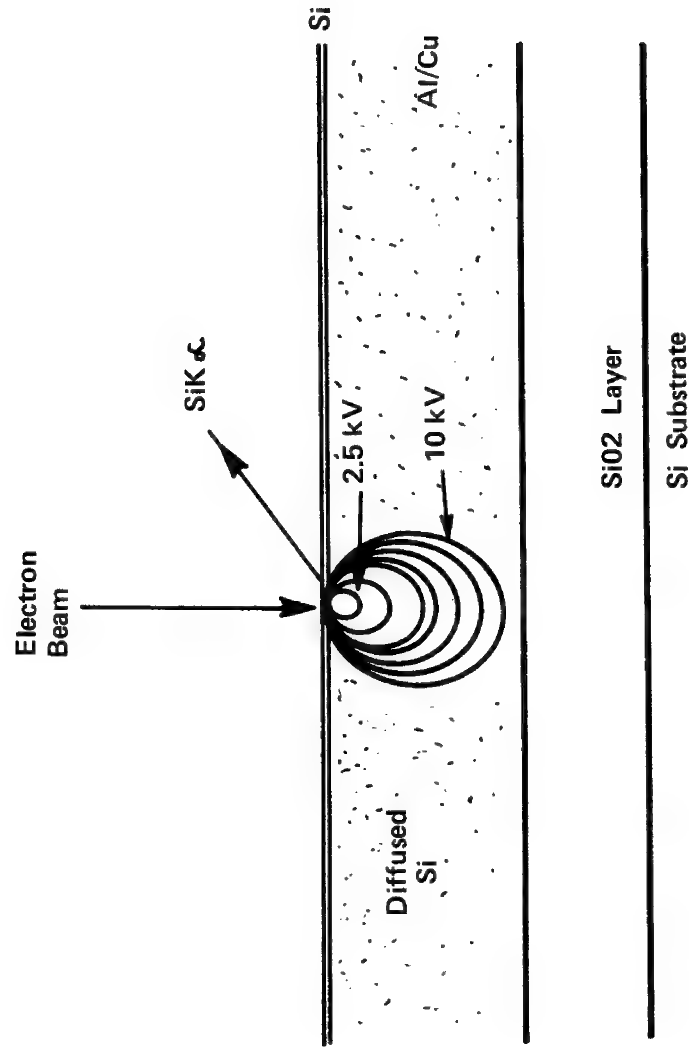
Fig. 1.   Sample structure and principle of measurement.

calculates the following:

1. The average diffusant concentration as a
    function of depth.
2. The local concentration or concentration profile.
3. Total Si content in g/cm^2 or A.%

The depth resolution is ~1000 Å and the gradient sensitivity
is about 0.1%/1000 Å, which is satisfactory for most applica-
tions.

Four groups of samples were prepared at different times to
determine process variation. The copper was co-deposited
with the aluminum to produce a 1 μm thick film containing
3.9% Cu. A silicon film was deposited on each Al/Cu blanket
and then sintered at 400°C to obtain depth concentration
profiles. The silicon film was in excess of the amount re-
quired to saturate the Al/Cu film at 400°C which has a solu-
bility of 0.45% Si. The silicon intensity was measured at
accelerating voltages varying from 2.5 to 10 kV in steps of
about 1 or 2 kV.[2] Pure silicon was used as a standard to
calibrate the Si Kα intensities from the samples which are
generated in an Al/4 Cu matrix. Obviously, the Si intensity
from the sample must be corrected mainly for absorption due
to the high absorption of Si Kα in Al. Atomic number and
secondary fluorescence corrections were neglected before com-
paring with the silicon intensity of the standard. It must be
noted that in any case the films were ≤ 1 μm, appearing infinitely
thick to a 10kV beam.

The silicon intensities from the samples and standard were
plotted vs. the accelerating potential. Because the pure sili-
con standard has no concentration gradient, one can plot X-ray
intensities vs. voltage scaled down to the concentration of
interest, e.g. 2%, to obtain concentration isograms. Figures 2
and 3 show the 2% intensity isogram and the intensities from two
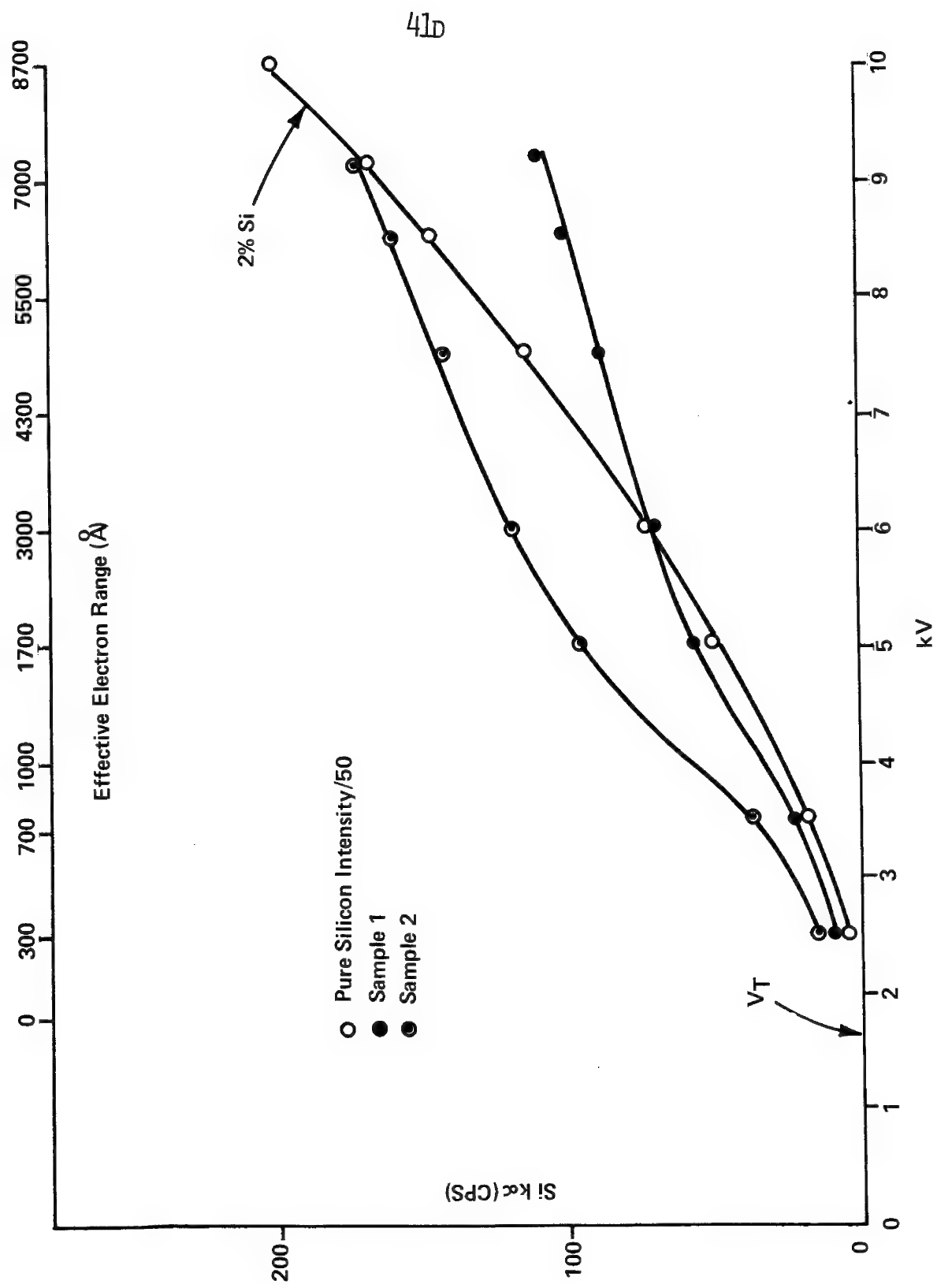
Fig. 2. Silicon X-ray intensity vs. accelerating potential.
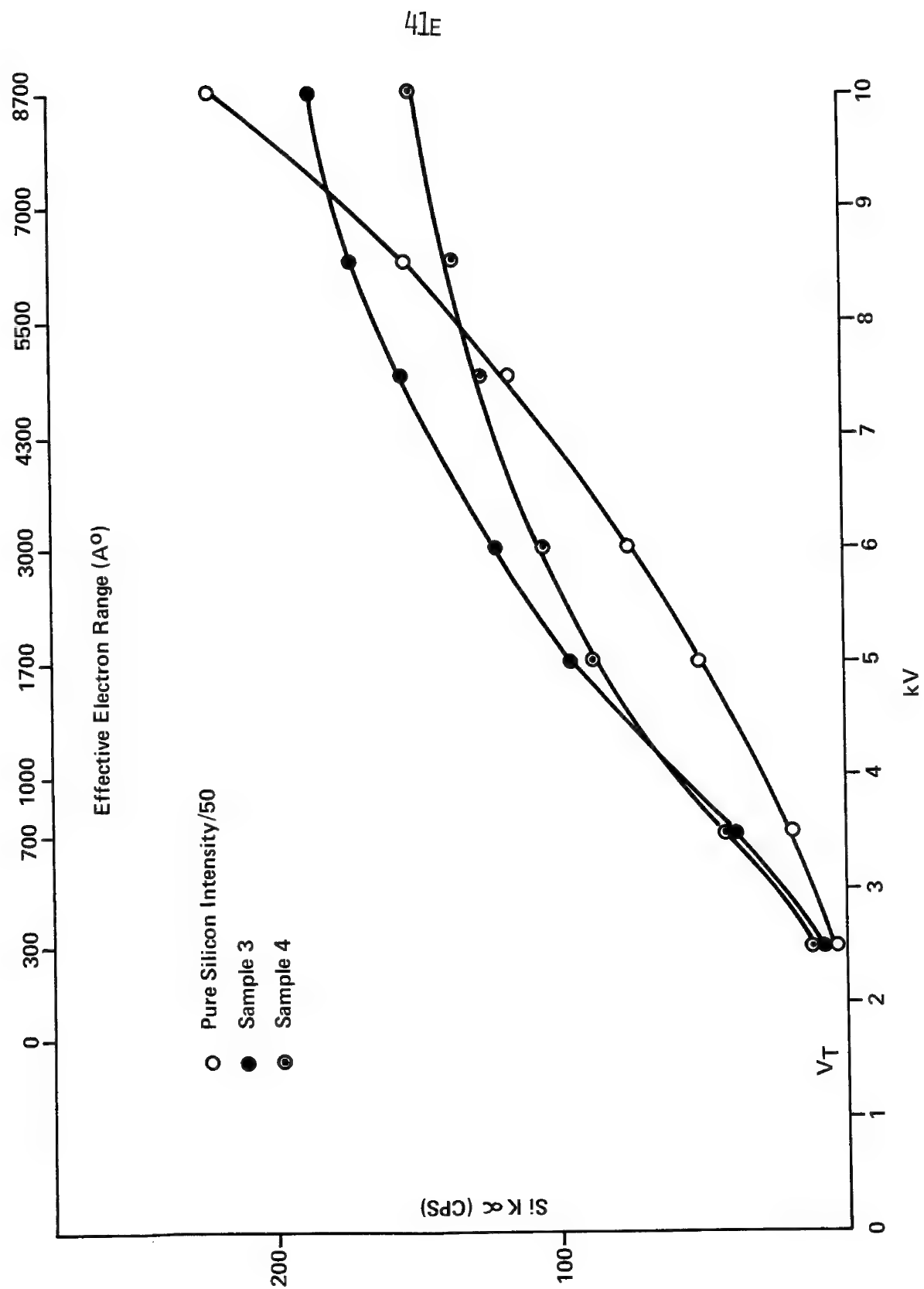
Fig. 3. Silicon X-ray intensity vs. accelerating potential.

samples versus accelerating potential. This data is also
interpreted and calibrated in terms of the effective electron
range scale, which is shown on top [1]. Next, one takes the
ratio of the Si intensity from the sample to that from the
standard at selected voltages to generate curves of average
Si concentration as a function of depth. This means that a
point on the solid curve in Figures 4 and 5 has average Si
concentration as the ordinate, and depth of analysis as the
abscissa. To obtain the local concentration or concentration
profile, the average concentration curve must be differentiated
with respect to depth. Figures 4, 5, and 6 illustrate this
graphically. By definition, the average concentration $\bar{c}$ is:

$$\bar{c}(X) = \frac{1}{X} \int_o^X c(X) dX \qquad (1)$$

from which one can write the differential:

$$\Delta (\bar{c}(X) \cdot X) = c(X) \cdot \Delta X \qquad (2)$$

If the area under the average concentration curve in Fig. 6
is divided into n vertical slices of thickness
$X_n - X_{n-1} = \Delta X$, the local concentration can be determined from
Eq. (2):

$$c(X_n) = \frac{\bar{c}(X_n) \cdot X_n - \bar{c}(X_{n-1}) \cdot X_{n-1}}{X_n - X_{n-1}} \qquad (3)$$

Eq. (3) is applied sequentially to adjacent points along the
curve from left to right to determine the concentration profile.
As mentioned earlier, this is done completely through an APL
program. Since the profile is obtained by a diffusion process,
the technique can be used to determine nondestructively (and on
microscopic areas) the diffusion coefficient on the basis of the
concentration, diffusion time, and geometry for the distribution
function dictated by the problem and boundaries. In the case of
infinite diffusant source and steep gradient, a simple error
function is adequate. In addition, the amount of Si initially
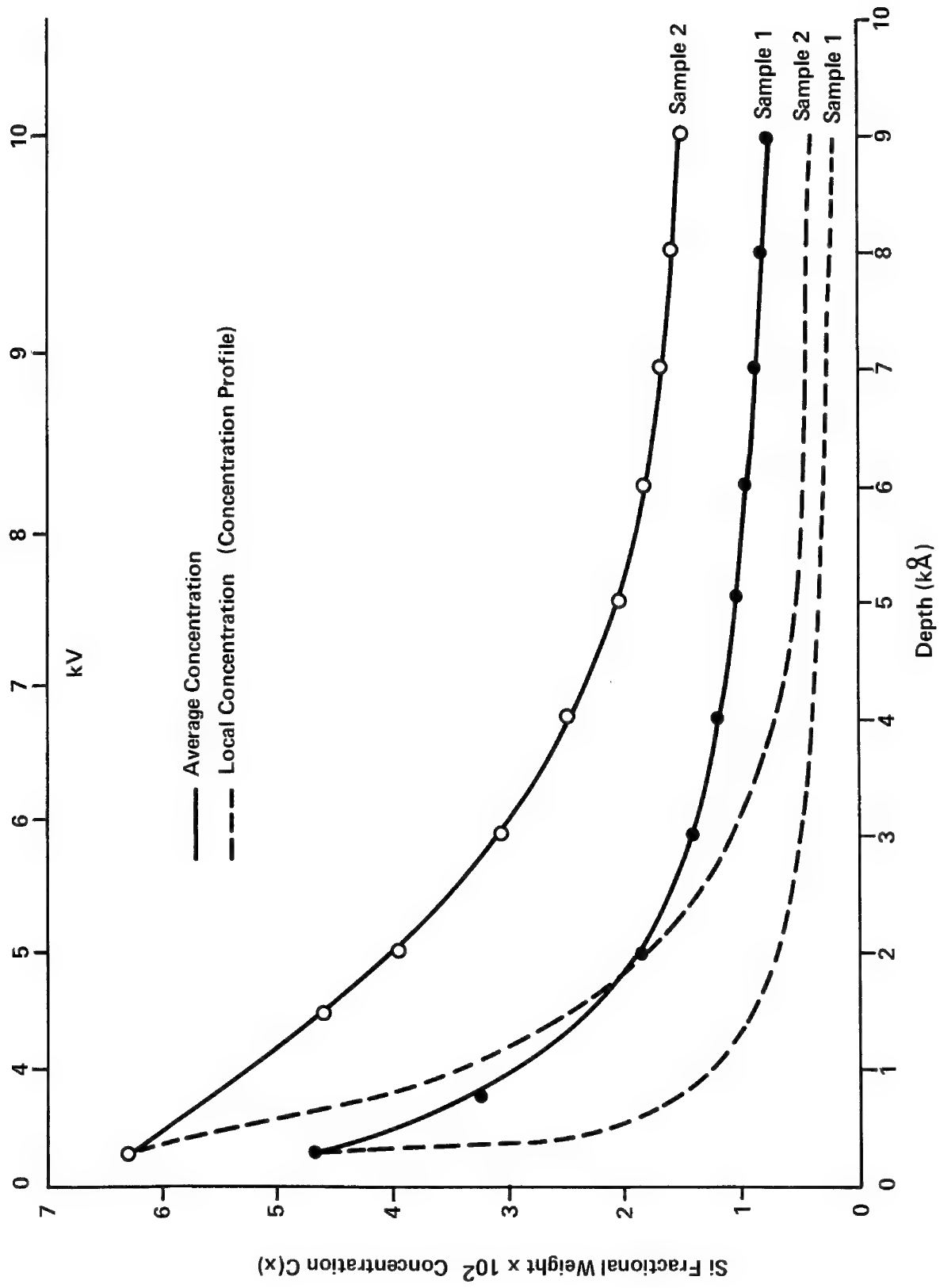
Fig. 4.   Average and local Si concentration vs. depth.
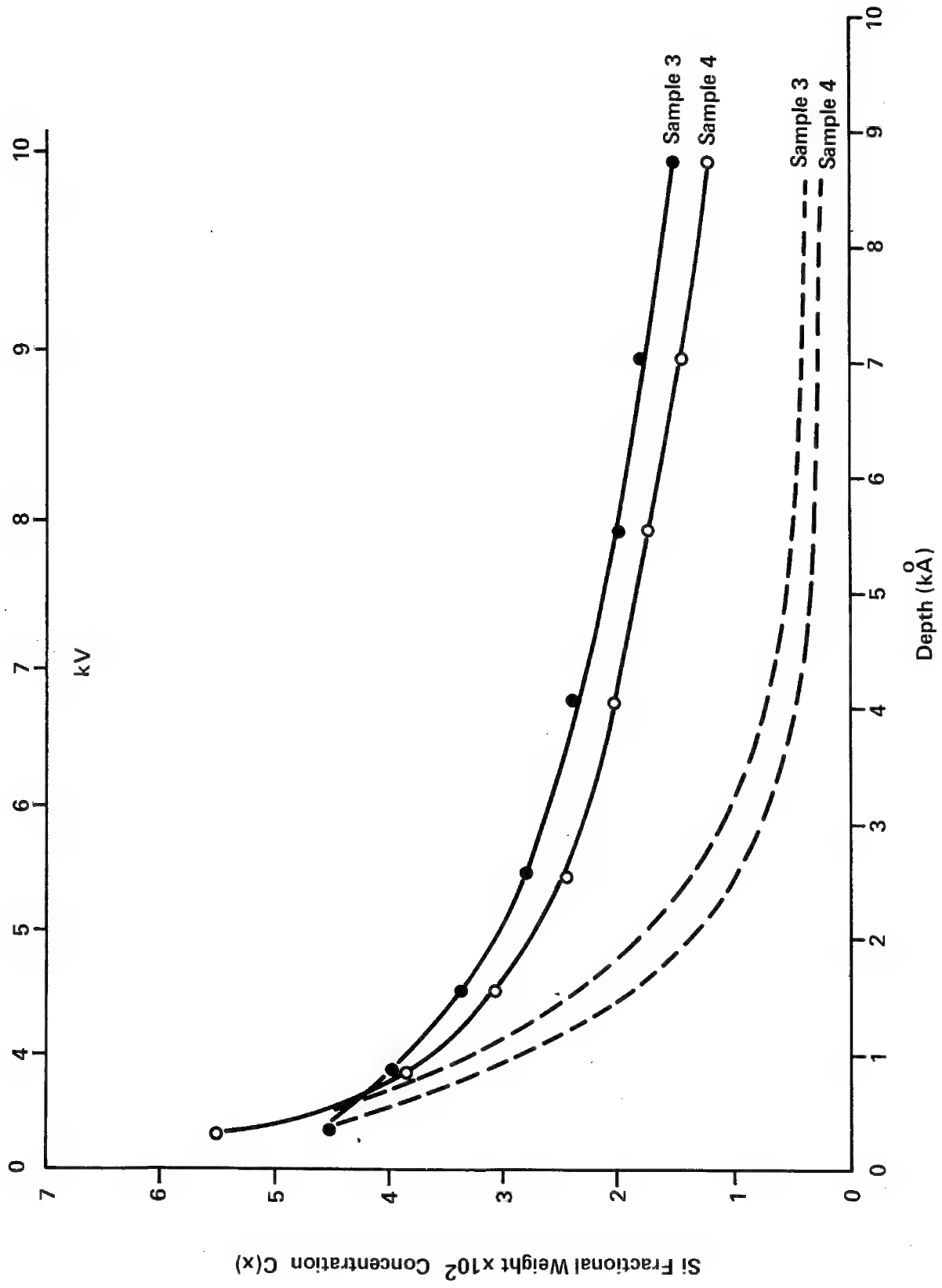
Fig. 5.   Average and local silicon concentration *vs.* depth.
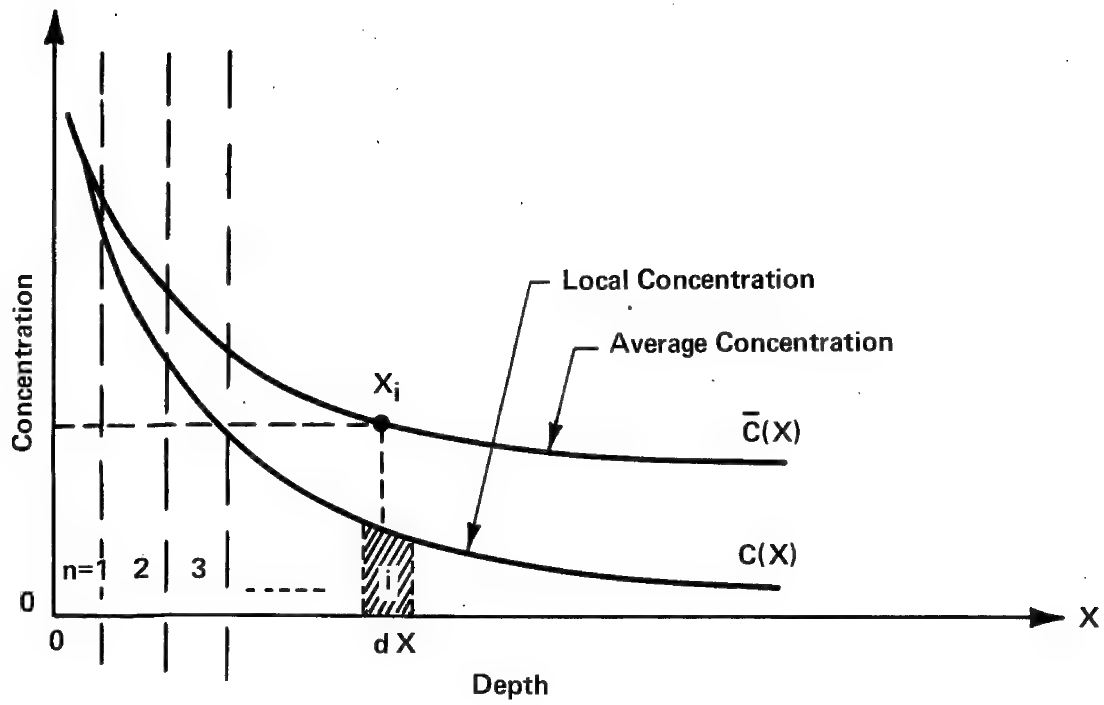
$$\bar{C}(X) = \frac{1}{X} \int_0^X C(X) \, dX$$

Fig. 6.   Local vs. average concentration.

evaporated per unit area is obtained from the measurement at highest voltage which covers the entire depth:

$$\bar{c}(X) \cdot \rho X = g/cm^2$$

or

$$10^{10} \cdot \bar{c}(X) = \overset{\circ}{A} \cdot \% \text{ units}$$

Table I shows the silicon mass density and equivalent pure Si thickness calculated from the X-ray data. The variation in the thickness calculated reflects the degree of process variation. The technique is important in microelectronic applications because (1) it is nondestructive; (2) it makes possible analysis of the concentration profile in product metallurgy stripes ≥2 μm wide without interference from adjacent Si in the substrate; (3) it has the required accuracy for quantitative analysis, and (4) it is expedited by the use of APL (Fig. 7).

ACKNOWLEDGEMENT

Table I.   Total Silicon from Surface to
~9000 Å Depth

Sample No.	Å · %	g/cm^2	Pure Si Equivalence (Å)	Approx. Å Deposited
1	~13,500	3.25X10^{-6}	135	100
2	~ 7,500	1.8 X10^{-6}	75	100
3	~12,500	3.0 X10^{-6}	125	100
4	~11,000	2.65X10^{-6}	110	100

```
      )FNS
- AVCONC  DER       DFT       PENETRATION       PROFILE

      ∇AVCONC[□]∇
    ∇ AVCONC
[1]   AVGCONC←STDCONC×SAMPLE÷STD
    ∇
      ∇DER[□]∇
    ∇ DER;P;Q
[1]   ACTCONC←AVGCONC[1]
[2]   P←1
[3]   P←P+1
[4]   Q←((AVGCONC[P]×DEPTH[P])-(AVGCONC[P-1]×DEPTH[P-1]))÷(DEPTH[P]-DEPTH[P-
[5]   ACTCONC←ACTCONC,Q
[6]   →((ρACTCONC)<ρAVGCONC)/3
    ∇
      ∇PENETRATION[□]∇
    ∇ J PENETRATION K
[1]   DEPTH←(10*4)×((10*(¯5.17))×J*1.71)÷K
    ∇
      ∇PROFILE[□]∇
    ∇ PROFILE
[1]   'ENTER STANDARD:'
[2]   STD←□
[3]   'ENTER SAMPLE:'
[4]   SAMPLE←□
[5]   'ENTER KV:'
[6]   KV←□
[7]   'ENTER DENSITY:'
[8]   D←□
[9]   'ENTER THRESHOLD ENERGY:'
[10]  VT←□
[11]  'ENTER CONCENTRATION OF STANDARD(ABSOLUTE,NOT PERCENT):'
[12]  STDCONC←□
[13]  (KV-VT) PENETRATION D
[14]  AVCONC
[15]  DER
[16]  'DEPTH',(20ρ' '),'CONCENTRATION'
[17]  5 3 27 3 DFT⍉(2,ρDEPTH)ρDEPTH,ACTCONC
    ∇
```

INPUT DATA

Fig. 7.   APL program.

REFERENCES

1. C. A. Anderson and M. F. Hasler, in "X-ray Optics and
    Microanalysis," Fourth International Congress on X-ray
    Optics and Microanalysis, Orsay, 1965.

2. N. Koopman and J. Gniewek, Fourth National Conference
    on Electron Probe Microanalysis, Chicago, Illinois,
    1969.

SCANNING AUGER MICROANALYSIS, Noel C. MacDonald, Physical
Electronics Industries, Inc. Edina, Minnesota 55435

This paper discusses applications of a system which incorporates
a scanned, focused electron beam to excite secondary electrons,
a cylindrical mirror analyzer to energy analyze the secondary
electrons and an ion gun to sputter etch the specimen. The
normal secondary electron and absorbed current images are used
to depict the surface topography of the specimen while Auger
images depict the two dimensional elemental composition of the
surface. The combination of ion sputter etching, Auger electron
spectroscopy and secondary electron imaging provides the means
to perform a complete three dimensional elemental and topographical
analysis of the specimen.

The electron optical properties of the scanning Auger microprobe
system are discussed. In particular the area of analysis for
Auger imaging is discussed for a system which incorporates a
cylindrical mirror analyzer. Experimental results are shown
that illustrate the relationship between the transmission and
energy resolution of the analyzer over the analysis area.

Selected energy analysis of the secondary electrons provides
a means to generate images other than the low energy secondary
electron image. Examples are presented that show the use of
the higher energy Auger electrons for mapping the spatial changes
of potential on a surface. The results of this voltage contrast
imaging technique are related to the discussion of the area
analysis properties of the cylindrical mirror analyzer.

Sputtering Aspects in Surface Analysis Methods

by

G. K. Wehner

Electrical Engineering Department

University of Minnesota

Minneapolis 55455

Sputtering plays an essential role in surface composition analysis methods based on ion bombardment [SIMS, ISS, GDMS, etc.]. In situ sputtering is used with other analysis methods [ESCA, AES, UPS, etc.] for sample cleaning, or for microsectioning of the sample when one disires a compositional depth profile.

A summary of our present knowledge about the sputtering process relevant to the various surface analysis techniques will be presented. Of particular concern in quantitative analysis are the possible compositional changes at the surface of multi-component targets under ion [or electron] bombardment. In sputtering of multi-component targets the sputtering yields of the bulk components are generally not applicable. We will present and discuss various experimentally established cases in which sputtering does not or does seriously alter the surface composition. We will try to speculate on some general trends which seem to emerge.

QUANTITATIVE AUGER SPECTROSCOPY OF A COPPER-GOLD BINARY ALLOY SERIES

by

D. K. Conley and D. F. Lesher
Western Electric Co.
Allentown, Pennsylvania

In a previous paper Bouwman, Toneman and Holscher[1] proposed an internal calibration method for the quantitative study of the surface composition of binary alloys. Three inter-metallic compound rods were fractured, in situ, and the auger spectra recorded immediately of the exposed surface. In their paper a calibration plot of platinum/tin alloys using Pt_3Sn, $PtSn$ and $PtSn_2$ was presented which demonstrated that the observed signal intensity ratios for the two chosen elemental auger emission peaks was proportional to the corresponding atomic ratio of the elements present. It was felt that this type of information should be extended to cover a much greater range of atomic ratios than those pre-sented, since only a tin to platinum atomic ratio of from 0.3 to 2.0 was covered. It is desirable to apply this technique to such applications as thin film interdiffusion, etc. where more limited solubilities and concentrations are involved. The copper-gold alloy system which exhibits a continuous series of solid solutions was therefore studied over a range from very low to very high atomic ratios of gold to copper. A series of ten alloys were prepared by quadruple arc melting, inverting between each melt and chill casting. The prepared alloys were then analyzed by wet chemical analysis to obtain the bulk chemistry. Subsequently, the alloys were analyzed by electron probe microanalysis and the correlation between the bulk chemistry and the chemistry of the surface (5000 Å) was excellent[2].

The samples were not fractured in the system; simultaneous ion sputtering and auger analysis was used in order to eliminate surface contamination and to maintain the clean surface from the redeposition of carbonaceous materials from within the system. Previous analyses of alloys by A.E.S. has shown that the composition of the surface layer can change during ion bombardment. (refs. 3, 4, 5, and 6.) This occurs due to dissimilar sputtering rates for the two elemental constituents of the alloy. The sputtering yield for gold and copper are relatively close for 500 ev xenon ions and the spectra for the various alloys reaches a steady state

condition as soon as the contaminants are sputtered away and do not change over extended periods of time. The yield or number of atoms sputtered per bombarding ion is higher for gold than for copper (3.0 vs 2.4). After the first few atomic layers are sputtered, the surface from which the auger signal originates (approximately 10-50 Å) is enriched in the lower sputter yield element copper and a steady state is reached. As noted by Morabito[8], once the steady state is reached, the magnitude of the auger peak ratio (Au/Cu) is a relative measure of the actual bulk composition of the alloy.

In the peak height ratio versus atomic ratio curve which is obtained, it is evident that for the major range of atomic ratios a linear relationship is obtained. However, it is observed that for the low gold composition alloys a drastic change in the slope of the curve occurs as the origin is approached. The reason for this is that the effective sputtering rates for the two elements is evidently concentration dependent in the low gold composition region.

The internal calibration method of Bouwman et al[1] to obtain quantitative analyses from auger data appears to be generally valid for homogenous samples of known composition by maintaining the same in-situ ion sputtering conditions, etc. However, in this study it was observed that when the faster sputtering component of the alloy became relatively low in concentration significant deviations from linearity are observed.

References

1. R. Bouwman, L. H. Toneman and A. A. Holscher, Vacuum, 23, no. 5, pp. 163-164, 1973

2. J. W. Colby, W. N. Wise and D. K. Conley, Advances in X-ray Analysis, Vol. 10, Plenum Press, N.Y., 19, pp. 447-461

3. M. L. Tarny and G. K. Wehner, J. Appl. Phys. 42, 2449, 1971

4. M. Ono, Y. Takasu, K. Nakayama and T. Yamashima, Surf. Sci. 26, 313, 1971

5. D. Quinto, U. S. Sundaram and W. D. Robertson, Surf. Sci. 28, 504, 1971

6. S. D. Dahlgren and A. G. Graybeal, J. Appl. Phys. 41, 3181, 1970

7. Ion Bombardment of Solids, G. Carter and J. S. Colligan Elsevier, N.Y., 1968

8. J. M. Morabito, Analytical Chemistry, Vol. 46, No. 2, 189-196, 1974

AUGER ELECTRON IMAGES IN A SCANNING ELECTRON MICROSCOPE

E. K. Brandis

IBM System Products Division
East Fishkill Facility, Hopewell Junction, N. Y. 12533

In 1971 N. C. MacDonald[1] showed that Auger Electron
Spectroscopy could be combined with Scanning Electron
Microscopy by attaching a small cylindrical mirror electro-
static analyzer to a commercial SEM. With this system he
was able to record an Auger electron image in 1.7 hours
with an electron beam <1μm in diameter.

In a SEM the spatial resolution is a function of the beam
diameter, the sample and the type of information displayed.
In the emissive mode the spatial resolution is limited by
the escape depth of the secondary electrons which is approx-
imately 50 $\overset{\circ}{A}$. Everhart[2] discussed the recordings of noise-
free secondary electron images and found that 10^4 electrons
are necessary for each picture point. To record an electron
image consisting of 500 x 500 = 250 000 picture points in
5 minutes, a current of 10^{-12}A is required.

Auger electrons ranging in energy from 10 - 2000 eV
have a mean escape depth of approximately 20 $\overset{\circ}{A}$. In principle,
therefore, it appears possible to form Auger electron images
with the same spatial resolution as secondary electron
images. However, only one in 10^5 reflected electrons is an

Auger electron. This means that a current of 10^{-7} A is necessary to record an Auger electron image in the same time.

The current in the final spot of a SEM depends on the aberration of the final lens, the brightness of the electron gun and diffraction. The final beam diameter can be calculated by adding in quadrature the diameter of the de-magnified image of the electron source and the discs of confusion due to spherical and chromatic aberration[3]. The results of these calculations are presented in Fig. 1. The diagram illustrates the relationship between beam current and beam diameter for an existing Cambridge Stereoscan MK IIa equipped with LaB_6 electron gun operating at a working distance of 25 mm and a beam energy of 20 kV. Provided that astigmatism and 60 Hz hum can be prevented it appears possible to focus a current of 10^{-7} A into a beam 0.25 μm in diameter. For comparison, the results of the calculation for FE and a tungsten filament gun are included.

The experimental results were obtained in a diffusion pumped Stereoscan Mk IIa employing the gas jet technique to prevent the carbon build-up.[4] Figure 2 depicts the surface of a 1500 mesh silver grid mounted on an aluminum stud with silver paint. Each Auger electron micrograph was recorded in 200 seconds. Clearly submicron spatial resolution and

several shades of gray are revealed. These results
exceed the spatial resolution observed on a Ag X-ray image
recorded on an ARL electron microprobe (Fig. 3).

Although the incident electron beam used to form the
secondary and X-ray image of the 1500 mesh grid was approx-
imately 0.5 μm in diameter, the X-ray image shows detail only
at around 1 μm. The loss of resolution is caused by
scattering of the electron beam inside the material
resulting in excitation of X-rays in a volume whose
diameter is larger than the incident electron beam.

Because the SEM-Auger technique displays the chemical
composition of the first few monolayers of the surface,
it complements the data measured with the electron micro-
probe. Making use of the information of both instruments,
a more complete characterization of a sample can be obtained.

REFERENCES

1.   N. C. MacDonald, Appl. Phys. Letters, 19, 9, 1971.

2.   T. E. Everhart, Dissertation, Cambridge University (1958).

3.   C. W. Oatley, et al, Advan. Electronics & Electron
      Physics, Vol. 21 (1965).

4.   E. Brandis, R. Hoover, Seventh National Conference,
      "Electron Probe Microanalysis," San Francisco, 1972.
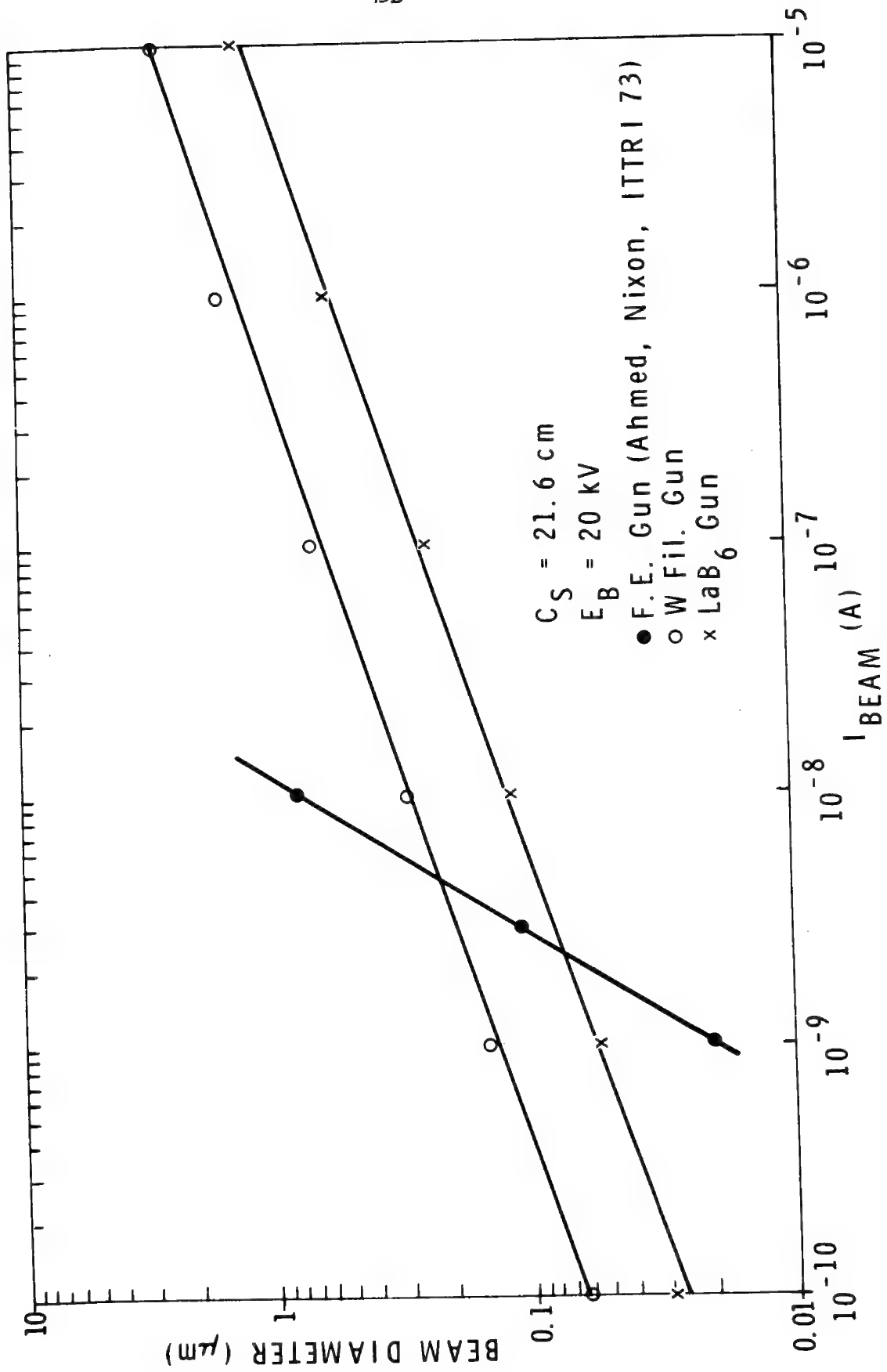
Fig. 1. Beam diameter versus beam current.

C$_{KLL}$

BACKSC.
ELECTRONS

O$_{KLL}$
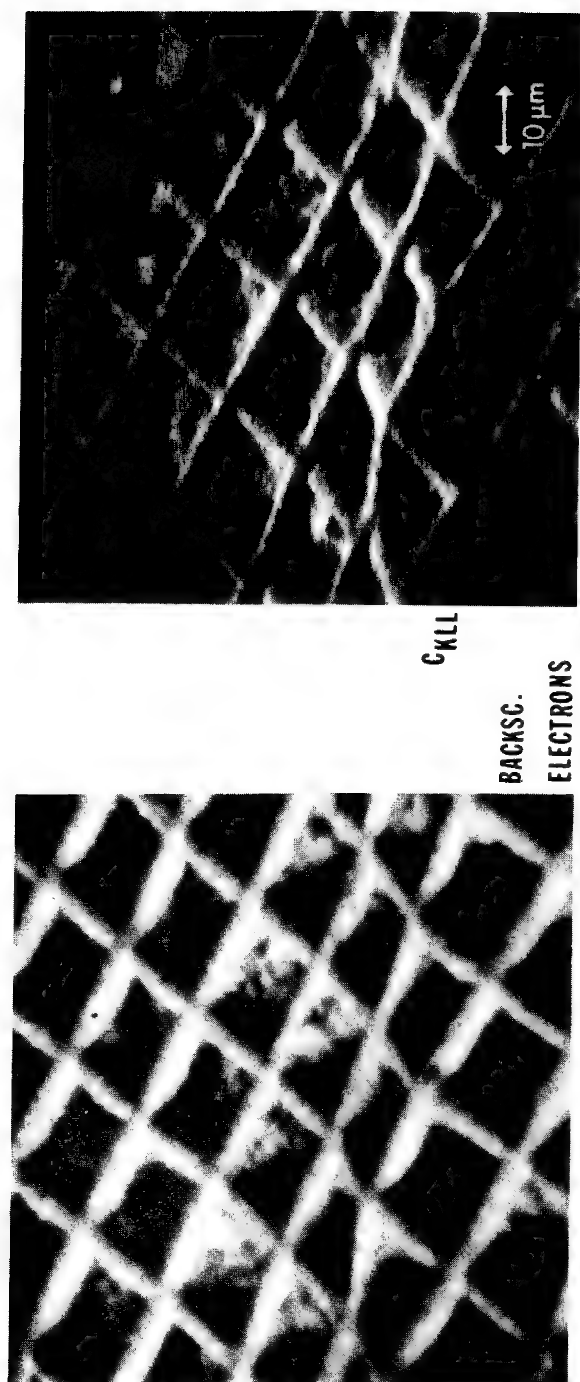
Ag$_{MNN}$

E_B = 20 KV I_{SPEC} = 4x10^{-7} A   RECORDINGTIME = 200 SEC.   (500 LINES)
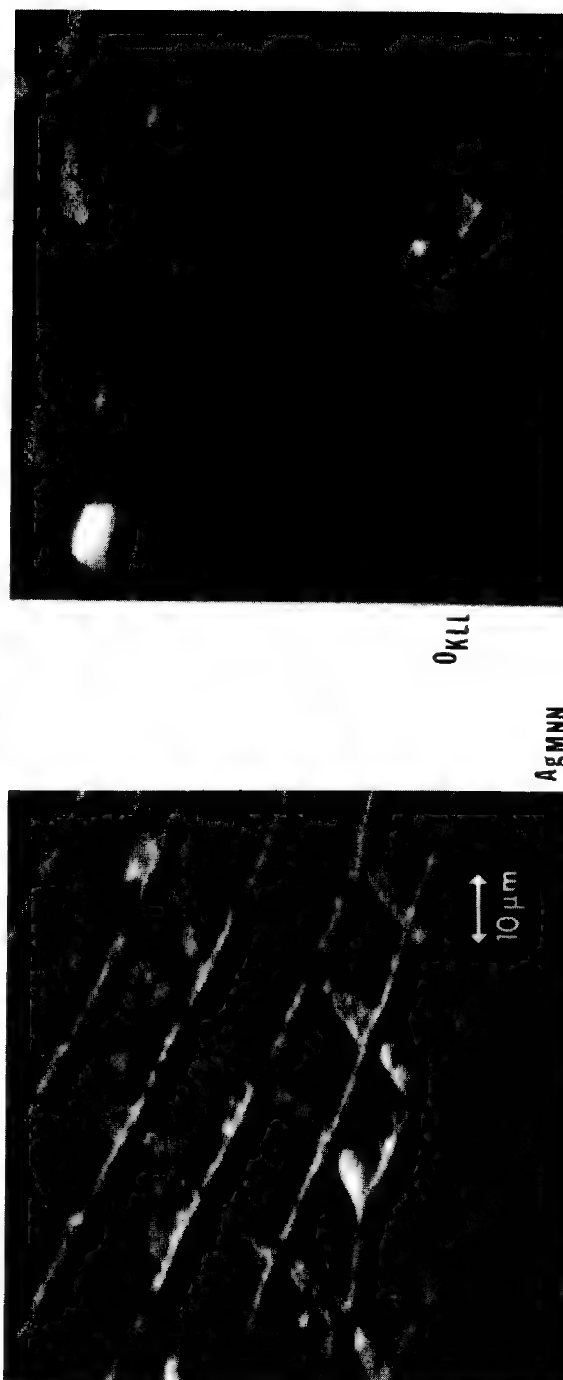
Fig. 2.   Surface of 1500 mesh silver grid.
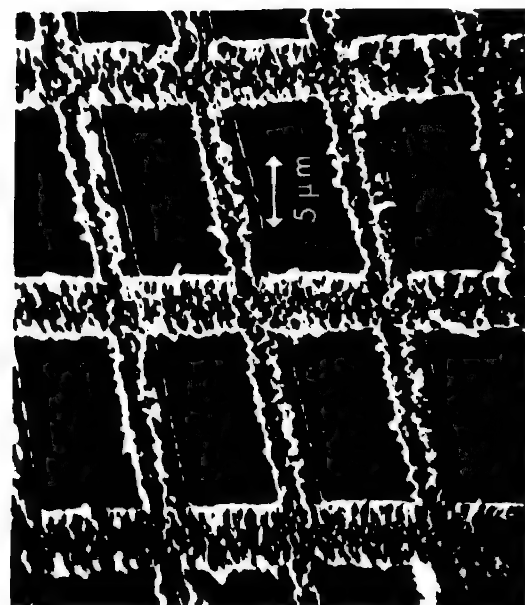
Secondary Electrons

SEM 20 kV

I_{spec} : 2×10^{-7}A, T:400 sec
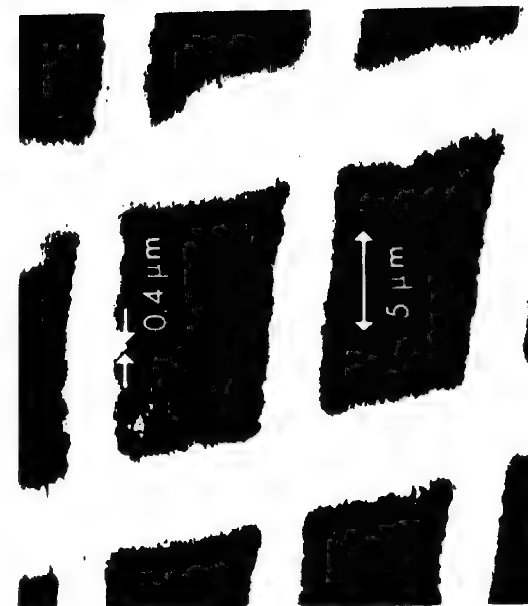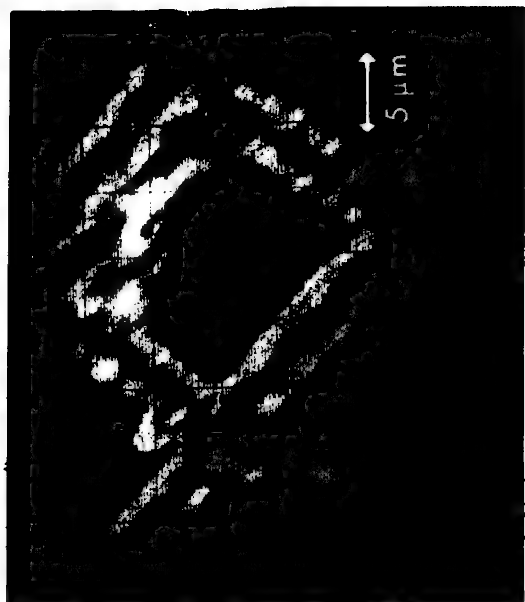
Electronmicroprobe 20 kV

I_{spec} = 5×10^{-9} A, T:200 sec

Ag La

AgMNN
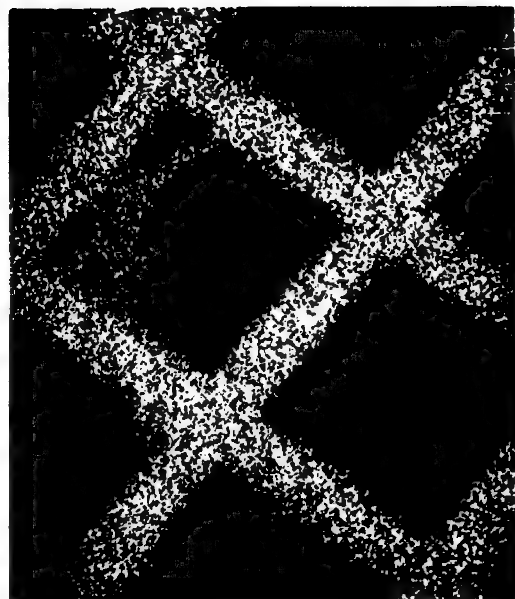
Fig. 3. Comparison between auger electron and X-ray image.

CHANGES IN THE TiO_2 AUGER AND APPEARANCE POTENTIAL SPECTRA INDUCED BY INCIDENT ELECTRON BEAM INTERACTION

J.S. Solomon
University of Dayton Research Institute
Dayton, Ohio 45469

M.B. Chamberlain*
W.L. Baun
Air Force Materials Laboratory
Wright Patterson Air Force Base, Ohio 45433

The Ti LMM Auger electron spectroscopy (A.E.S.) spectra and TiL_{III} appearance potential spectroscopy (A.P.S.) spectra reflect considerable changes in the chemical state of TiO_2 by the incident electron beam. Figure 1 shows these effects on the A.P.S. TiL_{III} and A.E.S. Ti LMM, or more appropriately LVV. In each case three spectra are shown, representative of different time intervals. The APS TiL_{III} spectra labeled 9 m or 9 minutes is shown as the first in this series since no noticeable changes occurred up to that time. After 45 minutes (spectrum labeled 45m) the disappearance of the high energy peak seen in the 9 minute spectrum is observed.
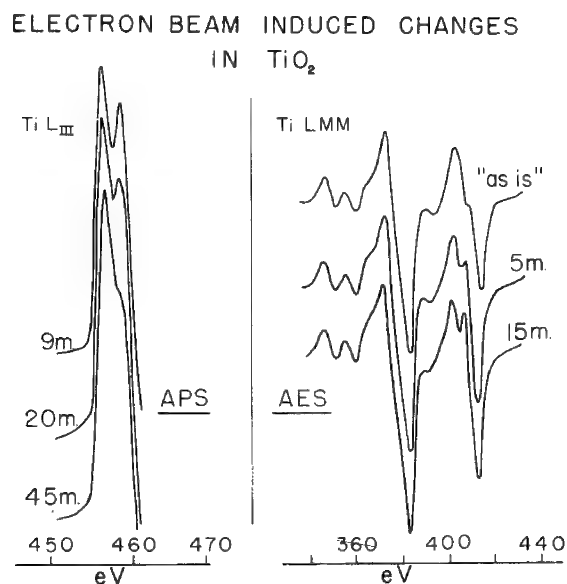
Figure 1. A.P.S. and A.E.S. spectra of TiO_2

The Auger $N'(E)$ spectra on the right of Figure 1 likewise show significant changes with time. The most evident change occurs to the Auger

lines representing valence band or bonding molecular orbital transitions as in the case of the APS TiL_{III} spectrum. These lines are located in the 390 to 420 eV range. The "as is" spectrum shows a symmetrical positive going feature at about 400 eV which after 15 minutes has undergone a splitting, representing a change in slope of N (E). The rate of change is different by comparison between the A.E.S. and A.P.S. spectra only because a much higher current density was used for the Auger excitation.

The changes in both A.E.S. and A.P.S. spectra are thought to be the result of oxygen desorption and the resulting reduction of TiO_2 at the surface to TiO like in character with Ti atoms at the surface and oxygen atoms extending below. An attempt is made to explain these changes by relating the Auger spectra to titanium x-ray emission band spectra from TiO and TiO_2 while the appearance potential spectra are compared to titanium x-ray absorption spectra.

Fischer has shown that the chemical effects on TiL emission and absorption spectra can be explained using a molecular orbital model energy level diagram[1]. In this molecular orbital model electron transitions involving bonding electrons are derived from titanium 3d, 4s-oxygen 2p molecular orbitals. Since the same electronic states are probed in Auger as in x-ray emission, as in this case the bonding molecular orbital to core level transitions, the Auger spectra can be interpreted in a similar manner. The differences in the features of the titanium Auger like the x-ray emission bands are explained by the difference in the occupancy of the titanium 3d-oxygen 2p molecular orbital levels. As TiO_2 is reduced the vacancies in these levels begin to be filled until the highest transition probability shifts from TiO_2 like molecular orbitals to ones with a TiO like character.

1. D.W. Fischer, Physical Review B, 5, 4219-26, (1973)

A COMPARISON OF SURFACE CHEMISTRIES OBTAINED BY USING
ION SCATTERING SPECTROMETRY AND AUGER ELECTRON SPECTROSCOPY

Wm. D. Bingle
National Steel Corporation
Research Center
Weirton, West Virginia   26062

The Ion Scattering Spectrometer (ISS) and Auger Electron Spectrometer (AES) were used to analyze the surfaces of galvanized steels. These steels were selected from welding and corrosion studies that are currently under investigation at National Steel Research. These methods of chemical analysis, though using different mechanisms generate information that is indicative of the surface composition. Both instruments have been described elsewhere (1, 2, 3) and only a brief description will be given here.

In ISS the surface to be analyzed is bombarded with noble gas ions which have an elastic collision with the surface atoms and undergo changes in energy. The distribution of scattered ion energy is presented as a ratio of final energy to incoming energy. Peaks arise from the gas ions scattering off the corresponding surface atoms. The energy of each peak corresponds uniquely to the mass of the element; the height of the peak is related to the quantity of the element in the outer monolayer. The same low energy ion beam which is doing the analysis is also simultaneously sputtering away the surface atoms to produce a depth profile analysis.

AES is accomplished by bombarding the sample surface to be analyzed with a primary electron beam while energy analysis is performed on the resultant secondary electrons. The Auger electron energy is directly related to core levels of the parent atom. Subsequent to ionization, the atom may decay to the equilibrium state through: (1) the Auger process in which the available energy is transferred to a third "Auger" electron or (2) the generation of x-rays in which the available energy is transferred to an x-ray photon. For light elements the Auger transitions dominate and they become comparable to x-ray production at higher energies. The sampling depth of AES is determined by the escape depth of Auger electrons. The low energy electrons from the light elements have only sufficient energy to escape from the outer surface, while the high energy electrons from the heavier elements have sufficient energy to escape from further below the outer surface and be detected.

Samples of galvanized steel from two different studies were examined using both instruments. In the first study three specific samples were analyzed. ISS showed O, Na, Mg, Al, S, Cl, Zn and Pb to be present on all three galvanized steels in varying amounts. Sample A also had indium present on the outer surface. Figure 1 is the ISS spectrum from sample B and shows the O, Na, Mg, Al, S, Cl, Zn and Pb peaks.

AES showed C, N, O, Mg, Al, Si, S, Cl and Zn on all three samples in varying amounts. Sample A also showed indium and tin to be present on the surface. Figure 2 is the AES spectrum from sample B and shows C, N, O, Mg, Al, Si, S, Cl and Zn.

The second study involved the examination of two other lots of galvanized steel. ISS showed O, F, Mg, Al, Cl, Zn and Pb to be present on both samples with F showing the largest variation. Variations in the amount of zinc of the two samples were determined using depth profiling while the surface was sputtered away. AES showed O, F, Mg, Al, S, Cl and Zn to be present on both samples with F showing the largest variation. No evidence of Pb was noticed in the AES spectrum and the S peak was not pronounced in the ISS spectrum.

Conclusions

The characterization of material surfaces using ion scattering spectrometry and Auger electron spectrometry is a relatively new technique that demands further investigation and development before quantitative analyses can be attempted. However, the relative variations in amount present, which may be related on a statistical basis to performance, should be worthwhile information for product design and development.

References

1. R. S. Carbonara, "Ion Scattering Spectroscopy for Microstructural Analysis," Microstructural Analysis Tools and Techniques, Plenum Publishing Corporation.
2. D. P. Smith, "Analysis of Surface Composition with Low Energy Backscattered Ions," Surface Science, 25, (1971), 171.
3. L. A. Harris, "Analysis of Materials by Electron Excited Auger Electrons," Journal of Applied Physics, 39, (1968), 1419.
4. G. A. Somorjai, Principles of Surface Chemistry, Prentice-Hall Inc., New Jersey, 1972, 177.
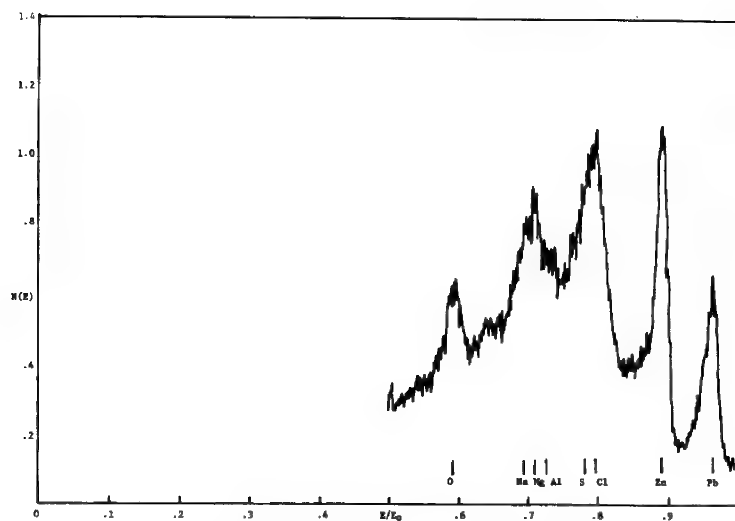
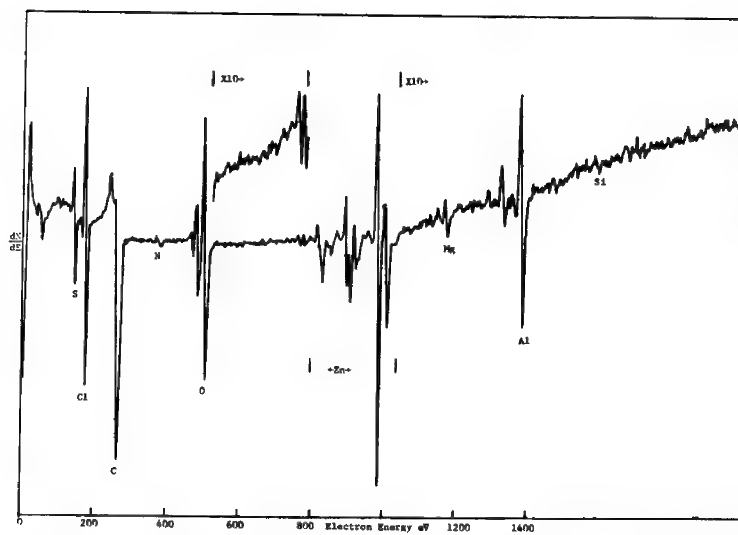Figure 1.   ISS spectrum from galvanize.   Sample B. ^{4}He ions 1500 eV

Figure 2.   AES spectrum from galvanize.   Sample B.

ION SCATTERING SPECTROMETRY DEPTH PROFILE ANALYSIS USING BEAM RASTERING AND SIGNAL GATING

J. A. Leys   J. T. McKinney   T. W. Rusch

Central Research Laboratories, 3M Company, P. O. Box 33221

St. Paul, Minn. 55133

Ion Scattering Spectrometry, (ISS) i.e. the measurement of energy loss of low energy noble gas ions backscattered from a specimen surface, has proven to be a valuable technique for the chemical analysis of surface atomic layers.[1] The sputtering action of the primary ion beam also exposes successive layers of the specimen surface for ISS analysis. The method is therefore useful for depth profile analysis of multilayered materials.

The ion intensity distribution of the cross section of the primary ion beam is gaussian. Therefore the ion beam sputters what might be described as a "dish" shaped crater into the specimen surface. Figure 1 shows a sputtered crater profile and the scattered ion acceptance band of the electrostatic analyzer. The acceptance band of the spectrometer in the narrow direction is generally small enough in relation to the primary ion beam size to preclude serious edge effects, however, the length-wise acceptance includes the edges of the crater. Since ion scattering data therefore originates from different depths within the sample, the technique has limited usefulness
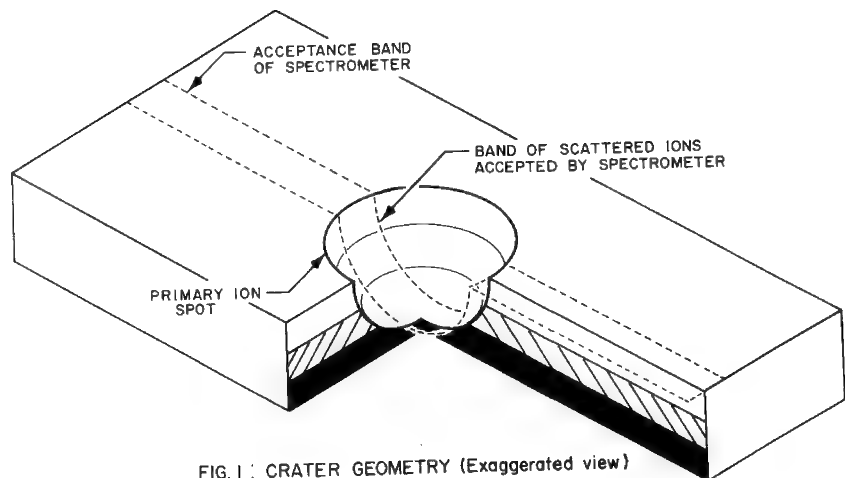
FIG. I : CRATER GEOMETRY (Exaggerated view)

when attempting to study problems such as possible diffusion
of sharp-boundary multilayered devices. In the past, it
has been customary to sputter with a wide defocused beam and
take ion scattering measurements with a smaller focused beam.
Mathematical manipulations of the data have also been used
to at least partially compensate for these edge effects. ②

A device has been constructed which permits rastering of the
ion beam in a horizontal and vertical direction on the specimen
surface. This rastering results in very uniform surface
sputtering in the center of the rastered area. An electronic
gating device is
utilized in con-
junction with
this rastering,
which senses the
position of the
scanning ion
beam and permits
the scattered
ion signal to
be accepted
only when the
beam is inside
a preselected
area within the
center of the
entire rastered

FIG. 2: RASTERING- GATING APPARATUS

area. A block diagram of the apparatus is shown in Figure 2.

Figure 3 shows ISS depth profile analyses of a copper film approximately 500Å thick using both a stationary beam as well as rastering and gating. The improvement in depth resolution with the rastering-gating is apparent.

The rastering-gating technique is also directly applicable to a related method of surface analysis, namely secondary ion mass spectrometry (SIMS). Comparison between stationary beam and rastering-gating depth profile analyses

FIGURE 3 ISS DEPTH PROFILE ANALYSIS OF 500Å COPPER FILM

Ne 20 ⟶ COPPER

INTENSITY

stationary beam

gating and rastering

TIME
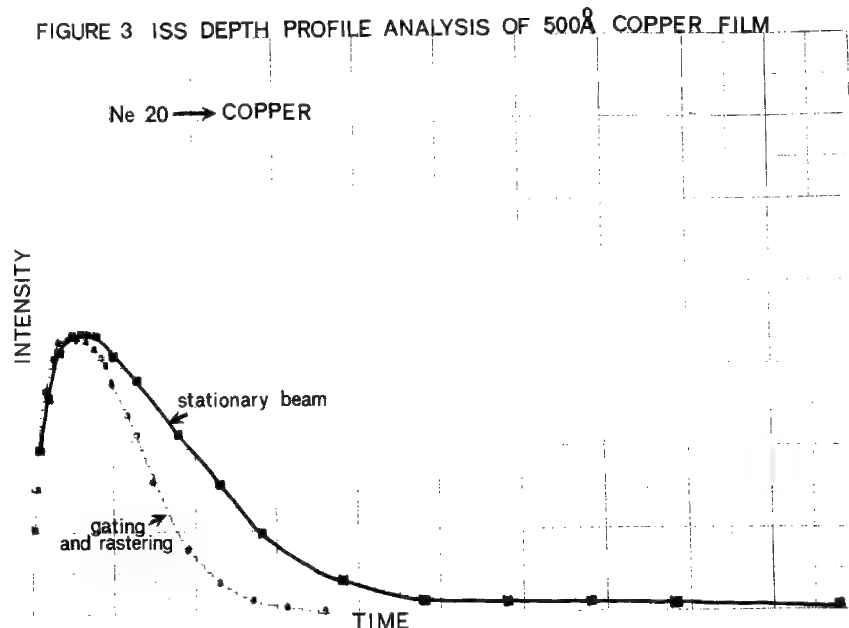
using SIMS generally shows an even more dramatic difference in resolution. It is well known that secondary ion yield is greatly enhanced by the presence of an "active" gas such as oxygen.③ As a surface is sputtered, the edges of the crater formed often contain a greater concentration of active gas than the center; as a result the secondary ion yield is greater at the edges of the crater than at the center. The use of the rastering-gating technique eliminates the need for mechanical or optical signal restricting apertures or slits in the SIMS apparatus in order to achieve good depth profile resolutions.

References

① See for example, F.W. Karasek, Research/Development 24 (1) pp 25-30 (1973); J.T. McKinney and J.A. Leys, Eighth National Conference on Electron Probe Analysis, Aug. (1973) New Orleans, La.; D.P. Smith, Surface Science 25 pp 171-191 (1971).

② D.W. Hoffman, Quantitative Depth Profiling by Ion Scattering Spectrometry, I.S.S. Users Conference, Sept. 1973.

③ C.A. Andersen, Int. J. Mass Spect. & Ion Physics 2 (1969).

MATERIALS CHARACTERIZATION BY
SECONDARY ION MASS SPECTROMETRY (SIMS)

by

J. M. Morabito

BELL TELEPHONE LABORATORIES, INCORPORATED
555 Union Boulevard
Allentown, Pennsylvania 18103

ABSTRACT

Secondary Ion Mass Spectrometry (SIMS) has unique
features for localized analysis, i.e. analysis of a small
preselected volume of material with good spatial and depth
resolution. All elements (excluding He, Ne) and their
isotopes depending on natural abundance can be detected with
sensitivities for many, but not all, elements in the ppm range.
The sensitivity possible for a given element depends on
secondary ion yield which is a function of parameters such
as surface chemistry, nature of the primary ion and primary
ion energy, etc..

In depth profile analysis is possible by monitoring a
selected ion mass(es) while sputtering through the sample,
and the depth resolution possible is on the order of 5-10%
of the thickness removed in the absence of crater wall effects,
knock on, and the redeposition of sputtered material. The
knock on or recoil effect is inherent in the sputtering
process and is a strong function of primary ion energy. Crater
wall effects and redeposition can be minimized by proper experi-

mental technique.

The secondary ions can also be used to obtain ion images which provide information on the spatial distribution of elements at the surface and within the bulk of the solid. The spatial resolution of the ion image is on the order of 1 μm and can be obtained by direct imaging using an ion optical system or by scanning the primary ion beam and intensity modulating a CRT.

Since the escape depth of the emitter secondary ions is within the surface region ($\leq$ 50 Å), qualitative surface analysis by SIMS is possible but complicated by hydrocarbon interference effects and the presence of surface oxides which enhance secondary ion yields. The presence of surface oxides and the dynamic implantation range of <u>reactive</u> primary ions has also been found to complicate the interpretation of SIMS in depth profile analyses within the first few hundred angstroms of the surface.

Quantitative analysis is possible by the use of standards which are similar to the sample under study and a method based on a thermal equilibrium model of the secondary ion emission process has also been developed.

The results obtained on silicon samples doped with B, P, As, O, C, and F, tantalum thin films containing N, O, and C, anodic tantalum oxide containing phosphorus, and platinum and platinum silicone films containing phosphorus are used to

demonstrate the capabilities and limitations of SIMS analyses.
When possible these results are compared to those obtained by
Auger electron spectroscopy.

A HIGH MASS RESOLUTION CAPABILITY FOR THE CAMECA ION ANALYZER

R. K. Lewis, Cameca Instruments, Inc., Elmsford, N.Y. 10523
J. Vastel, CAMECA, 92400 Courbevoie, France

In the Cameca direct imaging secondary ion mass analyzer (IMS 300), mass analysis results from the momentum analysis performed by the first magnetic deflection in the prism–mirror–prism design. This mass spectrometer system follows the original design proposed by Slodzian and Castaing.[1]

In spite of the fact that a rather high ion accelerating voltage (4.5 KV) is used in the IMS 300, the energy distribution, which ranges from tens to hundreds of eV for sputtered secondary ions, puts a limit on the mass resolution that can be achieved unless some form of energy filtering is used. This filtering has been accomplished in the IMS 300 by the electrostatic mirror on the high energy side of the distribution and by the low energy discriminator (LED) grid lens on the low energy side.

This filtering technique provides a very precise upper and lower limit on the energy band accepted by the analyzer system. A high energy limit is required to minimize chromatic abberation and the lower limit is very useful in minimizing mass interferences from large polyatomic clusters. Unfortunately, this filtering technique has the disadvantage of attenuating the transmission efficiency of the analyzer system when attempting to achieve a mass resolution exceeding 300 or so. This situation is unfavorable, for example, when compared to a mass spectrometer design such as the Mattauch–Herzog type which can be fitted with an ion probe. [2,3]

Fortunately, a mass resolution of 300 has been sufficient for the many application areas where secondary ion mass analysis has been employed. There are, however, many important areas where this analysis technique cannot be used effectively because of the serious mass interferences which are encountered at a mass resolution of 300. These interferences arise from the sputter ion bombardment process itself in which numerous polyatomic cluster ions (M_2, M_3, M_xM_y, etc.) are produced. In addition, when a primary oxygen beam is used or when oxygen is present in the sample M_xO_y combination ion species are also produced which further complicate the problem of mass interference. These interferences are most pronounced at the high mass end of the mass spectra since they are produced from combinations of elements at lower masses. For example, $^{27}Al_2$, $^{24}MgO_2$ and $^{28}Si_2$ interfere with both isotopes of iron (54 and 56) making the detection of iron very difficult in matrices containing

these elements in high concentrations. In addition to loss of detection sensitivity, mass interferences limit the accuracy of quantitative analysis [4] and isotope abundance measurements. Also, accurate mass measurement can often be quite useful in identifying unknown mass peaks.[5]

The need for a high mass resolution capability without sacrificing transmission efficiency in the IMS 300 has led us to consider the method described here. In this method nothing is altered in the imaging optics but a different ion path is used for mass spectral analysis (Fig. 1). The ion beam passes through a hole in the mirror and then through a 90° spherical electrostatic analyzer, forming with the 90° magnetic analyzer a small double-focusing Nier-Johnson type mass spectrometer. An electron multiplier is used for the ion detection. A spherical electrostatic analyzer was selected in order to limit the size and retain a good ion transmission associated with stigmatic focusing.

In the standard configuration, the position where high energy ions hit the mirror cathode is adjustable in order to provide a clean surface when this surface becomes contaminated. This cathode surface could already be moved from outside the vacuum with the instrument operating. A hole was drilled in an extreme position of the cathode to allow the beam to pass through. During mass spectral measurement, all parts of the mirror are grounded and switching from this mode to the ion imaging mode and back can be done in seconds. There is no interference with the direct viewing microscope or the sample air interlock system.

In Fig. 2 the complete separation between $^{56}Fe^+$ and $^{27}Al_2^+$ is shown, which implies a resolution around 3,500. The highest resolution obtained with the system so far was 5,000. Our studies have also demonstrated that the sensitivity remains practically constant up to a resolution of 3,000, and that the energy slit width used has a neglible effect on mass resolution.

References

1. Castaing, R., and Slodzian, G., J. Microsc., Vol. 1, 395, 1962.

2. Hernandez, R., Lanusse, P., Slodzian, G. and Vidal, G., Resch. Aerosp., No. 6, 313, 1972.

3. Hernandez, R., Lanusse, P., and Slodzian, G., Methodes Physiques d'Analyse (G.A.M.S.), Vol. 6, 411, 1970.

4. Morabito, J. M., and Lewis, R. K., Anal. Chem., Vol. 45, No. 5, 869-880, 1973.

5. Bakale, D. K., Colby, B. N., Evans, C. A. and Woodhouse, J. B., Eighth Nat. Conf. Elec. Probe Analys., 7, 1973.
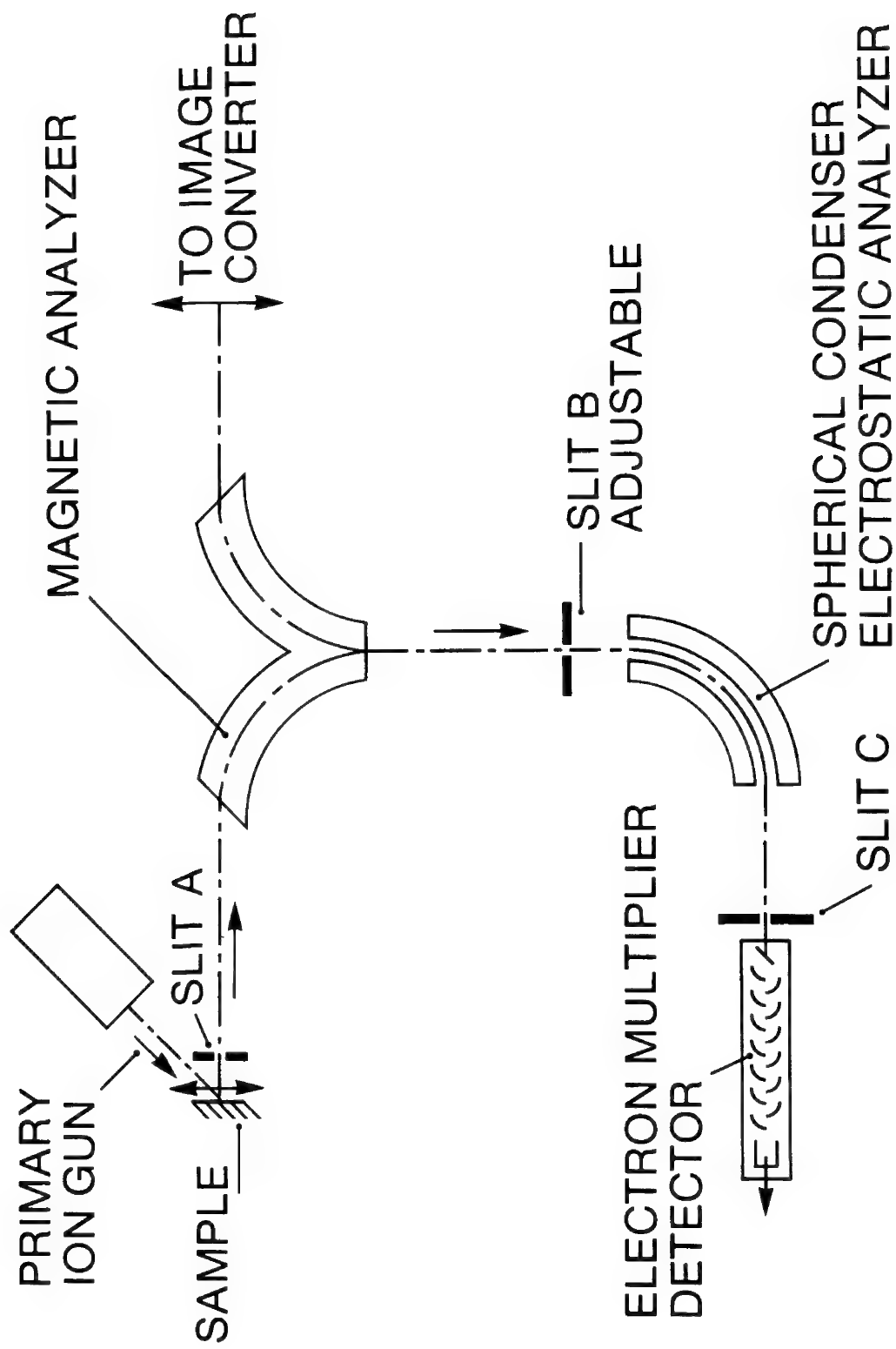
Fig. 1   IMS 300 ELECTROSTATIC ANALYZER ACCESSORY

^{27} Al$_2^+$
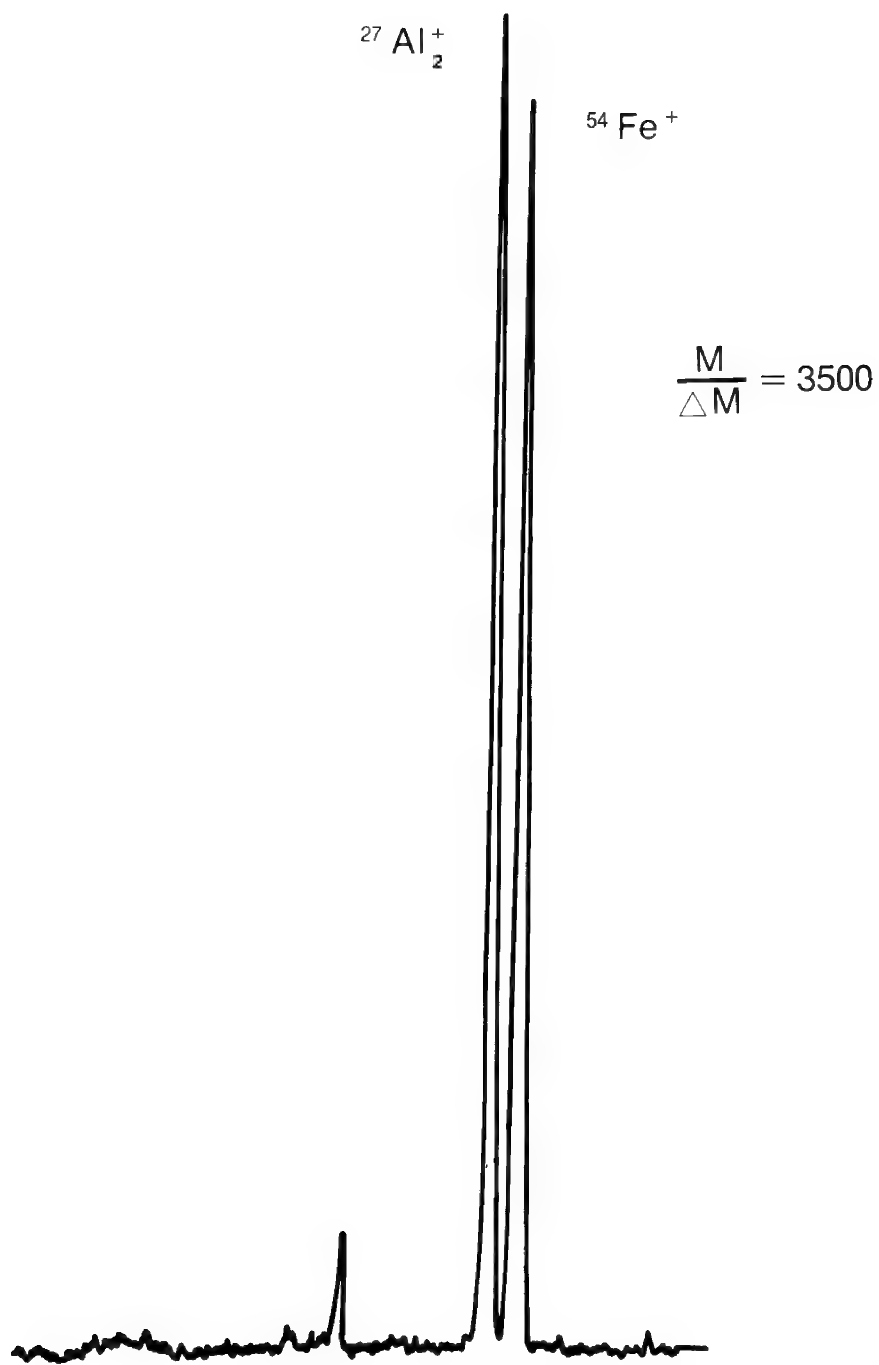
^{54} Fe$^+$

$$\frac{M}{\triangle M} = 3500$$

Fig. 2   MASS RESOLVING POWER
OF IMS 300 WITH
ELECTROSTATIC ANALYZER

METALLURGICAL APPLICATIONS OF
SECONDARY ION MASS SPECTROMETRY

by

J.M. Walsh
Pratt and Whitney Aircraft
Materials Engineering and Research Laboratory
East Hartford, Connecticut 06108

The technique of secondary ion mass spectrometry has been applied to
several metallurgical problems and has provided information difficult
or impossible to obtain with the conventional electron microprobe.

Titanium alloys have a very large solubility for oxygen and nitrogen
and can readily be contaminated by the rapid diffusion of these inter-
stitial elements into the metal during ingot production. When either
or both of these elements are present at levels significantly higher
than the alloy specification limit, they result in alpha stabilized
defects which are extremely detrimental to mechanical properties (1).
Unless these defects are large, it is impossible to determine by bulk
chemical analysis if oxygen or nitrogen is the cause. The ARL ion
microprobe mass analyzer was used for the characterization of several
alpha stabilized defects in Ti-6Al-4V.

The concentration of oxygen and nitrogen was measured on two defects
as a function of distance from the center of the defect. The $^{14}N^+/ ^{47}Ti^+$
ratio was taken as a relative indication of nitrogen concentration and
the $^{16}O^+/ ^{47}Ti^+$ as an indication of oxygen content. The primary beam
was N_2^+ for oxygen and O_2^+ for nitrogen.

Ion microprobe examination showed the first defect to be enriched in
nitrogen but not oxygen and resulted in the profile shown in Fig.1.
A microhardness profile was made through this same region (Fig.2) and
confirmed the decrease in interstitial content with distance from the
center of the defect. Bulk gas analyses for oxygen and nitrogen were
made by removing about one gram of material from the defect region
and from normal material away from the defect and yielded the following:

TABLE I
Bulk Chemical Analysis

	Nitrogen Content (ppm wt)	Oxygen Content (ppm wt)
Defect Area	2550	920
Normal Area	220	1570

These analyses confirm that the defect is due to nitrogen rather than
oxygen contamination. This procedure results in a highly diluted analysis
therefore the actual nitrogen content of the defect is most certainly
much higher.

Recent work by Morabito (2) describes quantitative nitrogen and oxygen
determinations in sputtered tantalum films by secondary ion mass spectrom-
etry using calibration standards. While no standards were available in

the present work, the nitrogen content of the defect was estimated by equating the $^{14}N^+/\ ^{47}Ti^+$ ratio measured on the normal area to the bulk nitrogen content measured chemically and extrapolating to the center of the defect. This procedure resulted in a nitrogen concentration of about 1.2 wt pct. Electron microprobe analysis at this site for Al, V, and Ti left a balance of 1.5 wt pct unaccounted for. If this balance were assumed to be all nitrogen then it would be in reasonable agreement with the extrapolated value.

Similar analysis of a second defect showed it to be oxygen rather than nitrogen enriched and resulted in the profile shown in Fig. 3. As was done for nitrogen, an estimate of 0.53 wt pct oxygen in the most oxygen rich portion of the defect was made by extrapolating from the unaffected material which showed 1600 ppm oxygen by bulk chemical analysis.

Another metallurgical problem studied by secondary ion mass spectrometry was boron segregation to grain boundaries in a nickel-base alloy. It is widely believed that boron segregation to grain boundaries of nickel alloys is responsible for the substantial improvements in creep properties that result from trace additions of boron.(3) Autoradiography (4) has been used to show boron segregation to grain boundaries, however, it has been found that secondary ion mass spectrometry can provide similar information in a more convenient manner.

Specimens of low carbon Udimet 700 nickel-base alloy doped with 0.03 wt pct boron were examined in the ARL ion microprobe mass analyzer and in the Cameca direct imaging analyzer. Both devices produced $^{11}B^+$ secondary ion images that clearly showed evidence for boron segregation to grain boundaries (Fig.4). Subsequent extraction electron metallography revealed evidence of boride precipitates in some grain boundaries but many grain boundaries were clean therefore it is thought that boron may be present as both a boride and an atomic segregation.

The ion microprobe data was provided by Applied Research Laboratories, Inc. and the direct imaging ion data was provided by Cameca Instruments, Inc.

REFERENCES

1. J. L. Henry, S. D. Hill, J. L. Schaller and T. T. Campbell: Met. Trans., 1973, vol. 4, pp. 1859-1864.
2. J. M. Morabito: Anal. Chem., 1974, vol. 46, pp. 189-196.
3. R. F. Decker and J. W. Freeman: Trans. TMS-AIME, 1960, vol. 218, pp.277-285.
4. P. S. Kotval, J. D. Venables and R. W. Calder: Met. Trans., 1972, vol. 3, pp. 453-458.
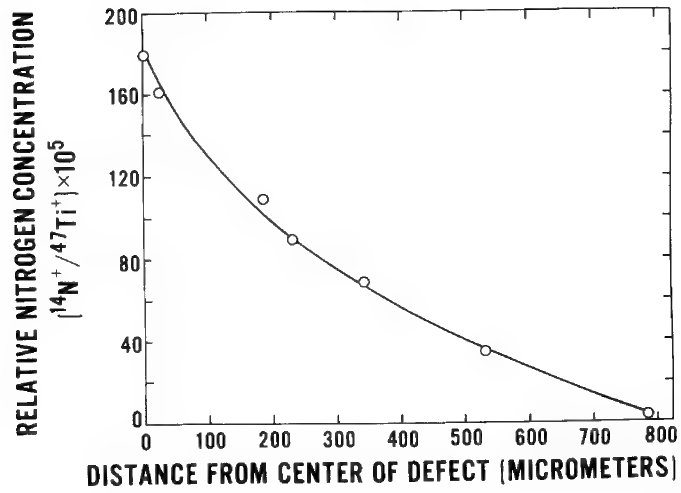
FIGURE 1: PROFILE OF RELATIVE NITROGEN CONCENTRATION VS. DISTANCE FROM CENTER OF DEFECT.
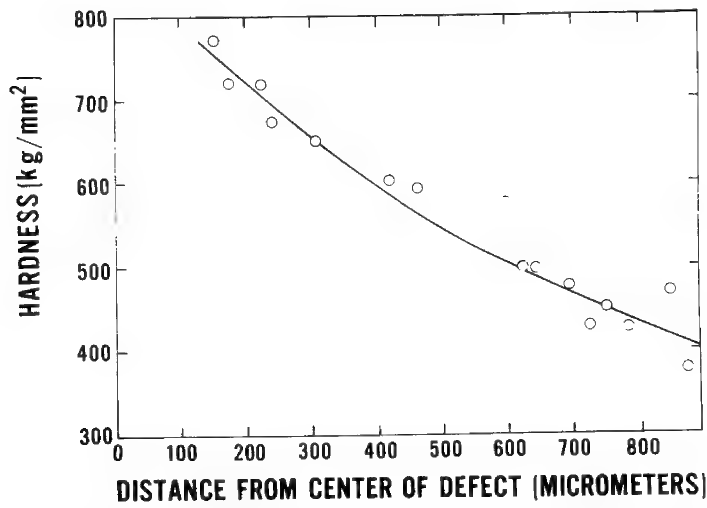

FIGURE 2: PROFILE OF HARDNESS VS. DISTANCE FROM CENTER OF NITROGEN STABILIZED DEFECT.
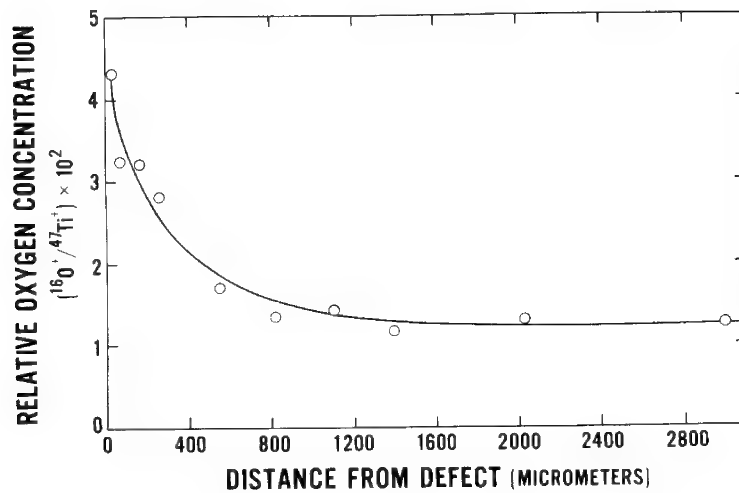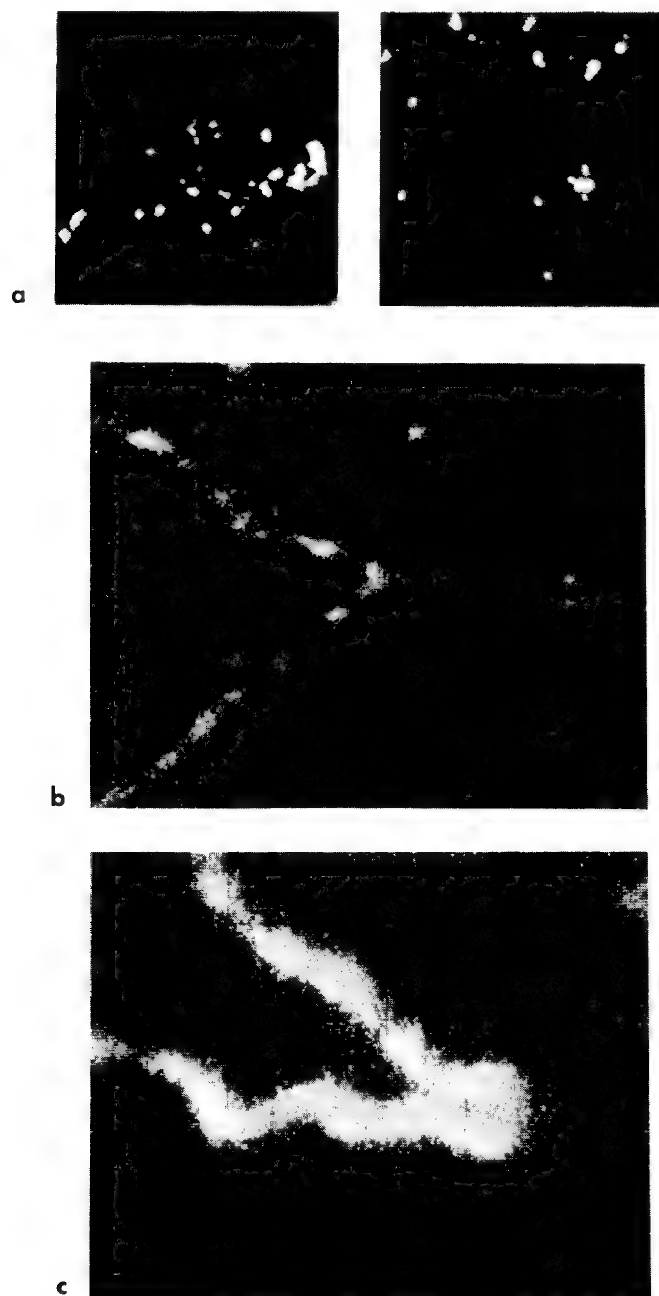

FIGURE 3: PROFILE OF RELATIVE OXYGEN CONCENTRATION VS. DISTANCE FROM DEFECT.

FIGURE 4: $^{11}B^+$ SECONDARY ION IMAGES OF U-700 MADE ON DIRECT IMAGING ION INSTRUMENT (A), ION MICROPROBE-FINE BEAM (B) AND ION MICROPROBE-COARSE BEAM (C).

K-7562

ION SCATTERING SPECTROMETRY AND SECONDARY ION MASS SPECTROSCOPY: TWO COMPLIMENTARY TECHNIQUES

J. A. Leys and J. T. McKinney

Central Research Laboratories, 3M Company, P. O. Box 33221
St. Paul, Minn. 55133

Simultaneous analyses by Ion Scattering Spectrometry (ISS) and Secondary Ion Mass Spectroscopy (SIMS) provide unique surface compositional data.

A schematic diagram of the instrument used to perform these analyses is shown in Figure 1. A beam of monoenergetic inert gas ions is directed onto the specimen surface. Primary inert gas ions scattered at 90° enter the energy analyzer. The energy of these ions provides information on the elemental surface composition of the specimen. Ions sputtered from

FIG. I : ISS-SIMS APPARATUS

the specimen surface are of considerably lower energy than the scattered noble gas ions and therefore can readily be analyzed in a quadrople mass analyzer. These ions pass through an energy pre-filter to eliminate the high background and peak broadening caused by higher energy sputtered or scattered particles.
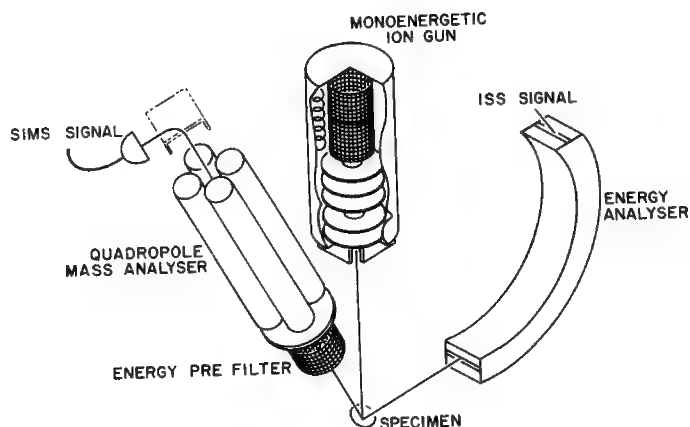
In analytical practice, it has been observed that the limitations of one technique are often offset by the strengths of the other. The following examples illustrate how the two methods complement each other and provide a more complete understanding of the specimen surface composition than can be achieved singly by either technique.

Figure 2a shows an ISS depth profile analysis of a chromate treatment on a copper foil of the type used in printed circuit boards. Figure 2b shows SIMS spectra taken simultaneously with the ISS data. Examination of the SIMS data shows that while the chromium and oxygen signals decrease as anticipated the copper signal does not increase correspondingly as the copper substrate becomes exposed by the sputtering of the ion beam. The explanation for this is related to the great dependency of the secondary ion

Figure 2a ISS DEPTH PROFILE OF CHROMATE TREATED COPPER FOIL
Ne 20 2500V
20 Angstroms   100 Angstroms   500 Angstroms

Figure 2b SIMS DEPTH PROFILE OF CHROMATE TREATED COPPER FOIL
Ne 20 2500V
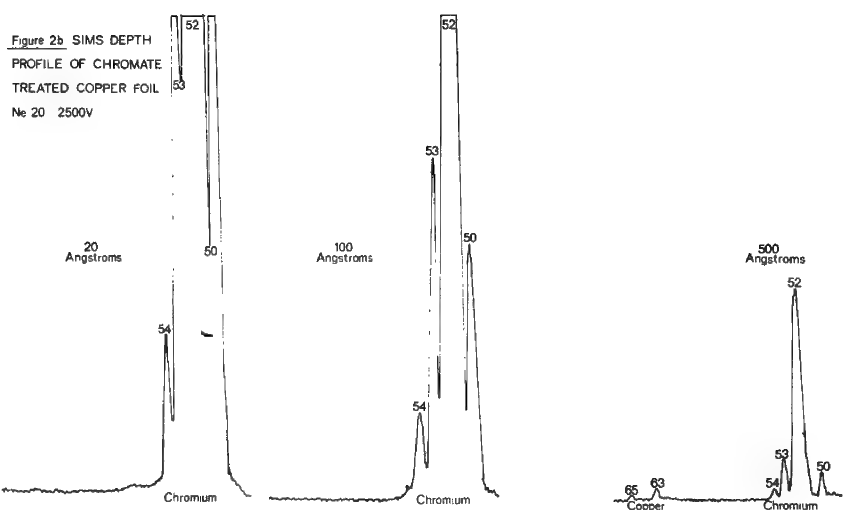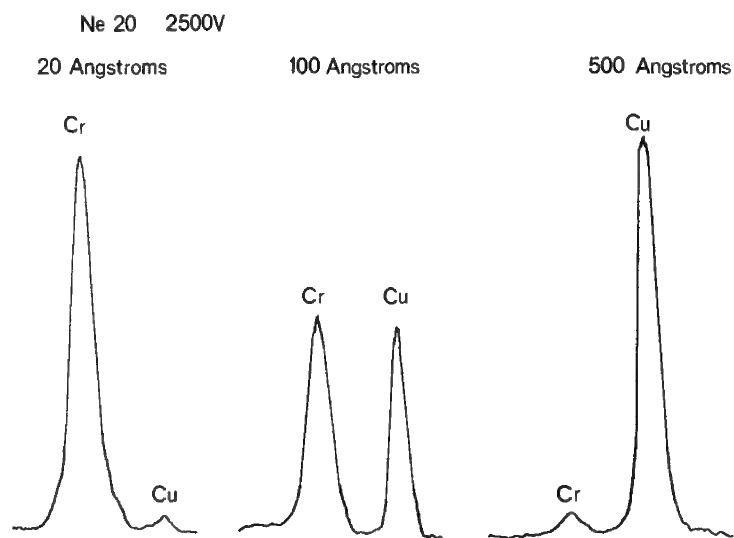
yield on the presence of an "active" gas such as oxygen. The
copper signal is thus very low because of the absence of oxygen.
Note that the isotopes of chromium are readily observed. This
mass resolution of SIMS is clearly an aid to ISS when examining
certain groups of elements having adjacent mass numbers which
cannot be resolved by ISS. Figure 3a shows the ISS spectra
of chemically cleaned aluminum and aluminum treated with a

dilute sodium
silicate solu-
tion. While the
slight shift in
the aluminum peak
position suggests
silicon, it is
insufficient
except for very
questionable
qualitative
analysis.
Figure 3b shows
the SIMS spectra
of the same

Figure 3

a. ISS SPECTRA

b. SIMS SPECTRA

samples. The ratio of silicon to aluminum in the outer layers
of the silicate treated aluminum appears to be about three to
one. Depth profile analyses showed the thickness of the silicate
coating to be only a few monolayers.

Figure 4a shows the ISS spectra of a Co_3O_4 catalytic surface
before and after exposure to a hydrogen atmosphere. The oxygen
signal is smaller and the Co signal greater on the hydrogen
treated surface indicating a partial reduction of the oxide.
SIMS spectra of the same samples are shown in Figure 4b. The
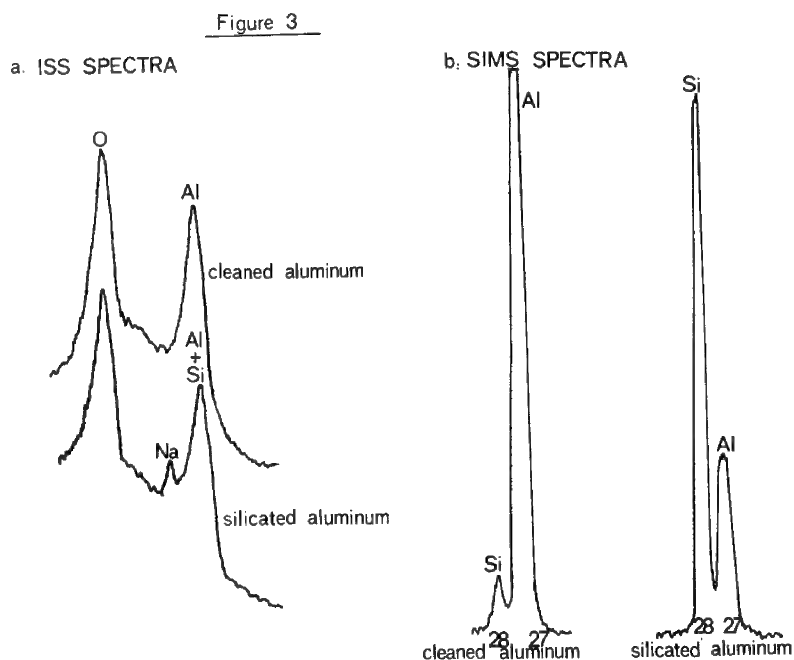
relatively large off-scale peak at mass 1 and 2 indicates the presence of a greater amount of hydrogen on the treated surface than on the untreated.

Figure 4a ISS SPECTRA OF Co_3O_4 POWDER
He 3 2500V

Figure 4b SIMS SPECTRA OF Co_3O_4 BEFORE AND AFTER HYDROGEN TREATMENT
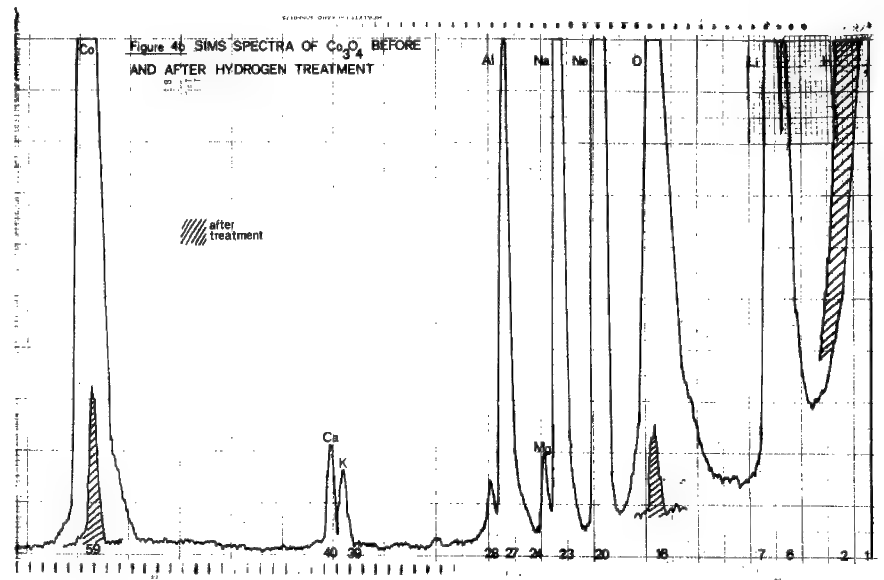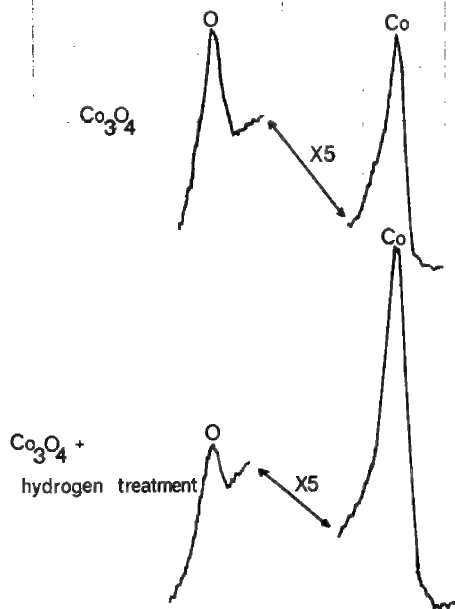
The oxygen and cobalt signals are lower on the hydrogen treated surface. The oxygen is lower because of partial reduction of the oxide which is also indicated by the ISS data. The cobalt signal is less intense even though there is more surface cobalt present because the cobalt secondary ion yield is strongly dependent on the presence of oxygen as was previously pointed out in the case of the CrO_3 treated copper. It is common practice to add oxygen to the primary ion beam to help alleviate this low secondary ion yield problem.① However, the use of oxygen in this case would result in both samples being analytically

the same even though they are catalytically very different. The use of oxygen is often unnecessary when ISS data is available to aid in quantitative interpretation.

Examination of SIMS data in Figure 4b shows peaks for Li, Na, Mg, Al, K and Ca which are not observed in the ISS data. The alkali and alkaline earth metals as well as other low mass elements are very sensitive by SIMS and are the most difficult to detect by ISS.

With the exception of low mass elements, the sensitivity of ISS is quite uniform [2] when compared to SIMS which varies by greater than four orders of magnitude. [3] Further, the ISS signal is not grossly dependent on such matrix effects as the presence of an active gas. Thus the simplicity of ISS spectra and the ease of semiquantitative analyses with ISS aids SIMS interpretation. On the other hand, the unit mass resolution, the high sensitivity to low mass elements, and the presence of structural data in SIMS aids ISS in obtaining more complete surface analyses.

<div align="center">References</div>

[1] C.A. Andersen, Int. J. Mass Spect. & Ion Physics 2, (1969)

[2] J.K. Rice, F.W. Bingham, Phys. Res. A 5 No. 5 (May 1972)

[3] C.A. Anderson, Int. J. Mass Spect. & Ion Physics 3 (1970)

THE USE OF SOLID STATE X-RAY DETECTORS
FOR OBTAINING FUNDAMENTAL X-RAY DATA
E. Lifshin
General Electric Corporate Research and Development

A combination of good energy resolution and a high collection efficiency makes Si(Li) detectors particularly well suited for measuring both characteristic and continuum production efficiencies. The experimental procedure required is to collect all of the x-rays emitted in a well defined solid angle, Ω, and calculate the generated x-ray signals for the continuum, N_E^g, and characteristic lines, N_A^g, according to the equations:

$$N_E^g = \frac{4\pi I_E^o}{\Omega f(\chi_E) R_E i_p C} \quad \text{photons/incident electron/KEV interval} \quad (1)$$

and

$$N_A^g = \frac{I_A^o}{\Omega f(\chi_A) R_A i_p C} \quad \text{photons/incident electron/steradian} \quad (2)$$

where $f(\chi)$ is the absorption factor, R is the backscatter factor, i_p is the probe current, C is the conversion factor for probe current to electrons and the subscripts E and A refer to the continuum and characteristic lines respectively. Considerable care must be taken to avoid spectral distortion associated with pulse pileup at high counting rates as well as to account for the influence of absorption and transmission effects on the detector collection efficiency.

Results obtained from this type of experiment shows that the spectral distribution of the continuum follows an equation of the form:

$$N_E^g = \frac{ZK_1(E_o-E)}{E} + \frac{ZK_2(E_o-E)^2}{E} \qquad (3)$$

where K_1 and K_2 are constants depending on both the beam voltage, E_o and the specimen atomic number, Z. At 40KV the results obtained by this method do not confirm Kramers' law[1] (equation 3 with $K_2=0$), however, better agreement can be found at lower voltages although K_1 remains dependent on both E_o and Z.

Once determined the spectral distribution of the generated continuum can be subtracted from the total generated spectra leaving only the characteristic line intensities which can easily be converted into x-ray production efficiencies. Figure 1 shows a comparison between data obtained by this technique with Green and Cosslett[2] for the voltage dependency of CuK_α and TiK_α and new data for AgL_α. The success of this background subtraction technique is illustrated in Figure 2 which shows the observed 40KV copper spectra before and after background subtraction.
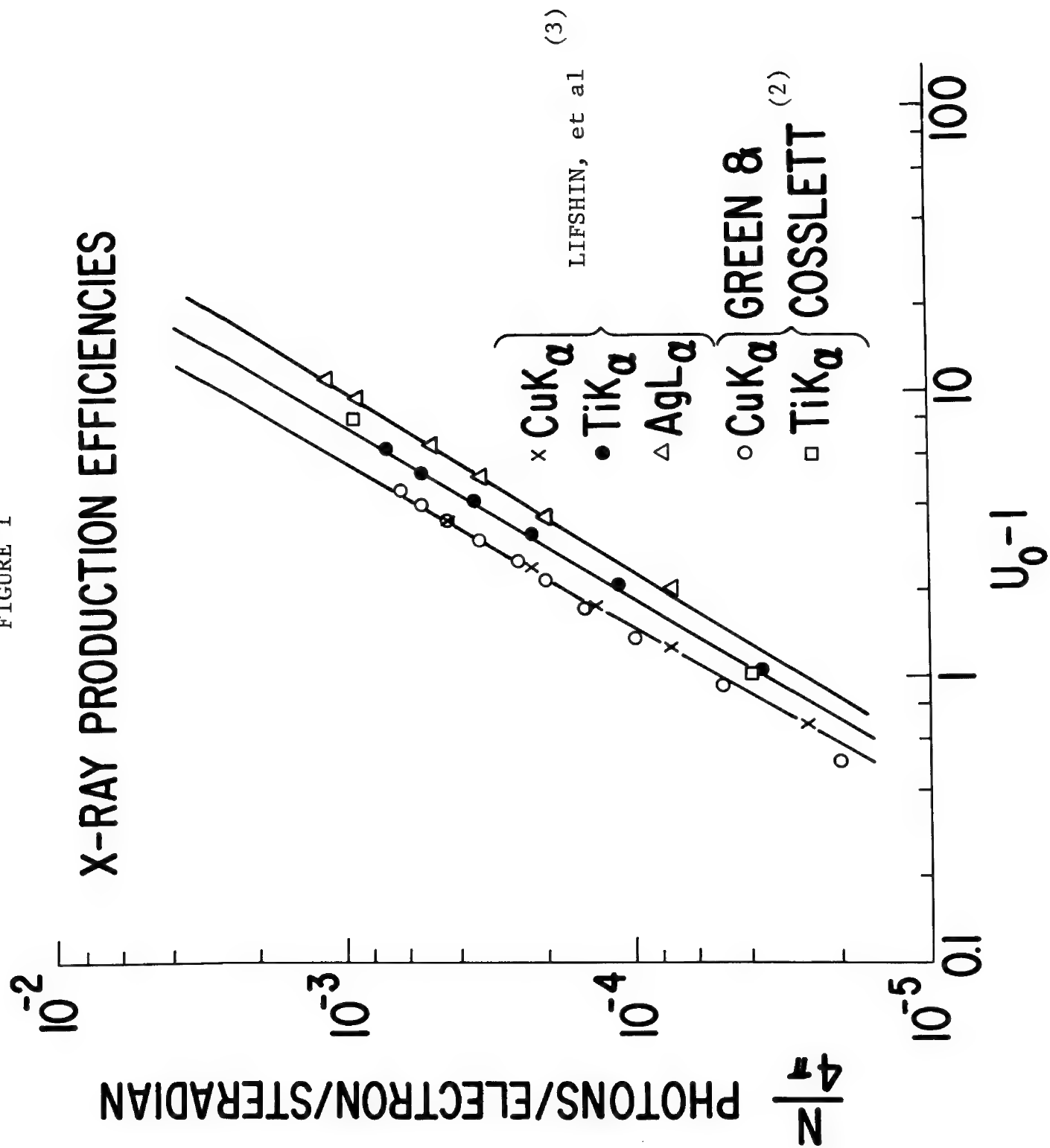
REFERENCES:

1. Kramers, H.A., Philosophical Magazine, Vol. 46, (1923)

2. Green, M. and Cosslett, V.E., Brit. J. Appl. Phys., (1966) Ser. 2, Vol. 1, p. 425

3. Lifshin, E., Ciccarelli, M.F. and Bolon, R.B. (1973) Proceedings of the Eighth National Conference on Electron Probe Analysis, New Orleans, August 13-17, Paper 29
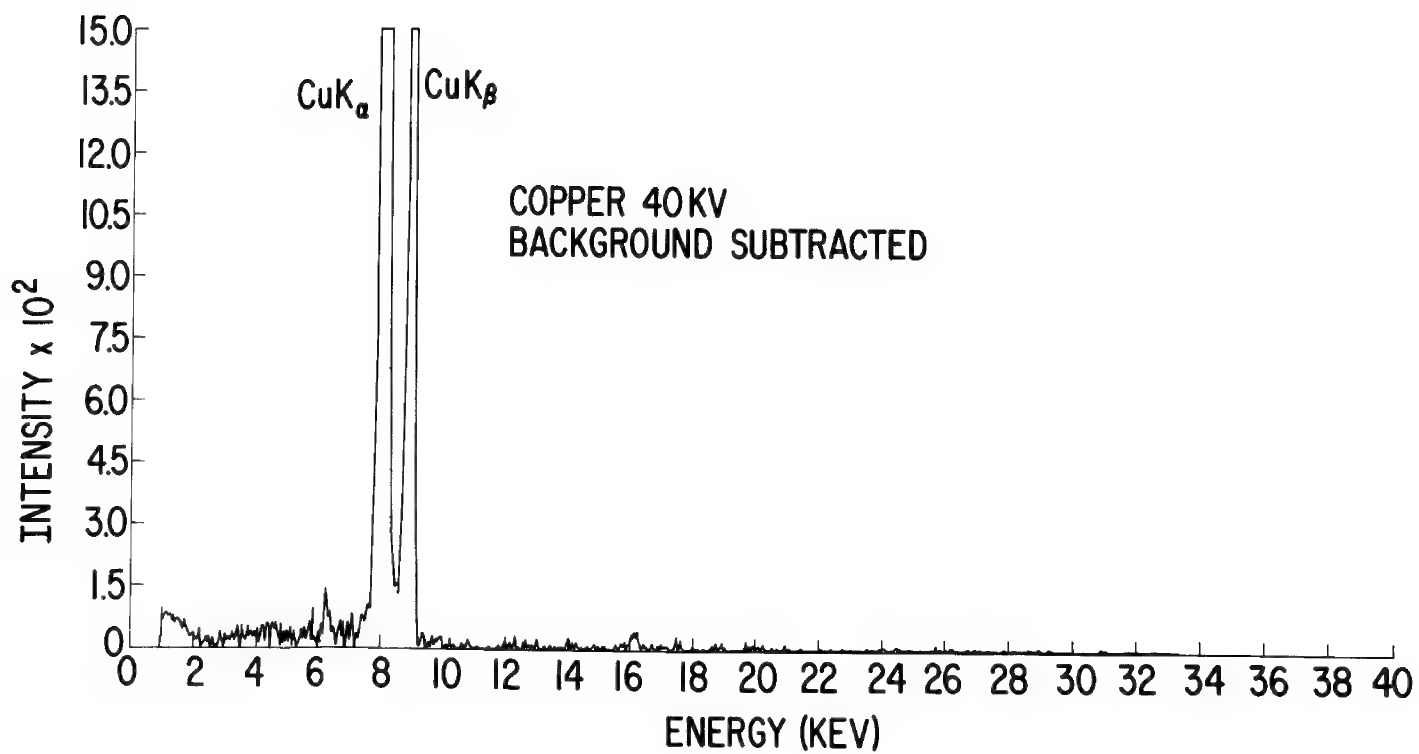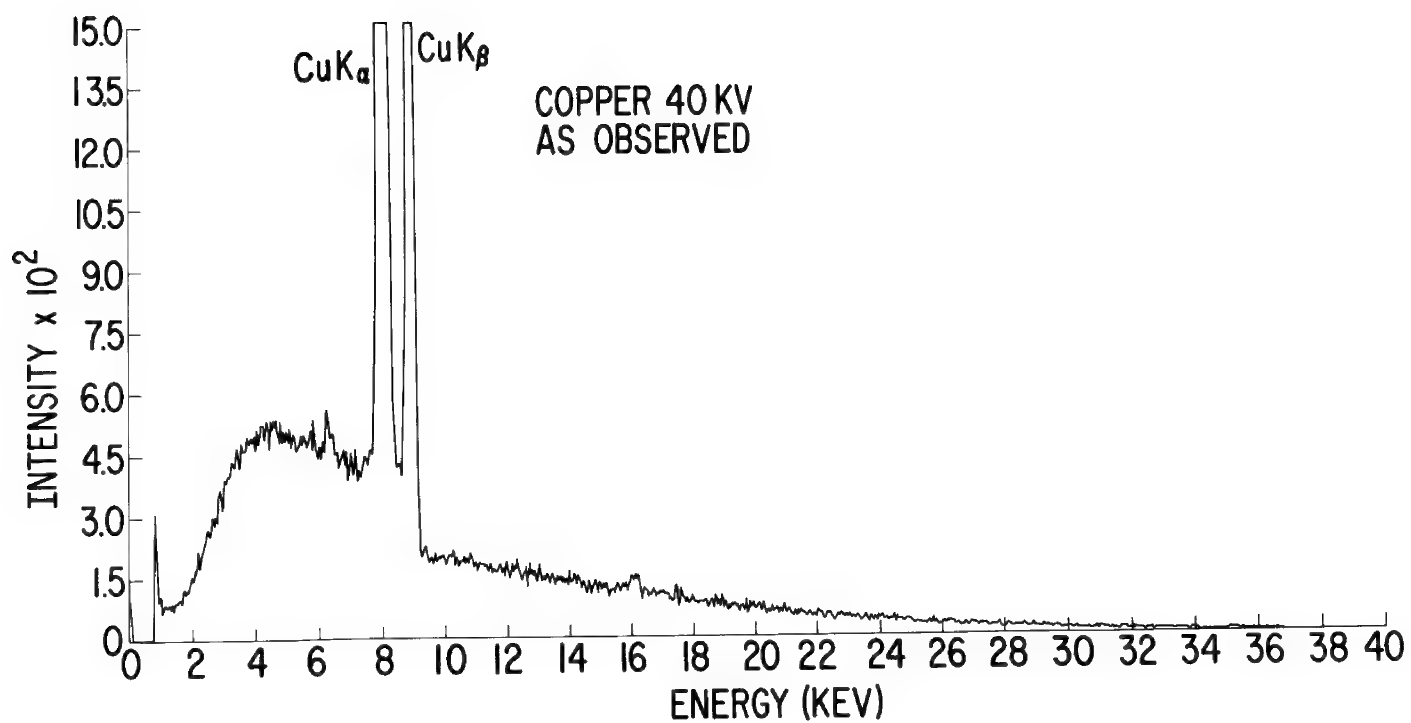
$$\frac{\eta}{4\pi} = \eta'\left(U_0-1\right)^n \qquad \text{to predict standard intensities}$$

FIGURE 1

X-RAY PRODUCTION EFFICIENCIES

TEM X-RAY ANALYSIS OF SUBMICRON PARTICLES

L. Berenbaum and A. S. Cammarano
IBM system Products Division
East Fishkill Facility
Hopewell Junction, N. Y.   12550

There are distinct advantages in using energy dispersive X-ray analysis (EDXRA) in the transmission electron microscope (TEM). The most significant advantage is the ability to do both EDXRA and selected area electron diffraction (SAED) sequentially on particles after they have been removed from substrates by extraction replication. These replicas consist of a thin carbon film with a random distribution of isolated particles where the carbon provides a lower background than could be achieved if the particles were examined while on their substrates. When the replica is placed in the TEM, it is possible to find the particles by following the topographic features of previously identified locations on these substrates.

The internal structure of the TEM differs considerably from the scanning electron microscope (SEM) and the electron microprobe (EMP). In the TEM, sample size is limited to a 3-mm diameter disc located in the microscope column below the objective lens but above the diffraction, intermediate, and projector lenses. A schematic cross-section through the column of the Philips EM 300 can be seen in Fig. 1.

SCHEMATIC OF CROSS-SECTION OF T.E.M. AT THE SAMPLE HOLDER
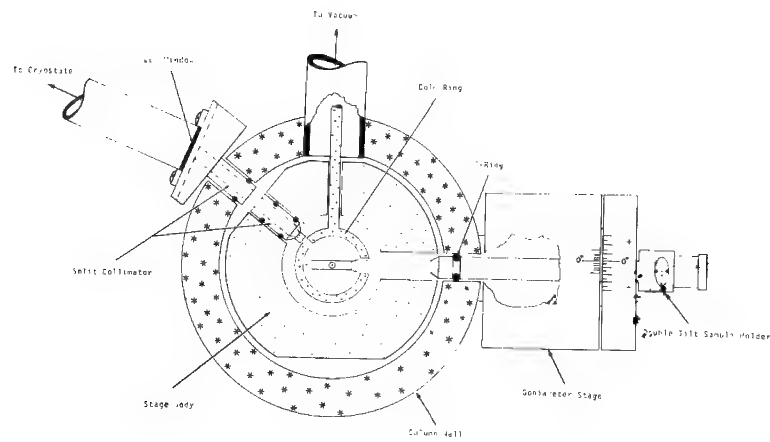
Fig. 1   Schematic of a cross section through the
          Philips EM 300 at the sample holder.

The X-ray detector is located outside the column with a line-of-sight path to the sample through a port in the column wall. For transmission electron microscopy it is important to use an anti-contamination device (cold ring) since the penetration power of electrons is seriously affected by increases in sample thickness; therefore, a hole is drilled through the cold ring to maintain the line of sight between the detector and the sample without eliminating the beneficial effects of the cold ring.

In this study, the following parameters were examined: 1) collimation (signal reduction and alignment), 2) sample-to-collimator positioning, 3) modification of the sample holder, 4) beam size, 5) accelerating voltage, and 6) counting time.

With the capability of utilizing 100 kV electrons, the amount of signal is no problem. In fact, it is very easy to generate excessive signals which swamp the detector during thin film analyses. This effect was remedied by reducing the internal diameter of the collimator and incorporating a pulse-pile up rejector/live-time corrector in the circuitry. Many collimator configurations were tried before a suitable diameter-to- length ratio was achieved.

The final structure consisted of a high-density nylon collimator holder with a 2.0mm i.d., 12.7mm long, spectrographically pure graphite insert.

Also, a problem existed in obtaining maximum alignment due to the massive liquid nitrogen Dewar attached by a long, narrow tube to the collimator assembly. . This condition was remedied by utilizing a split collimator (Fig. 2); thus the Dewar was in contact with only the portion of the collimator which connected to the microscope column while the critical section was separated. This latter section was machined to close tolerances so a perfect line-of-sight to the sample was always maintained.

After collimation and alignment was accomplished, it was necessary to examine the geometrical relationship of the plane of the sample to the electron beam so a maximum X-ray signal could be produced while minimizing the contributions from the internal structure of the microscope, particularly the sample holder.- The ideal condition was achieved by using a double tilt holder which allowed external sample positioning via two separate motor drives (Fig. 3).

It was recognized that we could operate in what was termed the "reflection" or "transmission" mode (Fig. 4), but for most problems, the transmission mode was most suitable.
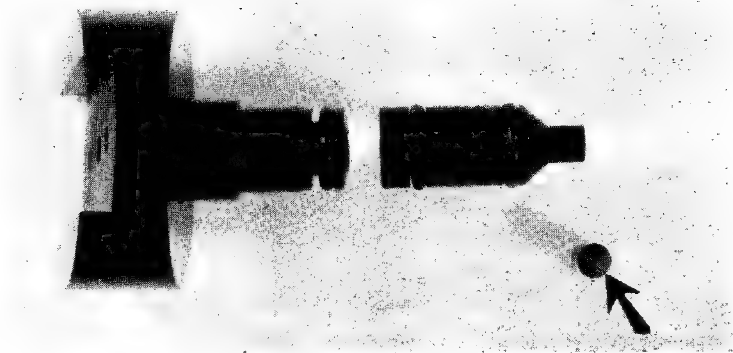
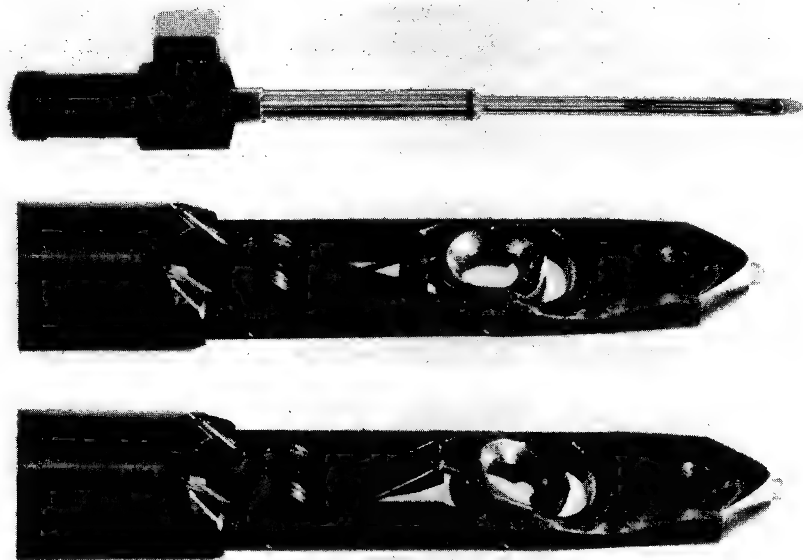Fig. 2 Split collimator showing the graphite
insert (arrow).

Fig. 3 Double tilt holder. Notice how the bucket can
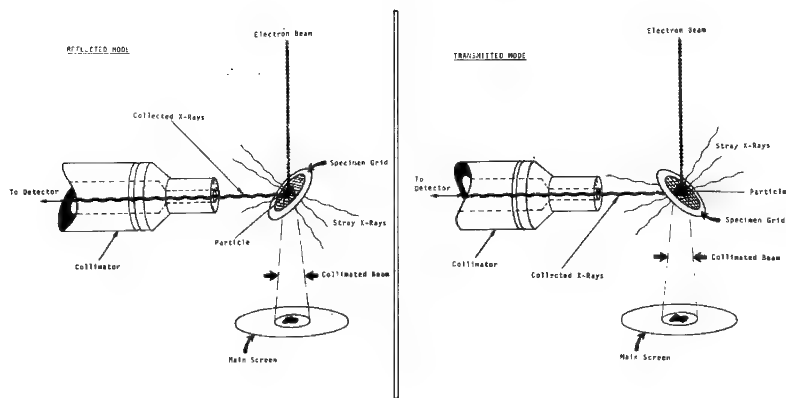be moved through ± 45° to the axis of the holder.

Fig. 4 Schematic of the sample to collimator position
in the "reflection" and "transmission" modes.

Elements which appeared in the background of the X-ray spectra were primarily Ni and Cu, although sometimes Cr and Zn were found. The presence of these elements was due entirely to the composition of the sample holder - a brass frame (accounting for the Zn and Cu) and a Ni "bucket" for the grid. By properly positioning the double diffraction holder, it was possible to eliminate the Cr and Cu peaks. The grids (Cu, Ti, or W) could be interchanged if a particular element was suspected of being in the sample; however, it is impossible to eliminate the peaks emanating from the grid without replacing them with non-detectable materials such as Be, C, or an organic material (e.g., nylon)*. The Ni peak from the "bucket" was reduced considerably by machining a channel in the sample holder to align with the collimator (Fig. 5).

Variations in beam energy were correlated to X-ray spectra for various samples. It was found that a 40- or 60-kV beam gave the best results for most of the samples, while occasionally an 80-kV beam gave superior results; 10, 20, and 100-kV beams never enhanced the X-ray spectra.

*The organic grids must be capable of dissipating the electronic charge.
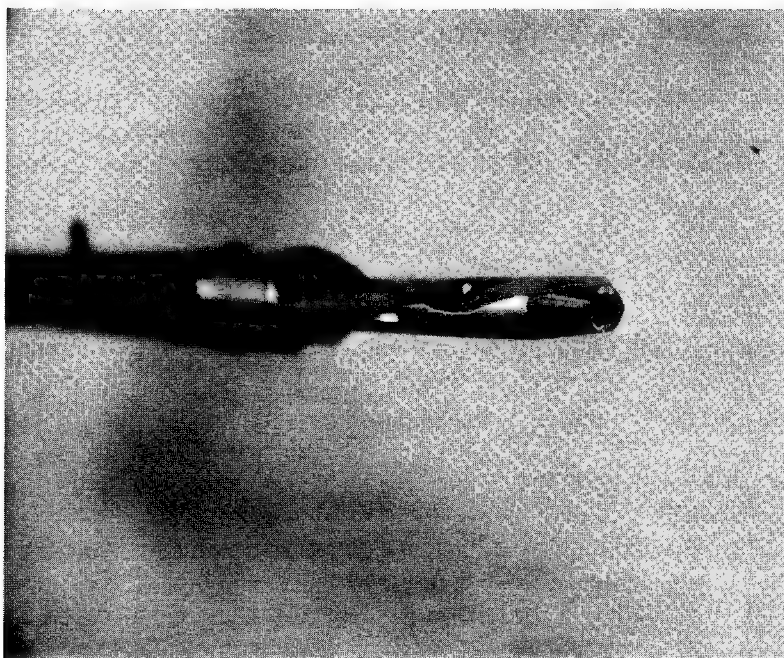
Fig. 5   Double tilt holder showing the groove machined
in the frame and the bucket to reduce the in-
tensity of the Ni peak.

Our main incentive for building this system was to
characterize sub-micron particulate matter mostly in the
0.2 to 0.5 μm range. To maximize the signal from such
a small volume ($\sim 10^{-15}$cc), beam size was reduced to a
minimum value of ~ 0.3 μm by varying the voltage to the
second condenser of the TEM. With a minimum beam size,
only a relatively small X-ray signal is generated, which
necessitates an increase in the counting time to obtain
a complete spectrum. It was determined that a counting
time of 300 sec. was adequate for the analysis of most
sub-micron particles.

An example of the effectiveness of this technique
was demonstrated by determining the composition of
0.3μm diameter particles where only a few reflections
could be obtained by electron diffraction. An X-ray
spectrum was generated with our EDXRA system (Fig. 6).
This system consists of a 158 eV, Li-drifted Si detec-
tor and a multi-channel analyzer with two separate
1024-channel memories. The Cu and Ni peaks are from
the grid and bucket, respectively. These peaks were
removed by spectrum stripping which left only the Ti
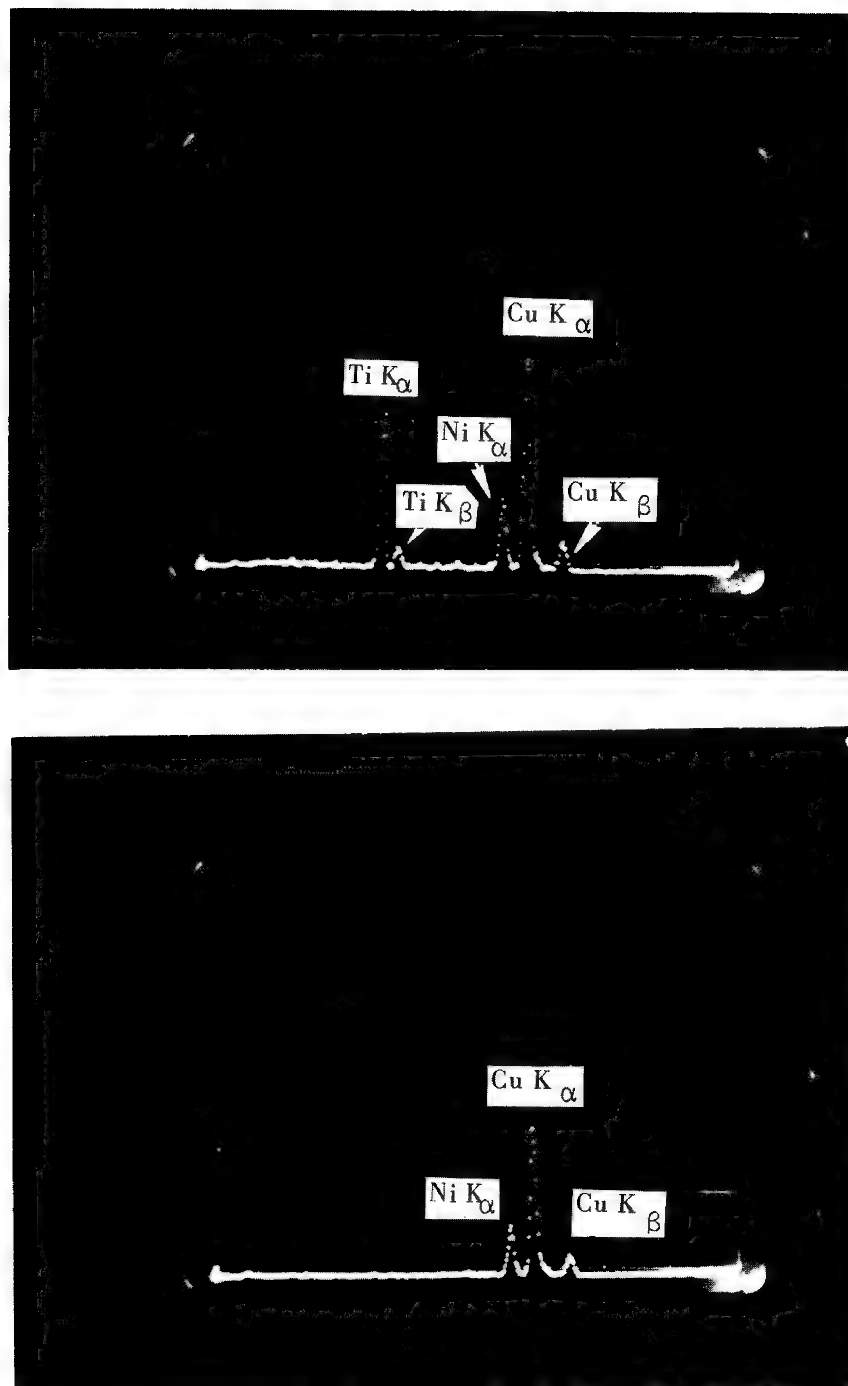peak as that emanating from the particle (Fig. 6).

Fig. 6   X-ray spectrum of an 0.3 μm particle removed
from a substrate by extraction replication.
a) Entire spectrum including the Ni and Cu
peaks from the bucket and grid, respectively;
b) Background away from particle.

With this knowledge, it was possible to index the electron diffraction pattern and identify the particle as the orthorhombic form of TiO_2. Other crystalline particles have been identified in a similar manner.

The identification of the elemental distribution within amorphous, sub-micron particles has also been quite valuable.

THE APPLICATION OF THE HARWELL ACTIVE PULSE PROCESSOR TO ENERGY DISPERSIVE X-RAY ANALYSIS IN THE ELECTRON MICROPROBE.

Peter J. Statham

Department of Mineralogy and Petrology,
University of Cambridge.

The rapid development of the lithium-drifted silicon detector and the mini-computer in recent years has made possible high-level automation in the electron-microprobe, with minimal operator intervention. With any system, however, quantitative reliability essentially depends on the integrity of the electronic processor and thus, its ability to minimise, or take account of, electronic noise, baseline drift, pulse overlap and dead-time measurement errors, all of which are agravated at high input counting rates. A useful assessment of the effects of such deficiencies has been carried out by Reed and Ware (1, 2, 3, 4). Reed (5) has shown that by working under controlled conditions, crystal-spectrometer accuracy with a detection limit of approximately .1% can be achieved in the field of silicate analysis, using fairly conventional nucleonics. However, the technique used involves empirical calibration, requires a number of precautions in setting-up and is restricted to a fixed range of elements.

A major advance in nucleonic design for energy-dispersive analysis has come from the work of Kandiah (6, 7) and Kandiah et al. (8) who have combined the use of opto-electronics for charge restoration at the input to the preamplifier with active pulse shaping involving time constants which are switched during the processing of each pulse. This work has given rise to a processor which has particular advantages over conventional systems with respect to automatic microprobe analysis. For example, resolution and gaussian peak profile are only slightly degraded and peak shift is small at high input counting rates. Our system gives a shift of 2.3 eV and a broadening of 20 eV for the Mn K line at an input rate of 50 k.P.P.S. when using a total processing time for a single pulse of 40 μs. Below 10 k.P.P.S. the shift and broadening are negligible. This performance gives useful latitude in operating conditions, the only important considerations being the usual reduction in output counting rate and the increased probability of pile-up events at higher input rates. The accumulation rate can, however, be greatly improved by using the technique of beam switching which may be incorporated with minor modification to the existing electronics (9). Pile-up is minimised by the use of a sophisticated pulse rejector system involving two detection channels which interact with the processor logic (10). An accurate livetime waveform, corrected for rejected events, is available and is used to gate a clock for live-time measurement. Analyses are thus simplified to recording a spectrum for a preset livetime, the accumulation being terminated automatically. In the Harwell equipment the electronic noiseline can be directly observed as part of the recorded spectrum during the course of an analysis. This, together with the Fano factor, provides the means of determining the spectral line width at any energy. A high linearity,

combined with low spectral distortion and small count-rate-dependent drift enable linear mathematical techniques which assume true gaussian profiles to be applied to the spectra to obtain maximal information.

As a direct consequence of the predictable and stable performance of the pulse-processing nucleonics, it has been possible to devise an operating system for quantitative microprobe analysis which requires no adjustments to the electronics by the operator. The system used in this work is the Harwell "Highspec" pulse analyser system 3074 which is interfaced to a D.G.C. Nova 1220 mini-computer, the spectrum being input directly to memory.

REFERENCES

(1)   REED S.J.B.   1972.   J. Phys. E: Sci. Instr. 5, 994.

(2)   REED S.J.B.   1972.   ibid.   5, 997.

(3)   REED S.J.B. and WARE N.G.   1972.   ibid. 5, 582.

(4)   REED S.J.B. and WARE N.G.   1972.   ibid. 5, 1112.

(5)   REED S.J.B. and WARE N.G.   1973.   X-ray Spectrometry, 2, 69-74.

(6)   KANDIAH K.   1966.   Radiation Meas. in Nucl. Power, (Inst. Phys and Physical Soc.), p. 420.

(7)   KANDIAH K.   1971.   Nucl. Inst. and Methods, 95, 289-300.

(8)   KANDIAH K., STIRLING A., TROTMAN D.L., and WHITE G.   (1968 Int. Symp. on Nucl. Electronics (Versailles).

(9)   STATHAM P.J., WHITE G., LONG J.V.P., and KANDIAH K.   1974. X-ray Spectrometry (in press).

(10) KANDIAH K.   1973.   Proc. 8th Nat. Conf. on Electron Probe Analysis, New Orleans   (E.P.A.S.A.).

A MONOCHROMATIC X-RAY PROBE FOR THE ANALYSIS OF TRACE ELEMENTS

P. S. Ong and H. L. Cox, Jr.
The University of Texas System Cancer Center
M. D. Anderson Hospital and Tumor Institute
Houston, Texas 77025

The photon excited energy dispersive x-ray analyzer has many attractive features for the analysis of trace metals in biological specimens. The sensitivity of such a system is greatest for x-ray energies in the 5-15 KeV range which coincides with the K and L energies of the trace elements of biological interest. Since a number of elements are simultaneously measured in an energy dispersive system, a trace element profile could be obtained. Such a profile determined in blood serum samples reflects the trace element balance in the human body, and therefore could be related to health and disease. Since the elemental composition of the matrix in biological samples is reasonably constant, Compton scattered radiation is proportional to the sample mass requiring only a simple callibration method to determine the total mass of the specimen. The results of trace element determinations could therefore be expressed directly in weight per cent. Also, the energy dispersive analyzer lends itself to automation and computerization for routine analyses in a clinical pathology laboratory.

Two basic problems are associated with the use of an energy dispersive x-ray analyzer for bio-medical material:

1. The matrix consists of elements with low atomic numbers. Therefore, Compton scattering is excessive. Typically, the photons emitted by the sample consist of more than 99 per cent scattered radiation.

2. The fluorescence cross section for photon excitation for the elements of interest is relatively small. Therefore, the sensitivity is below that of other techniques.

The limit of detectability in terms of concentration of an x-ray analyzer may be expressed as[1]

$$C_{DL} = 3.29 \; \underline{a} \; [I_0 Rt]^{-1/2}$$

in which C_{DL} is the minimum detectable concentration, I_0 the x-ray intensity, R the peak to background ratio to measuring time, and $\underline{a}$ a conversion parameter.

Since the background is basically scattered primary radiation, it is essential that the excitation radiation be completely monochromatic.

A clinical analytical instrument should be able to handle small specimens; this is particularly true for blood samples from infants and biopsies. A typical needle biopsy is about 2 mm in diameter or 2 cm in length. Serum samples from infants should be less than 500 µl.

A focusing x-ray monochromator is being constructed to study these characteristics and to produce an x-ray probe for analysis of trace elements in biological samples. The study will include the selection of one or more energies, most suitable for the proposed analyzer. The energies currently being considered and the elements for which these are to be used are shown in Table I.

TABLE I.

Target	Line	Energy (KeV)	For Excitation of
Zr	Kα	15.7751	Br, Se, As, Zn, Cu, Ni, Co, Hg (L), Pb (L)
Mo	Kα	17.4793	Br, Se, As, Zn, Cu, Ni, Co, Hg (L), Pb (L)
Cu	Kα	8.04778	Fe, Mn, Cr, V, Ti, Cd (L), I (L)

In its present form, the system consists of a high power (500 watt, sealed off, water cooled) x-ray tube with the appropriate target material, a line focusing Johannson type LiF crystal, a sample holder, and an energy dispersive analyzer. The 'source' is a pinhole, 300 to 600 micron in diameter.

In future refinements, a double focusing crystal, a viewing optical system, a sample stage, and a proportional counter for measuring the direct beam will be incorporated. This is shown in Fig. 1. Eventually, the pinhole source will be replaced by a high brilliancy fine focusing x-ray tube which could reduce the power requirements considerably.
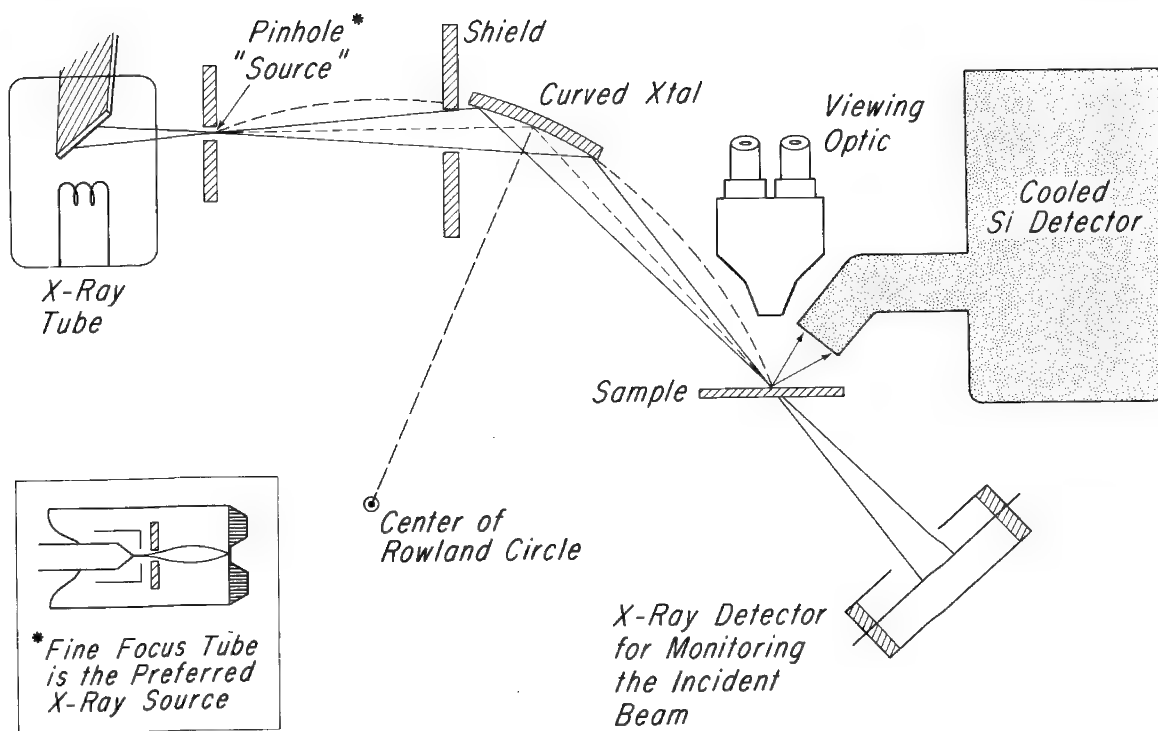
Pinhole "Source"

Shield

Curved Xtal

Viewing Optic

Cooled Si Detector

X-Ray Tube

Sample

Center of Rowland Circle

X-Ray Detector for Monitoring the Incident Beam

*Fine Focus Tube is the Preferred X-Ray Source

Fig. 1

Reference

1. Ziebold, T.O.: Precision and sensitivity in electron microprobe analysis. Anal. Chem. 39:858, 1967.

INDEX OF AUTHORS AND THEIR AFFILIATIONS

Brandis, E.K.	IBM System Products Division, East Fishkill Facility, Hopewell Junction, N.Y. 12533	45
Bronner, C.	Department of Physiology, Duke University Medical Centre, Durham, N.C. 27710	9
Brown, J.D.	Faculty of Engineering and Centre for Interdisciplinary Studies in Chemical Physics, The University of Western Ontario, London N6A 3K7	39
Cammarano, A.S.	IBM System Products Division, East Fishkill Facility, Hopewell Junction, N.Y. 12550	54
Chamberlain, M.B.	Air Force Materials Lab., Wright Patterson Air Force Base, Ohio 45433	46
Chatfield, E.J.	Department of Applied Physics, Ontario Research Foundation, Sheridan Park, Mississauga, Ontario	Tutorial 28
Ciccarelli, M.F.	General Electric Company, P.O. Box 8, Schenectady, N.Y. 12301	37
Claisse, F.	Laval University, Quebec, P.Q.	Tutorial
Coleman, J.R.	University of Rochester School of Medicine and Dentistry, Rochester, N.Y. 14642	12
Conley, D.K.	Western Electric Co., Allentown, Pennsylvania	44
Corlett, M.I.	Department of Geological Sciences, Queen's University, Kingston, Ontario	23
Cox, H.L., Jr.	The University of Texas System Cancer Center, M.D. Anderson Hospital and Tumor Instit., Houston, Texas 77025	56
Crewe, A.V.	Department of Biophysics, The University of Chicago, Chicago, Illinois	1
DeNee, P.B.	National Inst. for Occupational Safety and Health, P.O. Box 4292, Morgantown, West Virginia 26505	4,10
Devaney, J.R.	Hi-Rel. Labs., 2116 Huntington Dr., San Marino, Calif. 91108	31
DiGiacomo, G.	IBM System Products Division, East Fishkill Facility, Hopewell Junction, N.Y. 12533	41

Estill, W.B.	Materials Characterization Division 8314, Sandia Laboratories, Livermore, Calif. 94550	35
Fiori, C.E.	Inst. for Materials Research, National Bureau of Standards, Washington, D.C. 20234	5
Gelderman, A.H.	National Institute for Occupational Safety and Health, P.O. Box 4292, Morgantown, West Virginia 26505	10
Glover, E.D.	Department of Geology and Geophysics, University of Wisconsin, Madison, Wisconsin 53706	36
Gold, C.L.	Technical Equipment Corp., Denver, Colo. 80204	3
Goldak, J.	Carleton University, Ottawa, Ontario	14
Harada, Y.	JEOL Ltd., Akishima, Tokyo, 196, Japan	33
Hatfield, W.T.	General Electric Company, P.O. Box 8, Schenectady, New York 12301	37
Heinrich, K.F.J.	Inst. for Materials Research, National Bureau of Standards, Washington, D.C. 20234	5, 40
Ingram, F.D.	Department of Physiology and Biophysics, University of Iowa, Iowa City, Iowa 52242	11
Ingram, M.J.	Department of Physiology and Biophysics, University of Iowa, Iowa City, Iowa 52242	11
Jarosewich, E.	Department of Mineral Sciences, Smithsonian Institute, Washington, D.C. 20560	20
Jenkins, R.	Philips Electronic Instruments, 750 South Fulton Ave., Mount Vernon, N.Y. 10550	Tutorial
Jones, H.D.	Numerical Applications Division 8441, Sandia Laboratories, Livermore, Calif. 94550	35
Kane, W.T.	Corning Glass Works, Corning, New York 14830	32
Kirk, R.G.	Department of Physiology, Duke University Medical Center, Durham, N.C. 27710	9
Kirkendall, T.D.	Communications Satellite Corp., COMSAT Laboratories, Clarksburg, Maryland 20734	24

Kyser, D.F.	IBM Research Lab., San Jose, Calif. 95193	17
Lechene, C.	Biotechnology Resource in Electron Probe Microanalysis, Harvard Medical School, Boston, Mass. 02115	8,9 34
Lesher, D.F.	Western Electric Co., Allentown, Pennsylvania	44
Leys, J.A.	Central Research Laboratories, 3M Company, P.O. Box 33221, St. Paul, Minn. 55133	48,52
Lewis, R.K.	Cameca Instruments, Inc., Elmsford, N.Y. ·10523	50
Lifshin, E.	General Electric Company, P.O. Box 8, Schenectady, New York 12301	37
MacDonald, N.C.	Physical Electronics Industries, Inc., Edina, Michigan	42
Marsden, D.A.	Ontario Department of Health, 360 Christie St., Toronto, Ontario	29
McDonald, M.	Department of Geological Sciences, Queen's University, Kingston, Ontario	23
McKinney, J.T.	Central Research Laboratories, 3M Company, P.O. Box 33221, St. Paul, Minn. 55133.	48,52
Michel, C.	Philips Laboratories, Briarcliff Manor, N.Y. 10510	18
Moher, T.	Biotechnology Resource in Electron Probe Microanalyses, Harvard Medical School, Boston, Mass. 02138	34
Morabito, J.M.	Bell Telephone Labs. Inc., Allentown, Pennsylvania	49
Moran, P.	University of Rochester School of Medicine and Dentistry, Rochester, N.Y. 14642	12
Morettini, L.	Inst. di Metallurgia, V. le Risorgimmento, 4-Bologna, Italy	15
Murata, K.	IBM Research Lab., San Jose, Calif. 95193	17
Myers, R.M.	Canadian Conservation Inst., Ottawa, Canada K1A 0M8	16
Myklebust, R.L.	Inst. for Materials Research, National Bureau of Standards, Washington, D.C. 20234	6,40

Nelen, J.	Dept. of Mineral Sciences, Smithsonian Inst., Washington, D.C. 20560	20
Newbury, D.E.	Inst. for Materials Research, National Bureau of Standards, Washington, D.C. 20234	5,6 40
Nielsen, V.	Dept. of Applied Physics, Ontario Research Foundation, Sheridan Park, Mississagua, Ontario	28
Nixon, W.C.	Engineering Dept., Cambridge University, England	27
Obermeyer, C.	Department of Mineral Sciences, Smithsonian Inst., Washington, D.C. 20560	20
Ohyi, H.	JEOL Ltd., Akishima, Tokyo, 196, Japan	33
Okudera, S.	JEOL Ltd., Akishima, Tokyo, 196, Japan	33
Ong, P.S.	The University of Texas System Cancer Center, M.D. Anderson Hospital and Tumor Inst., Houston, Texas 77025	3,56
Parobek, L.	Faculty of Engineering Science and Centre for Interdisciplinary Studies in Chemical Physics, The University of Western Ontario, London N6A 3K7	39
Rusch, T.W.	Central Research Laboratories, 3M Company, P.O. Box 33221, St. Paul, Minn. 55133	48
Russ, J.C.	EDAX Laboratories, 4509 Creedmoor Rd., Raleigh, N.C. 27612	22
Sanderson, R.	Division of Engineering and Applied Physics, Harvard University, Cambridge, Mass. 02138	34
Schulson, E.M.	Atomic Energy of Canada Ltd., Chalk River Nuclear Lab., Chalk River, Ontario	29
Shaw, G.B.	Suite 703, Medical Tower, Jackson, Miss. 39216	10
Sheble, A.M.	Hi-Rel Labs., 2116 Huntington Dr., San Marino, Calif. 91108	31
Sicignano, A.	Philips Laboratories, Briarcliff Manor, N.Y. 10510	18
Solomon, J.S.	University of Dayton Research Inst., Dayton, Ohio	46
Solosky, L.F.	The Dow Chemical Company, Midland, Mich. 48640	26
Soni, S.L.	Department of Agriculture, Ottawa, Ontario	13

Springer, G.	Falconbridge Nickel Mines Ltd., 8810 Yonge St., Thornhill, Ontario	38
Statham, P.	Department of Mineralogy and Petrology, University of Cambridge, Cambridge, England	21,55
Steele, W.J.	Lawrence Livermore Lab., University of California, Livermore, Calif. 94550	19
Taylor, J.M.	Canadian Conservation Inst., Ottawa, Canada, K1A 0M8	16
Teel, T.P.	Hi-Rel Labs, 2116 Huntington Dr., San Marino, Calif. 91108	31
Tousimis, A.J.	Biodynamics Laboratories, Tousimis Research Corp., 6000 Executive Blvd., Rockville, Maryland 20852	7
Vastel, J.	CAMECA, 92400 Courbevoie, France	50
Walsh, J.M.	Pratt and Whitney Aircraft, Material Engineering and Research, 400 Main St., East Hartford, Conn. 06108	51
Warner, R.R.	Department of Physiology, Yale University School of Medicine, New Haven, Conn.	12
Wehner, G.K.	University of Minnesota, Electrical Engineering Department, Minneapolis, Minn.	43
Wells, O.C.	IBM Thomas J. Watson Research Center, P.O. Box 218, Yorktown Heights, N.Y. 10598	2
Welter, L.M.	Coates and Welter Instrument Corp., 777 N. Pastoria Ave., Sunnyvale, Calif. 94086	30
Wolf, R.C.,	Microspec. Inc., 999 Commercial St., Palo Alto, Calif. 94303	25
Wolff, U.E.	General Electric Co., Vallecitos Nuclear Center, Pleasanton, Calif. 94566	25
Yakowitz, H.	Inst. for Materials Research, National Bureau of Standards, Washington, D.C. 20234	5,6 40

MICROBEAM ANALYSIS SOCIETY

(formerly The Electron Probe Analysis Society of America)

BY-LAWS

ART I. Name.

The name of the Society shall be the Microbeam Analysis Society (formerly The Electron Probe Analysis Society of America). The Society is duly incorporated under the laws of the State of New York.

ART II. Purpose

The purpose of this Society shall be to provide continuity, advance planning, and a financing mechanism for annual meetings and to advance and diffuse knowledge concerning the principles, instrumentation, and applications of electron probes or related instrumentation, subject to the provisions of the Internal Revenue Code, Section 501(c) (3), (1954).

ART III Membership.

The membership of the Society shall consist of Regular Members, Honorary Members, Student Associates, and Sustaining Members.

Section 1. Eligibility:

i. Regular Members: Any person interested in the use of electron microprobes or related instrumentation shall be eligible for Regular Membership in the Society. Every person desiring to become a Regular Member shall in person or by authorized representative make application in writing for such membership.

ii. Student Associates: Any graduate or undergraduate college or university student interested in the use of electron microprobes or related instrumentation is eligible to become a Student Associate. Evidence of such interest must be certified by the faculty advisor for this student.

iii. Sustaining Members: Any business or corporation interested in supporting the aims and objects of the Society may become a Sustaining Member upon acceptance by the Executive Council and payment of the annual dues set for Sustaining Members. The Sustaining Member may designate one individual in his organization who shall have voting rights in the name of the Sustaining Member.

iv. Honorary Members: Any person whose contributions to the field of electron probe microanalysis are of the highest order is eligible for election to Honorary Membership in the Society. The number of Honorary Members shall not be increased so as to exceed two percent of the number of Regular Members.

Section 2. Nomination and Election: Application for all classes of membership except Honorary Members must be endorsed by at least two Regular Members and forwarded to the Secretary. Nominations to Honorary Membership must be endorsed by at least ten percent of the Regular Membership. A majority vote of approval of the members of the Executive Council present and voting at a regular or a special meeting shall constitute election to Honorary Membership.

Section 3. Privileges. The right to vote at elections and to hold office shall be restricted to and vested in the Regular Members of the Society in good standing. Regular Members representing a Sustaining Member shall retain their privileges as individual Regular Members.

Section 4. Termination of Membership: Membership in the Society may be terminated at any time for cause by a two-thirds majority vote of the Executive Council present and voting.

ART IV. Executive Council.

The affairs of the Society shall be managed by an Executive Council consisting of the President, Secretary, and Treasurer of the Society, the President-Elect, the immediate past President, and three Members-at-Large. A majority of the members of the Executive Council shall constitute a quorum.

A member of the Executive Council may designate an alternate to represent him at a specific council meeting with voting privileges. This alternate must be a member in good standing.

Section 1. Election of Officers: Any regular member of the Society shall be eligible for election to any office in the Society. Each year a Nominating Committee, selected in the manner specified below, shall nominate two or more candidates for each of the offices of the Society which will become vacant at the end of the year.

ART IV cont'd.

The Secretary shall read the names of the nominees at the annual business meeting. At that time, additional nominations may be made from the floor provided that those whose names are placed in nomination do agree to serve if elected. All nominations from the floor shall require three seconding affirmations. Election shall be by secret, written ballot. The Secretary shall distribute written ballots prior to October first. The deadline for receipt of marked ballots shall be November first. Election shall be by a plurality of those voting for each office.

Section 2. Terms of Office: The term of office for the President and President-elect shall be for one year. The term of office of the Secretary and Treasurer shall be for two years with one of these officers to be elected each year. The Secretary's two year term shall start in 1971 and the Treasurer's two year in 1972. One Member-at-large shall be elected each year to serve a three year term; he shall replace the Member-at-large whose term has expired. No officer except the Secretary and Treasurer may succeed himself in the same office.

The President-elect shall become President of the Society upon the expiration of the President's term of office. If the office of the Presidency becomes vacant before expiration, the President-elect shall assume the duties of the President. If a vacancy occurs in any other office, the Executive Council shall appoint a Regular Member of the Society to serve out the unexpired year of the term of the original officer. Thereafter the vacant office will be filled at the next regular election.

Section 3. Duties of the Officers:

i. President: The President shall be the executive officer of the Society, shall preside over all meetings of the Executive Council, and shall be responsible for the execution of all orders and resolutions of the Society.

The President shall appoint all committee members with the advice and assistance of the Executive Council.

ii. President-Elect: The President-Elect shall assume the duties of the President in his absence or incapacity and shall perform such other duties as may be delegated to him by the President or the Executive Council.

iii. Secretary: The Secretary shall keep precise and permanent records of the business of the Society including minutes of the annual meeting and Executive Council meetings.

He shall be responsible for all matters relating to membership including updating of membership lists.

iv. Treasurer: The Treasurer is responsible for all financial records of the Society. He shall prepare a financial report for each meeting of the Executive Council and the annual business meeting.

ART V. Committees

Section 1. Standing Committees: Any committee established to provide continuing assistance to the Executive Council shall be considered as a Standing Committee. The President shall appoint the Chairman and members of a Standing Committee; their terms of office shall expire on December 31st following appointment. The Chairman of each Standing Committee shall be an advisory member of the Executive Council and shall be invited to Executive Council meetings.

i. Nominating Committee: The Nominating Committee for officers shall be appointed by the Executive Council not later than February first of each year. The Nominating Committee shall consist of at least four members and shall include at least two regular Members who are not members of the Executive Council.

The Nominating Committee shall report in writing to the Secretary the names of those selected to be candidates for offices in the Society not later than two calendar months prior to the annual business meeting of the Society. The Committee shall ascertain, and so inform the Secretary, that each prospective nominee will serve if elected. The Secretary shall inform the membership of the names of the nominees at least one month prior to the annual meeting of the Society.

ii. Conference Committee: The Conference Committee shall consist of four members. The Chairman shall be the General Chairman of the National Conference for the present year. Other members shall be the General Chairman of the immediate past year and the two immediate future years. General arrangements and policy for the annual technical meeting shall be approved by the Conference Committee. The preliminary budget of an annual meeting shall be approved by the Executive Council in the fall of the year preceeding that meeting.

ART V cont'd.

iii. <u>Legal Committee</u>: The Chairman of the Legal Committee shall be appointed by the President. Other members of this Committee shall be the Secretary and one other Council member. This Committee shall advise the Executive Council on the legal matters of the Society.

Section 2. <u>Other Committees</u>: The Executive Council shall have the power to establish such other committees as it may deem desirable to aid in the management of the Society. The President shall appoint the chairman and members of each committee and designate the term of appointment.

ART VI. Dues.

Section 1. The Executive Council shall fix the annual dues, these dues being payable on January first of each year.

i. The dues for Regular Members shall not exceed ten dollars ($10.00).

ii. The dues for Student Associates shall be one-half that of Regular Members for the first five years of membership. After five years a Student Associate must apply for Regular Membership.

iii. The dues for Sustaining Members shall not exceed one thousand dollars ($1,000.00).

iv. There shall be no dues for Honorary Members.

Section 2. A person elected to membership becomes a member in good standing upon payment of the designated dues. If the dues of any class of member remain unpaid on July first, the Executive Council shall be empowered to remove such a member from the membership list.

Section 3. For dues and other fiscal purposes, the fiscal year shall be January first to December thirty-first.

ART VII. Meetings

Section 1. There shall be an annual technical meeting of the Society held in the period June through September whose location and exact dates shall be established by the Executive Council.

Section 2. There shall be an annual business meeting of the Society held concurrently with the annual technical meeting.

ART VIII. Local Sections.

Section 1. An organized group interested in becoming a local section of the Society may Petition the Executive Council for local section status. The petition should include:
   a. a list of officers and the date of expiration of their offices
   b. a copy of the Constitution and By-Laws of the local section
   c. a list of all current members of the local section

Approval of this petition by the Executive Council shall constitute establishment of the local section.

Section 2. The Constitution and By-Laws of such local sections shall be consistent and in harmony with the objectives and By-Laws of the Society. Authorization of a local section shall imply no financial obligations on the part of the Society, the Executive Council, or the local section.

Section 3. The local sections shall have the power to collect dues. All local sections shall submit an annual financial statement to the Treasurer of the Society at the end of each fiscal year (December 31st).

Section 4. Officers of the local sections must be Regular Members of the Society. The secretary of the local section shall inform the Secretary of the Society of the results of election of local officers. The secretary of the local section shall maintain a current roster of local members with the Secretary of the Society.

Section 5. The Executive Council has the power to suspend temporarily the affiliation of any local section not acting in the best interests of the Society. Permanent suspension shall be subject to confirmation by the membership of the Society.

ART IX. Amendments to the By-Laws.

Amendments to these By-laws may be proposed by the Executive Council or by a petition to the President signed by at least two percent of the total number of Regular Members. The text of the proposed amendment shall be circulated to all Regular Members by the Secretary at least two weeks in advance of the annual business meeting of the Society at which discussion is planned on the amendment. Members shall vote by written ballot and the amendment shall be adopted if it is favored by three-fifths of the members voting.

ART X. Dissolution of the Society

In the event of either voluntary or involuntary
dissolution of the Society, the funds
or assets of the Society remaining after
discharging all just debts of its officers
in the name of the Society shall be
distributed without encumbrance to
a non-profit group, organization, or
institution of learning within the
contemplation of Section 180 (c)(2) of
the Internal Revenue Code (1954). The
selection of the recipient or recipients
shall be made by the majority vote of the
Executive Council in office at the time
of dissolution, but in no event shall the
assets be distributed to any member or
employee of the Society.